"Analysis and design of microwave passive components in NRD-guide technology"

by
Piotr Jędrzejewski

A dissertation submitted in partial satisfaction of the
requirements for the degree of Doctor of Philosophy in
Electronic Engineering
in the
Faculty of Electronics, Telecommunications and Informatics
of the
Technical University of Gdańsk

Supervisor: Professor Michał Mrozowski, Faculty of Electronics,
Telecommunications and Informatics of the Technical University of Gdańsk

Reviewers: PhD Marek Kitliński, Faculty of Electronics,
Telecommunications and Informatics of the Technical University of Gdańsk
Professor Józef Modelski, Faculty of Electronics
of the Technical University of Warsaw

Gdańsk 1999

Contents

Symbol conventions

General symbols

$\mathbf{L}$	—	operator
u	—	function
α	—	scalar parameter
$\underline{\underline{A}}$	—	matrix
$\underline{a}$	—	vector of parameters
z	—	longitudinal direction
x, y	—	transverse directions
$\vec{A}$	—	vector function
$\vec{A}_x$	—	transverse x direction component of a vector function
$\vec{A}_y$	—	transverse y direction component of a vector function
$\vec{A}_z$	—	longitudinal component of a vector function
j	—	imaginary unity
$\vec{i}_x$	—	unit vector in transverse x direction
$\vec{i}_y$	—	unit vector in transverse y direction
$\vec{i}_z$	—	unit vector in longitudinal z direction
$\vec{n}$	—	unit vector normal to a surface
$(.)^*$	—	complex conjugation
$\|\| \cdot \|\|_2$	—	norm in a Hilbert space
Ω	—	region in a 2D space

Physical quantities

$\vec{E}$	—	electric intensity
$\vec{H}$	—	magnetic intensity
Ψ_e	—	electric Hertz potential
Ψ_h	—	magnetic Hertz potential
$\vec{J}$	—	current density
ϵ_0	—	permittivity of the free space
μ_0	—	permeability of the free space
ϵ_r	—	relative permittivity of the medium
μ_r	—	relative permeability of the medium
ϵ	—	complex permittivity of the medium

$\epsilon^{'}$	—	real part of complex permittivity of the medium
$\epsilon^{''}$	—	imaginary part of complex permittivity of the medium
c	—	speed of light in the free space
ω	—	angular frequency
f	—	frequency
λ	—	guide wavelength
β	—	phase constant
k	—	wavenumber
k_0	—	wave propagation constant; $k_0 = \omega\sqrt{\epsilon_0\mu_0}$
V	—	voltage
I	—	current
P	—	power
Z	—	impedance
R_s	—	surface resistance
K	—	impedance inversion factor

Operators

$\nabla_z \times (.)$	—	longitudinal rotation operator
$\nabla_t \times (.)$	—	transverse rotation operator
$\nabla_t(.)$	—	transverse gradient operator

Filter parameters

L_{A_r}	—	ripple level in pass band in [dB] for Chebyshev characteristic type
L_{A_e}	—	attenuation level in [dB] for band edge frequency
w_λ	—	fractional bandwidth in waveguide domain
w_f	—	fractional bandwidth in frequency domain
f_0	—	center frequency
f_1, f_2	—	band edge frequencies
Δf_0	—	relative center frequency error
Δw_f	—	relative fractional bandwidth error

Selected abbreviations

LSE	—	Longitudinal Section Electric
LSM	—	Longitudinal Section Magnetic
LPP	—	Low Pass Prototype
$HWSIP$	—	Half-Wave Step-Impedance Prototype
$FDTD$	—	Finite Difference Time Domain
TRM	—	Transverse Resonance Method
DUT	—	Device Under Test
VNA	—	Vector Network Analyzer
TRL	—	Thru-Reflect-Line Method

Chapter 1

Introduction

1.1 Background and Motivation

An incredible growth of new telecommunication systems has been observed in the past two decades. Novel services have been developed rapidly and located in the exploding market and the number of possible applications of telecommunication systems has grown up drastically. The conventional RF frequency band is now practically filled up and no more new systems can be located in this frequency region. Hence, the microwave and millimeter wave bands are treated as the frequency region where new technologies are placed [1]. In the usual classification scheme, the microwaves span from 300 MHz to about 30 GHz while the millimeter waves cover the frequencies from 30 to 300 GHz. The technology of microwave circuits and systems is well established by now and a lot of commercial and military systems use microwave band. However, the millimeter waves are gaining particular interest because of lack of free, sufficiently large, frequency windows in the microwave band, required by novel broadband systems. In addition, millimeter waves have some specific, very attractive features which distinguish them from the RF and microwave regions [2]. The most important are: possibility to re-use frequencies, high capacity, high resolution and quasi optical propagation. The devices working in millimeter waves have smaller size and lower weight than the microwave counterparts. The antennas achieve higher gain and have modest sizes suitable for mobile systems. Therefore the newest communication systems are located in the lower millimeter wave region spanning from 30 to 100 GHz. These systems include personal communication networks and systems (PCN, PCS), high speed data links for wireless LAN, car collision avoidance radar systems, intelligent motorways and various radar systems [3], [4] [5]. For some systems the research and development phase is almost finished, the obtained results are very promising and these systems are prepared to be commercially applied [6] [7].

Practical realization of the millimeter-wave systems requires the technology which ensures the possibility to build the elements and integrated circuits which are small in size, compact and offer low transmission losses. In addition, the incorporation of antennas into integrated systems, which is usually problematic, should be possible. Besides the technical features, the commercial factors play an important role in practical development of partic-

ular technology [6]. The key commercial factors are low manufacturing costs and relatively simple mass production. Several technologies are in use at present which fulfil more or less the criteria mentioned above. In general, the technologies suitable for the microwaves and millimeter waves can be classified into two groups [8]:

- **Planar technologies.** The planar technologies can be divided into three groups: MIC (Microwave Integrated Circuits), MMIC (Monolithic Microwave Integrated Circuits), MHMIC (Miniaturized Hybrid Microwave Integrated Circuits) [9] [10]. They offer the possibility to build integrated circuits. Recently, multi-layer technologies have been developing intensively [11]. The microstrip line, coplanar waveguide and slot line and their derivatives are usually used for making passive components. Some examples of commonly used guiding structures are presented in Fig. 1.1.
- **Non-planar technologies.** They can be divided into two categories [8]: metallic waveguides (rectangular waveguide, fin line, coaxial line) and dielectric waveguides (image line, NRD-guide and their derivatives). Examples of dielectric guides are shown in Fig. 1.2 and Fig. 1.3.

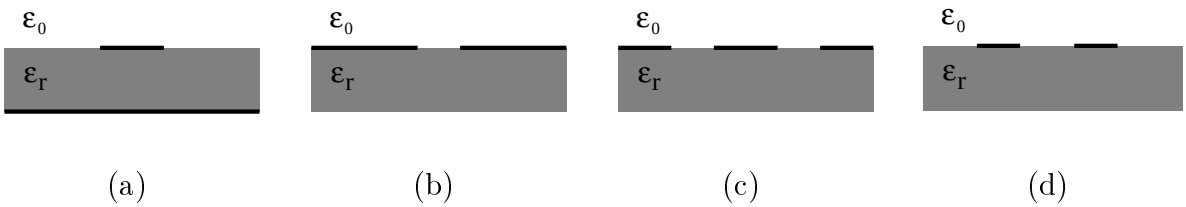

Figure 1.1: *Examples of planar structures: (a) microstrip line, (b) slot line, (c) coplanar waveguide, (d) coplanar strip line.*

The classical planar technologies were originally developed for circuits working in microwaves. The microstrip line is the most widely used planar guiding structure (Fig. 1.1 (a)) [12]. It offers simple mounting of lumped elements in series configuration. The back metalization allows easy fixing on metallic housing and can be used as a natural way of heat dissipation yielding high power handling capacity. On the other hand, the microstrip line suffers from high transmission loss, high dispersion and difficulty in mounting lumped elements in shunt configuration. Due to drawbacks of microstrip line, alternative guiding structures have been proposed. At present, the most popular ones are slot line (Fig. 1.1 (b)) [13] and coplanar structures (Fig. 1.1 (c) and (d)) [2]. Besides good electrical parameters they also offer easier mounting of lumped elements in shunt and series configurations. However, every planar guide has specific features which decide where it is applied. In general, planar structures have a large number of advantages such as high degree of integration, ease of mounting of active two- and three-port devices, small and compact circuit sizes and well established technology. Nevertheless, the serious limitation of planar technologies occurs at millimeter waves [8]. The loss factors of the guides become unacceptably high because

conducting losses increase with square root of the frequency and achieve high values at frequencies above 20 GHz. Moreover, if the circuits are not properly designed, the radiation losses and leakage at discontinuities appear and the circuits parameters can be seriously deteriorated. Another drawback is very high cost of the research and manufacturing. The critical dimensions such as microstrip width or slot width in coplanar waveguide are of order of μm at 20 GHz frequency. These dimensions become smaller if the frequency is increased or the dielectric materials with higher relative permittivity ϵ_r are used. Moreover, the integrated circuits are usually complicated, require combination of various advanced technologies in production process and very often it is not possible to design them in a single framework [9].

The non-planar technologies using metallic guides such as rectangular waveguide, groove guide or coaxial line are well known but suffer from high conducting loss at the millimeter waves and are bulky in building integrated circuits [8]. Therefore, they are limited only to specific applications where low level of integration is required.

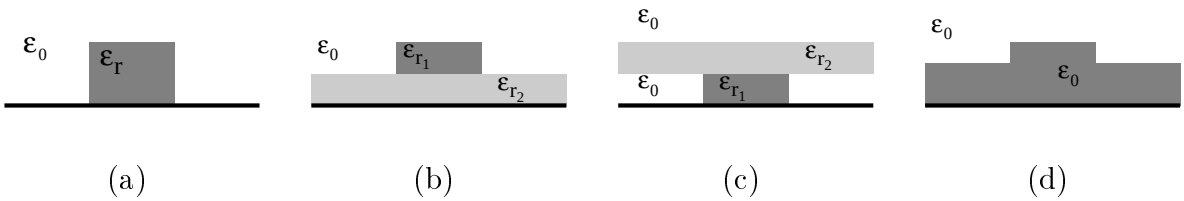

Figure 1.2: *Examples of dielectric guides: (a) image line, (b) insulated image line, (c) inverted strip guide, (d) rib image guide.*

As an alternative, the non-planar technologies involving dielectric guides are gaining growing attention. One of their main advantages over the planar structures is low level of transmission losses. Various dielectric guides have been proposed and selected examples of them are shown in Fig. 1.2. The image guide (Fig. 1.2 (a)) is one of the first proposed semi-open dielectric structures [14]. It has a simple geometry, but the conducting losses are on relatively high level due to the concentration of the field maximum near the the metallic plate. Therefore further developments of the image guide have been focused on diminishing the conducting losses by increasing the distance between the field maximum and the conducting plate. As a result the structures such as an insulated image guide (Fig. 1.2 (b)) [15], inverted strip image guide (Fig. 1.2 (c)) [16] and rib image guide (Fig. 1.2 (d)) [17] have been proposed. These guides have been used to design various components and applied in several systems. Nevertheless, the fundamental drawback of the presented dielectric guides is a very high level of radiation losses at discontinuities and bends. This feature limits their application mainly to the research area.

The invention of an NRD-guide (Non-Radiative Dielectric guide), shown in Fig. 1.3 (b), has changed this situation [19]. The structure is a modified version of H-guide (Fig. 1.3 (a)) [20]. The H-guide and NRD-guide differ in the plate separation. The distance is either smaller (for the NRD-guide) or greater (for the H-guide) than a half free space wavelength. Since its invention various modifications of a basic NRD-guide structure have been proposed

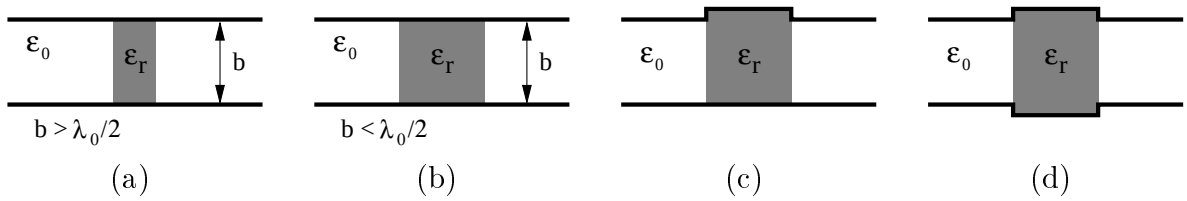

Figure 1.3: *Examples of dielectric guides: (a) H-guide, (b) NRD-guide, (c) AGNRD-guide, (d) hyper NRD-guide [6] or groove NRD-guide [18]*

such as AGNRD-guide (Asymmetrically grooved NRD-guide) (Fig. 1.3 (c)) [21] or hyper NRD-guide by Murata (Fig. 1.3 (d)) [6]. The latter structure is also called GNRD-guide (Grooved NRD-guide) [18]. The GNRD-guide and hyper NRD-guide differ in the depth of a groove. Larger depth of the groove for the hyper NRD-guide than for the GNRD-guide results in slight modification of the spectrum of guided modes .

The NRD-guide has gained great attention because it possesses attractive features such as

- **Good technical parameters.** Unlike other dielectric guides the NRD-guide has no radiation at bends and discontinuities due to cut-off property of a parallel plate waveguide. Moreover, the transmission losses are kept at very low level. The NRD-guide is less lossy than the corresponding insulated image guide.
- **Low cost of manufacturing.** The NRD-guide components are very simple (Fig. 1.3), the tolerance of elements dimensions is not critical. Relatively large dimensions, compared to guide wavelength, allow easy manufacturing of a complete circuit in large scale. Moreover, low cost dielectric materials can be used in production.
- **Possibility to integration.** The NRD-guide technology is suitable to build completely integrated circuits which can also easily incorporate NRD-guide antenna structures. Moreover, the integration with planar technologies such microstrip line or coplanar waveguide is possible. Such an approach allows one to combine the best features offered by both technologies.

The results presented in the technical literature show that a wide range of high quality NRD-guide components characterized by good technical parameters can be built. In consequence completely integrated circuits with good performance have been reported. At present, the majority of work in the NRD-guide technology is in the research phase but some prototype circuits have been prepared to work in commercially available systems. The state of the art in the NRD-guide technology is described in the following section.

1.2 Current status of NRD-guide technology

The NRD-guide technology has been proposed quite recently [19] as an attractive alternative for building millimeter wave circuits. Although several technologies have been exploited in

this frequency range, the NRD-guide technology has characteristic features, detailed in previous section, which make it competitive to the existing technologies. For the sake of an example, the comparison between NRD-guide technology and the two commonly used in millimeter wave frequencies technologies i.e. fin-line and MMIC technology is shown in Table 1.1.

Feature	Technology		
	NRD-guide	fin-line	MMIC
Production cost	Low	Medium	Very high
Production technology	Easy	Medium	Very difficult
Integration with antenna circuits within one technology	Yes	No	Yes
Loss in millimeter wave band	Very low	Low	High
Radiation at discontinuities	No	No	Yes

Table 1.1: *Comparison between the NRD-guide technology and two technologies commonly used in millimeter wave band: the fin-line and MMIC (after [22] and [2]).*

The comparison shows that the NRD-guide technology has some advantages, such as low loss level, possibility to integration with antenna circuits, and no radiation at discontinuities, over the related technologies. In addition to good electric parameters it offers low cost of manufacturing.

Since the invention of the NRD-guide technology a variety of passive components have been designed. The selected examples of them are listed below.

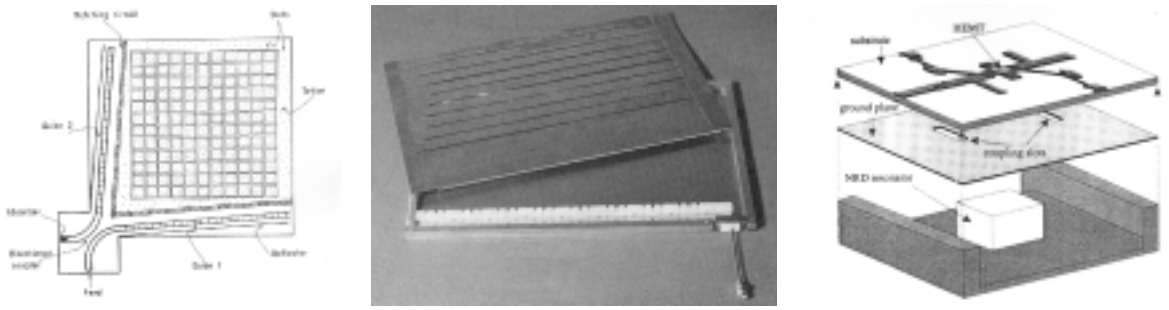

(a) (b) (c)

Figure 1.4: *Examples of NRD-guide passive components: (a) leaky NRD-guide-fed slot array antenna for circular polarization together with directional coupler [23], (b) planar antenna fed by broadside leaky NRD-guide [8], (c) rectangular resonator applied in the NRD-guide oscillator [9].*

- **Directional couplers.** Couplers with different coupling coefficients [24], [25] and quadrature couplers [26] have been proposed.
- **Filters.** Filters with bandpass and bandstop characteristics in various configurations have been investigated. The filters are described more precisely in chapter 4,

- **Circulators.** The circulator with half-wavelength step transformer [27] have been reported. Another structure which use a groove NRD-guide has been presented in [28].

- **Antennas.** Planar [23] (Fig. 1.4 (a)) and dielectric rod [29], [30] antennas have been constructed. Also leaky wave antennas have been investigated thoroughly [31], [32], [21] [8] (Fig. 1.4 (b)).

- **Resonators.** Different types of them have been inspected. Ring [33] [34], rectangular [35] [9] (Fig. 1.4 (c)) and cylindrical [36] [37] resonators are the main examples.

- **Power dividers and combiners.** The T-junction has been designed [38]. Three and five port devices have also been reported in [39].

- **Transitions.** Several transitions from an NRD-guide to other guides have been investigated. Among others there are the transition to microstrip line [40], [41], coplanar waveguide [42], strip line [43] and rectangular waveguide [44].

A majority of the presented research work and prototype elements were designed to work at millimeter wave bands where the atmospheric windows exist i.e. 35 GHz and 94 GHz. In the systems where the frequency re-use is essential, the frequency around 60 GHz has been selected where the maximum attenuation of the millimeter waves is observed. Some systems designed in Japan are reported to work near 50 GHz. This frequency has been chosen as a compromise between atmospheric and rain attenuation. Having in hand numerous elements, the integrated circuits have been build which include active elements. The oscillators [45], [46], balanced mixers [47] and amplifiers [48] are examples of them. The completely integrated systems have also been reported. The integrated transmitter (Fig. 1.5 (a)) and receiver (Fig. 1.5(b)) [49], [50] working in 35 GHz band achieved good technical parameters. The realization of a 60 GHz high-speed transreceiver designed to work in wireless LAN is shown in Fig. 1.6 [8]. Using the ASK modulation it assures the data transmission with the bit rate beyond 400 Mb/s [51].

Despite many advantages, the NRD-guide technology has also limitations. Most of active elements are connected with NRD-guide elements in a hybrid manner. Usually, active elements are mounted on additional high permittivity dielectric sheet which is inserted into the dielectric rod of an NRD-guide (Fig. 1.7 (a)). Serious mismatch between an NRD-guide and active element circuit can occur when the circuit is not properly designed and the whole circuit parameters are significantly deteriorated. But the more fundamental limitation of the technology is caused by the spacing between the metal plates. From the NRD-guide operation principle it should be less than half of a free space wavelength. When the frequency is increased the spacing is decreased, therefore for higher frequencies it is extremely difficult to mount, into the circuit structure, two- or three-terminal active devices, such as diodes and FET, HEMT or HBT transistors. The problem arises when the packaged devices have to be used.

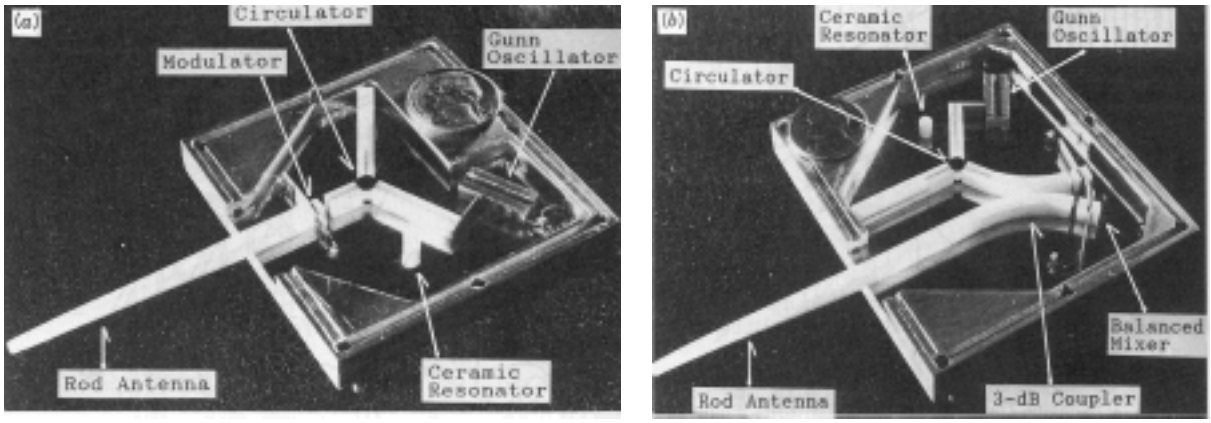

(a) (b)

Figure 1.5: *Integrated NRD-guide transmitter (a) and receiver (b) working at 35 GHz [49], [50].*

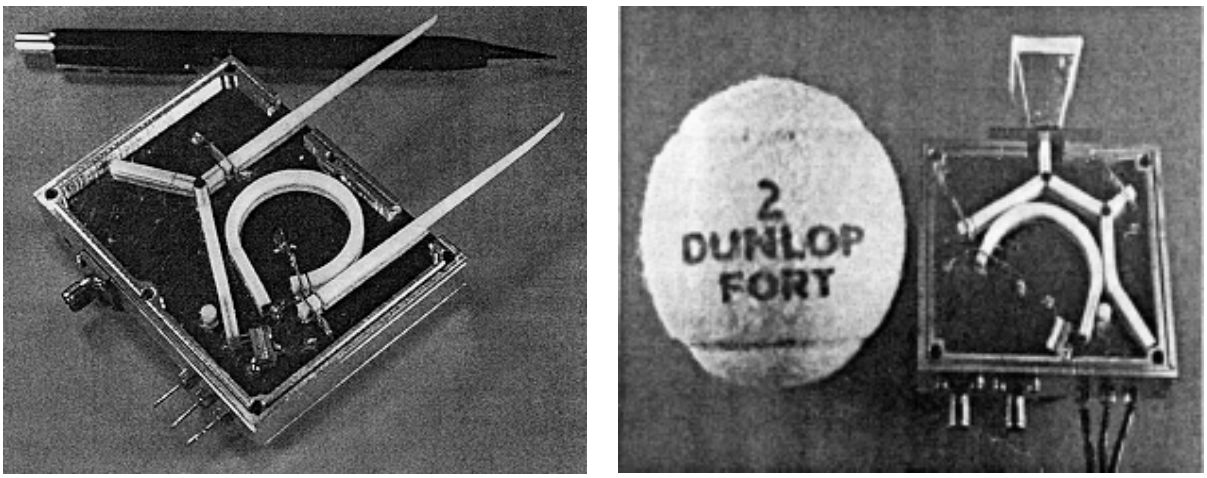

(a) (b)

Figure 1.6: *Integrated transreceivers working at 60 GHz frequency: (a) version with separate dielectric rod antennas [8], (b) version with shared horn antenna [51].*

Very recently the hybrid technology combining the NRD-guide and planar structures has been proposed [9] as a possible solution which obviate the NRD-guide technology limitations. This solution allows one to exploit the best features of both technologies and almost completely eliminates their disadvantages. In this technology the planar and NRD-guide structures share the same ground plane. The planar circuits are mounted on the outer side of the NRD-guide plates (Fig. 1.7 (b)). Several technologies such as coplanar waveguide, microstrip or slot line can be used to made the planar structure. The connection between the planar structures and NRD-guide components is made by aperture coupling. As an example of the possible coupling structure, the transition between an microstrip line and an NRD-guide can be presented [40].

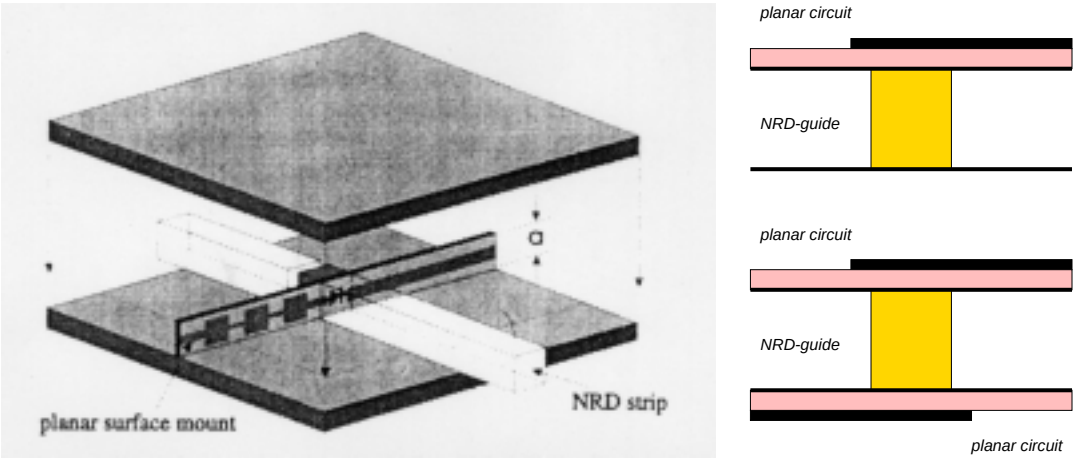

(a) (b)

Figure 1.7: *Integration of active elements with NRD-guide technology: (a) additional dielectric sheet with active elements inserted into the NRD-guide slab and (b) hybrid planar/NRD-guide integration technology with unilateral or bilateral aperture microstrip line to NRD-guide coupling [9].*

The presented hybrid technology offers features which make it very attractive. The integrated circuits can be as compact as possible because two sides of the NRD-guide can be used (Fig. 1.7 (b)). The location of different parts of the circuits on the opposite sides of NRD-guide allows almost complete suppression of unwanted cross-talks and electromagnetic couplings between these parts. For example when the transmitter and receiver circuits are located at the opposite sides of NRD-guide structure, nearly perfect isolation between them is obtained. In addition, they share the same NRD-guide passive elements such as filters or resonators. Easy mounting of active devices in planar parts of the circuits is another advantage. Moreover, multilayered, compact and space-saving structures can be realized. The results of recent works show that this technology can be one of the leading paths of the NRD-guide research and developments.

1.3 Scope and goals of this work

The modern methods used to design circuits working in millimeter waves differ significantly from the conventional methods applied for microwave circuits because several additional factors should be taken into account [52]. Firstly, the parasitic coupling, which is caused mainly by higher order modes, exists between circuit components. This coupling can significantly change circuits parameters and can not be neglected in many cases. Secondly, the guides used in millimeter waves have high dispersion while the conventional design formulae have been derived for non-dispersive guides or guides with low dispersion. Finally, the transmission losses and radiations on bends and discontinuities can not be neglected in many situations and the possible influence of this factor has to be inspected.

The methods of analysis and design of passive components are well established for con-

ventional technologies such as microstrip, coplanar waveguide or MMIC being used in the microwaves and millimeter waves. Moreover, many of these methods are implemented in commercially available microwave CAD software, therefore the design process is quick and significantly simplified. On the contrary, the method of analysis suitable for the NRD-guide technology and design are still under development. The problem of the proper choice of the method of design is still under research and various approaches have been investigated and proposed. Simple application of the well established methods to the NRD-guide technology is ineffective in many cases because these methods were originally developed for the structures such as coaxial line, microstrip line and rectangular waveguide which support TEM, quasi-TEM, or waveguide modes of TE or TM type, respectively. In contrast to these guiding structures the NRD-guide supports another type of modes, the hybrid LSM and LSE modes. Moreover, the classical method usually assumes that the device operates with the first order mode. This is not true for the NRD-guide devices where the first higher order mode, the LSM_{11} mode is usually employed. This feature is an additional difficulty in simple adaptation of the conventional methods and shows that the specific methods of design of the NRD-guide components are required.

The analysis of the NRD-guide components, presented in the technical literature, commonly involves the electromagnetic simulation of the whole structure [53] [54] [55]. Usually, to this end, grid based numerical methods in the time or frequency domain, such as FDTD, FDFD, FEM, TLM, are used [56] [57] [58] [59]. In these methods the 3D volume is covered with various types of grid and then the unknown fields are searched at the grid points by solving Maxwell's equations. Next, parameters such as scattering parameters or loss factors are found [52]. This procedure leads to large problems which have to be solved [60] [61]. Consequently, the numerical cost is very high because the methods require huge amount of computer memory and computing resources, especially when large or more complicated 3D problems are investigated [62] [63]. The second way of analysis is to employ advanced analytical approach, with relatively low numerical costs. This is usually time consuming in application and theoretically involved. In addition it is suitable only for structures with uniform geometry and requires additional effort spent on developing unique software tools.

From the designer's point of view, the synthesis methods are even more essential than the analysis ones. The synthesis is useful when one designs the device which has to meet parameters required by a technical specification. The synthesis is also applied when the determination of the starting points, such as structure dimensions or material parameters, are required for optimization procedures. The classical synthesis procedures were originally developed for the TEM structures [64]. In the NRD-guide, the hybrid modes are propagated. Therefore, the traditional TEM synthesis formulae can not directly be applied to design NRD-guide components and they should be suitably modified accordingly to yield proper results.

There are very few publications concerning to application of simple, well established and accurate methods suitable for analysis and synthesis of the NRD-guide components. None of the commercially available microwave CAD tools has incorporated design procedures devoted to NRD-guide components and circuits. There are no specialized tools which simplify

practical realization of selected NRD-guide components and integrated circuits. Such situation substantially limits the development and practical applications of the NRD-guide technology.

Therefore simple, quick and accurate design procedures suitable for NRD-guide technology need to be developed. The main goal of this work is to show that the selected NRD-guide elements can be designed accurately using simple and quick procedures. This thesis is focused on the ways of analysis of NRD-guide and design methods of NRD-guide impedance transformers, NRD-guide band pass filters and NRD-guide couplers.

The original contribution of this work is not an originally proposed novel synthesis or analysis method of NRD-guide components but rather

- The application of several well known methods allowing analysis of the NRD-guide and synthesis of NRD-guide bandpass filters, NRD-guide proximity couplers and transitions between an NRD-guide and a rectangular waveguide.
- The development of complete design procedures.

Compared to the conventional techniques mentioned in previous paragraphs the proposed design procedures and synthesis methods have the following advantages

- **Simple design formulae.** Well known, simple and established method are applied at every phase of the procedure.
- **Low numerical cost.** The methods can be implemented on an average PC hardware and the computation time is almost negligible. Numerical methods are used to characterize the most basic discontinuities.
- **Good level of accuracy.** Although the selected methods are approximate they assure the results which fulfil the accuracy criteria required for practically realized circuits.

This thesis makes the following claims:

- **Design of passive components in NRD-guide technology does not require time consuming computer simulation of entire structure.**
- **Conventional synthesis procedures can be used provided that several basic parameters are computed using full-wave computer tools.**
- **Accuracy of design of NRD-guide band-pass filter can be considerably improved if the half-wave impedance prototype is used instead of the conventional low pass prototype.**

The outline of this thesis is as follows. In chapter two the properties of NRD-guide are investigated. First, the analysis on the NRD-guide is provided by means of Hertz potentials. The analysis covers semi-open NRD-guide and the simplified closed NRD-guide structures

which can be more easily analyzed in various 3D CAD software. Then the impedance definitions suitable for NRD-guide are introduced and computed for typical NRD-guide. The accuracy of the presented approach is discussed. Next, the loss characteristics of two first hybrid modes are determined. Subsequently properties of the NRD-guide air-gap discontinuity are investigated. The discontinuity is used later on as an essential part of NRD-guide bandpass filters.

Chapter three presents the design method of a transition between a rectangular waveguide and an NRD-guide. A modification of the synthesis method, originally developed for TEM structures, is discussed. A pair of the transitions working in X-band is designed and manufactured. To determine the transition parameters, the calibration procedure is developed and the NRD-guide calibration kit is designed and manufactured. Numerical and experimental results of the designs are presented.

In chapter four, the design synthesis methods of bandpass filters are presented. Firstly the method with low-pass prototype is presented and treated as a reference. Then the method with half-wave step-impedance prototype is proposed to design NRD-guide filters. This method is thoroughly investigated numerically in order to determine its accuracy for different filter design specifications. At the end of the chapter the experimental verification of the selected designs is presented.

The conclusions gather the most important results of the work. The design procedure of NRD-guide couplers is presented in the appendix A. The approximate method, which use the transverse resonance method and coupled mode method, is described. Numerical and experimental results are shown and discussed. In the remaining appendixes the TRL calibration method applied to NRD-guide is shown, the field expressions for two NRD-guide structures are presented and remarks concerning theoretical characteristics of the NRD-guide bandpass filters are given.

Chapter 2

An NRD-guide

2.1 Introduction

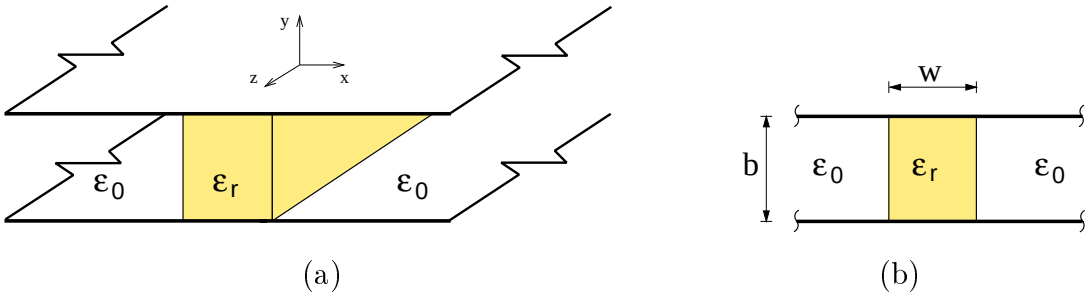

Figure 2.1: An NRD-guide: (a) general view, (b) cross section.

The Non-Radiative Dielectric Guide - NRD-guide has been proposed by Yoneyama Nishida in 1981 as a new transmission line suitable for applications working in millimeter wave range [19]. The NRD-guide is composed of two parallel metal plates with a dielectric rod sandwiched between them. The rod is rectangular in section with height b, width w and relative permittivity ϵ_r (Fig. 2.1).

The waves of which the half wavelength is greater than the plate separation ($\lambda_0/2 > b$) are attenuated and their guidance is impossible in the classical parallel plate waveguide. Therefore, the distance between the metal plates of NRD-guide is less than the half free space wavelength λ_0. The dielectric rod inserted between the plates changes locally the propagation conditions, thus the waves are guided inside the rod and are attenuated in the air-filled region. Accordingly all discontinuities which have proper symmetry are pure reactances and the structure suppresses strongly the unwanted interferences and radiations coming from bends and discontinuities. The radiation on the discontinuities is a serious problem in the majority of dielectric guides, therefore complete elimination of the radiation is the main advantage of the NRD-guide.

A similar structure, known as the H-guide, was proposed before the advent of the NRD-guide [20]. The H-guide looks like an NRD-guide, but the plate separation is larger than

half the free space wavelength λ_0. Although, the H-guide offers very low transmission losses, the parasitic radiation on bends and discontinuities strongly limits its application in practical circuits. The NRD-guide acts as the H-guide when the frequency is increased to the value where the non-radiation condition $b < \lambda_0/2$ does not hold any longer. The dominant LSM_{11} mode, which is described more precisely later on in this chapter, offers low transmission losses and is usually used in the NRD-guide. Thus the usable bandwidth of the guide is limited by the cut-off frequency $f_{c_{LSM_{11}}}$ of LSM_{11} mode from the bottom and by the $f_{c_{nr}}$ the cut-off frequency of the non-radiation condition from the top

$$f_{c_{LSM_{11}}} < f_g < f_{c_{nr}} = \frac{c}{2b}. \tag{2.1}$$

These two advantages of NRD-guide (i.e. lack of radiation on discontinuities and bends and low transmission losses) make it suitable for construction of compact and high quality millimeter wave integrated circuits. In addition, the NRD-guide allows mounting of active elements and offers the possibility of integration with other technologies such as microstrip [40] or coplanar waveguide [42].

The geometry of an NRD-guide and its modes are best described in the cartesian coordinate system (Fig. 2.1 (a)). The time dependence of the fields in the form of $e^{j\omega t}$ and the field propagation in the z direction described by the factor $e^{j\beta z}$ are assumed. The discrete spectrum of the modes, which can propagate in an NRD-guide, is composed of two sets of orthonormal hybrid modes and one TEM mode. The TEM mode, with the cut off frequency equal zero, may exist in the guide, but it is not of practical importance and its description is omitted here. The hybrid modes are characterized by the lack one of the electric or magnetic field component in the direction perpendicular to the air-dielectric interface [65]. These modes modes can be classified into two groups in the following manner.

- LSM_{mn} - *Longitudinal Section Magnetic* modes, also referred as TM^x or E^x modes. The magnetic field component H_x does not exist in these modes.
- LSE_{mn} - *Longitudinal Section Electric* modes, also referred as TE^x or H^x modes. The electric field component E_x does not exist in these modes.

The indices m refer to the order of the solution of an transcendental equation in the x direction. The first solution is denoted by $m = 1$, therefore $m = 1, 2, \ldots$. In some publications the m index starts from 0 instead of 1 by analogy to the mode nomenclature used for a dielectric plate [66]. This can lead to some misunderstandings in mode description, for example the first LSE mode is denoted by either LSE_{11} [8] or LSE_{01} [33] depending on the convention used. In this work the m indexes start from 1. The index n describes the order of the scalar equation solution in the y direction or, in the other words, the number of a half wavelength between the metal plates, thus $n = 0, 1, 2, \ldots$.

2.2 NRD-guide analysis

The NRD-guide is an semi-open structure in x direction. However, in the numerical analysis it is often assumed that lateral screens of either PEC or PMC are placed at a large distance

from the slab. This is because available microwave CAD packages often can not handle truly open structures. In this work two different closed structures, described in detail later on, are proposed to investigate an NRD-guide properties. In addition, the analytical solution of semi-open structure of NRD-guide is also provided and treated as a reference. The analysis of the closed structures is important because it can determine the position of the closing electric or magnetic walls which assure accurate results when compared to exact solution. The knowledge of the proper position of closing walls is essential in CAD software where NRD-guide elements are analyzed. If the walls are placed too far away, the computation time increases. On the other hand, placing of the walls too close can disturb the fields in the structure in such way that they do not resemble the NRD-guide modes but rather other types of waveguide modes.

The theoretical analysis of an NRD-guide can be carried out in various ways. In this section the scalar Hertz potentials are used to determine the NRD-guide equivalent structure properties. To begin with, the structure of a parallel plate transmission line filled with dielectric slabs, which are placed in parallel to the plates, is introduced (Fig. 2.2(a)). This structure was analyzed, using the scalar potentials, by Mrozowski in [67]. In this section the structure is modified in the following manner. The number of slabs is reduced to three; the central slab has the relative permittivity equal ϵ_r and two remaining slabs are treated as the air filled regions. The permeability of all three regions is assumed to be μ_0. The electric walls are located at $y = 0$ and $y = b$. As a result the structure of a rectangular waveguide with dielectric slab located in the symmetry plane is obtained (Fig. 2.2(b)). The structure is also called a closed NRD-guide [68]. The second structure has the magnetic walls instead of electric walls at $x = 0$ and $x = a$ (Fig. 2.2(c)). Both structures can be treated as a conventional NRD-guide provided that the distances from the dielectric slab to the walls, which are located at $x = 0$ and $x = a$, are sufficiently large. The walls should not disturb the fields of the NRD-guide hybrid modes. The third structure has the side walls at $x = 0$ and $x = a$ removed, therefore the regions A and C become semi infinite in the x direction (Fig. 2.2(d)). The fields in these regions decay exponentially towards $-\infty$ and $+\infty$. This structure describes exactly the fields in the NRD-guide but only the solutions for the propagated modes can be obtained from the analysis. This drawback disappears for the structure with electric or magnetic walls, where also the behavior of the modes below cutoff frequencies can be determined.

The analysis of these three structures can be carried out in the same manner, therefore only the closed NRD-guide is analyzed in detail in this section. The key expressions for potentials and fields for the remaining structures are presented in appendix C. Another reason for this selection is that this structure with electric walls appears in the transition between an NRD-guide and a rectangular waveguide. Hence, the results of the foregoing analysis are applied directly to the design procedure of the transition discussed in chapter 3.

Starting from the Maxwell equations the wave equations for the structure shown in (Fig.

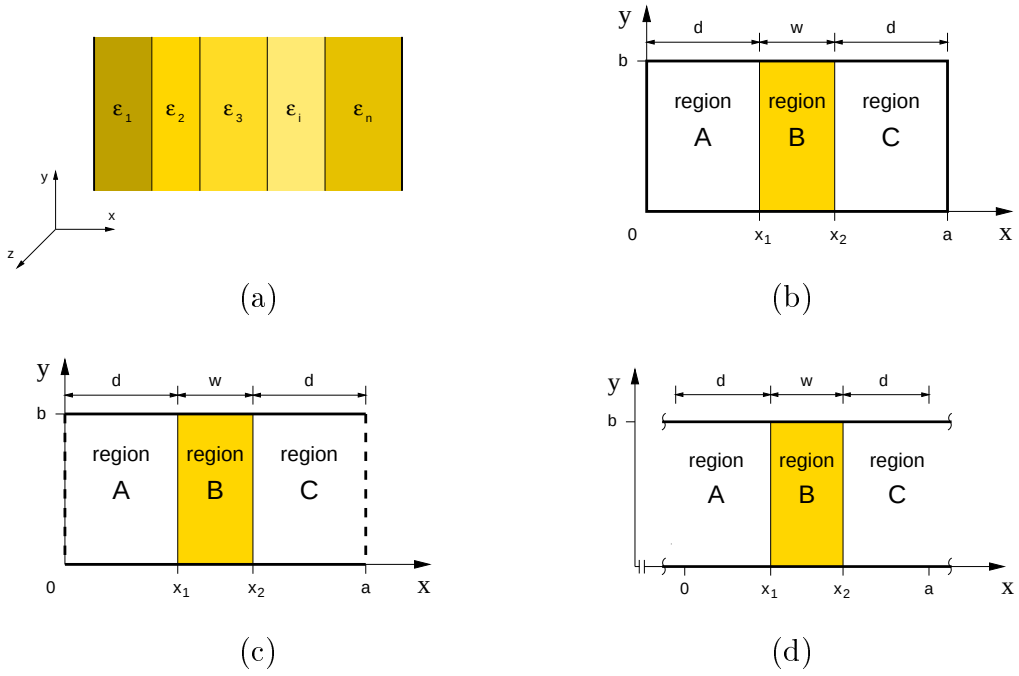

Figure 2.2: *(a) Parallel plate transmission line filled with dielectric slabs. (b) NRD-guide with electric walls at $x = 0$ and $x = a$ (closed NRD-guide), (c) NRD-guide with magnetic walls at $x = 0$ and $x = a$, (d) NRD-guide.*

2.2(a)) can be derived. The equations are written in the following form [67]

$$\left(\nabla_t{}^2 + \epsilon(x)\frac{\partial}{\partial x}\frac{1}{\epsilon(x)}\frac{\partial}{\partial x} + k_0^2\mu(x)\epsilon(x)\right)\Psi_e = 0 \tag{2.2}$$

$$\left(\nabla_t{}^2 + \mu(x)\frac{\partial}{\partial x}\frac{1}{\mu(x)}\frac{\partial}{\partial x} + k_0^2\mu(x)\epsilon(x)\right)\Psi_h = 0 \tag{2.3}$$

where Ψ_e and Ψ_h are the scalar potentials given separately for each layer and defined as

$$\epsilon_0\epsilon(x)E_x = -\nabla_t^2\Psi_e \qquad \mu_0\mu(x)H_x = -\nabla_t^2\Psi_h. \tag{2.4}$$

Using the potentials, the complete electric E and magnetic H fields can be expressed as

$$\vec{E} = \frac{1}{\epsilon_0\epsilon(x)}\nabla_t\frac{\partial}{\partial x}\Psi_e - j\omega\nabla_t\times\Psi_h\vec{i}_x - \frac{1}{\epsilon_0\epsilon(x)}\nabla_t^2\Psi_e\cdot\vec{i}_x \tag{2.5}$$

$$\vec{H} = \frac{1}{\mu_0\mu(x)}\nabla_t\frac{\partial}{\partial x}\Psi_h + j\omega\nabla_t\times\Psi_e\vec{i}_x - \frac{1}{\mu_0\mu(x)}\nabla_t{}^2\Psi_h\cdot\vec{i}_x. \tag{2.6}$$

The fields and their derivatives have to fulfil the continuity condition at the interfaces between the layers. Therefore, the Hertz potentials have to meet the following continuity conditions on the boundaries between the adjacent layers

$$\Psi_e = const \tag{2.7}$$

$$\frac{1}{\epsilon(x)}\frac{\partial}{\partial x}\Psi_e = const \tag{2.8}$$

$$\Psi_h = const \tag{2.9}$$

$$\frac{1}{\mu(x)}\frac{\partial}{\partial x}\Psi_h = const. \tag{2.10}$$

The boundary conditions for the potentials have the following form at the electric wall

$$\Psi_h = 0 \tag{2.11}$$

$$\frac{\partial}{\partial x}\Psi_e = 0 \tag{2.12}$$

and in the case of magnetic wall they take up the form

$$\Psi_e = 0 \tag{2.13}$$

$$\frac{\partial}{\partial x}\Psi_h = 0. \tag{2.14}$$

In general, the wave equations (2.2) and (2.3) can be written in the form of an eigenvalue problem. The coordinate system is separable, therefore we can denote the separation constant $\nabla_t(\cdot)$ by δ and express the eigenvalue problem in the following manner

$$\mathbf{L}\underline{\Psi} + \delta\underline{\Psi} = 0 \tag{2.15}$$

where

$$\mathbf{L} = \begin{bmatrix} \mathbf{L_e}\epsilon(x) & 0 \\ 0 & \mathbf{L_h}\mu(x) \end{bmatrix} \tag{2.16}$$

$$\underline{\Psi} = \begin{bmatrix} \Psi_e \\ \Psi_h \end{bmatrix} \tag{2.17}$$

$$L_e = \frac{\partial}{\partial x}\frac{1}{\epsilon(x)}\frac{\partial}{\partial x} + k_0^2\mu(x) \tag{2.18}$$

$$L_h = \frac{\partial}{\partial x}\frac{1}{\mu(x)}\frac{\partial}{\partial x} + k_0^2\epsilon(x). \tag{2.19}$$

The operators L_e and L_h have the form of a classical Sturm-Liouville operator. The analyzed structures are assumed to be lossless and the side walls have the form of electric and magnetic walls for closed structures and for the semi-open structure the exponential field

decay is assumed. Under these conditions the operators L_e and L_h are self-adjoint [67]. Therefore each operator has the infinite number of real eigenvalues and its eigenfunctions form complete set of orthogonal functions in the Hilbert space with properly defined inner product. Investigating the form of the operator $\mathbf{L}$ for our structure it can be noted, that there is no coupling between the eigenfunctions Ψ_e and Ψ_h which form the vector $\underline{\Psi}$. Hence the general eigenproblem (2.15) is decomposed into pair of independent scalar eigenproblems

$$(\mathbf{L_e} + \epsilon^{-1}(x)\nabla_t{}^2)\Psi_e = 0 \tag{2.20}$$

$$(\mathbf{L_h} + \mu^{-1}(x)\nabla_t{}^2)\Psi_h = 0. \tag{2.21}$$

The eigenvalues and eigenfunctions for each scalar eigenproblem are found separately. Accordingly, modes existing in the NRD-guide are classified into two groups of modes related to the Hertz potentials Ψ_e and Ψ_h, and labeled as *LSE* and *LSM* modes. Looking at the Hertz potentials definitions (equation 2.4) it is seen, that these two groups of modes can be characterized by lack one of the field component, perpendicular to the boundary between the regions in the structure, E_x or H_x for *LSE* or *LSM* modes respectively. This classification of the mode spectrum is the most commonly used in the technical literature, therefore it has been introduced in the previous section and is used in this work.

For both groups the expressions for fields can be obtained from (2.5) and (2.6) by setting the $\Psi_e = 0$ (*LSE* modes) or $\Psi_h = 0$ (*LSM* modes). Detailed analyses of *LSE* and *LSM* modes are presented in the followed sections.

2.2.1 Field solution for the LSE modes and electric walls

The E_x component does not exist for the *LSE* modes and the electric potential equals zero

$$\Psi_e = 0. \tag{2.22}$$

By applying condition (2.22) to the field expressions (2.5) and (2.6), the field components, given in rectangular coordinate system, can be written for each region in the NRD-guide in the following form

$$\vec{E}_x = 0 \tag{2.23}$$

$$\vec{E}_y = -j\omega\frac{\partial}{\partial z}\Psi_h\vec{i}_y \tag{2.24}$$

$$\vec{E}_z = j\omega\frac{\partial}{\partial y}\Psi_h\vec{i}_z \tag{2.25}$$

$$\vec{H}_x = -\frac{1}{\mu_0\mu(x)}\left(\frac{\partial^2}{\partial y^2} + \frac{\partial^2}{\partial z^2}\right)\Psi_h\vec{i}_x \tag{2.26}$$

$$\vec{H}_y = \frac{1}{\mu_0 \mu(x)} \frac{\partial^2}{\partial y \partial x} \Psi_h \vec{i}_y \tag{2.27}$$

$$\vec{H}_z = \frac{1}{\mu_0 \mu(x)} \frac{\partial^2}{\partial z \partial x} \Psi_h \vec{i}_z. \tag{2.28}$$

The boundaries of the structure from Fig. 2.2 (b) are in the form of electric walls, therefore the magnetic potential, which has to fulfil the boundary conditions in the structure, is defined separately for each region of an NRD-guide and is expressed as

$$\Psi_{h_A} = A \sin(k_{x0} x) \cos(k_y y) e^{-\gamma z} \tag{2.29}$$

$$\Psi_{h_B} = [B \cos(k_{xd} x) + C \sin(k_{xd} x)] \cos(k_y y) e^{-\gamma z} \tag{2.30}$$

$$\Psi_{h_C} = D \sin(k_{x0}(a - x)) \cos(k_y y) e^{-\gamma z}. \tag{2.31}$$

Accordingly to the coordinate system shown in Fig. 2.2 (b), the transverse wavenumbers k_{x0} and k_{xd} are the wavenumbers in the x direction in the air-filled regions and dielectric region, respectively, while k_y is the wavenumber in the y direction. The longitudinal propagation constant in the z direction is denoted by γ. In general, $\gamma = \alpha + j\beta$ where α is the attenuation constant and β is called the phase constant. For lossless structure $\alpha = 0$ hence, $\gamma = j\beta$. The lossy structures are discussed in section 2.4.

The substitution of the scalar potentials given by (2.29) $\div$ (2.31) into the equations (2.23) $\div$ (2.28) yields the field expressions for each region. The coefficient $e^{-\gamma z}$ is omitted in all equations for simplicity.

Region A

$$\begin{array}{rcl} E_x &=& 0 \\ E_y &=& jA\omega\gamma \sin(k_{x0} x) \cos(k_y y) \\ E_z &=& -jA\omega k_y \sin(k_{x0} x) \sin(k_y y) \\ H_x &=& \frac{A}{\mu_0 \mu(x)} (k_y^2 - \gamma^2) \sin(k_{x0} x) \cos(k_y y) \\ H_y &=& -\frac{A}{\mu_0 \mu(x)} k_{x0} k_y \cos(k_{x0} x) \sin(k_y y) \\ H_z &=& -\frac{A}{\mu_0 \mu(x)} \gamma k_{x0} \cos(k_{x0} x) \cos(k_y y) \end{array} \tag{2.32}$$

Region B

$$\begin{array}{rcl} E_x &=& 0 \\ E_y &=& j\omega\gamma [B \cos(k_{xd} x) + C \sin(k_{xd} x)] \cos(k_y y) \\ E_z &=& -j\omega k_y [B \cos(k_{xd} x) + C \sin(k_{xd} x)] \sin(k_y y) \\ H_x &=& \frac{1}{\mu_0 \mu(x)} (k_y^2 - \gamma^2) [B \cos(k_{xd} x) + C \sin(k_{xd} x)] \cos(k_y y) \\ H_y &=& -\frac{1}{\mu_0 \mu(x)} k_{xd} k_y [-B \sin(k_{xd} x) + C \cos(k_{xd} x)] \sin(k_y y) \\ H_z &=& -\frac{1}{\mu_0 \mu(x)} \gamma k_{xd} [-B \sin(k_{xd} x) + C \cos(k_{xd} x)] \cos(k_y y) \end{array} \tag{2.33}$$

Region C

$$\begin{aligned} E_x &= 0 \\ E_y &= jD\omega\gamma \sin(k_{x0}(a-x)) \cos(k_y y) \\ E_z &= -jD\omega k_y \sin(k_{x0}(a-x)) \sin(k_y y) \\ H_x &= \frac{D}{\mu_0 \mu(x)} (k_y^2 - \gamma^2) \sin(k_{x0}(a-x)) \cos(k_y y) \\ H_y &= \frac{D}{\mu_0 \mu(x)} k_{x0} k_y \cos(k_{x0}(a-x)) \sin(k_y y) \\ H_z &= -\frac{D}{\mu_0 \mu(x)} \gamma k_{x0} \cos(k_{x0}(a-x)) \cos(k_y y) \end{aligned} \tag{2.34}$$

The unknown amplitude coefficients are found by solving the matrix equation written as follows

$$\underline{\underline{M}}\, \underline{x}_c = 0 \tag{2.35}$$

where $\underline{x}_c$ is a vector of amplitude coefficients

$$\underline{x}_c = \begin{bmatrix} A \\ B \\ C \\ D \end{bmatrix}. \tag{2.36}$$

The matrix $\underline{\underline{M}}$ is created from the continuity conditions for the magnetic Hertz potential at the region interfaces located at $x = x_1$ and $x = x_2$

$$\underline{\underline{M}} = \begin{bmatrix} \cos(k_{xd} x_1) & -\cos(k_{xd} x_1) & -\sin(k_{xd} x_1) & 0 \\ -k_{x0} \sin(k_{x0} x_1) & \frac{k_{xd}}{\epsilon_r} \sin(k_{xd} x_1) & -\frac{k_{xd}}{\epsilon_r} \cos(k_{xd} x_1) & 0 \\ 0 & \cos(k_{xd} x_2) & \sin(k_{xd} x_2) & -\cos(k_{x0}(a - x_2)) \\ 0 & -\frac{k_{xd}}{\epsilon_r} \sin(k_{xd} x_2) & \frac{k_{xd}}{\epsilon_r} \cos(k_{xd} x_2) & -k_{x0} \sin(k_{x0}(a - x_2)) \end{bmatrix}. \tag{2.37}$$

The wavenumbers in the direction x, k_{x_0} and k_{x_d}, and longitudinal phase constant β are found in the following manner. The separability condition for the air-filled regions has the form

$$k_0^2 = {k_{x_0}}^2 + {k_y}^2 + \beta^2 \tag{2.38}$$

similarly, the separability condition for the dielectric region is expressed by

$$\epsilon_r k_0^2 = {k_{x_d}}^2 + {k_y}^2 + \beta^2. \tag{2.39}$$

Because the sinusoidal field dependence is assumed in y direction, the wavenumber k_y in y direction is written as

$$k_y = \frac{n\pi}{b} \tag{2.40}$$

where b is a guide height. The nontrivial solution of the matrix equation (2.35) exists when

$$det \underline{\underline{M}} = 0. \tag{2.41}$$

By combining separability conditions (2.38) and (2.39) with above equation the wave numbers k_{x_d}, k_{x_0} and β can easily be found.

2.2.2 Field solutions for LSM modes and electric walls

For the LSM modes the H_x component does not exist and the magnetic potential equals zero

$$\Psi_h = 0. \tag{2.42}$$

By applying the above condition (2.42) to the field expressions (2.5) and (2.6), the field components are obtained in the same manner as for the LSE modes

$$\vec{E}_x = -\frac{1}{\epsilon_0 \epsilon(x)} \left(\frac{\partial^2}{\partial y^2} + \frac{\partial^2}{\partial z^2} \right) \Psi_e \vec{i}_x \tag{2.43}$$

$$\vec{E}_y = \frac{1}{\epsilon_0 \epsilon(x)} \frac{\partial^2}{\partial y \partial x} \Psi_e \vec{i}_y \tag{2.44}$$

$$\vec{E}_z = \frac{1}{\epsilon_0 \epsilon(x)} \frac{\partial^2}{\partial z \partial x} \Psi_e \vec{i}_z \tag{2.45}$$

$$\vec{H}_x = 0 \tag{2.46}$$

$$\vec{H}_y = j\omega \frac{\partial}{\partial z} \Psi_e \vec{i}_y \tag{2.47}$$

$$\vec{H}_z = -j\omega \frac{\partial}{\partial y} \Psi_e \vec{i}_z. \tag{2.48}$$

The structure is the same as in the case of LSE modes. The electric Hertz potential in each region is given by

$$\Psi_{e_A} = A \cos(k_{x0} x) \sin(k_y y) e^{-\gamma z} \tag{2.49}$$

$$\Psi_{e_B} = [B \cos(k_{xd} x) + C \sin(k_{xd} x)] \sin(k_y y) e^{-\gamma z} \tag{2.50}$$

$$\Psi_{e_C} = D \cos(k_{x0}(a - x)) \sin(k_y y) e^{-\gamma z}. \tag{2.51}$$

The expressions for fields are obtained by putting the scalar potentials into the field equations (2.43) $\div$ (2.48). The factor $e^{-\gamma z}$ is omitted for simplicity.
Region A

$$\begin{array}{rcl} E_x &=& \frac{A}{\epsilon_0 \epsilon(x)} (k_y^2 - \gamma^2) \cos(k_{x0} x) \sin(k_y y) \\ E_y &=& -\frac{A}{\epsilon_0 \epsilon(x)} k_{x0} k_y \sin(k_{x0} x) \cos(k_y y) \\ E_z &=& \frac{A}{\epsilon_0 \epsilon(x)} \gamma k_{x0} \sin(k_{x0} x) \sin(k_y y) \\ H_x &=& 0 \\ H_y &=& -jA\omega\gamma \cos(k_{x0} x) \sin(k_y y) \\ H_z &=& -jA\omega k_y \cos(k_{x0} x) \cos(k_y y) \end{array} \tag{2.52}$$

Region B

$$\begin{aligned} E_x &= \tfrac{1}{\epsilon_0\epsilon(x)}(k_y^2-\gamma^2)\left[B\cos(k_{xd}x)+C\sin(k_{xd}x)\right]\sin(k_y y) \\ E_y &= \tfrac{1}{\epsilon_0\epsilon(x)}k_{\times d}k_y\left[-B\sin(k_{xd}x)+C\cos(k_{xd}x)\right]\cos(k_y y) \\ E_z &= -\tfrac{1}{\epsilon_0\epsilon(x)}\gamma k_{xd}\left[-B\sin(k_{xd}x)+C\cos(k_{xd}x)\right]\sin(k_y y) \\ H_x &= 0 \\ H_y &= -j\omega\gamma\left[B\cos(k_{xd}x)+C\sin(k_{xd}x)\right]\sin(k_y y) \\ H_z &= -j\omega k_y\left[B\cos(k_{xd}x)+C\sin(k_{xd}x)\right]\cos(k_y y) \end{aligned} \tag{2.53}$$

Region C

$$\begin{aligned} E_x &= \tfrac{D}{\epsilon_0\epsilon(x)}(k_y^2-\gamma^2)\cos(k_{x0}(a-x))\sin(k_y y) \\ E_y &= \tfrac{D}{\epsilon_0\epsilon(x)}k_{x0}k_y\sin(k_{x0}(a-x))\cos(k_y y) \\ E_z &= -\tfrac{D}{\epsilon_0\epsilon(x)}\gamma k_{x0}\sin(k_{x0}(a-x))\sin(k_y y) \\ H_x &= 0 \\ H_y &= -jD\omega\gamma\cos(k_{x0}(a-x))\sin(k_y y) \\ H_z &= -jD\omega k_y\cos(k_{x0}(a-x))\cos(k_y y). \end{aligned} \tag{2.54}$$

The wave numbers k_{x_0}, k_{x_d} and β and the unknown amplitude coefficients are found using the same approach as for the LSE modes. The only difference is in the form of matrix $\underline{\underline{M}}$. For the LSM modes this matrix is created from the continuity conditions for the electric Hertz potentials at the air-dielectric interfaces ($x = x_1$ and $x = x_2$)

$$\underline{\underline{M}} = \begin{bmatrix} \cos(k_{xd}x_1) & -\cos(k_{xd}x_1) & -\sin(k_{xd}x_1) & 0 \\ -k_{x0}\sin(k_{x0}x_1) & \frac{k_{xd}}{\epsilon_r}\sin(k_{xd}x_1) & -\frac{k_{xd}}{\epsilon_r}\cos(k_{xd}x_1) & 0 \\ 0 & \cos(k_{xd}x_2) & \sin(k_{xd}x_2) & -\cos(k_{x0}(a-x_2)) \\ 0 & -\frac{k_{xd}}{\epsilon_r}\sin(k_{xd}x_2) & \frac{k_{xd}}{\epsilon_r}\cos(k_{xd}x_2) & -k_{x0}\sin(k_{x0}(a-x_2)) \end{bmatrix}. \tag{2.55}$$

2.2.3 Numerical results

For the sake of the example the parameters of the NRD-guide working in the X-band are presented in this section. Such selection is proposed because this guide is used later on for constructing NRD-guide bandpass filters (see chapter 4). The guide parameters are: $w = 10.16$ mm, $b = 15$ mm, $\epsilon_r = 2.53$ (Rexolite 1422).

Dispersion characteristics. The dispersion characteristics for the NRD-guide are shown in Fig. 2.3. The mode with the lowest cut off frequency LSE_{11} and the higher order LSE modes are considered as the parasitic modes in practical circuits. The first higher order mode LSM_{11} is used as a operating mode. The single-mode operating region for LSM_{11} spans from 8.5 GHz (f_c of the LSM_{11} mode) to 10.05 GHz (f_c of the LSM_{21} mode).

Field distribution. Looking at the mode pattern of the transverse electric field of the LSM_{11} mode (Fig. 2.4 (b)) it can be easily seen, that this mode can easily be excited using the rectangular waveguide TE_{10} mode (the excitation of an NRD-guide is discussed in chapter 3). The fields of the LSE_{11} and LSM_{11} modes in the section of the NRD-guide are plotted in Fig. 2.6 and Fig. 2.5. The dominant fields in the LSE_{11} mode are the E_y and E_z fields. For LSM_{11} mode the fields E_x, E_y and E_z are over the order of magnitude larger than the remaining ones. For both modes the fields are confined within the dielectric slab.

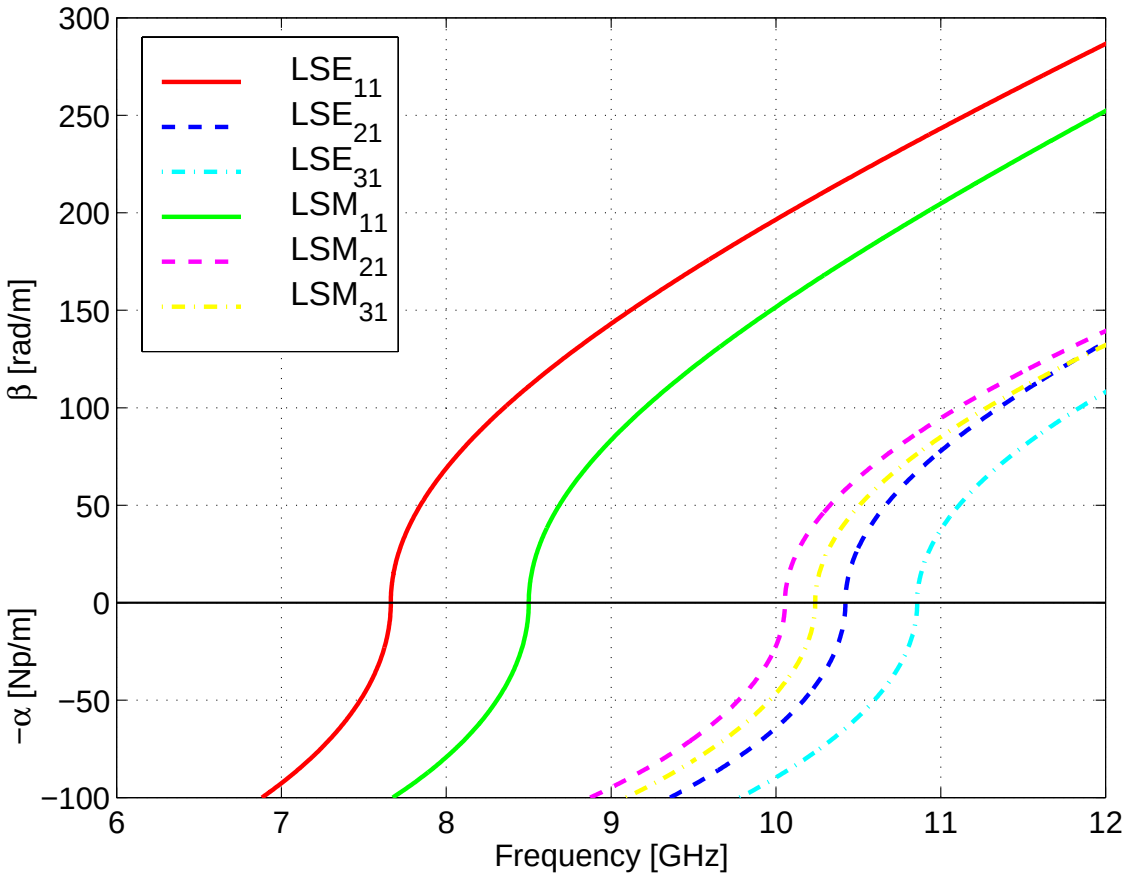

Figure 2.3: *Dispersion characteristics of the first six NRD-guide modes. Guide parameters are given in text.*

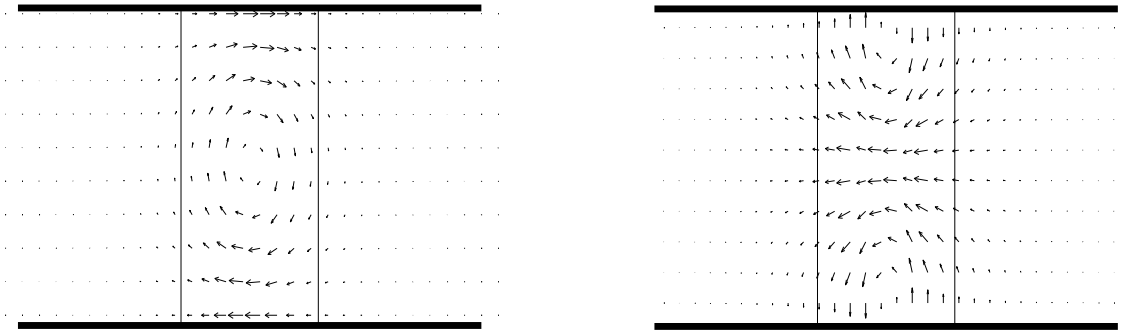

(a) (b)

Figure 2.4: *Plot of the field pattern in an NRD-guide: (a) LSE_{11} mode, magnetic field, (b) LSM_{11} mode, electric field.*

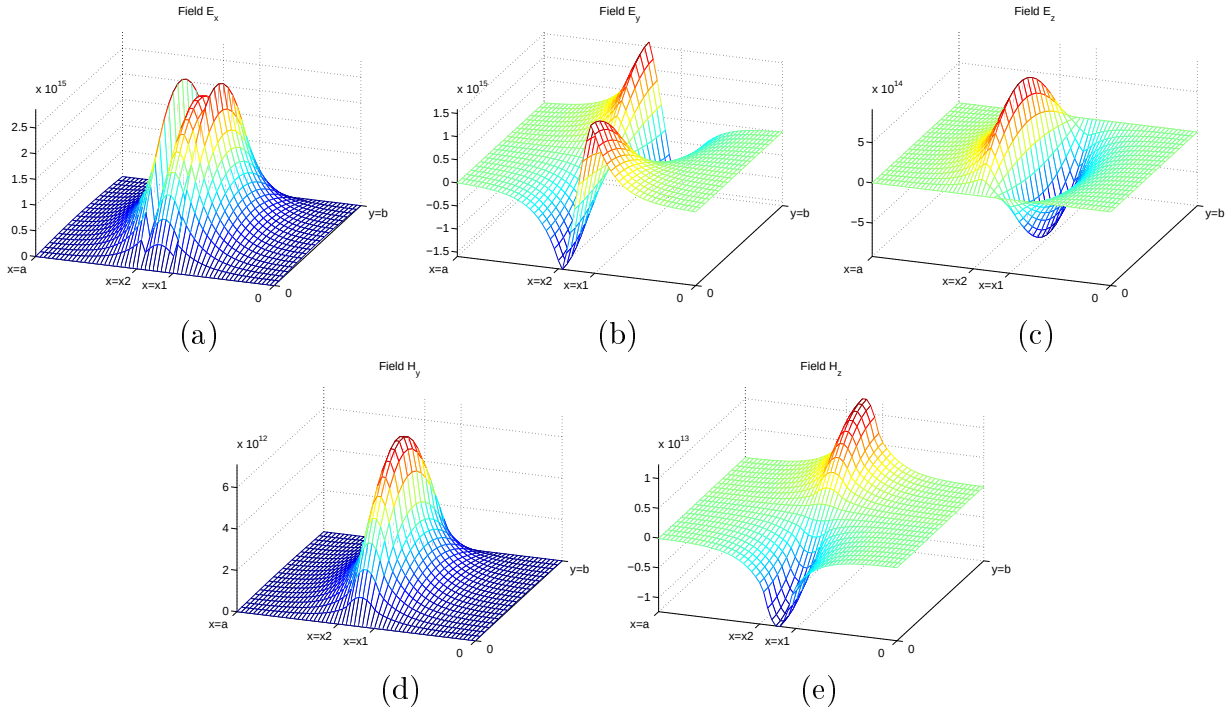

Figure 2.5: *Plot of the LSM_{11} mode field in a section of an NRD-guide: (a) E_x, (b) E_y, (c) E_z, (d) H_y, (e) H_z*

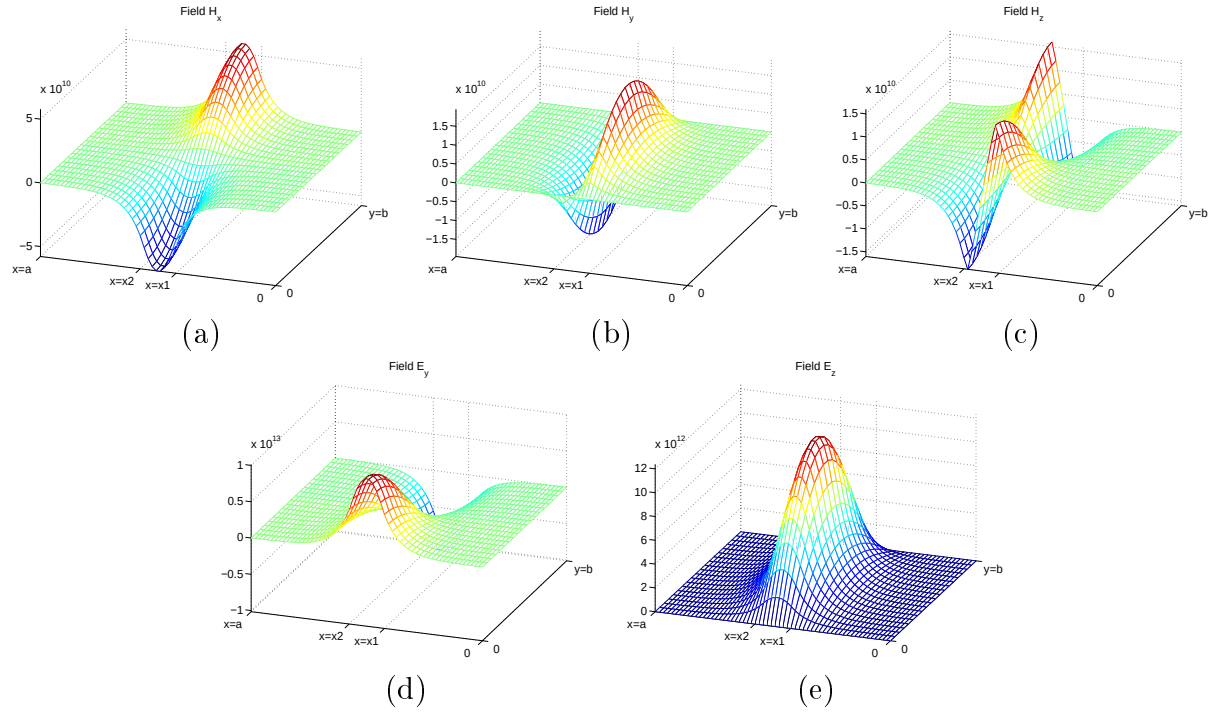

Figure 2.6: *Plot of the LSE_{11} mode field in a section of an NRD-guide: (a) H_x, (b) H_y, (c) H_z, (d) E_y, (e) E_z*

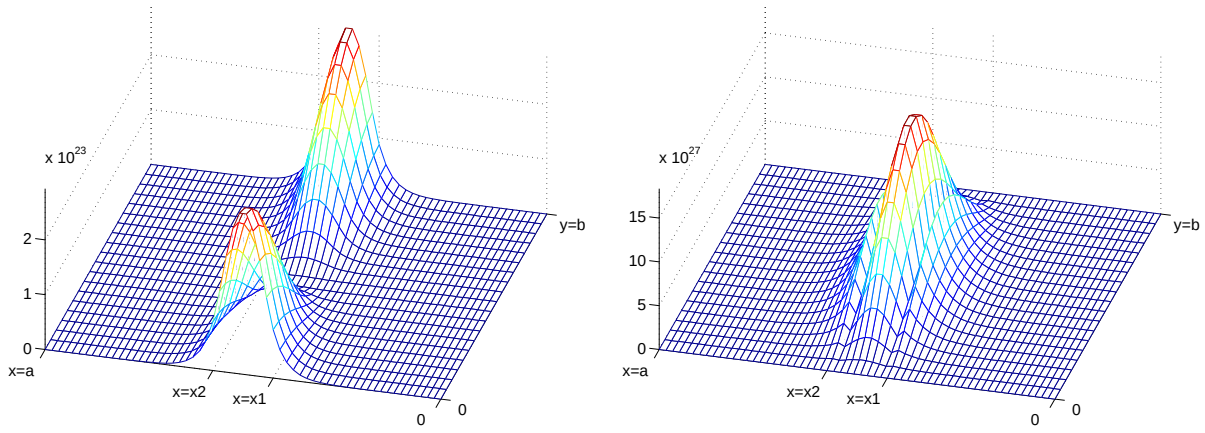

Figure 2.7: *Plot of the magnitude of Poynting vector for first two hybrid modes in NRD-guide: (a) LSE_{11} mode, (b) LSM_{11} mode.*

Power distribution. The plots of the Poynting vector for the LSE_{11} and LSM_{11} modes are shown in Fig. 2.7. The energy is mainly concentrated in the dielectric slab for both modes. For the LSM_{11} mode the energy is concentrated in the central part of the dielectric slab, while for the LSE_{11} the maximum of the energy is located near the metallic plates. The LSM_{11} mode offers lower transmission losses when compared to LSE_{11} mode (see discussion in section 2.4).

The β dependence on closing wall distance. The two structures, one with electric walls and the other with magnetic walls, are investigated in order to find the accuracy of the phase constant β approximation, when the distance between the side walls and the dielectric varies. Finding the proper distance d which assures relatively small errors of the computed guide parameters, is essential, especially in the case, where the larger structures such as filters, are simulated in the numerical simulators, which use numerical methods such as FDTD, FDFD or FEM. Too large structure generates larger problem size and increases computation time. On the other hand, too small distance d results in smaller structure and shorter computation time but the obtained results are inaccurate.

The computations are performed at frequency $f_0 = 9.0$ GHz for the LSM_{11} and LSE_{11} modes. In addition, the result for the LSE_{10} mode are presented. Although this "distorted" TE_{10} is usually not investigated, it is discussed here because this mode appears in the transition between an NRD-guide and a rectangular waveguide (see chapter 3 for details). The results obtained for the structure with analytical solution in the open regions are taken as a reference. The accuracy of the approximation is expressed in the term of relative error defined as

$$\Delta\beta = \frac{\beta_d - \beta_r}{\beta_r} \cdot 100 \quad [\%] \tag{2.56}$$

where β_d is the phase constant for electric or magnetic walls, located at the distance d, and β_r is the reference value.

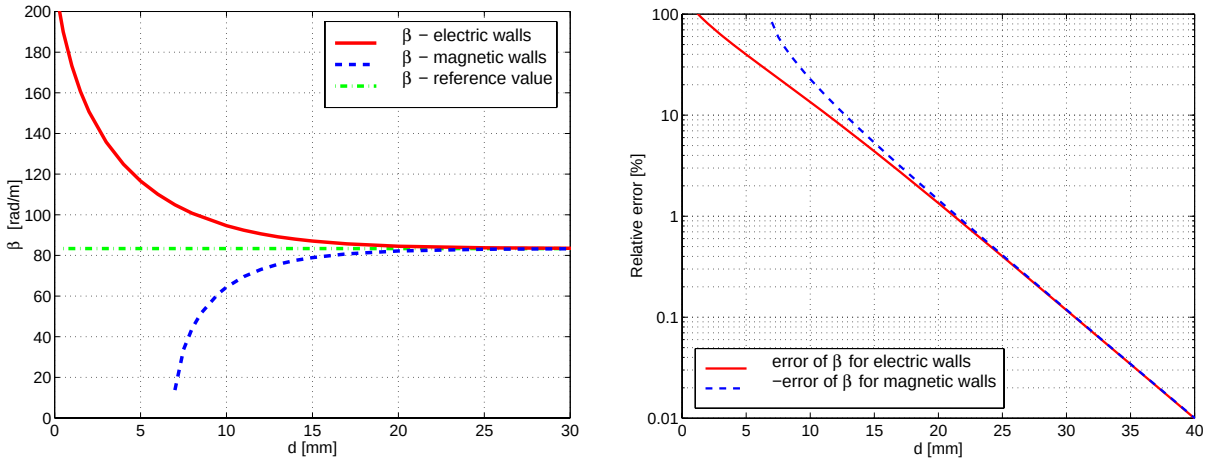

(a) (b)

Figure 2.8: *(a) Phase constant β of the LSM_{11} mode at $f_0 = 9.0$ GHz and (b) its relative error as a function of distance d between dielectric rod and side walls. Guide parameters: $w = 10.16$ mm, $b = 15$ mm, $\epsilon_r = 2.53$ (Rexolite 1422).*

Results for LSM_{11} mode. As it is shown in Fig. 2.8 (a) the LSM_{11} mode phase constant β increases when the electric walls are moved towards the dielectric strip. On the contrary, in the case of magnetic walls the decrease of the distance d results in lower values of β. For both cases the increase of d to sufficiently large value results in the β convergence to an accurate value. Fig. 2.8 (b) shows that the relative error is greater for the case of magnetic than for electric walls, when the walls are relatively close to the dielectric slab. When the walls are pushed away from the slab, the error vanishes and reaches the same value for both cases. The accuracy of 1% is obtained for the distance equal approximately 20 mm. The guide wavelength of the LSM_{11} mode is $\lambda_g = 75.34$ mm, hence the distance d equal $\lambda_g/2$ ($d = 37.67$) mm is sufficient to obtain accurate results with the relative error below the 0.1% level.

Results for LSE_{11} and LSE_{10} modes. For the LSE_{10} and LSE_{11} modes the β values are greater for magnetic walls and smaller for electric walls than the reference value when the walls are near the dielectric strip (Fig. 2.10 (a)) and (Fig. 2.9 (a)). The wavelength λ_g of the LSE_{10} mode equals 24.8 mm. At the distance $d = \lambda_g/2$ (d=12.4 mm) the relative error is at the level of 0.4 % (Fig. 2.10 (b)). Better results are observed for the LSE_{11} mode. The distance $d = \lambda_g/2$ (d=21.95 mm) assures the error well below 0.1 % level (Fig. 2.9 (b)). It can be seen, that in some cases, β is not computed for small values of d. For example, the β is computed only for d greater than 7 mm in the case of LSM_{11} mode and electric screens. This effect occurs, because for small values of d the cutoff frequency of the investigated mode is greater than the selected frequency $f_0 = 9.0$ GHz.

Conclusions. The results of the discussion concerning the influence of lateral screen position on the accuracy of β computation can be presented as follows.

- For the LSM_{11}, LSE_{11} and LSE_{10} modes the errors introduced by magnetic and

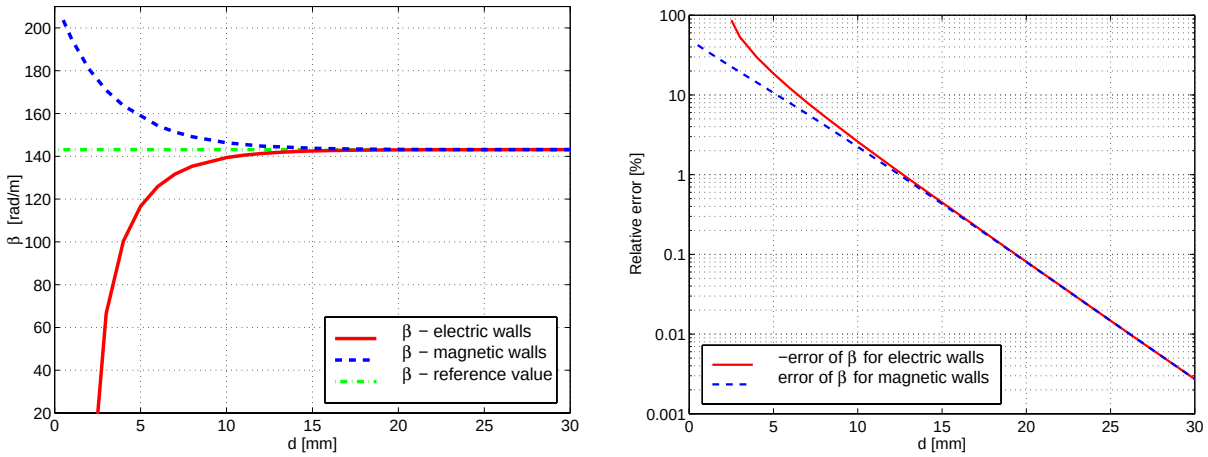

(a) (b)

Figure 2.9: *(a) Phase constant β of the LSE_{11} mode at $f_0 = 9.0$ GHz and (b) its relative error as a function of distance d between dielectric rod and side walls. Guide parameters: $w = 10.16$ mm, $b = 15$ mm, $\epsilon_r = 2.53$ (Rexolite 1422).*

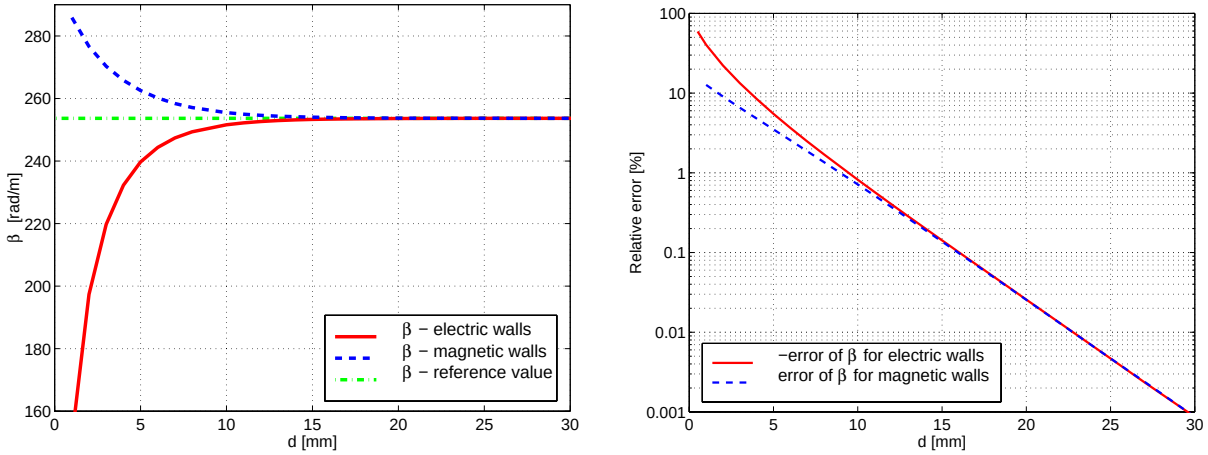

(a) (b)

Figure 2.10: *(a) Phase constant β of the LSE_{10} mode at $f_0 = 9.0$ GHz and (b) its relative error as a function of distance d between dielectric rod and side walls. Guide parameters: $w = 10.16$ mm, $b = 15$ mm, $\epsilon_r = 2.53$ (Rexolite 1422).*

electric walls are nearly the same at the distance $d \geq \lambda_g/2$, where λ_g refers to the wavelength of the investigated mode.

- The selection of $d \geq \lambda_g/2$, where λ_g corresponds to LSM_{11} mode, ensures that the relative error of β computation of LSM_{11}, LSE_{11} and LSE_{10} modes is below 0.1 % level.

2.3 NRD-guide impedances

Although the impedance does not directly describe the field behavior in the NRD-guide structure, it is an important parameter widely used in design of microwave and millimeter wave elements and circuits.

The impedance is employed in various synthesis and analysis procedures, originally developed for TEM structures. These procedures describe the structure in terms of the circuit theory. The synthesis of matching networks or filtering structures, discussed in the followed chapters, are examples of the application of impedance in design. Therefore, the impedances defined for NRD-guide are investigated in this section. The obtained results will be used later on.

Two main types of impedance are defined in waveguides [69]. These are:

- **Wave impedance.** The wave impedance can be defined for an arbitrary point inside the guide, as the ratio of two perpendicular magnetic and electric field components of the guide.
- **Characteristic impedance.** The characteristic impedance is expressed in terms of circuit quantities such as current, voltage and power. The definition of these quantities is specific for each waveguide and depends on waveguide shape and field distribution in a particular waveguide and selected mode.

The detailed descriptions of different impedances, which can be defined in the NRD-guide, and their characteristics features are presented in sections that follows.

2.3.1 Wave impedance

The wave impedance, defined as a ratio of two transversal magnetic and electric field components, can be defined as follows

$$Z = \frac{E_x}{H_y} \tag{2.57}$$

or

$$Z = -\frac{E_y}{H_x}. \tag{2.58}$$

The hybrid LSE and LSM NRD-guide modes do not have one of the transverse components in the x direction, hence the wave impedance definition has to be given for each mode class. Expressions (2.57) and (2.58) are used for LSM and LSE modes, respectively.

In general, when the inhomogeneous structures are investigated with ϵ_r and μ_r as a function of transverse coordinates, i.e. $\epsilon_r = f(x, y)$ and $\mu_r = f(x, y)$, the value of the wave impedance depends on the location of the point where the impedance is defined. The NRD-guide is inhomogeneous only in the x direction, therefore $\epsilon_r = f(x)$ and μ_r is constant in the entire area. Looking at the field expressions of the NRD-guide modes one can note that

the wave impedance of *LSE* modes does not depend on the location of the point where it is defined. On the contrary, for *LSM* modes the values of the wave impedance are different for air and dielectric regions[1]. Although the wave impedance can be defined at an arbitrary point, for consistency of this work, the NRD-guide wave impedance is defined as a ratio of two perpendicular electric and magnetic field components at the symmetry point of the NRD-guide.

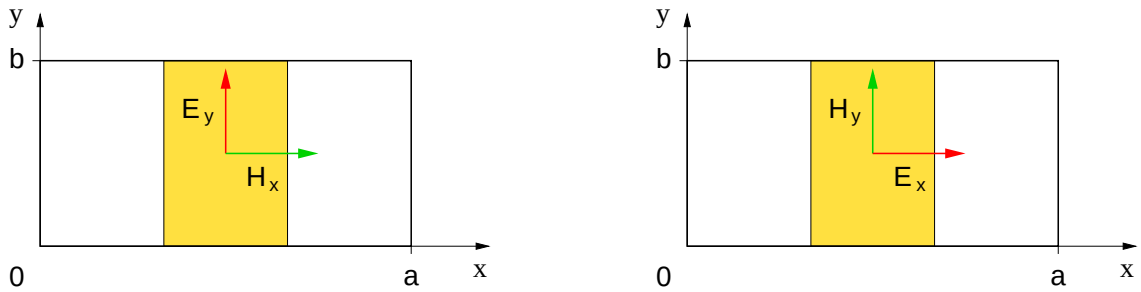

Figure 2.11: *Fields components taken to wave impedance definition in a closed NRD-guide: (a) E_y and H_x for LSE modes, (b) H_y and E_x for LSM modes.*

2.3.1.1 Wave impedance of *LSE* modes

The equation (2.58) is used for wave impedance definition for *LSE* modes (Fig. 2.11 (a)). Usually the wave impedance is defined in the symmetry point of a guide which has in our case the coordinates $x = a/2$ and $y = b/2$. Substituting the E_y and H_x field expressions given by (2.33) into (2.58) we arrive at

$$Z = \frac{\omega\beta\mu_0\mu_r}{k_y^2 + \beta^2} \tag{2.59}$$

where k_y is a wavenumber in the y direction and β is a longitudinal phase constant.

2.3.1.2 Wave impedance of *LSM* modes

The wave impedance of the *LSM* modes is defined by (2.57) (Fig. 2.11 (b)). The field values, at the point with coordinates equal $x = a/2$ and $y = b/2$, are taken in the impedance definition. Substituting the E_x and H_y field expressions given by (2.53) into (2.57) we get

$$Z = \frac{k_y^2 + \beta^2}{\omega\epsilon_0\epsilon_r\beta} \tag{2.60}$$

where k_y and β have the same meaning as in the case of *LSE* modes.

[1] In fact, these values are related by the relative permittivity ϵ_r of a dielectric slab.

2.3.1.3 Numerical results

The computations of wave impedances for an example NRD-guide are carried out in order to determine the smallest distance between dielectric rod and the walls, which yields accurate results when closed structures have to be investigated instead of open one. The impedances defined in the previous sections have been computed at frequency 9.0 GHz for the NRD-guide with the following parameters: $w = 10.16$ mm, $b = 15.0$ mm, $\epsilon_r = 2.53$ (Rexolite 1422). The distance d between dielectric rod and the walls varies from zero to 50 mm. The results of computation for two structures closed by electric and magnetic walls, where the LSM_{11}, LSE_{11} and LSE_{10} modes are propagated, are shown in Fig. 2.12 ÷ Fig. 2.14. The results obtained for the semi-open structure are taken as the reference. The relative error is defined as follows

$$\Delta Z = \frac{Z_d - Z_r}{Z_r} \cdot 100 \quad [\%] \tag{2.61}$$

where Z_d is the impedance value at distance d and Z_r is the reference value of the impedance. For few cases the impedances are not computed for small values of d due to the shift of the cutoff frequency of the investigated mode over the frequency selected for computation $f_0 = 9$ GHz.

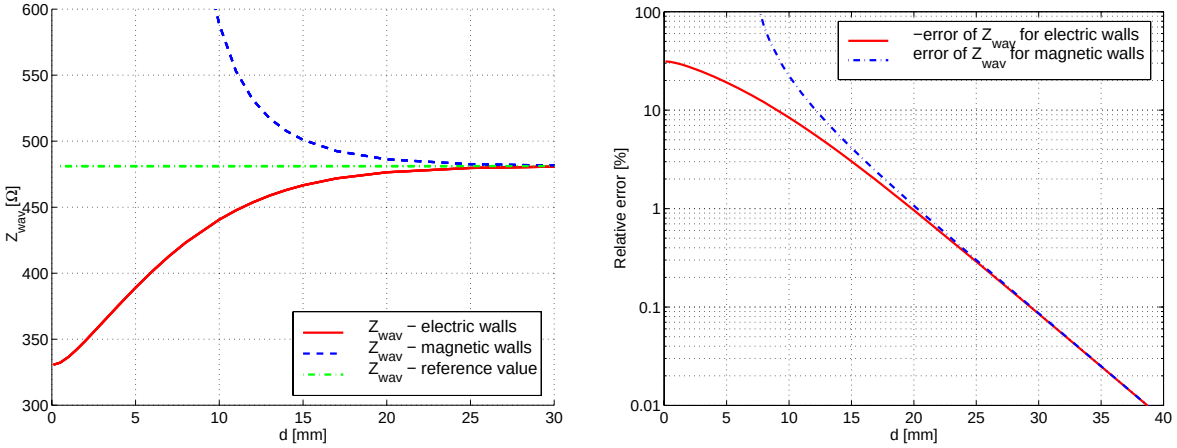

(a) (b)

Figure 2.12: *(a) Wave impedance Z_{wav} of the LSM_{11} mode and (b) its relative error as a function of a distance d between dielectric rod and side walls at $f_0 = 9.0$ GHz. Guide parameters: $w = 10.16$ mm, $b = 15$ mm, $\epsilon_r = 2.53$.*

For magnetic walls the LSM_{11} mode impedance is greater and for electric walls it is smaller than the reference value when the walls approach the dielectric slab (Fig. 2.14 (a)). Similar results are obtained for LSE_{11} and LSE_{10} modes (Fig. 2.14 (a) and Fig. 2.14 (a)). Although for all cases the impedance converges to accurate value rapidly, the same level of the relative error is obtained for different d. For the LSE_{10} mode $d = \lambda_g/2$ (d=12.4 mm) the error reaches 0.4%. The errors of the LSE_{11} and LSM_{11} modes are at the level of 0.02

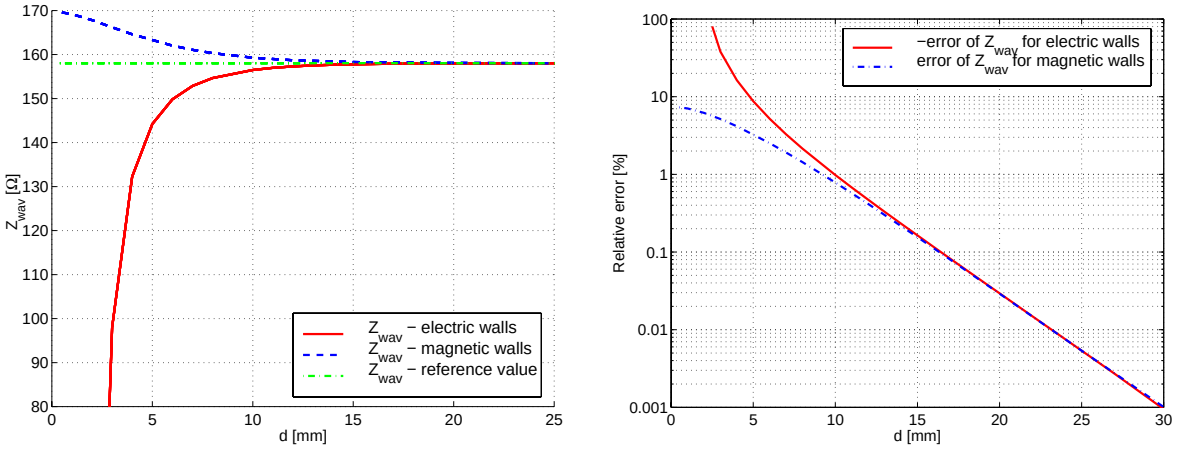

(a) (b)

Figure 2.13: *(a) Wave impedance Z_{wav} of the LSE_{11} mode and (b) its relative error as a function of a distance d between dielectric rod and side walls at $f_0 = 9.0$ GHz. Guide parameters: $w = 10.16$ mm, $b = 15$ mm, $\epsilon_r = 2.53$.*

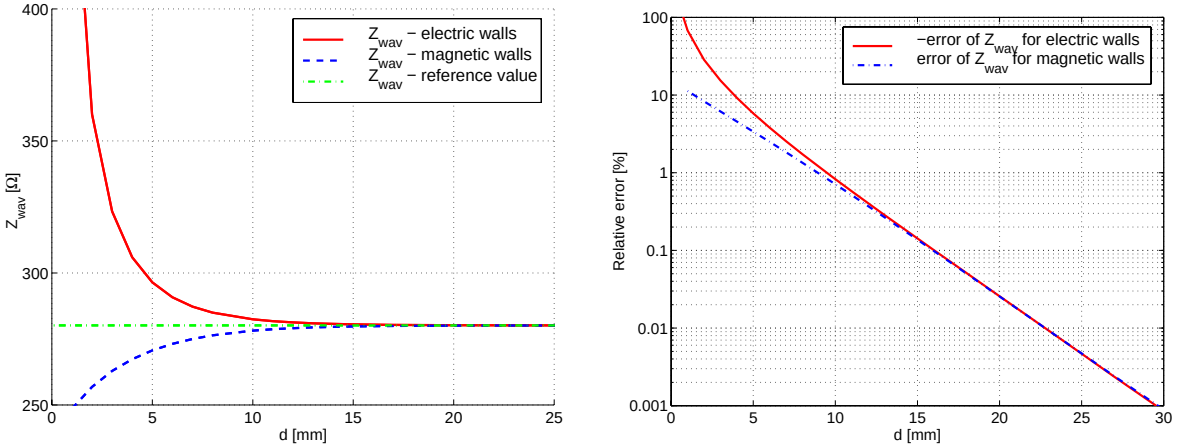

(a) (b)

Figure 2.14: *(a) Wave impedance Z_{wav} of the LSE_{10} mode and (b) its relative error as a function of a distance d between dielectric rod and side walls at $f_0 = 9.0$ GHz. Guide parameters: $w = 10.16$ mm, $b = 15$ mm, $\epsilon_r = 2.53$.*

% for both cases at the same distance $d = \lambda_g/2$ which for these modes are equal d=21.95 mm and d=37.67 mm, respectively.

Conclusions. The above discussion can be summarized as follows.

- The relative error for PEC and PMC is almost the same when the d is greater than $\lambda_g/2$ of a particular mode.
- The relative error of computation of the wave impedance of all investigated modes is kept below the 0.1 % level when the d is equal or larger than $d = \lambda_g/2$ of the LSM_{11} mode.

Similar conclusion has been obtained in the previous section where the accuracy of β computation has been investigated. This similarity appears because the wave impedance is a simple function of β.

2.3.2 Characteristic impedance

The definition of characteristic impedance is ambiguous in the guides where hybrid modes propagate. There is an uncertainty about which two out of the following three quantities: voltage, current or power should be taken to form the impedance definition. In addition, voltage or current definitions are non unique and they are selected depending on the guide and the particular mode. In general, three different definitions of characteristic impedance are commonly used [70]:

- Voltage-current impedance

$$Z_0 = \frac{V}{I} \tag{2.62}$$

- Voltage-power impedance

$$Z_0 = \frac{\mid V \mid^2}{2P^*} \tag{2.63}$$

- Power-current impedance

$$Z_0 = \frac{2P}{\mid I \mid^2} \tag{2.64}$$

where I and U are the current and voltage defined in the way that is the most suitable for a particular waveguide and the complex power P is expressed as

$$P = \frac{VI^*}{2}. \tag{2.65}$$

These three impedance definitions usually yield different values depending on the way the current, the voltage and the power were determined. Sometimes it is possible to obtain the same value for each type of impedance provided that the current, the voltage and the power are not defined arbitrarily but their definitions are linked one to the another [70].

The voltage-power definition is usually used in the NRD-guide case because of easy interpretation of the power and voltage an NRD-guide structure [71]. The field configuration is different for LSM and LSE modes, therefore the definition of the voltage-power impedance is introduced separately for each class of modes.

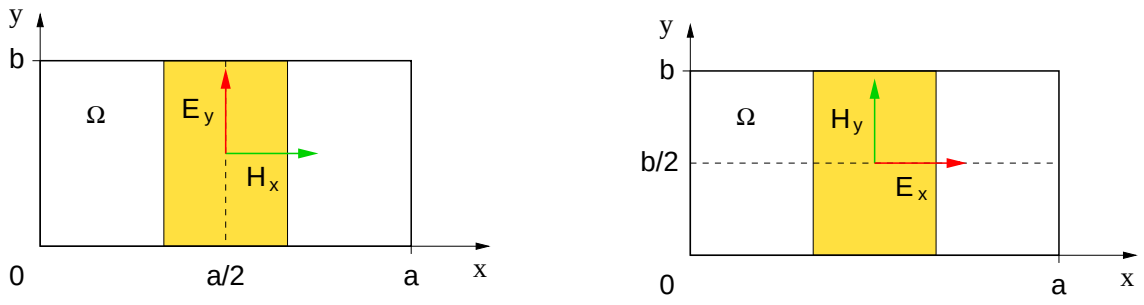

(a) (b)

Figure 2.15: *Power-voltage impedance definition for the LSE modes in a closed NRD-guide: (a) LSE modes, (b) LSM modes.*

2.3.2.1 Power-voltage impedance for the *LSE* modes

The voltage is defined as a line integral of the E_y field in the middle of the dielectric slab ($x = a/2$) (Fig. 2.15 (a))

$$V = \int_0^b E_y \, dy \qquad for \qquad x = \frac{a}{2}. \tag{2.66}$$

However, it should be pointed out here, that this voltage definition is valid only for modes with $n = 0$ [2]. For other LSE modes, with $n \neq 0$, the integral (2.66) is equal zero due to the form of the scalar potential in the y direction. The power is defined as the integral of the Poynting vector over the 2-D region Ω in a cross section of the guide

$$P = \frac{1}{2} Re \int_\Omega \vec{E} \times \vec{H}^* d\Omega \vec{i}_z = \frac{1}{2} Re \int_0^a \int_0^b (E_x H_y^* - E_y H_x^*) \, dx \, dy. \tag{2.67}$$

The E_x field component does not exist in the LSE modes, therefore the above expression for the power can be simplified to the form

$$P = -\frac{1}{2} Re \int_0^a \int_0^b E_y H_x^* \, dx \, dy. \tag{2.68}$$

2.3.2.2 Power-voltage impedance for the *LSM* modes

The voltage is defined as a line integral of the field E_x along the line perpendicular to the air-dielectric interface which is located at $y = b/2$ between the NRD-guide plates (Fig. 2.15 (b))

$$V = \int_0^a E_x \, dx \qquad for \qquad y = \frac{b}{2}. \tag{2.69}$$

[2] There is no field variation in the y direction.

The power is defined, similarly as for the case of *LSE* modes, in the form of field integral of the Poynting vector over the cross section of an NRD-guide (equation 2.67). The H_x field component does not exist in the case of *LSM* modes, hence the power, given by (2.67) can be written in a simpler form

$$P = \frac{1}{2} Re \int_0^a \int_0^b E_x H_y^* \, dx \, dy. \tag{2.70}$$

2.3.2.3 Numerical results

The power-voltage impedance are computed for the structures with electric and magnetic walls located at the distance d, and the semi-open structure with exponential field decay in the outer regions. The meaning of d is obvious for first two structures but for the latter one it determines the fraction of the fields, described by the exponential function, which are taken in the computation of the impedances. For the distances greater than d, the fields are equal zero. The relative error of the power-voltage impedance is computed using the definition (2.61). The impedance obtained for the structure with exponential field decay with $d \longrightarrow \infty$ mm is taken as the reference value. The dimensions of the example guide are the same as in the case of the computation carried out for wave impedance, the frequency $f_0 = 9.0$ GHz.

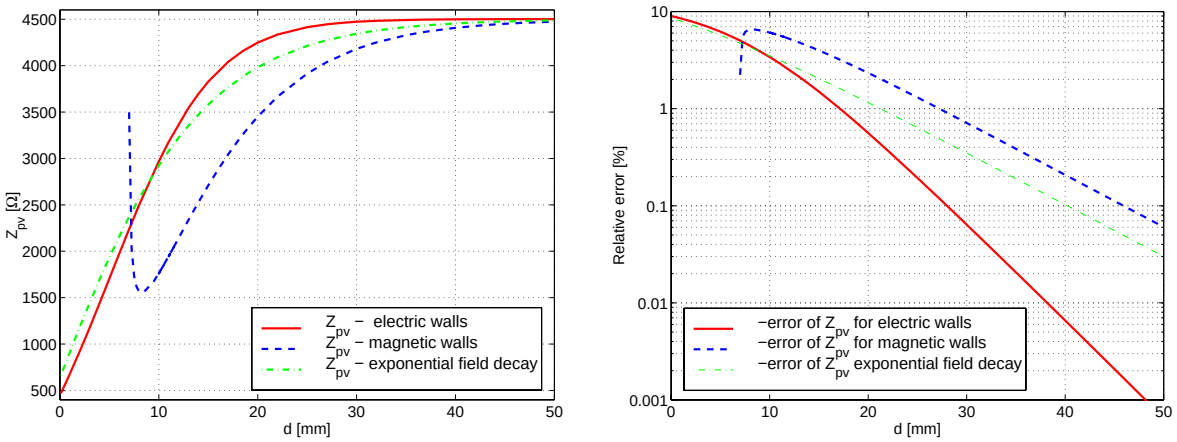

(a) (b)

Figure 2.16: *(a) Power-voltage impedance Z_{pv} LSM_{11} mode and (b) its relative error as a function of a distance d between dielectric rod and side walls at $f_0 = 9.0$ GHz. Guide parameters: $w = 10.16$ mm, $b = 15$ mm, $\epsilon_r = 2.53$.*

Discussion. For the LSM_{11} mode, the results obtained for electric walls are better than the corresponding ones for exponential field decay, the application of magnetic walls gives in the worst results. (Fig. 2.16 (a)). The sharp increase of impedance of the structure with magnetic walls for $d < 8.5$ mm is caused by the proximity of the cutoff frequency. The $d = \lambda_g/2$ (d=37.67 mm) assure the error equal ≈ 0.1 % for electric walls (Fig. 2.16 (b)). For the remaining structures the errors are more than one order of magnitude greater. To

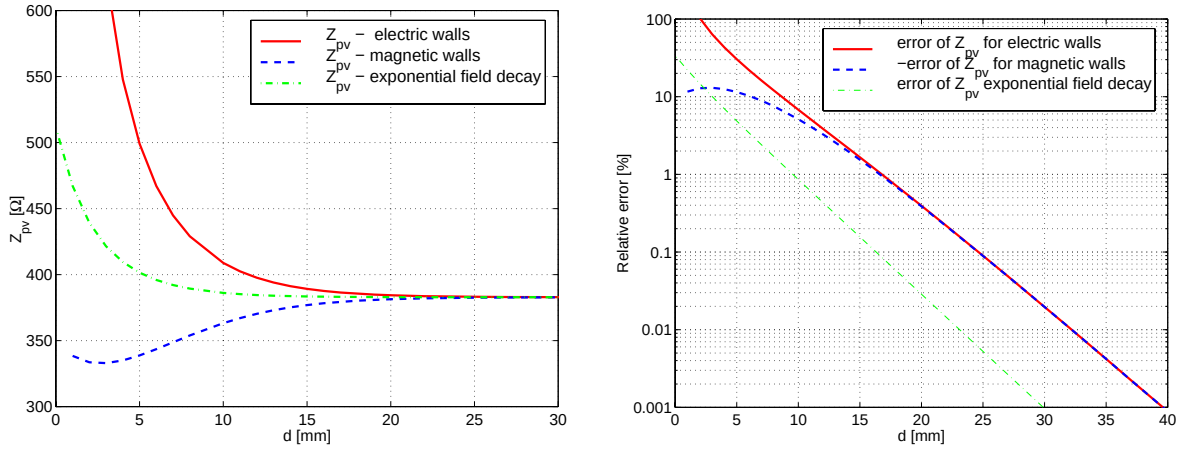

Figure 2.17: *(a) Power-voltage impedance Z_{pv} LSE_{10} mode and (b) its relative error as a function of a distance d between dielectric rod and side walls at $f_0 = 9.0$ GHz. Guide parameters: $w = 10.16$ mm, $b = 15$ mm, $\epsilon_r = 2.53$.*

obtain 0.1 % level d should be increased to $3\lambda_g/4$. The quickest convergence of the LSE_{10} mode impedance is observed for the structure with exponential field decay (Fig. 2.17 (a)). Although the relative errors of the closed structures are almost one order of magnitude greater than the error computed for semi-open structure, they are over one order of magnitude lower than for the best results obtained for LSM_{11} mode (Fig. 2.17 (b)). The walls located at the $d = \lambda_g/2$ (d=12.4 mm) result in the error $\approx 4\%$. The reduction of the error to 0.1% level requires the increase of d to $d = \lambda_g$ (d=24.8 mm), where λ_g refers to the LSE_{10} mode.

The significant difference between the LSM_{11} and LSE_{10} mode errors suggests, that the way the voltage is defined has great influence on the computation results. When the voltage is defined in the dielectric region (LSE modes) the error is caused mainly by the inaccurate approximation of the power. For the LSM modes the voltage is computed as a line integral of the electric field existing in air and dielectric regions. Therefore, the contribution of an inaccurate voltage computation in the overall error is increased due to significant influence of the walls on the electric fields in the outer regions.

Conclusions. The main points of the discussion are presented below:

- The results for the structure with PEC are over one magnitude better than for the remaining structures, when LSM_{11} mode is considered.
- The voltage definition has a significant influence on the error of impedance computation.
- Selection of $d = \lambda_g/2$, where λ_g corresponds to LSM_{11} mode, results in the relative error at level of 0.1% for almost all cases.

2.4 Loss in NRD-guide

The transmission losses are one of the important factors to be take on into account when selecting a waveguide for building millimeter-wave integrated circuits. The NRD-guide offers lower transmission loss than other dielectric guides. In order to determine the losses introduced by NRD-guide components, such as filters discussed in chapter 4, the knowledge of loss parameters of an NRD-guide is necessary. Therefore, the method of determination of NRD-guide loss factors of LSE and LSM modes is discussed in this section. Theoretical analysis is illustrated by numerical results obtained for two NRD-guides.

The losses in the NRD-guide are caused by two factors. The wave energy is dissipated in a lossy dielectric rod and on the resistive surface of metal plates. The dielectric losses are characterized by dielectric attenuation constant α_d while symbol α_c is used to describe attenuation constant of a conductor. The attenuation constants are defined as follows

$$\alpha_c = \frac{P_c}{2P_t} \tag{2.71}$$

$$\alpha_d = \frac{P_d}{2P_t} \tag{2.72}$$

where P_c and P_d denote the powers dissipated per unit length of the guide due to conductor loss and dielectric loss, respectively. P_t is the total power guided in the NRD-guide. Power refers to the energy transmitted by selected mode. In our case, the first hybrid LSE_{11} mode and the operating LSM_{11} mode are considered but the analysis is valid also for other higher order modes. The total attenuation constant α_t of the guide is the sum of the attenuation constants described above

$$\alpha_t = \alpha_c + \alpha_d. \tag{2.73}$$

Perturbation method. In general, the problem of finding the losses associated with lossy dielectric or lossy conductor is rather complicated. To obtain the exact solution a new boundary-value problem, which takes into consideration the losses, has to be solved. This task is usually simplified by applying a well-established perturbation method which allows one to find the analytical expressions of the attenuation constants α_c and α_d. These constants are found using expressions describing the fields in the structure. In the perturbation method, two structures of an guide are investigated. First one, called the basis structure, has ideal conducting plates and lossless dielectrics. The second one is created by introducing a perturbation into the basis structure. In our case this perturbation is caused by dielectric or conductor losses. The key assumption of the method is that the perturbation of a basis structure is very small and the fields in the lossy (perturbed) structure are almost the same as in the basis structure. Therefore, the fields in perturbed structure have the form found from the solution of a boundary value problem for the basis structure. Having determined the fields in lossy structure the perturbation formulae for α_c and α_d are derived.

2.4.1 Determination of α_d using perturbation method

The attenuation constant α_d of the NRD-guide is determined using variational expression of propagation constant derived from mixed formulation applied to the case of waveguide volume perturbation [72]. The method can be presented in the following way. The NRD-guide with lossless dielectric and perfect conducting walls is chosen as a basis structure. The field distribution in this structure is described in section 2.2. The perturbed structure forms the same NRD-guide but the lossy dielectric in assumed in this case. The field vectors are split into transversal and longitudinal parts, $E(x,y)$ and $H(x,y)$ express the dependence on transversal coordinates while the dependence in the z direction is described by the factor $e^{-j\beta z}$ for the lossless structure. Hence, the fields can be written in the following form

$$\vec{E} = \vec{E}(x,y)e^{-j\beta z} \tag{2.74}$$

$$\vec{H} = \vec{H}(x,y)e^{-j\beta z}. \tag{2.75}$$

Similarly the rotation operator is separated into transverse and longitudinal parts

$$\nabla \times (\cdot) = \nabla_t \times (\cdot) + \nabla_z \times (\cdot). \tag{2.76}$$

Substituting the fields given by (2.74) and (2.75) into the Maxwell equations and applying (2.76) the Maxwell equations for the basic structure are expressed as

$$\nabla_t \times \vec{E} + j\omega\mu\vec{H} = j\beta\vec{i_z} \times \vec{E} \tag{2.77}$$

$$\nabla_t \times \vec{H} - j\omega\epsilon\vec{E} = j\beta\vec{i_z} \times \vec{H} \tag{2.78}$$

where $\vec{i_z}$ is a unit vector in the z direction. The permittivity of the structure depends on x direction only, so $\epsilon = \epsilon(x)$ and the permeability of the whole structure is assumed to be $\mu = \mu_0$. Next, equations (2.77) and (2.78) are multiplied by E^* and H^* respectively and integrated over the cross section S of the NRD-guide. Finally, the resulting equations are subtracted and we obtain the variational expression for the phase constant β of the basic structure as a function of the fields existing in this structure

$$\beta = \frac{\omega \int_S \vec{E^*} \cdot \epsilon\vec{E} ds + \omega \int_S \vec{H^*} \cdot \mu\vec{H} ds + j \int_S \vec{E^*} \cdot \nabla_t \times \vec{H} - j \int_S \vec{H^*} \cdot \nabla_t \times \vec{E}}{\int_S H^* \cdot \vec{i_z} \times \vec{E} ds - \int_S E^* \cdot \vec{i_z} \times \vec{H} ds}. \tag{2.79}$$

The method assumes that the fields in the lossy structure are very well approximated by the fields of the basis structure. In the lossy structure the constant β is modified in order to express the losses. In our case, only the dielectric losses are assumed ($\alpha = \alpha_d$) therefore, propagation constant β_1 of lossy structure is expressed as

$$\beta_1 = \beta - j\alpha_d. \tag{2.80}$$

On the other hand the losses of the dielectric of the perturbed structure are described by the complex permittivity of a dielectric

$$\epsilon_1 = \epsilon_1' - j\epsilon_1'' \tag{2.81}$$

where $\epsilon'' = \epsilon' \tan\delta'$ and $\tan\delta$ is the loss tangent of the dielectric material. The permeability is the same as in the case of basic structure $\mu_1 = \mu_0$. Taking the fields of the basic structure as the trial fields in the perturbed structure the expression for β_1, similar to (2.79), can be written

$$\beta_1 = \frac{\omega \int_S \vec{E^*} \cdot \epsilon_1 \vec{E} ds + \omega \int_S \vec{H^*} \cdot \mu \vec{H} ds + j \int_S \vec{E^*} \cdot \nabla_t \times \vec{H} - j \int_S \vec{H^*} \cdot \nabla_t \times \vec{E}}{\int_S H^* \cdot \vec{i}_z \times \vec{E} ds - \int_S E^* \cdot \vec{i}_z \times \vec{H} ds}. \tag{2.82}$$

Then by subtracting β from β_1 the perturbation formula for attenuation constant α_d is obtained

$$\alpha_d = \frac{j\omega \int_S \vec{E^*}(\epsilon_1 - \epsilon)\vec{E} ds}{\int_S \vec{H^*} \cdot \vec{i}_z \times \vec{E} ds - \int_S \vec{E^*} \cdot \vec{i}_z \times \vec{H} ds}. \tag{2.83}$$

Attenuation constant α_d of LSM modes. In the case of LSM modes, in particular the dominant LSM_{11} mode, for which the $H_x = 0$, equation (2.83) is simplified to

$$\alpha_d = \frac{j\omega \int_S \vec{E^*}(\epsilon_1 - \epsilon)\vec{E} ds}{2 \int_S E_x H_y ds}. \tag{2.84}$$

In the above expression the numerator represents the power dissipated in the dielectric per unit length while the denominator corresponds to the power transmitted in the LSM_{11} mode (compare with 2.70). The analytical expressions for the attenuation constants α_d of the LSM_{11} mode derived using the perturbation method to the NRD-guide structure with the field attenuated exponentially in the outer regions was reported by Yoneyama [73]. The following relation, presented here as a reference, is written based on cited article

$$\alpha_d = \frac{k_0^2 \epsilon_r \tan\delta}{2\beta} \left[\frac{q_0 b + \left(1 - \frac{2q_0^2}{k_0^2 \epsilon_r}\right) \sin(q_0 b)}{q_0 b + (\epsilon_r - 1)\frac{k_0^2}{p_0^2} \sin(q_0 b)} \right] \tag{2.85}$$

where

$$q_0 = k_{x_d} \qquad\qquad p_0 = j k_{x_0} \tag{2.86}$$

k_{x_d} and k_{x_0} are the wavenumbers in dielectric and air regions of an NRD-guide respectively. The dielectric parameters are described by the dielectric loss factor δ and effective permittivity ϵ_r, β is the phase constant of the dominant LSM_{11} mode of an NRD-guide, b is a guide width.

Attenuation constant α_d of LSE modes. For the LSE modes, $E_x = 0$ so the relation (2.83) is converted to

$$\alpha_d = -\frac{j\omega \int_S \vec{E^*}(\epsilon_1 - \epsilon)\vec{E} ds}{2 \int_S E_y H_x ds}. \tag{2.87}$$

Similarly to LSM modes, the numerator and denominator refer to the power dissipated per unit length in dielectric and transmitted in the LSE_{11} mode, respectively.

2.4.2 Determination of α_c using perturbation method

For determine the α_c as the basis structure the NRD-guide with perfectly conducting walls and lossless dielectric is taken. The perturbation of the structure is introduced by losses of the conductor described by the surface resistance expressed as

$$R_s = \sqrt{\frac{\omega\mu_0}{2\sigma}} \tag{2.88}$$

where σ is the conductivity of metal plates. The total power dissipated in metallic wall surfaces A is expressed as

$$P_c l = \frac{R_s}{2}\int_A \vec{J}_s\vec{J}_s^* dA \tag{2.89}$$

where l is a unit length of a guide and P_c is a dissipated power per unit length, $\vec{J}_s$ is the current density on the metal plate surfaces A and $\vec{J}_s$ is computed from

$$\vec{J}_s = \vec{n}\times\vec{H} \tag{2.90}$$

where $\vec{n}$ is an unit vector perpendicular to the plate surface. The fields of the basis structure are used as trial fields in the perturbed one.

Attenuation constant α_c of LSM modes. For the LSM modes $H_x = 0$, therefore only $\vec{J}_x$ component exists. Equation (2.89) can be simplified to line integral over the cross section S

$$P_c = \frac{R_s}{2}\int_0^a \mid H_z\mid^2 dx \tag{2.91}$$

where P_c is the power per longitudinal length dissipated in one metallic wall. The total power per unit of length transmitted in the NRD-guide is given by equation (2.70). Hence, the α_c is computed by substituting (2.91) and (2.70) into (2.71) resulting in the following expression

$$\alpha_c = \frac{2R_s\int_0^a \mid \vec{H}_z^2 \mid dx}{\int_0^b\int_0^a E_x H_y dxdy}. \tag{2.92}$$

The exact formula for α_c of LSM_{11} mode, obtained by means of perturbation method, for the case of a guide in the exponential attenuation in outer regions was published by Yoneyama [73]. The following relation, written based on this work, is given here as a reference

$$\alpha_c = 2R_s\frac{\omega\epsilon_r\epsilon_0}{h_0^2\beta a}\left(\frac{\pi}{a}\right)^2\left[\frac{q_0 b + \left(1+\frac{q_0^2}{p_0^2\epsilon_r}\right)\sin(q_0 b)}{q_0 b + (\epsilon_r - 1)\frac{k_0^2}{p_0^2}\sin(q_0 b)}\right] \tag{2.93}$$

where a is a guide height, b is a guide width, h_0 is related to the transversal wavenumbers by the following relation

$$h_0^2 = \epsilon_r k_0^2 - q_0^2 = k_0^2 + p_0^2 \tag{2.94}$$

q_0 and p_0 are given by (2.86), β is the phase constant of the LSM_{11} mode.

Attenuation constant α_c of LSE modes. For the LSE modes $\vec{J}_x$ and $\vec{J}_z$ components of surface current exist; the power dissipated in metallic walls of guide of unit length l is given by equation (2.89), where the wall surface $A = 2al$. The longitudinal dependence of the fields has the form of $e^{-j\beta z}$ therefore the equation (2.89) is simplified to line integral over the cross section

$$P_c = \frac{R_s}{2} \int_0^a \mid H_x\mid^2 + \mid H_z\mid^2 dx \tag{2.95}$$

where P_c is the power per longitudinal length dissipated on one metallic wall. The total power transmitted in an LSE mode is given by equation (2.68). Hence, combining (2.95) with (2.68) and (2.71) the expression for α_c is obtained as follows

$$\alpha_c = -\frac{2R_s \int_0^a \mid H_x^2\mid^2 + \mid H_z^2\mid^2 dx}{\int_0^b \int_0^a E_y H_x dx dy}. \tag{2.96}$$

2.4.3 Attenuation constant α_d of plane wave in lossy media

As the frequency is increased the power of a guided wave is concentrated in the dielectric strip of an NRD-guide. For the comparison the attenuation of a plane wave in the dielectric media is computed and included into the loss characteristics as a reference value.

The exact expression describing attenuation constant of an uniform plane wave in unbounded media is given by [66]

$$\alpha_d = \omega\sqrt{\mu\epsilon}\left\{\frac{1}{2}\left[\sqrt{1+\left(\frac{\sigma}{\omega\epsilon}\right)^2} - 1\right]\right\}^{1/2} \tag{2.97}$$

where σ is the conductivity of the medium. For good dielectrics the displacement current density is much greater than the conduction current density therefore the following condition holds

$$\left(\frac{\sigma}{\omega\epsilon}\right)^2 \ll 1. \tag{2.98}$$

Hence, the exact equation (2.97) for the attenuation constant can be simplified to

$$\alpha_d = \frac{\sigma}{2}\sqrt{\frac{\mu}{\epsilon}}. \tag{2.99}$$

Sometimes this expression is transformed into more convenient form where technical parameters of a dielectric are apparent [8]

$$\alpha_d = \frac{\pi}{\lambda}\tan\delta\sqrt{\epsilon_r} \tag{2.100}$$

where λ is a plane wave wavelength in dielectric medium, $\tan\delta$ is a loss tangent of a dielectric and ϵ_r is its relative dielectric constant.

2.4.4 Numerical results

The loss characteristics of two NRD-guides, which are used later on in the filter design, are presented below. The losses are computed for the LSE_{11} and the dominant LSM_{11} in both cases. The NRD-guides are characterized as follows:

- **The NRD-guide designed for the X-band.** The guide has the dielectric rod made of Rexolite 1422 and the metal plates made of brass. The technical parameters of the guide are as follows: width $w = 10.16$ mm, height $b = 15$ mm, $\epsilon_r = 2.53$. The loss factor for Rexolite 1422 $\tan\delta = 0.005$ at 10 GHz; the conductivity of brass is equal $\sigma = 2.56 \cdot 10^7$ S/m. The computed results are obtained using the perturbation methods for the closed structure with the electric walls located at the distance $d = 35.56$ mm from the dielectric slab.

- **The NRD-guide designed for the U-band.** The dielectric slab of the guide is made of Teflon ($\epsilon_r = 2.04$, loss factor $\tan\delta = 1.5 \cdot 10^{-4}$) the metal plates are made of copper for which the conductivity $\sigma = 5.8 \cdot 10^7$ S/m is assumed. The guide has the following dimensions: width $w = 3.5$ mm, height $b = 2.7$ mm. The computation are performed for the closed structure with the electric walls located at the distance $d = 7$ mm from the dielectric slab.

Discussion of X-band guide results. The loss characteristics of X-band NRD-guide are shown in Fig. 2.18. The dielectric losses of the LSM_{11} mode (Fig. 2.18 (a)) are relatively high at the cutoff frequency, they decrease subsequently and reach their minimum of 8.1 dB at 10 GHz, and start to grow up for higher frequencies. Away from the cut-off frequency the dielectric losses have nearly the same level as for the plane wave losses in the dielectric medium which has the permittivity of the NRD-guide rod. The conductor losses are over one order lower than the dielectric ones and decrease when the frequency is increased. The total losses of the NRD-guide are almost equal to the dielectric losses, hence the conductor losses can be omitted and only dielectric losses can be considered in practical applications. The dielectric losses of the LSE_{11} mode are nearly two times greater than for the LSM_{11} mode in the entire X-band (Fig. 2.18 (b)). They are very high near cutoff frequency and fall down to about 16 dB at higher frequencies. Unlike for the LSM_{11} mode, they are also significantly greater than the plane wave losses. Although conductor losses are greater than for the LSM_{11} mode they are still more than one order of magnitude lower than the dielectric ones and can be neglected in practice.

Discussion of U-band guide results. The loss characteristics of the U-band NRD-guide are shown in Fig. 2.19. Near cutoff frequency the conductor and dielectric losses of the LSM_{11} mode (Fig. 2.19 (a)) are relatively high. As the frequency increases, they fall down drastically. The dielectric losses decrease to approximately 1.6 dB at 55 GHz and start to increase for higher frequencies. They have the same character as the losses of an uniform plane wave in the dielectric medium with the permittivity of the NRD-guide rod. Also the values of the dielectric losses are nearly the same as for the plane wave, especially for higher frequencies. The conductor losses decreased with frequency but level is comparable to the

level of the dielectric losses. Hence, for the computation of the total losses of the guide both loss factors should be taken into consideration. For the frequency 49.5 GHz, the center frequency of the filters described in chapter 4, the conductor losses are even greater than the dielectric ones.

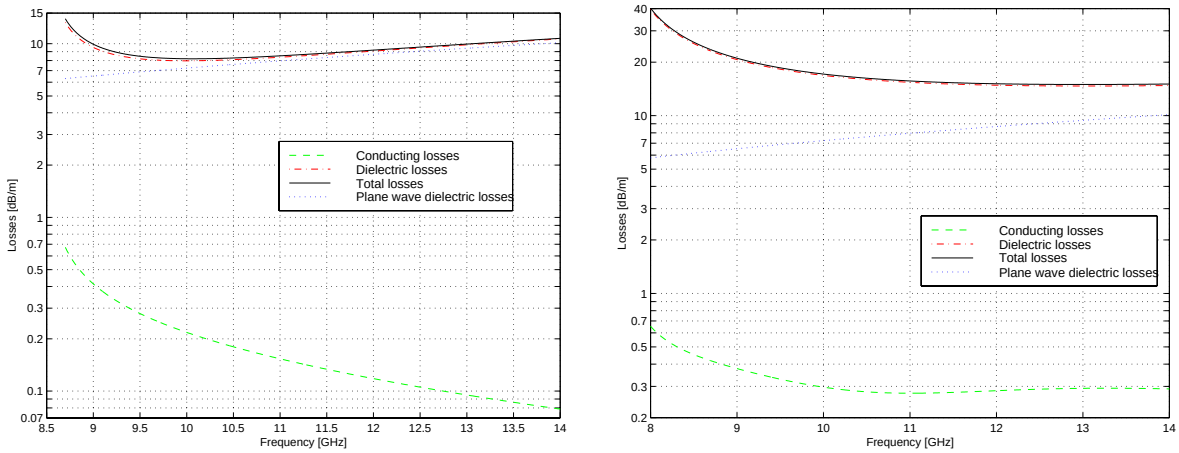

Figure 2.18: *Theoretical transmission losses of the guide working at the X-band: (a) LSM_{11} mode, (b) LSE_{11} mode. Guide parameters are given in text.*

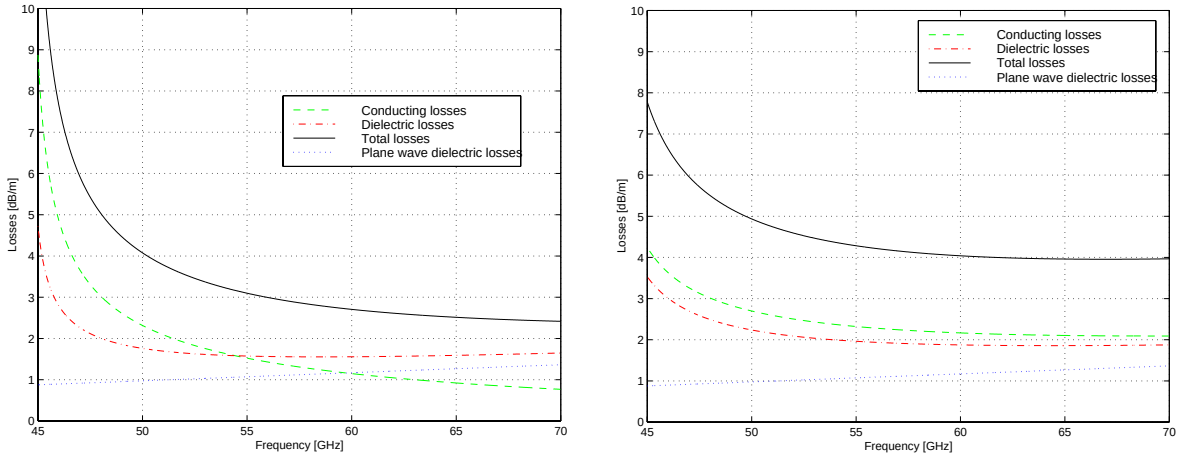

Figure 2.19: *Theoretical transmission losses of the guide working at U-band: (a) LSM_{11} mode, (b) LSE_{11} mode. Guide parameters are given in text.*

The losses of the LSE_{11} mode are greater than the ones for the LSM_{11} mode (Fig. 2.19 (b)). The total losses are on the level of 5 dB at 49.5 GHz and fall down to approximately 4 dB at higher frequencies. At U band they are about 1 dB higher than for the LSM_{11} mode, for higher frequencies the difference is increased to 1.6 dB. The conductor losses are greater

than the dielectric ones in entire frequency band shown in Fig. 2.19 (b) but both types of losses are at the similar level.

Conclusions. The presented discussion can be summarized as follows:

- The total loss of the LSM_{11} mode are lower than for the LSE_{11} mode in microwaves and millimeter waves.
- The conductor losses can be neglected when the NRD-guide works in microwaves. In millimeter waves the conductor losses are at the same level as the dielectric ones, therefore they have to be taken into consideration. Moreover, in some cases they are even greater than the dielectric losses.
- The dielectric losses of the LSM_{11} mode can be approximated by plane wave losses in unbounded dielectric medium if the investigated frequency lies sufficiently far away from the cutoff frequency.

2.5 An NRD-guide air gap discontinuity

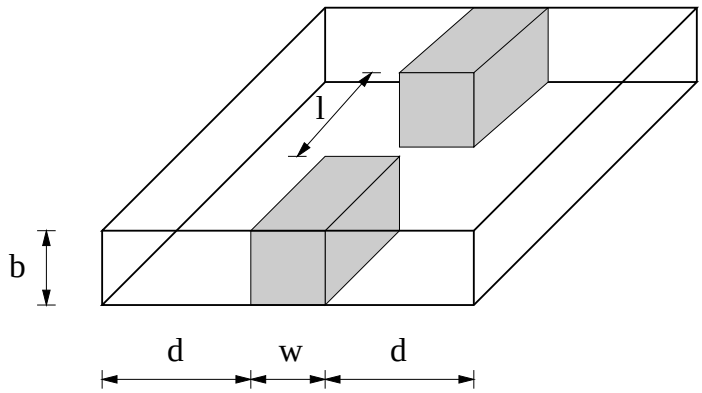

Figure 2.20: *An air gap discontinuity in the closed NRD-guide.*

The air gap discontinuity in the NRD-guide (Fig. 2.20) is investigated in this section because it is a basic component used in the synthesis of coupled cavity filters discussed in chapter 4. The scattering parameters of the discontinuity are computed using the FDTD software. Selection of the distance d where the bounding walls should be placed has a significant influence on the size of generated problem and, consequently, on the computation time. This choice is important when a single discontinuity analysis is performed and became critical for analysis of larger structures such as bandpass filters which are composed of the cascade of such air gap discontinuities; these filters are more precisely described in chapter 4.

Previous tests showed that for calculating of the phase constant or the wave or characteristic impedance of the NRD-guide the lateral screens can be placed at $d = \lambda_g/2$ to obtain

results with accuracy at 0.1 % level for almost all cases. However, in the case of the air gap discontinuity the fields are scattered on the discontinuity and the distance d appropriate for straight guide can be insufficient. Therefore, the air gap is investigated in order to find the influence of the side walls position for the accurate computation of the air gap parameters.

The NRD-guide parameters are the same as for β and impedance computations (i.e. $w = 10.16$ mm, $b = 15$ mm, $\epsilon_r = 2.53$ (Rexolite 1422)). The frequency $f_0 = 9.5$ GHz, the center frequency of the bandpass filters discussed in chapter 4, has been selected. The S parameters are calculated for the operating LSM_{11} mode, for which guide wavelength $\lambda_g = 51.95$ mm. The air gap of length $l = 13$ mm ($\approx \lambda_g/4$) is chosen. All computations have been performed on the PC Pentium II 233 MHz with 64 MB RAM using commercial *QuickWave-3D* software [74].

The parameters of the scattering coefficients and their relative errors are plotted in Fig. 2.21 and Fig. 2.22. The relative error of the S_{11} and S_{21} parameters versus the distance d is defined as follows

$$\Delta S_{i1}(d) = \frac{S_{i1}(d) - S_{i1_{ref}}}{S_{i1_{ref}}} \cdot 100 \quad [\%] \tag{2.101}$$

where $i = 1$ for reflection coefficients and $i = 2$ for transmission coefficient. The results for the $d = 50$ mm are taken as the reference values $S_{i1_{ref}}$. For each structure with different d, the computation time has been longer than 1500 s (PC Pentium II 233 MHz with 64 MB RAM). In the following discussion it is shown that such time guarantees that the accuracy of the computation is better than 0.01 %.

S parameters error vs. d dependency. The relative error of the amplitudes reaches the level of 1% at the distance equal $\lambda_g/2$ ($d = 25.98$) mm (Fig. 2.21 (b)). The same conclusion can be observed for the phases (Fig. 2.22 (b)). Recall, that $d = \lambda_g/2$ ensures the accuracy β computation of 0.1 %, here at the same distance the S parameter errors are nearly one order of magnitude higher reaching 1% level.

This leads to the conclusion that for the scattering parameters computation the walls should be placed at larger distance d equal nearly $\frac{3\lambda_g}{4}$ instead of $\frac{\lambda_g}{2}$ as it is for the β case.

S parameters error vs. time dependency. Having found d which assures 0.1 % accuracy in terms of the relative error of the scattering parameters computation, the convergence of the scattering parameters to the accurate value in a given frequency band versus the computation time (or the number of iterations) of the FDTD software is examined.

The normalized relative error describing the accuracy of the scattering parameters computation in the frequency band spanned from f_1 to f_2 has the form

$$\Delta S_{i1}(k) = \frac{\| \underline{S}_{i1}(k) - \underline{S}_{i1ref} \|_2}{\| \underline{S}_{i1ref} \|_2} \tag{2.102}$$

where $\underline{S}_{i1}(k)$ is the vector of scattering parameter values computed at discrete frequency points within the examined frequency band. Factor k can be interpreted either as the number of iterations or the computation time (these two quantities are proportional one to another). Index $i = 1$ for reflection coefficients, and $i = 2$ for transmission coefficients. As

the reference vectors $\underline{S}_{i1ref}$, the values obtained for the computation time equal 1500 sec. are taken.

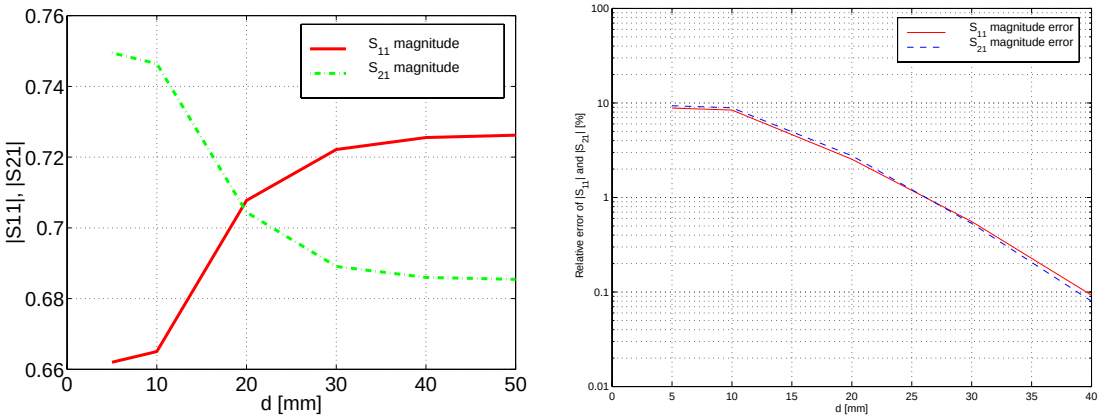

(a) (b)

Figure 2.21: *Results of FDTD method computation: (a) amplitudes of the scattering parameters S_{11} and S_{21} and (b) their relative error versus distance d of the NRD-guide with air gap of $l = 13$ mm. Guide parameters: $w = 10.16$ mm, $b = 15$ mm, $\epsilon_r = 2.53$.*

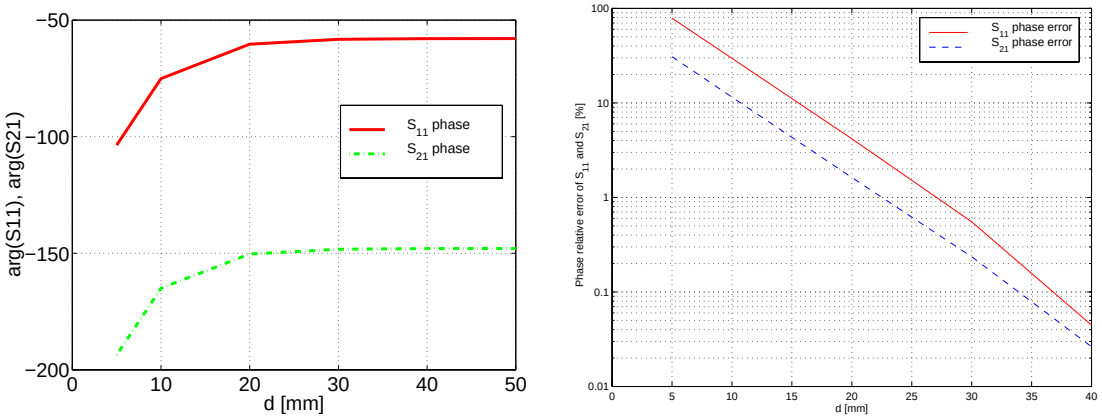

(a) (b)

Figure 2.22: *Results of FDTD method computation: (a) phases of the scattering parameters S_{11} and S_{21} and (b) their relative error versus distance d of the NRD-guide with air gap of $l = 13$ mm. Guide parameters: $w = 10.16$ mm, $b = 15$ mm, $\epsilon_r = 2.53$.*

For the discussed structure the scattering coefficients have been computed in the frequency band spanned from 8.5 GHz to 12 GHz. The plots of the relative error versus the number of iterations and computation time are shown in Fig. 2.23. The accuracy of 1% relative error level is obtained after 400 sec. The error is decreased to 0.1 % for 650 sec. Further investigation of the relative error characteristics leads to the conclusion that doubling the computation time results in the accuracy improvement at last one order of magnitude.

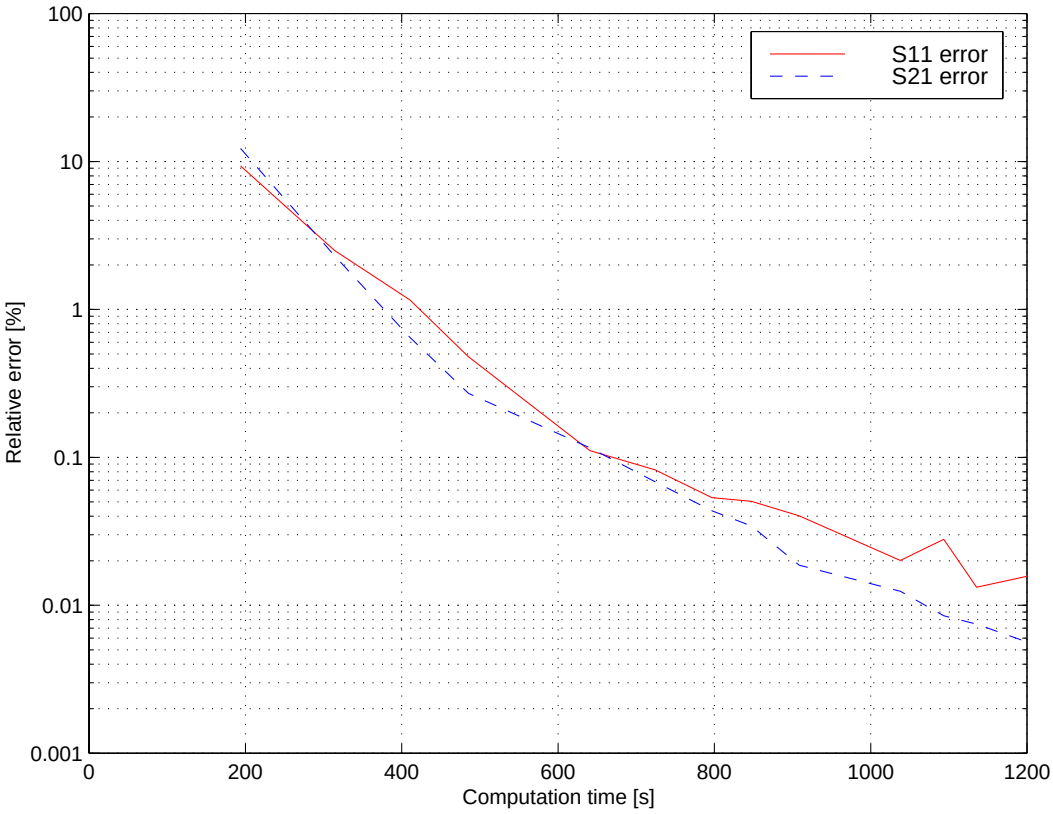

Figure 2.23: *Relative error versus number of iterations of the S_{11} and S_{21} amplitudes of the NRD-guide with air gap of $l = 13$ mm and distance $d = 35.56$ mm. Results for the FDTD software.*

Conclusions. The main conclusions of the presented discussion are:

- The lateral PEC screens should be placed at the distance $d = 3\lambda_g/4$ to achieve the 0.1 % accuracy of the scattering parameters computation.
- When the FDTD software is used, the accuracy of the computation of S parameters is improved one order of magnitude when the computation time is doubled.

Chapter 3

Transition between an NRD-guide and a rectangular waveguide

3.1 Introduction

The rectangular waveguide and coaxial line are used as standard transmission lines in a majority of power sources and measurement devices which work in the microwave and millimeter wave frequency bands. The operating mode of an NRD-guide is the LSM_{11} mode, therefore the problem has to be solved of how to excite this mode in practically realized NRD-guide circuits.

The LSM_{11} mode of an NRD-guide can easily be excited by the TE_{10} mode of a rectangular waveguide due to similarity of electric field patterns of these modes. Therefore, a rectangular waveguide is usually employed to excite the trial NRD-guide circuits and components for testing and development. To make the measurements possible, the transition between an rectangular waveguide and NRD-guide is required. However, it should be noted, that in practically realized hybrid integrated circuits where the dimensions of NRD-guide components are as small as possible, this kind of transition is not used because of its relatively large dimensions. The NRD-guide circuits or elements are excited in a different manner, for example microstrip lines can be used as a luncher [40].

In this chapter the composite transition between a rectangular waveguide and an NRD-guide is investigated. The approximate synthesis is presented and applied to design several transitions. The projects are verified numerically and a selected design is used to build a pair of transitions. The experimental verification is carried out in the X-band.

The transition between a rectangular waveguide and an NRD-guide should have the following features:

- Geometry of the transition which guarantees the conversion from TE_{10} rectangular waveguide mode to LSM_{11} NRD-guide mode in a required frequency range
- Relatively wide operational bandwidth
- Small input return loss in the operational bandwidth (about -20 dB and less)

- Small geometrical dimensions (short length of a transition)

The practical criteria such as easy way of fabrication and low cost of manufacturing should also be taken into account.

When the circuit theory is applied, two different waveguides can be treated as the transmission lines, each with different impedance. In this case the problem of proper connection between waveguides is converted into the classical problem of matching of two transmission lines. A transmission line section, with a length l and a variable impedance profile $Z(l)$, is used to match two other lines with different impedances denoted by Z_1 and Z_2. The impedance profile $Z(l)$ of the matching section has the shape which ensures the minimal level of return loss when the output is terminated by the line with impedance Z_2.

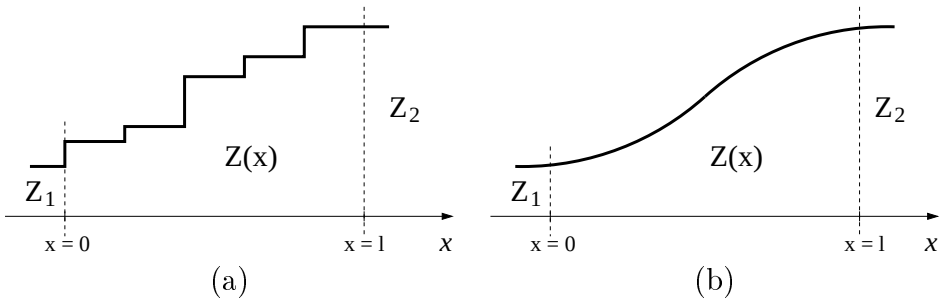

Figure 3.1: *Matching section with: (a) stepped impedance profile, (b) continuous impedance profile.*

Two types of impedance profile are commonly used [69]:

- a stepped impedance profile (Fig. 3.1 (a)),
- a continuous impedance profile (Fig. 3.1 (b)).

Both profiles offer different features and the decision which one is used depends on a particular case.

Transition with stepped impedance profile. The transition with a stepped impedance profile is usually designed as a quarter-wave transformer or a half-wave filter [75] and can be build of non-dispersive (TEM) or dispersive guides (non-TEM). Huge amount of technical literature is concerned with these devices [64] [76] [77]. A simple quarter-wave transformer ensures perfect match at one wavelength. To obtain broad band matching, a series of quarter-wave transformers is used. The basic parameter, which describes the mismatch between the lines, is the input to output impedance ratio R. For stepped impedance transformers built of a cascade of quarter-wave transformers parameter R is relatively small. Another form of a matching section is a cascade of line sections, each being half-wave long, which creates a half-wave filter. This structure is used to match the lines for which R has relatively large values, but the definition of R is slightly changed and now R has the meaning of the maximum VSWR computed as a product of internal VSWR's. The close relationship exists between the quarter-wave transformer and the half-wave filter structures.

The performance of the former can be determined directly from the characteristics of the latter one. For both cases, the most commonly used analytical design expressions describe the maximally flat or Chebyshev response obtained for a given number of sections n and specified R. The quarter-wave transformers and the half-wave filters work as typical band-pass structures. The larger n, the better is the impedance match over the wider bandwidth. On the other hand, the total length of the matching section and the transmission losses are increased. Hence, the classical trade off exists between structure length, operational bandwidth and transmission losses.

The transition with continuous impedance profile. The transitions with continuous impedance profile are usually designed to obtain the optimal performance. Usually, the optimal transition is either the one which has the minimal magnitude of reflection coefficient through the specified frequency band when the length of the transition is given, or the transition for which the minimal length is found for a given tolerance of reflection coefficient at the design frequency.

The problem of a design of the optimal transition, with continuous impedance profile, between two TEM lines has been studied extensively in past decades (e.g. Colin [78], Klopfstein [79] and papers referenced therein). In Klopfstein's work the designed transition, with optimal impedance profile, has the minimal length for a given reflection coefficient, yet the drawback of his method is appearance of the impedance steps at both ends of the transition, which deteriorate matching between the lines. Moreover, the parasitic modes can be excited at the discontinuities. The near-optimum design of the matching section without impedance steps was proposed by Hecken in [80]. His method yields the transition only a slightly part longer than the optimal one. Although Hecken's synthesis is focused on TEM lines, some remarks about approximate analysis of the tapers made of dispersive guides are also given in the paper cited above. In general, continuous tapers work as high pass filtering structures. The shortest possible length of the transition is determined by the longest wavelength for which the input reflection coefficient does not exceed the specified value. Therefore, a trade off exists in this case between the transition length and pass band edge frequency, when the reflection level is fixed. On the other hand, for fixed frequency, the increase of the transition length assures a lower level of return loss. Theoretically the infinitely long transition built of lossless line yields perfect match.

Discussion. Selection of the impedance profile. The comparison between the stepped impedance transformers and the corresponding continuous tapers, presented in [77], shows, that the impedance transformers with stepped impedance profile yield better results over commonly used bandwidths and impedance ratios R. Despite that, continuous tapers possess features which make them attractive. In contrast to the stepped impedance transformers, they do not introduce additional discontinuities which can generate unwanted modes. This property is of great importance for an NRD-guide, where the first higher order mode LSM_{11} works as the operating mode and thus the possible excitation of the lower LSE_{11} mode should be avoided. In the transitions discussed in the sections that follows, not only are the dispersive guides applied, but also the propagation constant β varies along the taper length. For the taper with continuous impedance profile a simple modification of the

algorithm can be applied in order to incorporate the β variation into synthesis. As a result, the continuous impedance profile is chosen to design the transition between a rectangular waveguide and an NRD-guide and is discussed at length in the following sections.

3.2 Design of the transition with continuous impedance profile

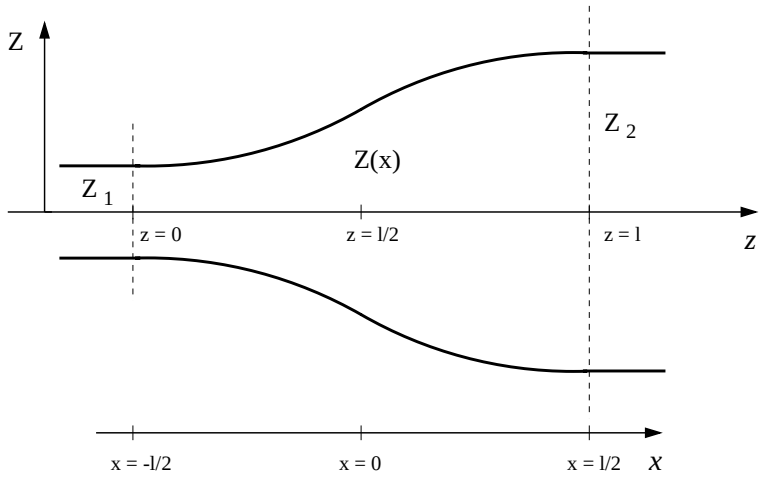

Figure 3.2: *A nonuniform matching section of length l between two lines with impedances Z_1 and Z_2.*

The design of a transition with a continuous impedance profile is discussed in this section. The transition is shown in Fig. 3.2 together with the coordinates used in the description of the method. The key points of the synthesis method based on the Hacken's procedure [80] are presented. The method assumes that only dominant mode is propagated in the structure and the influence of the other modes is neglected. The design procedure can be described in the following manner.

Design procedure. For a clear presentation of the method, the design procedure is divided into steps.

Step 1. The method starts from the determination of the design frequency f_0, at which the maximal input reflection coefficient r_{max}, is specified. In general, an input return loss L_r and an input reflection coefficient r are related by

$$L_r = -10\log(|r|^2) = -20\log(|r|) \qquad [dB] \tag{3.1}$$

L_r equals the value of r_{max} specified in dB. Therefore, in the following text, the r_{max} given in dB is used to describe the return loss.

The value of r_{max} is determined by two factors: the initial reflection r_0 existing between the mismatched lines and the minimal level of reduction of the reflection coefficient ϵ_{max} introduced by the matching section. The index max of ϵ_{max} can cause misunderstanding,

but it stands for maximal level of the ripple function ϵ (defined later on) or in the other words, the maximal reflection level introduced by the matching section in the worst case. In the procedure the quantities r_{max}, r_0 and ϵ_{max} are related one to another by

$$r_{max} = tanh(r_0 \epsilon_{max}). \tag{3.2}$$

Since $\tanh(x) \approx x$ with the error less than 0.01 for $x < 0.3$ equation (3.2) can be approximated by

$$r_{max} = r_0 \epsilon_{max} \tag{3.3}$$

with very good accuracy. This is because the value of $\epsilon_{max} r_0$ is almost always less than 0.3 in practical situations. The dependencies (3.2) and (3.3) are usually expressed in the logarithmic scale

$$r_{max}[dB] = r_0[dB] + \epsilon_{max}[dB] \tag{3.4}$$

where r_0 and ϵ_{max} are determined in the steps that follows.

Step 2. For given impedance values Z_1 and Z_2 at the transition ends, the initial reflection coefficient caused by impedance step between Z_1 and Z_2 is computed using the formula

$$r_0 = \tanh(y_0) \tag{3.5}$$

where the mismatch is computed as

$$y_0 = \ln \sqrt{\frac{Z_2}{Z_1}}. \tag{3.6}$$

Equation (3.5) is an equivalent of the classical expression

$$r_0 = \frac{Z_2 - Z_1}{Z_2 + Z_1}. \tag{3.7}$$

Step 3. When the r_0 and r_{max} are known, the desired value ϵ_{max} of the matching section is determined using (3.2) or (3.4).

Step 4. Next, the expression for the transition length is derived. The local reflection coefficient $F(x)$ along the transition length l is related to ripple function $f(\beta)$ in the frequency domain by the Fourier transform. Here, β is the phase constant. For near-optimum taper without impedance steps the $f(\beta)$ is specified by the modified Dolph-Chebyshev response as follows

$$f(\beta) = y_0 \epsilon \tag{3.8}$$

where

$$\epsilon = \frac{B}{\sinh B} \frac{\sin \sqrt{(\beta l)^2 - B}}{\sqrt{(\beta l)^2 - B}} \tag{3.9}$$

and the value of B is found from (3.10) using ϵ_{max} determined in step 3. The first maximum of expression (3.8) for $\beta l > 0$, has the value given by

$$\epsilon_{max} = \frac{B}{\sinh B}(0.217236). \tag{3.10}$$

Note that the maximum of the ripple function ϵ depends entirely on B, the parameter of Dolph-Chebyshev response. Even if B=0, $\epsilon_{max} = 0.217236$, which corresponds to the return loss of $L_{\epsilon_{max}} = 13.2614$ dB. This fact should be highlighted, because it means that the design procedure allows one to design the transitions which improve the the return loss level by the value not lower than 13.2614 dB.

The minimal transition length l_{min} is found from (3.9) and (3.10) and is expressed by the equation written below

$$(\beta_0(x)l)_{min} = \sqrt{B^2 + 6.523} \tag{3.11}$$

where $\beta_0(x)$ is a longitudinal wavenumber, which corresponds to the largest wavelength (determined by the design frequency f_0) in the assumed frequency band. The method is originally intended to TEM transmission lines, hence in such case the choice of l_{min} is evident, because $\beta_0(x)$ has the same value for each x. However, in the case of non-TEM lines for some designs, $\beta_0(x)$ varies along the transition length and determination of l_{min} is not obvious. For sake of the example the plots of β_0 versus the transition length, related to the composite transition discussed in section 3.4.1, are shown in Fig. 3.3.

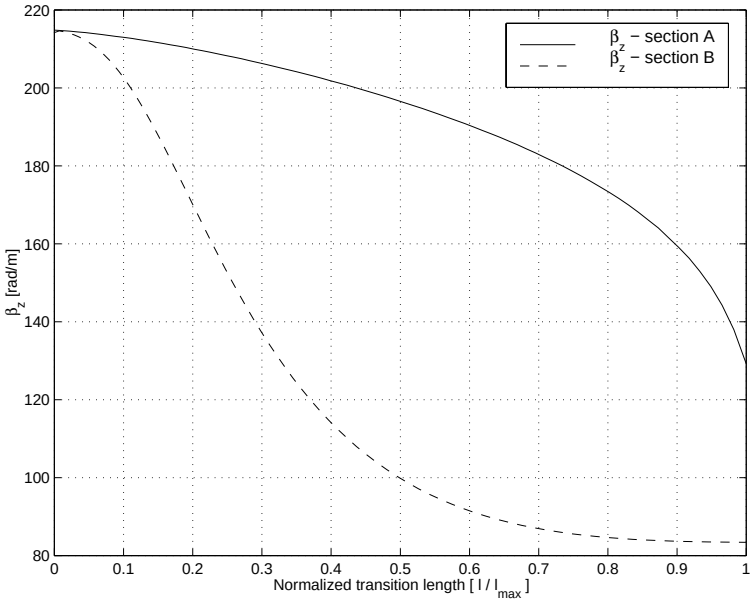

Figure 3.3: *The variation of the propagation constants β at $f_0 = 9$ GHz versus the taper length of two sections of the composite transition discussed in section 3.4.1.*

For fixed β the possible choices of transition length l lie between l_{min} and l_{max}, which correspond to β_{max} and β_{min} respectively; β_{max} and β_{min} are the largest and the lowest

values of the propagation constant which occur in the transition at the design frequency f_0. Usually, l_{min} differs significantly from l_{max}. The optimal choice is l_{max}, but it may happen that for that choice the transition length is relatively long and, in addition, too high transmission losses are introduced. Therefore, one should choose a shorter taper length l, for which a fraction of $\beta_0(x)$ does not fulfil the condition (3.11). It is evident that the trade off exists between the transition length and a distribution of $\beta_0(x)$ is helpful in the proper choice of l.

Step 5. In the last step the impedance profile of the transition $Z_c(\xi)$ is found from

$$\ln Z_c(\xi) = \frac{1}{2}\ln(Z_1 Z_2) + \frac{1}{2}\ln\left(\frac{Z_2}{Z_1}\right) G(B,\xi) \tag{3.12}$$

where $\xi = 2x/l$, and $G(B,\xi)$ is a function described by the following relation

$$G(B,\xi) = \frac{B}{\sinh B}\int_0^{\xi} I_0\left\{B\sqrt{1-\xi'^2}\right\} d\xi' \tag{3.13}$$

where $I_0(x)$ is the modified Bessel function of the first kind. Note that $G(B,\xi)$ has odd symmetry so $G(B,\xi) = -G(B,-\xi)$.

As noted before, the synthesis, presented in [80], is intended for TEM lines and waveguides for which the β value is constant along the taper length. Therefore, for the case for which this assumption is not fulfilled an additional procedure is required which incorporates the variation of β into the synthesis. In general, the synthesis of such taper is intricate, but Lund [81] and Bolinder [82] showed, that the problem could be simplified by performing synthesis in the terms of electrical lengths instead of physical lengths. This is equivalent to introduction the *phase correction* procedure to the synthesis.

Phase correction. The procedure can be described as follows. First, the values of the impedances are determined for the discrete number of points n located along the z direction and separated by equal distance

$$\Delta l = \frac{l}{(n-1)} \tag{3.14}$$

where l is the section length. The transition is divided into equal subsections with length equal Δl each. Next, the phase constant β_i is determined within each subsection, and then the electrical length $\Delta\phi_{e_i}$ of each subsection is computed as

$$\Delta\phi_{e_i} = \Delta l \beta_i. \tag{3.15}$$

The values of β depend on guide dimensions which are determined by the required value of impedance. Within each section β is computed for the guide dimensions corresponding to the point located in the middle of the section. Because β varies along the transition length, the electrical distances between the adjacent points are not equal, therefore the physical distances Δl_i are adjusted to make the electrical distances $\Delta\phi_{e_i}$ equal. Next, once again the propagation constants, which correspond to the impedance values at points located in the middle of the modified sections, are computed within each section, and procedure is repeated. The *phase correction* procedure is an iterative process. The convergence of the process is fast and only a few iterations are required to fulfil the stopping criterion.

3.3 Design of the transition between an NRD-guide and rectangular waveguide

So far only few transitions between an NRD-guide guide and a rectangular waveguide have been presented in the technical literature. One example, presented in [83] is the transition in the form of rectangular waveguide horn with dielectric wedge placed inside. Unfortunately, the paper provides only the measurement results for several transitions with different dimensions. No synthesis procedure is described. Another structure of the composite transition built of two sections, each with the continuous profile, has been shown in [44] by Malherbe. Both sections of the transition have been designed using the method outlined in [80]. The wave impedance definition has been assumed in the analysis and design. The slight modification of this transition has been introduced in [84] by inserting a piece of a uniform rectangular waveguide with dielectric filling between the transition components in order to avoid coupling of the higher order modes between the transition parts.

In this chapter the composite transition, similar to the one presented by Malherbe, is investigated (Fig. 3.4). The transition is composed of two cascaded sections, A and B. Each section is independent of the other. Accordingly the synthesis of the transition is divided into two parts, in which each section is designed independently. The procedure described in section 3.2 is applied for design each section.

3.3.1 Geometry of the transition

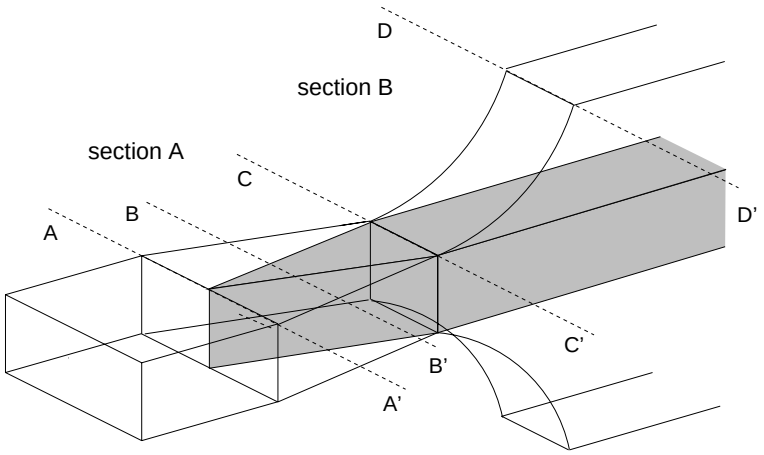

Figure 3.4: *General view of the transition from a rectangular waveguide to an NRD-guide.*

Section A of the transition is an impedance transformer from a standard air-filled rectangular waveguide to a rectangular waveguide with reduced width and dielectric filling of relative permittivity ϵ_r. Section B transforms the impedance between the rectangular waveguide with reduced width and a closed NRD-guide. To simplify the synthesis it is assumed that the distance between the outer walls in the section A changes linearly, while the width

of the dielectric slab is computed for selected points along the transition length. The dielectric rod in section B has a constant width, and only the distance between the rod and electric walls increases gradually. The design procedure yields the impedance profile. The dimensions ensure this profile are subsequently calculated.

The cross-sections of the transition in the characteristic planes are presented in Fig. 3.5 together with the dominant E field component.

3.3.2 Modes in the transition

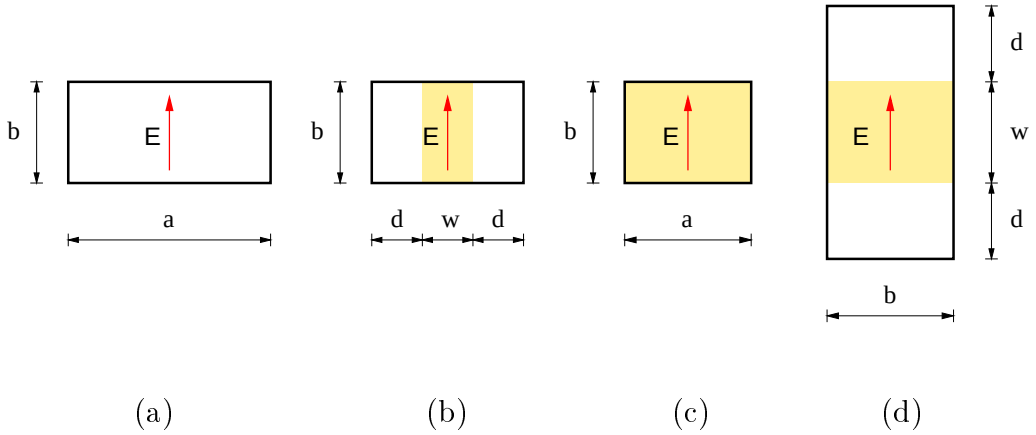

Figure 3.5: *Cross sections in the selected planes of a transition from a rectangular waveguide to an NRD-guide; a dominant electric field component in a propagated mode is presented: (a) rectangular waveguide filled with air, section A–A', mode TE_{10}, (b) rectangular waveguide with dielectric slab, section B–B', mode LSE_{10} ("distorted" TE_{10} mode), (c) rectangular waveguide filled with dielectric, section C–C', mode TE_{10}, (d) closed NRD-guide, section D–D', mode LSM_{11}.*

The design procedure assumes that only the fundamental mode propagates in each part of transition and higher order modes are neglected in the analysis.

The input of the transition is excited by the TE_{10} mode of a standard rectangular waveguide. Then the rectangular waveguide is transformed into the rectangular waveguide with dielectric slab operating with the LSE_{10} mode. This mode is also sometimes called a "distorted" TE_{10} mode [85] due to its similarity of the fields components to the TE_{10} mode [1].

The slab width increases gradually from zero at section A–A' to the waveguide width at section C–C'. At this section the transition reduces to the dielectric-filled rectangular waveguide, where the mode TE_{10} propagates. Next, the waveguide is transformed into the rectangular waveguide with dielectric slab, where the LSM_{11} mode is guided. The distance between the dielectric rod and the electric walls increases gradually. If the distance is large enough, the waveguide can be treated as the closed NRD-guide (section D–D').

[1] In fact, this mode is converted into TE_{10} mode at both ends of section A.

3.3.3 Impedance definitions in the transition

The first step of the synthesis procedure is the choice of the impedance definition which will be used in the design. In his work, Malherbe used the wave impedance definitions given by the relations (2.59) and (2.60). In this section a different definition is adopted in order to investigate the possibility of improvement of the design procedure. The power-voltage definition of characteristic impedance is selected because of the natural simplicity in the determination of the power and the voltages in the transition structure [71]. The definitions for LSE and LSM modes in a rectangular waveguide with dielectric slab are presented in section 2.3. For convenience, the power-voltage and wave impedances of a standard rectangular waveguide TE_{10} mode, which are also used in the procedure, are recalled here [86]:

$$Z_{PV_{TE}} = \frac{2b}{a}\frac{\omega\mu_0\mu_r}{k_z} \tag{3.16}$$

$$Z_{wav_{TE}} = \frac{\omega\mu_0\mu_r}{k_z} \tag{3.17}$$

where a and b are waveguide dimensions and k_z is a longitudinal wavenumber for the TE_{10} mode.

3.4 Design examples

The transition designed in this chapter is used to excite NRD-guide filters working at X-band (see chapter 4). The center frequency of the filters is 9.5 GHz, therefore, the design frequency of the transition is set to $f_0 = 9.0$ GHz so as to assure good matching in the frequency range starting from 9.0 GHz, the upper limit is not specified because for the investigated transition the increase of the frequency results in lower level of reflected power. Several transitions have been designed by means of the procedure described in section 3.2. To discuss the main features of the synthesis method the results obtained for four selected designs are presented in this section. Two designs use the power-voltage impedance definition, others two employ wave impedance.

Waveguide parameters. The following dimensions of the guides used to build the transition have been chosen:

- The parameters of a rectangular waveguide at the input of the section A are: $a = 22.86$ mm, $b = 10.16$ mm, $\epsilon_r = 1.0$. These are the dimensions of a standard WR90 waveguide designed to work in the X-band.

- The rectangular waveguide with dielectric filling at the output of section A and input of section B has the parameters: $a = 15.0$ mm, $b = 10.16$ mm, $\epsilon_r = 2.53$.

- Closed NRD-guide at the output of the section B parameters are: $w = 10.16$ mm, $b = 15.0$ mm, $d = 35.56$ mm, $\epsilon_r = 2.53$.

The *Rexolite 1422* ($\epsilon_r = 2.53$) is used as a dielectric slab due to its low transmission loss at microwave frequency band and very good mechanical properties.

Selection of the return loss levels. To determine the desired return loss level, the values of the wave and power-voltage impedances at the ends of both sections and the corresponding initial return loss have been computed. The results are shown in Table 3.1.

Section	Wave impedance			Power-voltage impedance		
	Z_1 [Ω]	Z_2 [Ω]	r_0 [dB]	Z_1 [Ω]	Z_2 [Ω]	r_0 [dB]
A	549.995	330.778	12.08	488.88	448.09	27.22
B	330.778	481.018	14.65	448.09	4492.98	1.74

Table 3.1: *Values of the impedances at the input and output ports of sections A and B together with the initial return loss* r_0. *Design frequency* $f_0 = 9.0$ *GHz.*

The results obtained for the power-voltage impedance definition show, that the section A introduces very low return loss at level of 27 dB, while the section B has a high mismatch between its ports equal to 1.74 dB. The synthesis procedure described in section 3.2 allows one to design the transition, which reduces the return loss by no less than ϵ_{max}=13.27 dB (see discussion in section 3.2). Because section A has a mismatch of 27 dB level, the overall reflection for this section is set to 42 dB. Consequently, the second section has to be designed with the same level of r_{max} so as not to deteriorate the parameters of the whole transition. As a results for power-voltage impedance the transition with overall return loss equal $r_{max} = 42$ dB is chosen. In the second design, with the power-voltage impedance definition, r_{max} is increased by 20 dB to 62 dB to investigate the improvement of results when the design parameter is changed. The same levels of r_{max} have been assumed in the two corresponding designs based on wave impedance.

Selection of the section lengths. Section length l is determined by (3.11). The phase constant β varies along section length, therefore determination of l is not straightforward. To simplify selection, values of β have been computed at the ends of both sections (Table 3.2). Also the knowledge of β distribution along section length is helpful. Example plots of such dependency are shown in Fig. 3.3. The optimal length of the transition is different for each design. The length depends on the longest wavelength at design frequency and the parameters obtained from the synthesis procedure. Here, for all investigated transitions the lengths of the sections A and B are equal $l_A = 40$ mm and $l_B = 50$ mm respectively. This choice is a compromise between the reasonable length and the matching parameters of the transition.

In the sections that follow, the design results of four transitions are described. The optimal lengths l_{max} and l_{min} are shown together with key parameters of the procedure. In

Section	β_z [rad/m]	
	input	output
A	129.2	214.8
B	214.8	83.4

Table 3.2: *Values of the propagation constant β at the input and output ports of sections A and B. Design frequency is $f_0 = 9.0$ GHz.*

addition, in each plot, the results of the synthesis without the *phase correction* procedure are included in order to highlight the importance of this correction.

3.4.1 Transition with power-voltage impedance and $r_{max} = 42dB$

The results obtained for transition designed using power-voltage impedance definition and $r_{max} = 42$ dB are shown in Fig. 3.6 and Fig. 3.7. For section A, the initial reflection loss is equal 27.22 dB, therefore the section has to reduce return loss by $\epsilon_{max} = 14.78$ dB. The parameter B=1.0426 and $(\beta_0 l)_{min} = 2.7586$ giving $l_{max} = 21.4$ mm and $l_{min} = 12.8$ mm. For section B, $\epsilon_{max} = 40.26$ dB is required; the procedure yields B=5.5788 and $(\beta_0 l)_{min} = 6.1356$, so $l_{max} = 73.6$ mm and $l_{min} = 28.7$ mm.

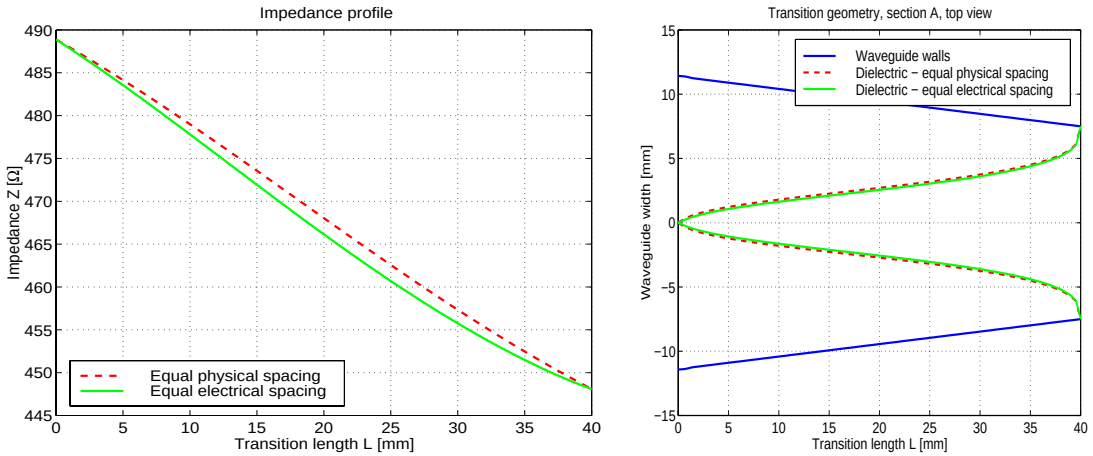

(a) (b)

Figure 3.6: *Results of the synthesis for section A with $r_{max} = 42$ dB using the power-voltage impedance: (a) impedance profile, (b) transition geometry (top view).*

The phase correction procedure slightly modifies the impedance profile of the section A, while in the case of section B the modification is significant. The changes in impedance profile correspond to modifications of the transition geometry. The change of dielectric wedge dimensions in the section A is relatively small while, the modification of the electric wall profiles in the section B is noticeable.

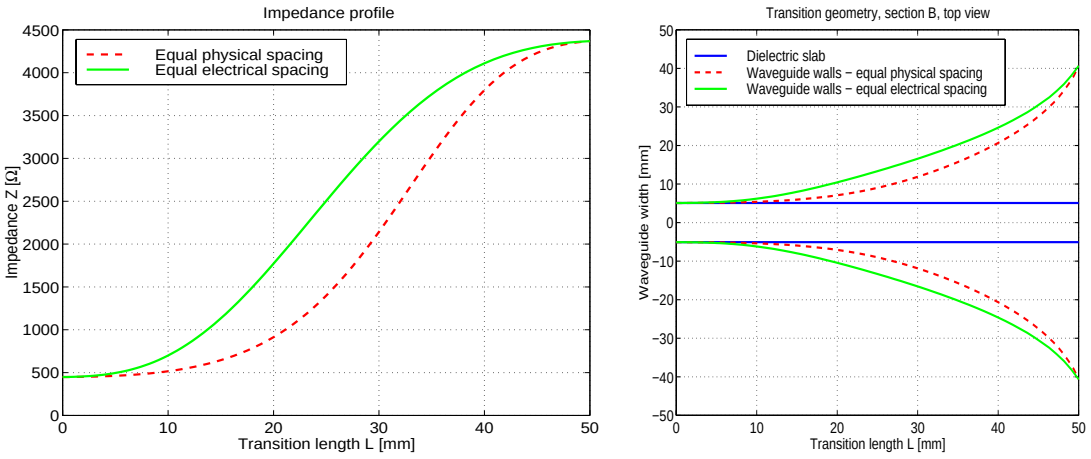

(a) (b)

Figure 3.7: *Results of the synthesis for section B with $r_{max} = 42$ dB using the power-voltage impedance: (a) impedance profile, (b) transition geometry (top view).*

3.4.2 Transition with power-voltage impedance and $r_{max} = 62dB$

The results obtained for the transition designed using power-voltage impedance definition and $r_{max} = 62$ dB are shown in Fig. 3.8 and Fig. 3.9; r_0 of section A equals 12.08 dB, therefore the additional reduction of 49.92 dB is required. The parameter B=*4.7253* and $(\beta_0 l)_{min} = 5.37$ resulting in $l_{max} = 41.6$ mm and $l_{min} = 25.0$ mm. For section B the loss reduction has to be equal 60.26 dB; the procedure yields $B = 8.2757$ and $(\beta_0 l)_{min} = 8.6608$, implying $l_{max} = 103.8$ mm and $l_{min} = 40.3$ mm.

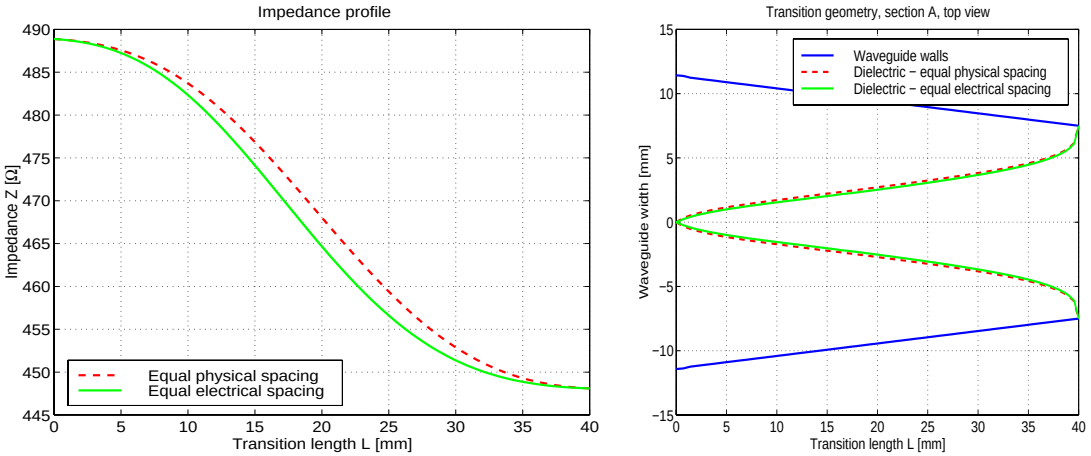

(a) (b)

Figure 3.8: *Results of the synthesis for section A with $r_{max} = 62$ dB using the power-voltage impedance: (a) impedance profile, (b) transition geometry (top view).*

It is seen that the phase correction procedure affects the impedance profile and geometrical dimensions even to a greater extent than for the 42 dB case. The dielectric wedges

are nearly the same for both cases, but in section B a larger shift of the metallic walls from the dielectric rod is noticed for 62 dB design. As expected, the transition lengths of both sections are greater in the 62 dB design.

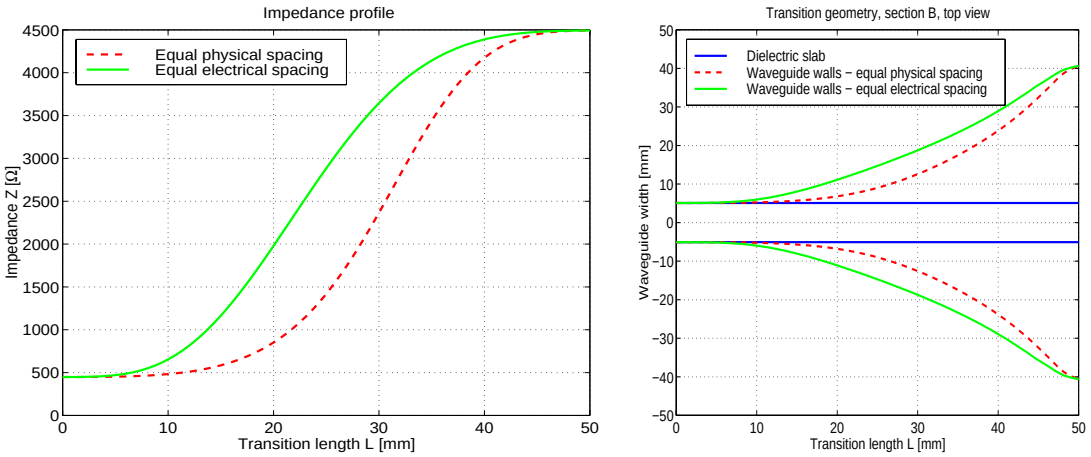

(a) (b)

Figure 3.9: *Results of the synthesis for section B with $r_{max} = 62$ dB using the power-voltage impedance: (a) impedance profile, (b) transition geometry (top view).*

3.4.3 Transition with wave impedance and $r_{max} = 42dB$

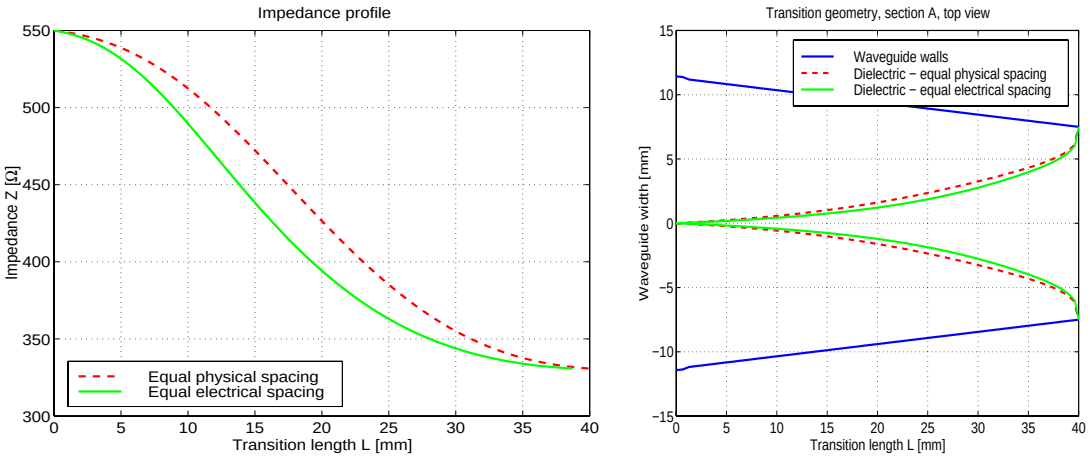

(a) (b)

Figure 3.10: *Results of the synthesis for section A with $r_{max} = 42$ dB using wave impedance: (a) impedance profile, (b) transition geometry (top view).*

Both designs were repeated for wave impedance. The results obtained for transition designed using the wave impedance definition and $r_{max} = 42$ dB are shown in Fig. 3.10 and Fig. 3.11. In the case of wave impedance the initial reflection of the section A is equal 12.08

dB, therefore the additional reduction of 29.92 dB is required. The parameter $B = 4.02515$ and $(\beta_0 l)_{min} = 4.767$ giving $l_{max} = 36.9$ mm and $l_{min} = 22.2$ mm. For section B ϵ_{max} has to be equal 27.35 dB; the procedure yields $B = 8.2757$ and $(\beta_0 l)_{min} = 8.2757$, resulting in $l_{max} = 50.3$ mm and $l_{min} = 20.6$ mm. As in two previous designs a greater influence of

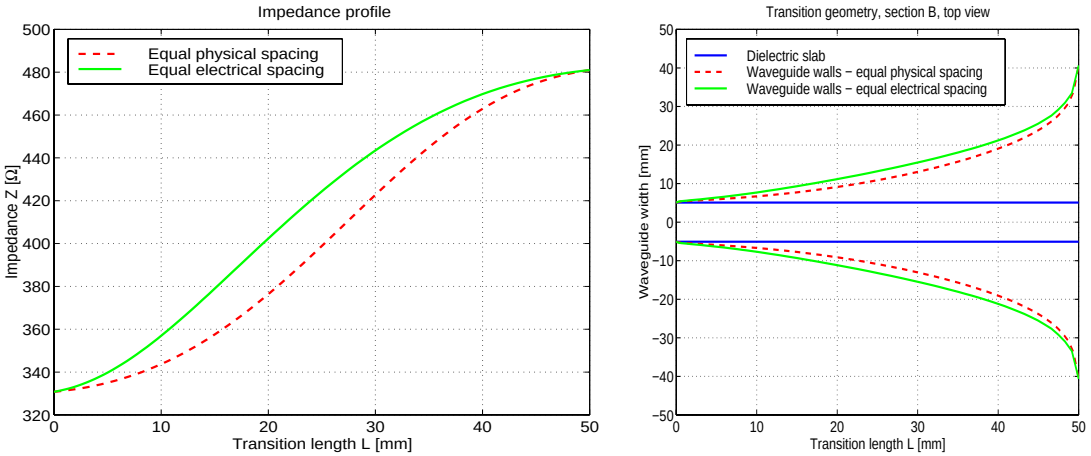

(a) (b)

Figure 3.11: *Results of the synthesis for section B with $r_{max} = 42$ dB using wave impedance: (a) impedance profile, (b) transition geometry (top view).*

phase correction is observed for the section B. The dielectric wedge is thinner for corrected design and the metallic walls of section B are moved out noticeably.

3.4.4 Transition with wave impedance and $r_{max} = 62dB$

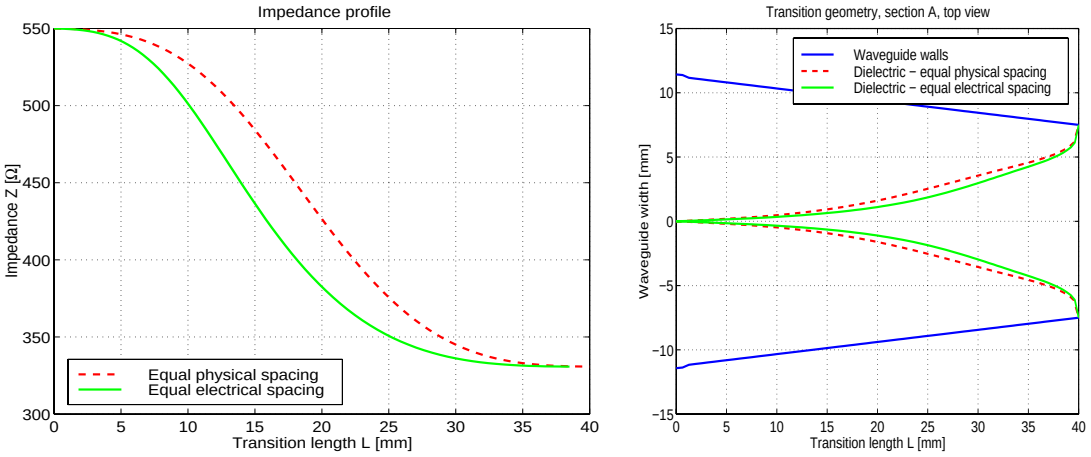

(a) (b)

Figure 3.12: *Results of the synthesis for section A with $r_{max} = 62$ dB using wave impedance: (a) impedance profile, (b) transition geometry (top view).*

The impedance profiles and the geometry of the transition designed using wave impedance definition and assumed $r_{max} = 62$ dB are presented in Fig. 3.12 and Fig. 3.13.

The initial reflection loss of section A equals 12.08 dB, hence, the section has to reduce return loss by 49.92 dB to achieve 62 dB. The parameter $B = 6.8606$ and $(\beta_0 l)_{min} = 7.321$ resulting in $l_{max} = 56.7$ mm and $l_{min} = 34.1$ mm. For section B the loss reduction of 47.35 dB is required; the procedure yields $B = 6.5$ and $(\beta_0 l)_{min} = 6.9846$ giving $l_{max} = 77.9$ mm and $l_{min} = 30.3$ mm.

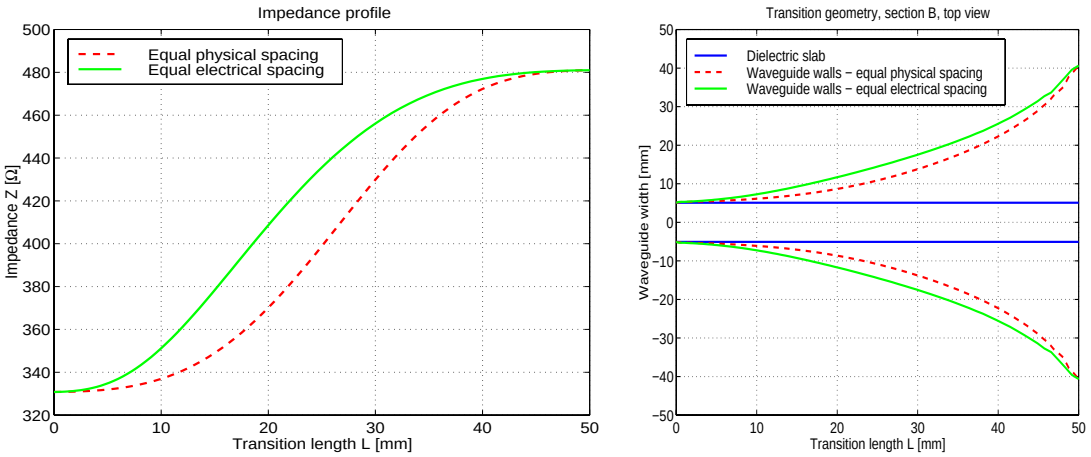

(a) (b)

Figure 3.13: *Results of the synthesis for section B with $r_{max} = 62$ dB using wave impedance: (a) impedance profile, (b) transition geometry (top view).*

The effect of phase correction has the same character as in the case 42 dB wave impedance design. The difference in shape of the dielectric wedge is very small between the 42 dB and 62 dB design. However, a significant move of the metallic walls in the outer direction is observed for 62 dB design.

3.4.5 Comparison of the designs

To verify the results obtained from the synthesis, the parameters of four composite transitions, described in sections 3.4.1 to 3.4.4, have been computed numerically by means of the FDTD software *QuickWave-3D*. In this section the results of the computations are discussed. In addition, the results of non-optimal transition are also presented to illustrate the advantages of the optimized transitions. For this transition the shapes of dielectric wedge in section A and metallic walls in section B are described by simple linear function.

For each transition a geometrical model has been created similar to the one shown in Fig 3.14. The nonuniform continuous profiles of the dielectric wedge in section A and conducting walls in section B have been approximated by a piecewise linear function. Additional pieces of uniform waveguides are added at input and output ports to ensure the proper identification of the TE_{10} and LSM_{11} modes. Lossless dielectric and conducting walls are assumed in the simulations. The results of the computations are presented in

Fig 3.15 to Fig 3.17. The S_{11} parameter shown in the plots corresponds to r_{max} parameter of the design procedure.

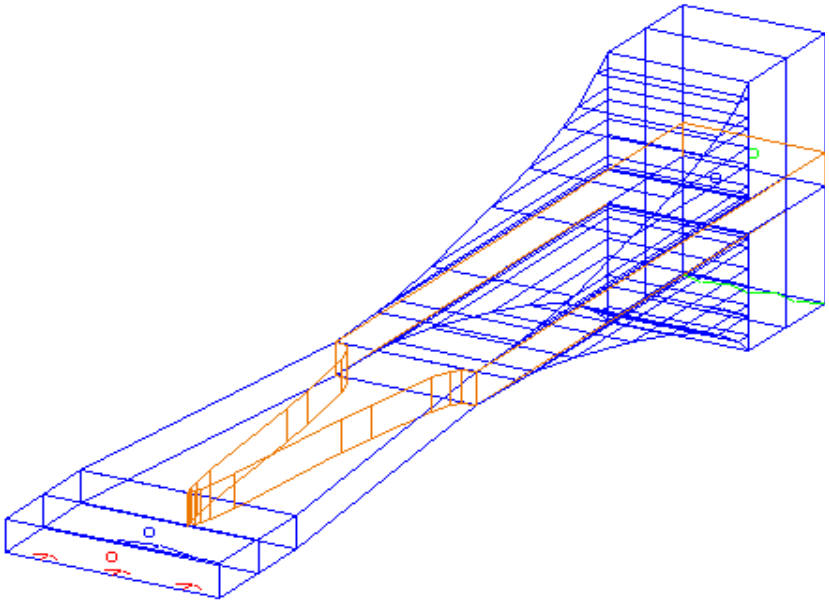

Figure 3.14: *Geometrical model of the transition for which the power-voltage definition is applied and $r_{max} = 42$ assumed. This structure has been analyzed using FDTD software.*

S_{11} results for composite transitions. The average value of S_{11} equals about -17 dB for the wave impedance designs in the frequency range from 9 GHz to 10.5 GHz, then, for higher frequencies, the S_{11} falls down to -20 dB at 12 GHz (Fig. 3.15). Surprisingly, the results for 62 dB design are slightly worse than the 42 dB design. Still, both designs have much higher return loss level than the one assumed in the synthesis. It should be highlighted however, that the level of S_{11} is significantly lower for the power-voltage impedance designs than for wave impedance ones. Nearly 45 % of the band $9 \div 12$ GHz is below the -20 dB level for the 42 dB design. In addition, a wide minimum equal -31 dB is observed at 10.25 GHz. The maximum of -18 dB is reached at 9.3 GHz and 11.3 GHz. For the 62 dB design the results are even better. The S_{11} falls below -25 dB for about 42 % of the band $9 \div 12$ GHz. The local maximum equal -22 dB is observed at 9.5 GHz. Although the 62 dB design does not fall to -30 dB level, in the investigated frequency band, it nevertheless assures the matching better than -22 dB for all frequencies in 9 - 12 GHz band. The transition with linear profiles yields the matching on the average level of S_{11} equal -10 dB, which is the worst result of the presented ones.

S_{21} results for composite transitions. The results obtained for the S_{21} parameter show, that the transmission losses do not exceed -0.5 dB in the frequency band ranging from 8.5 GHz to 12 GHz (Fig. 3.16 (a)). In the band, for which the filters are designed e.g. 9 to 10.5 GHz, S_{21} is better than -0.15 dB for almost all frequencies and the results of the power-voltage impedance are consistently better than those for the wave impedance designs.

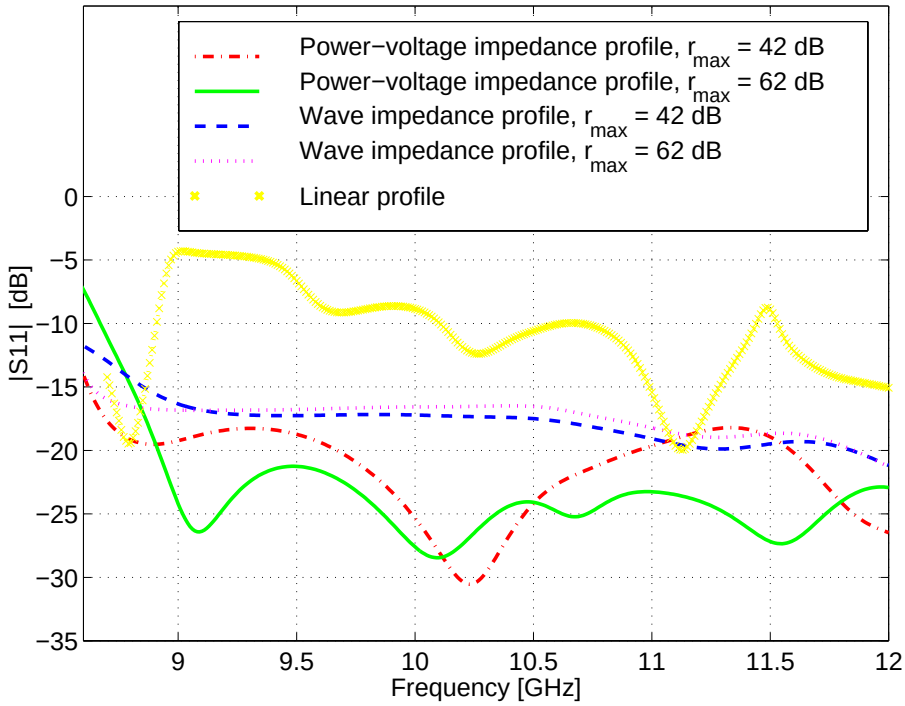

Figure 3.15: *The numerical results of the magnitudes of S_{11} parameter of five transitions. The results are obtained using FDTD software.*

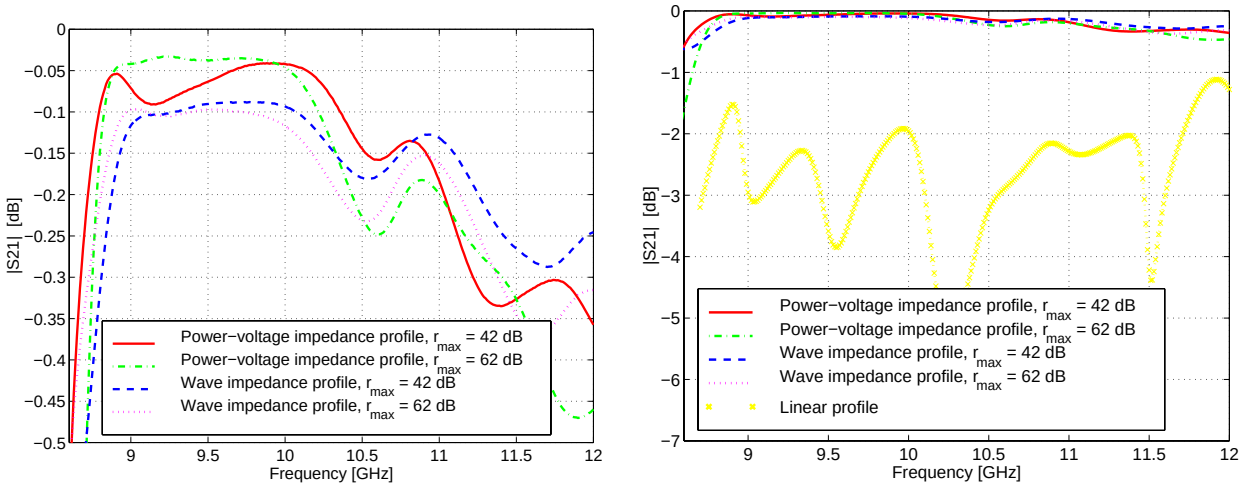

Figure 3.16: *The numerical results of the magnitudes of S_{21} parameters of designed transitions: (a) detailed view, (b) general view. The results are obtained using FDTD software.*

Because the investigated structures are lossless, the S_{21} results should theoretically correspond to the S_{11} results. The plots shows that this is not true. The discrepancy between the transmission and reflection parameters becomes significant for frequencies above 10.5 GHz, for all designs the S_{21} falls below -0.25 dB and reaches even about -0.47 dB at 11.8 GHz

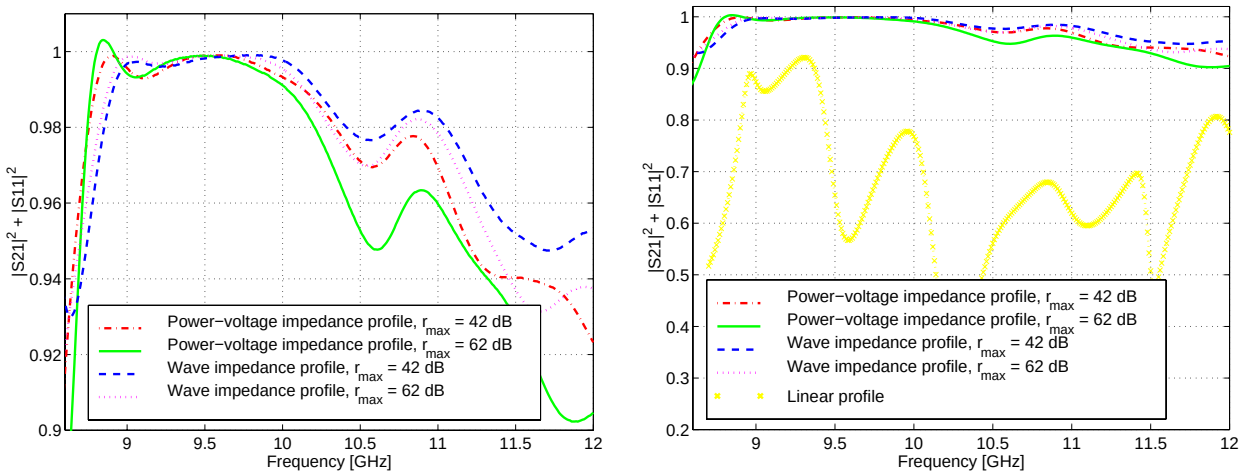

Figure 3.17: *Numerical results of the energy conservation condition of five transitions: (a) detailed view, (b) general view. The curves are computed for the results obtained from FDTD software.*

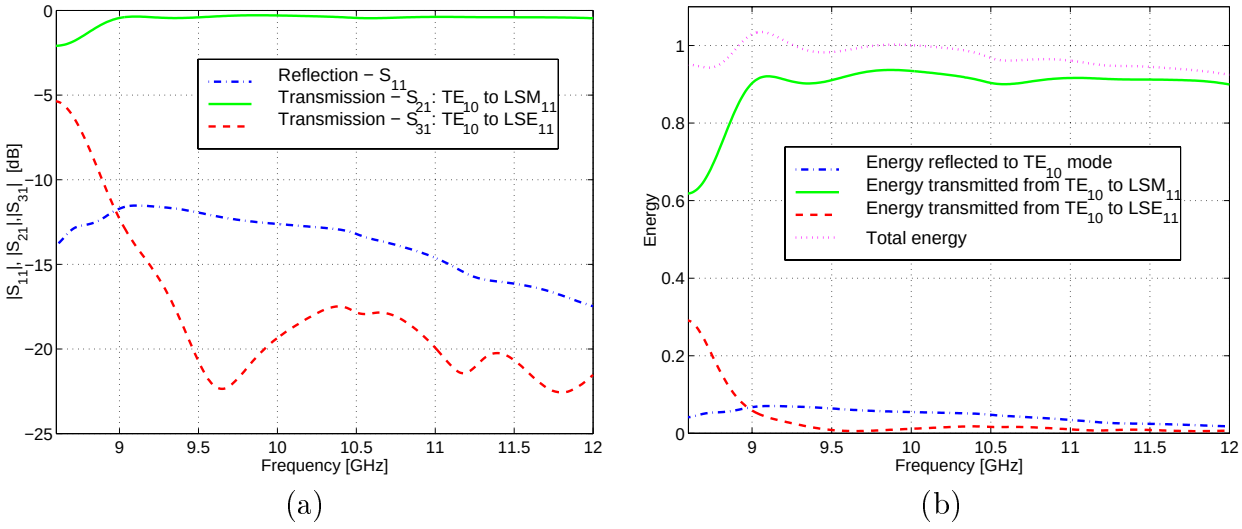

Figure 3.18: *Numerical results for the transition with wave impedance profile and $r_{max} = 62$ dB: (a) reflection and multimode transmission, (b) reflected and transmitted energies.*

for the 62 dB power-voltage design. This effect, caused by approximate mode extraction algorithm used by the FDTD software, is discussed in the following paragraph.

Sources of errors in the FDTD software. *QuickWave-3D* computes the scattering parameters of an analyzed structure as follows. First, the standard FDTD method is used to determine the fields within the structure. Next, the fields corresponding to a specified mode (i.e. mode template) are computed at the input and output ports. Then, the inner product of the FDTD solution and the mode template at a port is calculated to determine the amplitude of a selected mode at a port. Finally, the S parameters are computed using

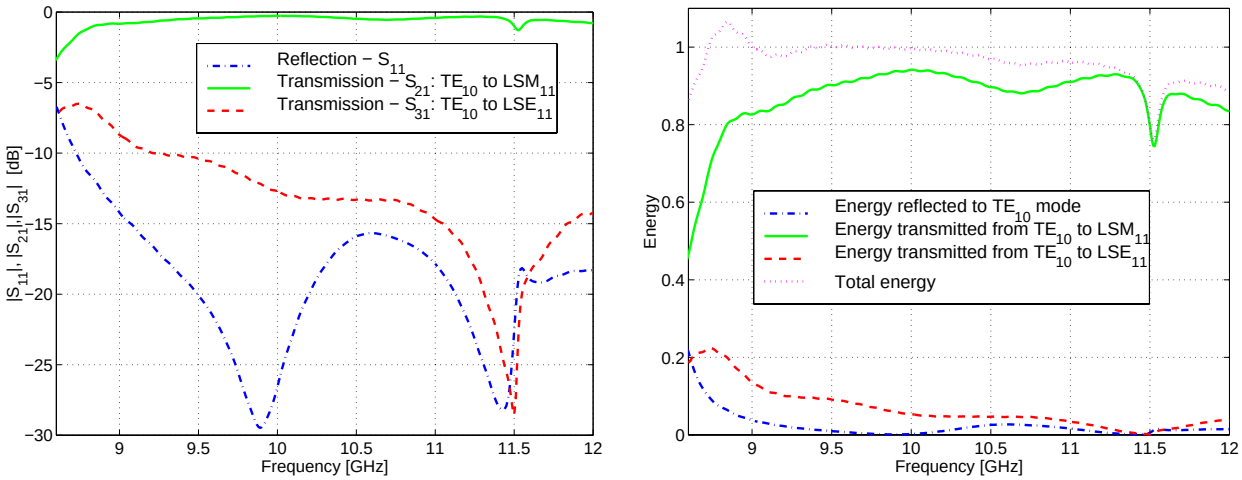

Figure 3.19: *Numerical results for the transition with power-voltage impedance profile and* $r_{max} = 62dB$ *: (a) reflection and multimode transmission, (b) reflected and transmitted energies.*

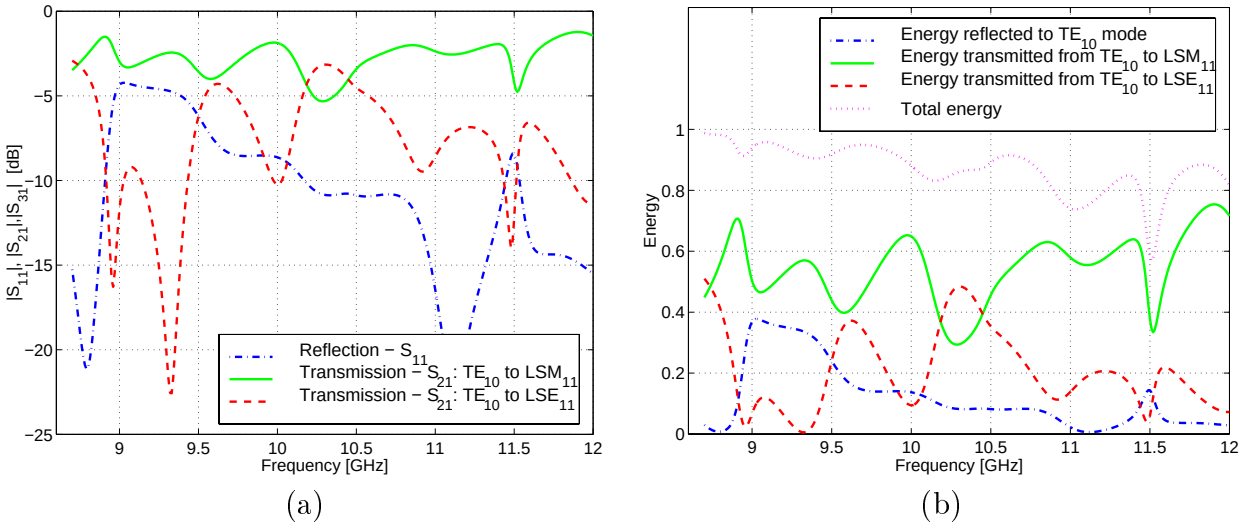

Figure 3.20: *Numerical results for the transition with linear profile: (a) reflection and multimode transmission, (b) reflected and transmitted energies.*

the amplitudes of modes obtained at the ports.

The mode templates are computed at one selected frequency f_0. Then these templates are taken into the calculation of inner product at other frequencies. Slight errors in calculating amplitudes occur because the field distribution of an mode in NRD-guide changes with frequency. To obtain accurate results, the mode templates at another frequency should be computed. Another source of errors is caused by the fact that due to discretization inherent to FDTD the mode templates obtained in the software are not orthogonal one to another, even at a single frequency.

To estimate the computation error, the energy conservation condition is calculated for all optimized designs (Fig. 3.17 (a)). The result shows that the accurate results are obtained for $f_0 = 9.5$ GHz, i.e. the frequency selected for the template computation. This corroborates the above reasoning. For other frequencies the energy is computed with accuracy of about 0.5 % in the band ranging from 9 to 10 GHz. For higher frequencies the error grows rapidly and reaches about 10 % at 12 GHz, for the worst case.

Very good agreement between the curves of energy conservation condition and the S_{21} results demonstrates that the inaccuracy of the S parameters computation is caused mainly by the error in computation of the S_{21} while in the S_{11} parameters are calculated more accurately. This observation is in good agreement with previous explanations. The S_{11} is computed for the TE_{10} mode, which does not change the field distribution when the frequency is changed. On the contrary, S_{21} represents transmission between the TE_{10} mode and the LSM_{11} mode. While the TE_{10} mode does not change, the fields of the LSM_{11} mode vary for different frequencies. The fields of the LSM_{11} mode are more concentrated in the dielectric slab when the frequency increases.

The transition with the linear profiles yields the S_{21} results on average level of -2.5 dB in 9-12 GHz band (Fig. 3.16 (b)). This means that only about 65 % of the energy is transmitted through the transitions. This observation is confirmed by the results obtained for the energy conservation condition (Fig. 3.17 (b)). A similar effect, in a smaller scale, is observed for optimized transitions. The energy conservation condition is smaller than unity, even for the $f_0 = 9.5$ GHz. The analyzed structures are lossless and do not radiate any energy outside. It suggests, that the rest of the energy is converted into the parasitic modes excited in the transition. This problem is discussed in greater detail in the next paragraph.

Results of multimode analysis. The NRD-guide works with first higher order mode LSM_{11}. The LSE_{11} mode has lower cutoff frequency, therefore the conversion to this mode can occur at discontinuities. To inspect this phenomena three transitions have been analyzed, for which the transmission to the LSM_{11} and LSE_{11} modes have been observed. The following transitions have been selected: the transition with power-voltage impedance profile and $r_{max} = 62$ dB, the transition with wave impedance profile and $r_{max} = 62$ dB and the transition with linear profile. The results are shown in (Fig. 3.18) $\div$ (Fig. 3.20).

For all transitions the conversion from the TE_{10} to LSE_{11} mode occurs. For the linear transition about $20 \div 40$ % of the TE_{10} mode energy is transmitted to the LSE_{11} mode (Fig. 3.20 (b)). Moreover, for frequencies around 10.3 GHz more energy is transmitted to the LSE_{11} mode than to the LSM_{11} mode. Better results are obtained for the transition with wave impedance profile (Fig. 3.18 (b)). Almost all transmitted energy appears in the LSM_{11} mode. Still, the total energy is not one, even for $f_0 = 9.5$ GHz, probably because the modes are not completely orthogonal. The best results are obtained for the transition with power-voltage impedance profile and $r_{max} = 62$ dB (Fig. 3.19 (b)). Although the transmission to the LSE_{11} mode is noticeable in entire frequency band under investigation, the energy conservation condition is satisfied at frequency $f_0 = 9.5$ GHz.

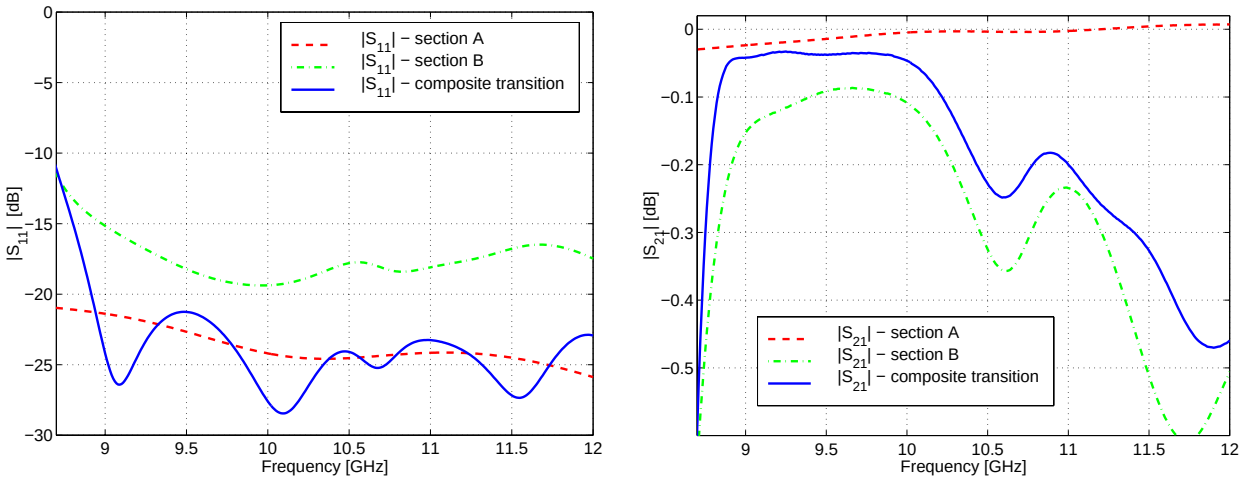

(a) (b)

Figure 3.21: *Response of the sections A and B of the composite transition with power-voltage impedance and $r_{max} = 62$ dB: (a) return loss, (b) transmission. The results are obtained using FDTD software.*

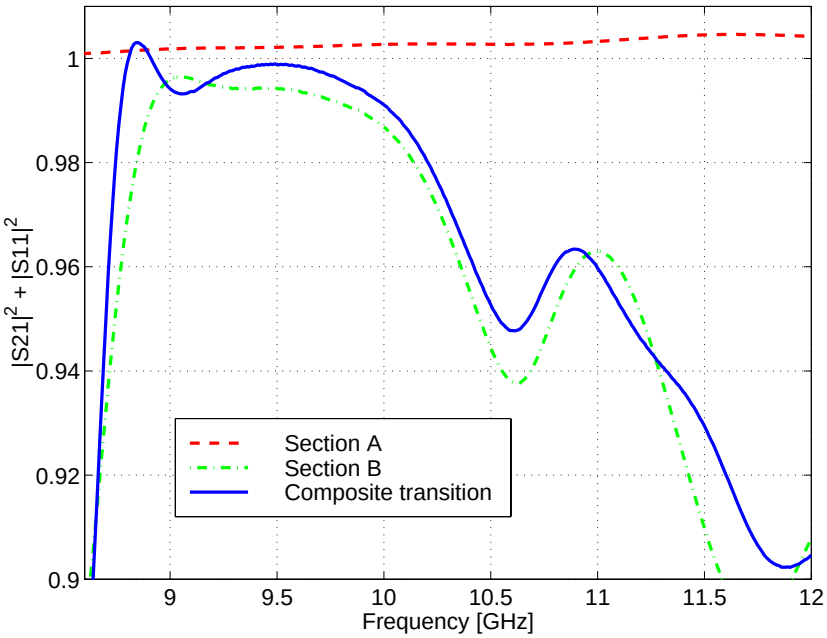

Figure 3.22: *Energy conservation condition for sections A and B of the composite transition with the power-voltage impedance and $r_{max} = 62$ dB: The results are obtained using FDTD software.*

Section A and B results. Two sections A and B of the composite transition designed with the power-voltage impedance and $r_{max} = 62$ dB are analyzed separately in order to determine the influence of each section on the transition parameters. The return loss of section A is about $5 \div 7$ dB lower than for section B (Fig. 3.21(a)). The average level of

the S_{11_A} is about -23 dB while for the S_{11_B} the loss is equal -18 dB in 9-12 GHz band.

The transmission of section A is nearly ideal, while for section B the roll off down to -0.62 dB at 11.75 GHz is observed in $9 \div 12$ GHz band (Fig. 3.21(b)). The response of section B alone is very similar to the response of the whole cascade. This conclusion is also confirmed by the energy conservation condition computed for discussed structures (Fig. 3.22). The difference in the transmission through sections A and B is caused mainly by inaccuracies in the FDTD mode identification at the section ports.

Conclusions. The results of simulation suggest that the applied synthesis method allows one to design transition, which assures the average matching equal -25 dB for the best case. The power-voltage impedance definition yields better results than the wave impedance one. Still, the discrepancy between the design values of return losses and the obtained results is very high for both impedance designs. The changes of dielectric wedge shape are relatively small for wave and characteristic impedances, if the design specification is changed from $r_0 = 42$ dB to $r_0 = 62$ dB. For the same case, the differences in the metallic wall profile are more significant. However, the changes are made in the area where the walls which are located nearly the output of the sections B and placed in a relatively high distance from the dielectric slab. Their position does not affect significantly the fields of the LSM_{11} mode (chapter 2). Consequently, the theoretical change of the structure parameters has little influence on the real modes existing in a transition. It could suggest that synthesis based on the circuit theory has only limited scope when non-TEM lines are used.

The comparison between the optimized transitions and the transition with linear profiles shows the importance of the proper design. Not only do the optimized transitions assure the matching in the worst case on the -17 dB level, but also offer good conversion from the TE_{10} to the LSM_{11} mode.

The latter feature seems to have greater importance because the influence of improper matching can be reduced by applying one of the calibrating method such as a TRL method presented in appendix B.

The discussion presented in this section can be summarized as follows.

- The application of the power-voltage impedance definition, proposed in this thesis, to the design gives consistently better results than the wave impedance used by other authors.

- The proposed design procedure allows one to design the transition with input return loss at 25 dB level. Better results could not be achieved because the method, based on the circuit theory and assumption of monomode propagation, has limited accuracy in the case on non-TEM guides.

- The conversion to the LSE_{11} mode occurs in all transitions. This effect is reduced significantly in the case of optimized designs.

Figure 3.23: *Transition from a rectangular waveguide to an NRD-guide. The upper metal plates are removed in sections A and B to demonstrate the transition structure.*

3.5 Experimental results

Two composite transitions between a rectangular waveguide and an NRD-guide have been manufactured [87]. The dimensions of the transitions have been obtained from the synthesis where the power-voltage impedance definition was applied and return loss equal $r_{max} = 62$ dB assumed. These results, are presented in section 3.4.2. The structure of one of the transitions is presented in Fig. 3.23. In both sections, the upper metal plates are removed for better presentation of the structures. The metal parts of the transitions are made of brass, the Rexolite 1422 is used as a dielectric. To determine the parameters of each transition separately, the TRL calibration technique is applied. The calibration procedure is described in detail in appendix B. Only the results of the procedure are shown here. The de-embedded parameters of the transitions, obtained from the measurements, are shown in Fig. 3.24 together with the numerical results.

Measurement results of a single transition. The small discrepancy between the S_{11} and S_{22} of the same transition is caused by inaccuracies of the de-embedding process. Additionally the transitions are not identical due to inaccuracies in a conventional machining process. Especially the designed profile of the dielectric wedges is difficult to obtain. As a results of these inaccuracies, the dimensions vary from the desired ones by about $\pm$ 0.2 mm. In addition, both ends of the dielectric wedges have some discontinuities and one wedge is about 1.0 mm shorter than the assumed length. In the frequency band spanning from 9 to 11 GHz, the reflection in near 55% of the band is below -20 dB level for the worst case and for the best case over the 80 % of the band is below -20 dB level (Fig. 3.24 (a)). In the 9-10 GHz band the average reflection parameters are in the -19 dB level while in 10-11 GHz

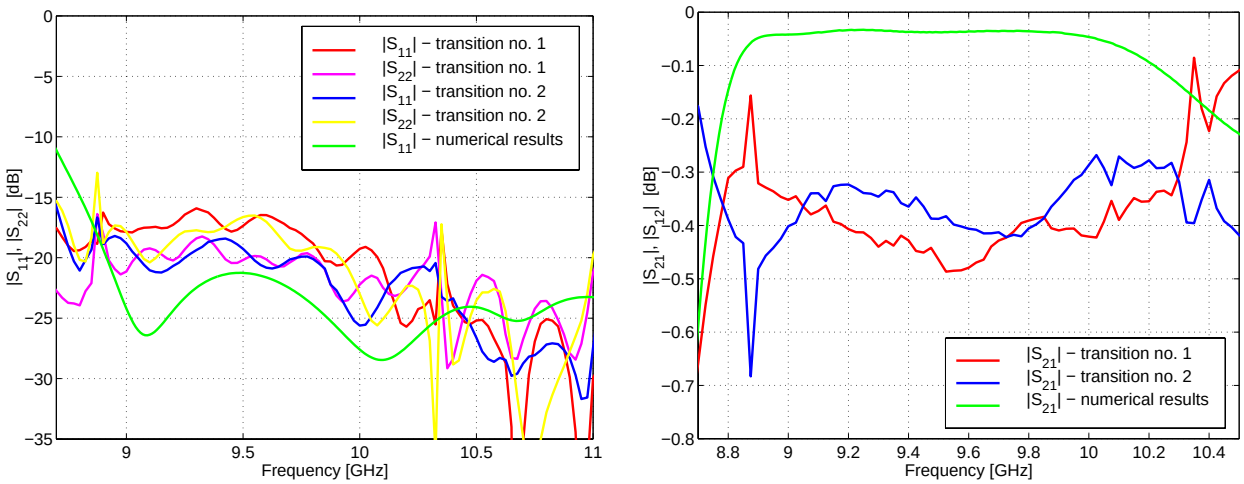

(a) (b)

Figure 3.24: *The measured and numerically computed parameters of the transitions designed with power-voltage impedance definition and insertion loss level* $r_{max} = 62$ *dB: (a) reflection, (b) transmission.*

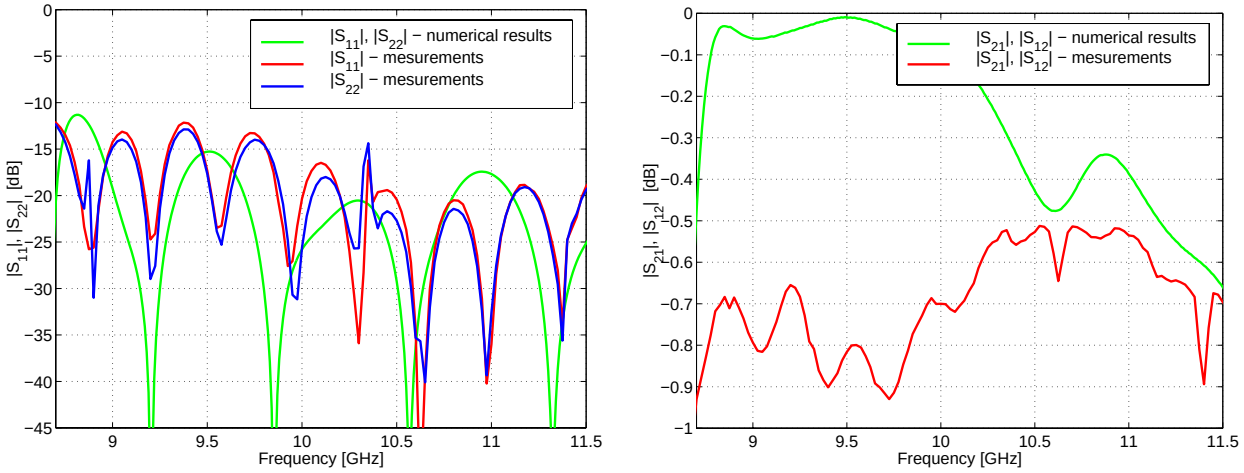

(a) (b)

Figure 3.25: *The measured and numerically computed parameters of the cascade of the transitions connected back-to-back: (a) reflection, (b) transmission. The power-voltage impedance definition and insertion loss level* $r_{max} = 62$ *dB are assumed in the design.*

band the average level is almost -25 dB. Better matching is observed for higher frequencies, where the transition length is longer in terms of wavelengths. These results are in good agreement with the numerical simulations.

The de-embedded transmission parameters S_{21} are approximately on -0.37 dB level for both transitions, hence one can assume that the losses of the one transition equal approximately 0.37 dB. The theoretical losses can be approximated using the results shown in section 2.4. The overall theoretical losses introduced by the one transition equal approxi-

mately 0.55 dB. The agreement between the theoretical approximation and the measurement results is fairly good. The difference is caused mainly by the inaccuracy of de-embedding of the transmission parameters.

Measurement results of the cascade of two transitions. The two transitions were connected back-to-back and the performance of such structure was measured. The results of numerical computations and measurements are shown in Fig. 3.25. The agreement between measurements and the numerical computations is even better than in the case of de-embedded transitions (Fig. 3.25(a)). The measured reflection parameters of the cascade are nearly the same for forward and backward directions. Because the reflection from both ends exists in the structure, the resonance occurs in the measurement results. The losses in the cascade are equal about 0.7 dB over the 9-11 GHz band (Fig.3.25(b)), this result is in fairly good agreement with the theoretically determined losses of the cascade which equal about 1.1 dB.

The results of the numerical simulations and the experimental verification show that the transitions with the reflection level about -25 dB are feasible. That result may be regarded as quite satisfactory when the measurements of the other NRD-guide components have to be done.

Discussion. From the foregoing section it is evident that it is impossible to achieve better results by means of the assumed synthesis procedure, even if the design specification assumes the return loss at 42 and 62 dB levels. This discrepancy can be attributed mainly by the approximations made in the synthesis method. The simple method intended originally for the TEM line transitions was applied to non-TEM guides for which, in addition, the propagation constant varies along the transition length. Nevertheless, the results are good. The closer investigation of the synthesis results reveals that the circuit theory description of a physical structure of a transition has only a limited scope. For example the procedure modifies profile of the metallic walls of section B of the transition but this modification has practically no effect to the fields of the modes guided in the structure. One of the possible solutions of the problem of an inaccurate design is to apply the more advanced and sophisticated method to design the transition, such as this one presented in [88], which applies to the design of the transition which supports purely non-TEM modes. On the other hand, the possibility of the practical realization of a transition with very low return loss should be considered. For some types of transitions it is practically impossible to obtain the matching better than certain level of return loss. For example it has been reported in [88] and [89] that due to technological constrains for the fin-line tapers the matching better than -35 dB is practically impossible to obtain in realized structures.

Chapter 4

NRD-guide filters

4.1 Introduction

High-quality filters are one of the key elements of the integrated circuits built in the NRD-guide technology. Various filter configurations have been investigated and different filter design techniques were adapted to meet the demands of this technology. This introduction reviews main NRD-guide filter configurations described in the technical literature.

Filters realized in NRD-guide technology usually have bandpass or bandstop transmission characteristics with classical equiripple or maximally flat response. The bandpass filters found more practical applications in integrated circuits built in NRD-guide technology therefore they are studied more extensively than the bandstop filters. The band pass filters built in the NRD-guide technology often have a form of a series of resonators coupled by some coupling structures in the form of the discontinuities. The coupling between the resonators has reactive character and can be described in various ways depending on the convention used. The same coupling can be treated either as an impedance step or an impedance inverter or a discontinuity described by the scattering matrix. The coupling structures in the form of discontinuities are more precisely described in more detail in section 4.1.2.

Depending on the type of a resonator used to construct a filter, filters can be divided into two main groups. In the first one standard single mode resonators, usually in the form of a uniform section of a transmission line with the proper electrical length, are used, while in the second group dual mode resonators are employed.

Besides the direct coupled cavity filters topology there exist other filter topologies, which are used to build bandstop or band pass filters in NRD-guide technology. Examples of these topologies include channel-dropping filters which use ring resonators [90], filters with cylindrical resonators [90] and some filtering structures with cylindrical resonators where, the higher order modes called whispering gallery modes are used [91]. Although some of these filters have interesting performance, they are rarely found in practical applications. In addition their synthesis methods are different from the methods presented in this thesis. Therefore they are not discussed in this work.

4.1.1 NRD-guide filters

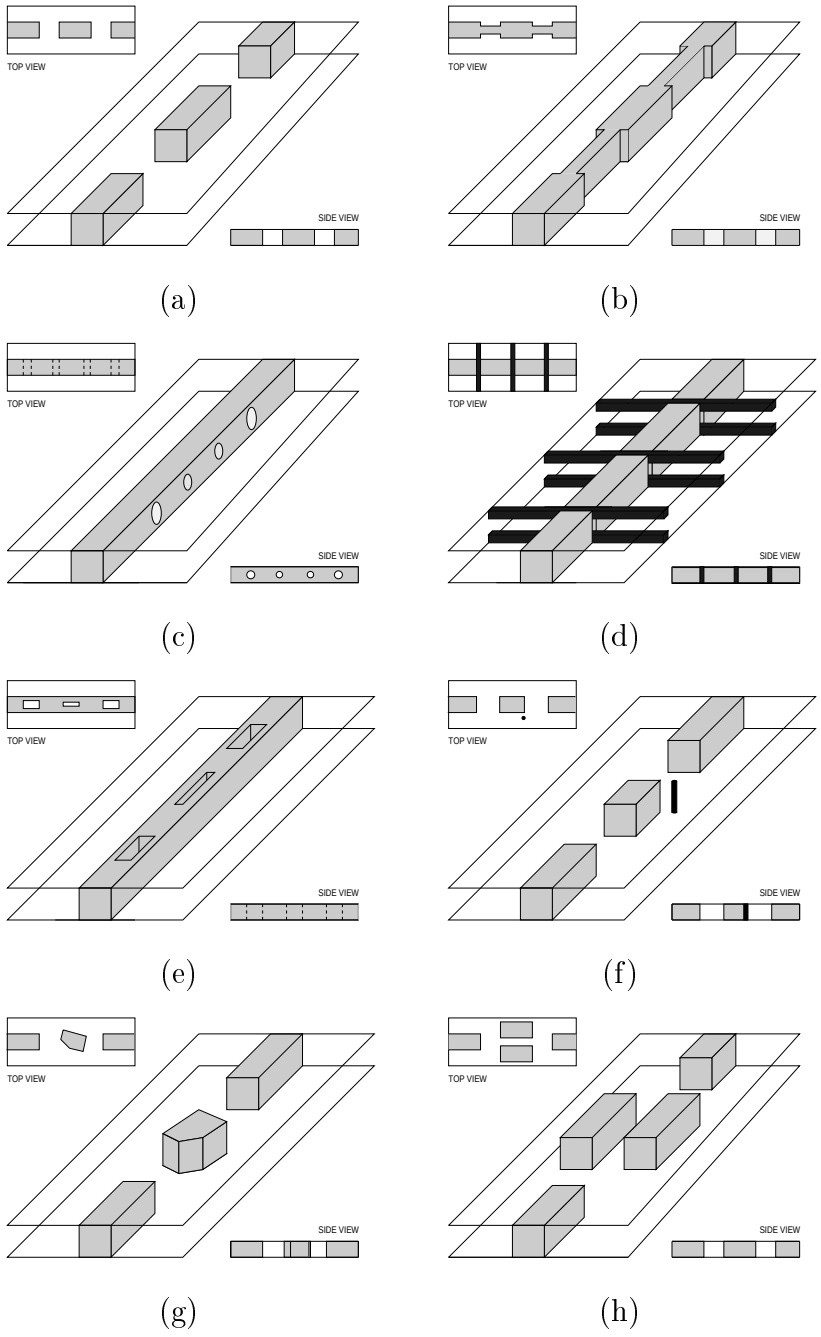

Figure 4.1: *NRD-guide filter configurations: a) air-gap coupled filter, b) dielectric strip coupled filter, c) round hole coupled filter, d) metal window coupled filter, e) double strip NRD-guide filter, f) dual mode resonator filter with metallic post, g) dual mode resonator filter with cut resonators, h) two path NRD-guide filter.*

Direct coupled-cavity bandpass filters. One of the first bandpass NRD-guide filters were proposed by Yoneyama in 1984 [73]. They were composed of series NRD-guide resonators coupled either by air gaps (Fig. 4.1 (a)) or by thin dielectric strips (Fig. 4.1 (b)). For the first filter, there was a difficulty in establishing the proper relative positions of resonators, therefore the thin dielectric strips, which allow one to keep the constant distance between the resonators, were added and the second filter topology was created. Both filters had satisfactory transmission characteristics. Malherbe and Oliver [92] described a similar topology with dielectric resonators coupled by round holes made in the NRD-guide dielectric rod (Fig. 4.1 (c)). Other coupling mechanism was proposed by F. Bonne and Ke Wu in [93]. The series of resonators were coupled by double strip NRD-guide (Fig. 4.1 (e)). The advantage of both presented filter topologies is ease of manufacturing. The significant reduction of filter length was achieved by Ke Wu et al. [94]. They proposed a filter composed of a cascade of resonators where the coupling between them was achieved by the so called metal windows (Fig. 4.1 (d)). It results in a 25 % reduction in length and steeper transmission characteristic in the stop band. Although filters shown in Fig. 4.1 (c) and (d) offer easy manufacturing or shorter length, higher order modes are excited in the discontinuities which create the filter structure. These modes occur because the discontinuities are not uniform in the vertical direction. Higher order modes can seriously deteriorate the filter response. Due to this fact the filter synthesis is more complicated, because these modes should be taken into consideration.

Having in mind drawbacks of the presented filter structures, the filter composed of dielectric rectangular resonators and air gaps has been selected as a trial structure in this thesis. This filter structure is investigated in detail in the reminder of this chapter.

The advantages of the filters described above include: a well known and not complicated design technique, high-quality transmission parameters and, in some cases, easy manufacturing. Nevertheless, when the steeper characteristics are required, the filter has to have more poles so that more filter section are needed. As a result a longer filter structure is obtained which has, in addition, greater transmission losses. One of the possible solutions, which can reduce some of these drawbacks, is to employ dual mode resonators.

Dual-mode bandpass filters. A slight, appropriate asymmetry in a dual-mode resonator gives the possibility of the excitation of two degenerate and orthogonal modes which have resonant frequencies very close to the resonant frequency on undisturbed resonator. This feature of dual-mode resonators offers the possibility to construct a two pole filtering section using only one resonator. This gives the opportunity to construct more compact filters with smaller transmission losses and better transmission characteristics. The dual-mode filters with modified rectangular resonators were presented by Ferezza et al. in [95]. They studied two types of dual mode filters. In the first group, the filters were built of rectangular resonators, where the asymmetry was introduced by a post or screw located near the resonator (Fig. 4.1 (f)). In the second type of filters the resonators symmetry was broken by a cut of a resonator corner (Fig. 4.1 (g)). Because theoretical prediction of the filter characteristic is quite complicated, only experimental investigation of the filters was reported in the quoted paper. Another filter structure, which works with dual mode

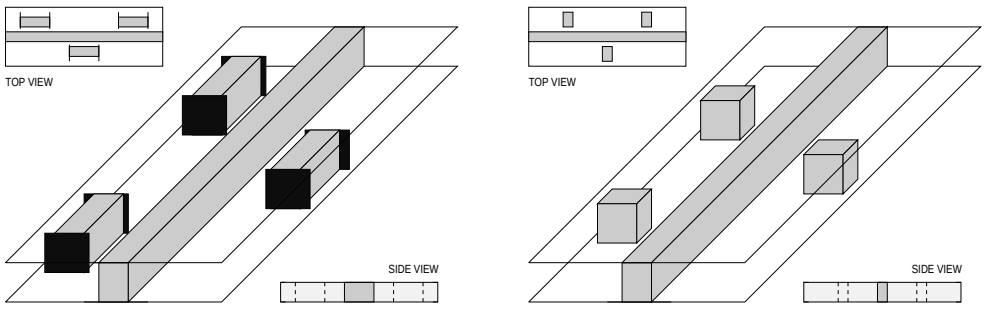

(a) (b)

Figure 4.2: *NRD-guide bandstop filter configurations: a) filter with coupled guides which are terminate by short circuits at the ends, b) filter with dielectric resonators coupled perpendicularly to the main guide.*

resonators was proposed by Wu and Huang [96]. In this case, the dual mode resonator was composed of two path NRD-guide (Fig. 4.1 (h)). The trial filter had a better transmission characteristics than the conventional air-gap counterpart.

Bandstop filters. Although bandstop filters are not the subject of this work some configurations of them are presented here for completeness.

The conventional design procedure of stop band filters makes use of the canonical low pass Chebyshev or Butterworth prototype circuit. Then this circuit is transferred in a band pass equivalent network composed of transmission line sections connected in series with coupled shunt stubs. The stubs are realized in a form of resonators, therefore a typical filter configuration is composed of resonators coupled to the main center guide [64]. The first bandstop filter was designed from the prototype circuit with open-circuited shunt stubs [97]. The stubs were realized as the coupled guides placed in parallel to the main guide and terminated with short circuits at the ends. (Fig. 4.2 (a)). The resonators made of rectangular section of an NRD-guide can be placed perpendicularly to the main guide yielding a slightly different filter configuration (Fig. 4.2 (b)) [98]. For both filters one of the most difficult aspects of a theoretical analysis was the determination of the coupling between the main guide and a coupled resonator, hence in [97] approximate formulae were given while in [98] only experimental data were presented. The filters with circular and cylindrical resonators in a structure have also been reported [91].

4.1.2 NRD-guide discontinuities

The NRD-guide discontinuities are discussed in this section because they are key elements of the bandpass filters investigated in this thesis. Discontinuities in the NRD-guide technology can be realized in many ways and some selected examples of them are described below. All of the presented discontinuities are symmetrical and they can be treated as a practical realization of an impedance inverter.

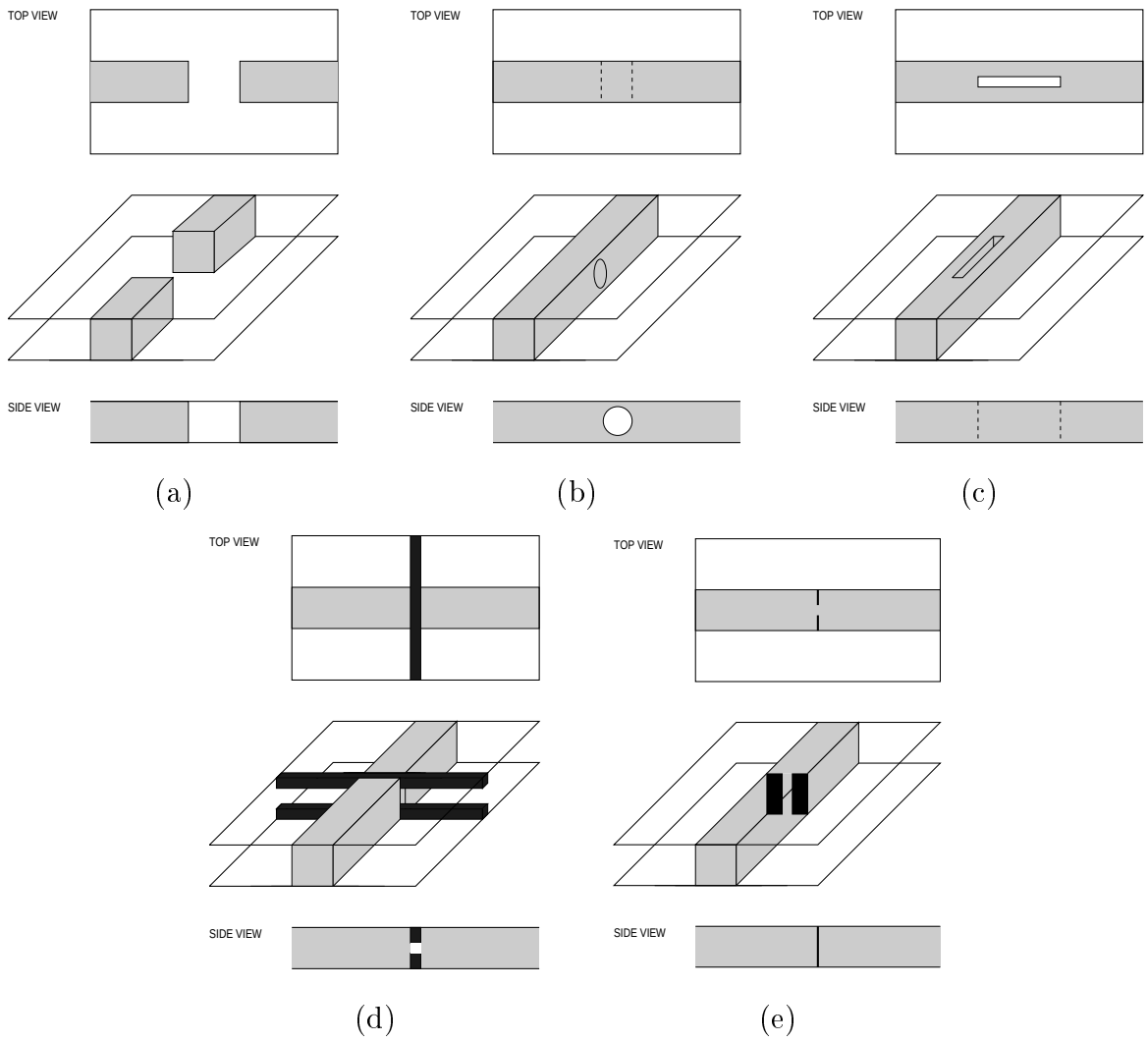

Figure 4.3: *NRD-guide discontinuities: a) air gap in uniform NRD-guide, b) round in shape hole made which is in parallel to NRD-guide metal plates, c) rectangular in shape hole made in direction parallel to the air-dielectric interface, d) metal window in NRD-guide, e) vertical diaphragm in dielectric rod of NRD-guide.*

The simplest discontinuity is created by an air gap between two straight NRD-guides (Fig. 4.3 (a)). This discontinuity was selected to construct the coupled-cavity filters. Other possible realization of a discontinuity is a hole placement in a dielectric rod of an NRD-guide. The hole can have any shape but due to simplicity of analysis and manufacturing, the holes that are round or rectangular in shape are used in practical applications. Two examples of a hole discontinuity are shown in Fig. 4.3. The first one is round in shape and placed in parallel to the NRD-guide metal plates (Fig. 4.3 (b)). The second hole is rectangular in shape and located perpendicularly to the metal plates (Fig. 4.3 (c)). The discontinuities described above are easy to manufacture. All the same, they have relatively large geometrical dimensions. The insertion of metal obstacles into an NRD-guide creates

a discontinuity with shorter length, but it is more complicated in theoretical analysis and labor consuming in practical realization. The so called metal window is an example of such discontinuity. Two NRD-guides are separated by an air gap in which two metal stripes in a form of a capacitive diaphragm are placed (Fig. 4.3 (d)). One of the other possible realizations is a vertical diaphragm shown in (Fig. 4.3 (e)). It is formed of two infinitely thin metal strips placed symmetrically inside the dielectric rod of an NRD-guide.

4.2 Synthesis of NRD-guide pass band filters

The problem of direct-coupled cavity filter synthesis is discussed in this section. The investigated filters are composed of a series of resonators, in the form of a half-wave transmission line section, and the coupling reactances are realized as the discontinuities in a uniform transmission line. Being the simplest to realize, the air gap discontinuity is considered, but the discussion can be easily applied to the filters with other types of discontinuities presented in section 4.1.2. A general structure of the filter is presented in Fig 4.4. The filter is composed of a series of dielectric resonators of length d_i separated by the air gaps of length l_i.

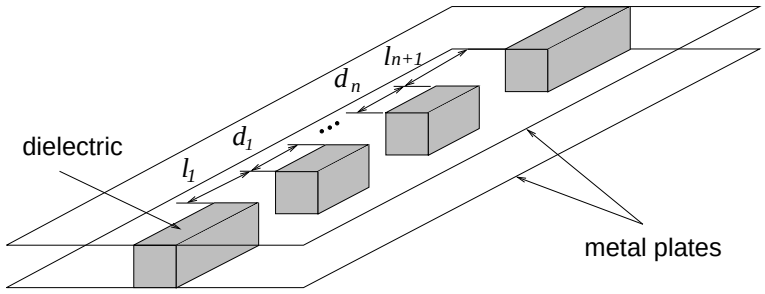

Figure 4.4: *A general view of an NRD-guide bandpass filter.*

In the classical filter design the filter synthesis starts from the desired filter response described by the center frequency, bandwidth, response type and the attenuation levels in pass and stop bands. As a result of a synthesis procedure the physical filter dimensions in given technology are obtained.

There are generally two major well established methods used to design direct-coupled cavity filters [64]:

- The first method uses the low pass prototype as a starting point of the filter synthesis.
- The second method starts from the distributed half-wave step-impedance prototype.

Previous approaches to the synthesis of NRD-guide filters employed the low pass prototype method. For this reason, a slight modification of the low pass prototype design [73] is used as a reference. In this work the approach based on a half-wave step-impedance

prototype is explored as an alternative design technique. Since this approach has not been used so far in the NRD-guide technology, it is described in detail.

Both methods are of hybrid nature. They made an assumption that some parameters, important in the design process, are known or can be calculated using an analytical method or a numerical technique. The methods are approximate, they assume that only the dominant mode propagates in the NRD-guide. The air gap discontinuity is described in terms of an impedance inverter or a scattering matrix of the dominant mode which means that only this mode can be propagated though the gap. The methods assume that other modes excited at the discontinuity decay very quickly in the parallel plate region due to the cut off condition of the parallel plates separated by a distance less than half a wavelength. This simplification is valid even for relatively small gaps.

For both methods, a theoretical part, which includes design equations, is described at the beginning of the suitable section; then the results of numerical tests for chosen filter structures are collected and experimental verification of selected filter examples is provided. For the half-wave step-impedance design method several filters are synthesized and their parameters are investigated in order to test the possible areas of applications and the limitations of the method. The filters with Chebyshev and maximally flat response having the bandwidth ranging from 1% to 10 %, the number of sections from $n = 2$ to $n = 5$ and the attenuation in the pass band from 0.1 dB to 3 dB, are investigated. For each filter the response obtained, computed with the FDTD software, is compared with the theoretical one.

The NRD-guide technology is usually used in a millimeter-wave frequency range, but the cost of manufacturing of a trial filter working in this band is relatively high. Therefore the filters were scaled to work at X-band where the experimental verification was possible. In addition the X-band transitions from rectangular waveguide to NRD-guide, which are necessary during the measurements, were designed and manufactured (see chapter 3 for details about transitions).

4.2.1 Filter synthesis using low-pass prototype

The synthesis method of direct-coupled cavity filters having relatively wide bandwidths was presented by Cohn in [99]. The method is based on a low pass prototype circuit and is suitable to design band pass filters which use waveguides or TEM-mode transmission lines. The application of the method to design various filter's configurations is described in the classical work of Matthaei, Young and Jones (chapter 8 in [64]). The method was successfully used to design different types of bandpass waveguide filters such as waveguide filters with inductive strip-planar circuits mounted inside a waveguide [100], coplanar waveguide filters [101] as well as NRD-guide filters [73].

The method introduced by Cohn gives good results for certain cases of the filters with the maximum bandwidth up to 20 % (i.e. filters with Chebyshev response and the VSWR level not lower than 1.1). Young presented two conditions which have to be fulfilled in order to obtain good accuracy for a bandwidth up to 10% [75]. Deeper investigation of these

conditions showed that Cohn's theory gives accurate results for any filter specification, only to a bandwidth less than 5% [102]. This means that the procedure yields accurate results only for certain bandwidths and is suitable for relatively narrow band filter design.

The design procedure described in this section is a slight modification of the NRD-guide filter synthesis outlined by Yoneyama at al. in [73] and can be presented as follows [1].

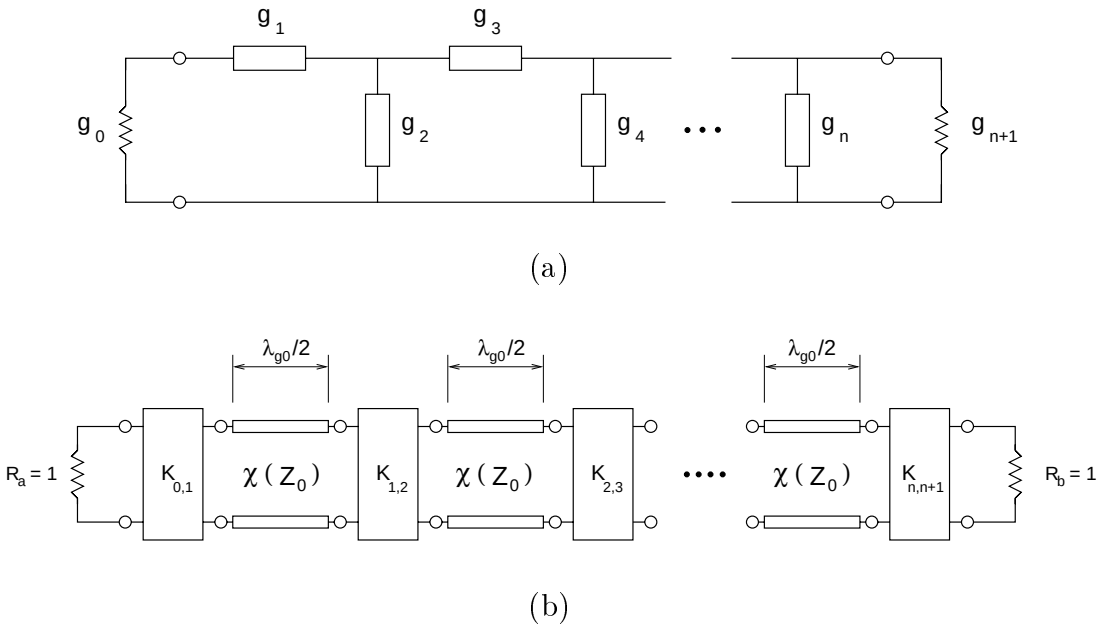

Figure 4.5: *(a) Equivalent circuit of a low pass prototype filter and (b) the corresponding equivalent network of a half wave band pass filter.*

Step 1. At the beginning of the filter design one has to specify the required filter parameters such as type of a filter response, center frequency f_0, bandwidth w_f and the attenuation levels in pass and stop bands.

Step 2. In the second step of the procedure the elements of a low pass prototype are determined. Having defined the required filter response, the standard pass band to low pass mapping is applied to transform the filter response from the band pass domain into the low pass domain (chapter 8 in [64]). Then the number of filter sections n is calculated using the standard technique appropriate for Chebyshev or maximally flat response. For the cases where n is given in advance, the frequency mapping is omitted. Next, the normalized elements g_i of a filter low-pass prototype equivalent circuit (fig. 4.5 (a)) are found using well known equations where only the number of sections n, the attenuation level in pass band and the normalized band edge frequency are required (chapter 4 in [64]).

Step 3. During the third step of the procedure the low pass prototype filter is transformed into the distributed half-wave pass-band prototype filter composed of the series of the impedance inverters and resonators (Fig. 4.5 (b)). The resonators consist of sections of

[1] The main difference between the procedure presented here and the Yoneyama's work lies in the way the impedance inverters parameters have been computed. Here these parameters are determined numerically using FDTD software while in the referenced article variational method was used.

uniform transmission line with the length equal $\lambda_{g_0}/2$ where λ_{g_0} corresponds to the center frequency f_0. The inversion coefficients $K_{i,i+1}$ of the inverters are found from the following equations (chapter 8 in [64])

$$K_{01} = \sqrt{\frac{R_a \chi w_\lambda}{g_0 g_1 \omega_1'}} \tag{4.1}$$

$$K_{i,i+1} = \frac{w_\lambda}{\omega_1'} \sqrt{\frac{\chi_i \chi_{i+1}}{g_i g_{i+1}}} \qquad i = 1, \ldots, n-1 \tag{4.2}$$

$$K_{n,n+1} = \sqrt{\frac{R_b \chi_n w_\lambda}{g_n g_{n+1} \omega_1'}} \tag{4.3}$$

where R_a, R_b are normalized unit resistances of a source and load ($R_a = 1, R_b = 1$). The ω_1' is a pass-band edge angular frequency and the χ is the reactance slope parameter; The fractional bandwidth w_λ is defined as follows

$$w_\lambda = \frac{\lambda_{g_1} - \lambda_{g_2}}{\lambda_{g_0}} \tag{4.4}$$

where λ_{g_1} and λ_{g_2} are the guide wavelengths corresponding to band edge frequencies f_1 and f_2.

Step 4. The last step includes the application of the procedure results to the selected technology. The practical realization of the impedance inverters and resonators depends strictly on the technology used. Also the methods used to compute their parameters are changed according to the analyzed structure.

4.2.2 Synthesis of an NRD-guide filter using low-pass prototype

The procedure outlined above shall be applied to synthesis of the NRD-guide filter. The first part of the synthesis has been presented in the previous section. The procedure determines the required values of the inversion coefficients $K_{i,i+1}$ of the impedance inverters appeared in the half-wave band-pass prototype. The knowledge of the reactance slope parameter χ is assumed, the exact expression for χ of an NRD-guide is presented in [73]. The impedance inverter in the form of symmetrical discontinuity can be realized in various manner as shown in section 4.1.2. In this thesis the impedance inverter realized as a symmetrical air gap in the uniform NRD-guide (Fig. 4.6) is used as an example in order to explain the procedure, but any other type of the inverter can be used as well. The inversion coefficient K and the electrical length ϕ of the impedance inverter are described as follows

$$K = \mid \tan \frac{1}{2} (\tan^{-1} b_s - \tan^{-1} b_o) \mid \tag{4.5}$$

$$\phi = -\pi - \tan^{-1} b_s - \tan^{-1} b_o \tag{4.6}$$

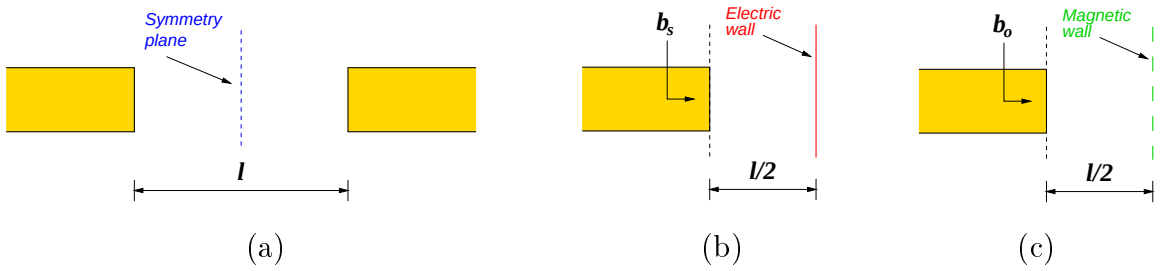

Figure 4.6: *(a) Impedance inverter realization as an air gap in NRD-guide and the equivalent structures used for determination normalized input susceptances b_s and b_o: (b) electric wall boundary in the symmetry plane, (c) magnetic wall boundary in the symmetry plane.*

where b_s, b_o are normalized short and open input susceptances of an NRD-guide air-gap discontinuity with the electric or magnetic wall located at the symmetry plane. When the electric wall is placed in the middle of the inverter, susceptance b_s is obtained (Fig. 4.6 (b)) and, similarly susceptance b_o is determined with the magnetic wall located in the same position (Fig. 4.6 (c)). In the procedure presented in this section the susceptances b_s and b_o are computed numerically using FDTD software. As an example, the results for the X-band NRD-guide (width $w = 10.16$ mm, height $b = 15$ mm, $\epsilon_r = 2.53$) are presented in Fig. 4.7. The computations have been performed at $f_0 = 9.5$ GHz for the LSM_{11} mode.

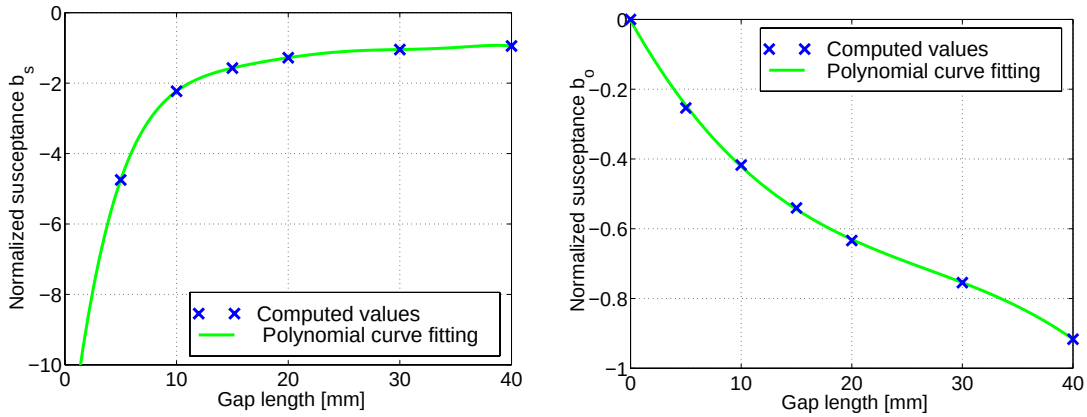

Figure 4.7: *The normalized susceptances b_0 and b_s versus gap length (a) input short susceptance b_s, (b) input open susceptance b_s. Computation were performed with FDTD software. Guide parameters are given in text.*

Having computed b_s and b_o the corresponding values of the inversion coefficient $K(l)$ and electrical length $\phi(l)$ are found using the relations (4.5) and (4.6). The results for the example are presented in Fig. 4.8.

Since the required inversion coefficients $K_{i,i+1}$ and the inverter parameters K and ϕ are known, the dimensions of the NRD-guide air gap coupled filter are calculated. The air gap lengths l_i, which meet the required values of the inversion coefficients $K_{i,i+1}$ for each

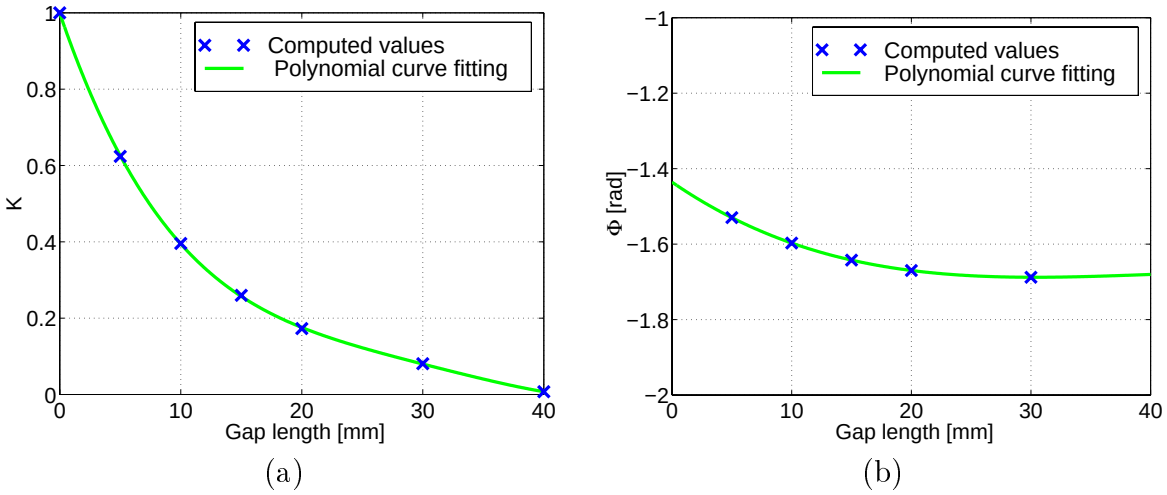

Figure 4.8: *Computed parameters of the impedance inverter versus the gap length l: (a) inversion coefficient K and (b) phase angle ϕ. Guide parameters are given in text.*

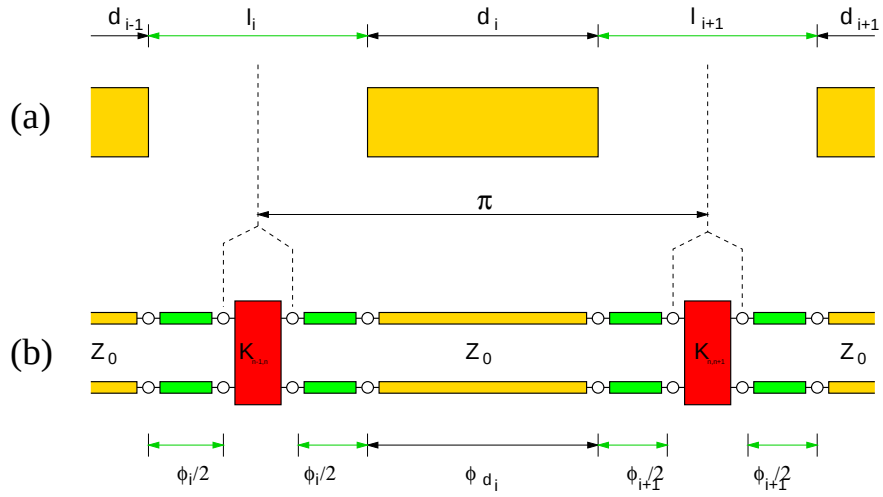

Figure 4.9: *Phase relations for the unit section of the filter: (a) the physical structure and (b) the corresponding K-inverter equivalent network.*

impedance inverter, are determined using the plot presented in Fig. 4.8 (a). If one knows the values l_i, the corresponding values of ϕ_i are determined using the plot presented in Fig. 4.8 (b). Next, the lengths of the NRD-guide half wave resonators are found in the way presented graphically in Fig. 4.9. As shown in Fig. 4.8 (b), the air gap has negative electrical length for every value of l_i. These negative electric lengths are realized by combining the electrical lengths of two adjacent impedance inverters with the electrical length of the half wave resonator which is located between the inverters. Since the electrical length between two adjacent impedance inverters is $\pi/2$ for the half wave filter, the obtained physical length

of the $i-th$ resonator is shortened and its value is calculated as follows

$$d_i = \frac{1}{\beta_0}(\pi - \frac{\phi_i + \phi_{i+1}}{2}) \tag{4.7}$$

where β_0 is propagation constant of the LSM_{11} mode at f_0.

4.2.3 Filter synthesis using distributed half-wave step-impedance prototype

The method with half-wave step-impedance prototype has been under development over a few decades. The brief description of its main developments is presented below.

One of the first filter synthesis methods of direct coupled cavity filters which used the quarter-wave transformer or distributed low pass prototype filter, was proposed by Young [75]. Young's method works very well for bandwidths up to 20 % or even more and low standing wave ratio VSWR in the pass band, of order 1.07 or less. The accuracy of the methods depends on parameters of a particular filter. The main drawback of the method is difficulty in practical use. The method requires the knowledge of one of the prototype circuit parameters, which is usually unknown and need to be guessed. Hence the so called trial-and-error procedure has to be used. Based on work of Young, Levy proposed another method where the design is also based on a distributed low pass prototype circuit [102]. When compared with Young's procedure this method offers simplicity in use and very accurate results for all filters excluding the most extreme configurations. The method can be applied to the design of the filters which can have relatively large bandwidth (up to 40 %) and low VSWR down to 1.01. The limitations of the method in a particular case depend on various coefficients such as the type of response, bandwidth, required VSWR level, cutoff frequencies, stop band attenuation and so on. The important drawback of the method of Levy is lack of the explicit formulae for the element values of the prototype filter like those available for the filter design in the lumped domain. In addition, in the distributed domain, the bandwidth scaling factor can not be neglected but its form is different for various bandwidths. Therefore the incorporation of the scaling factor into the explicit formulae is not straightforward. The solution of this problem was presented by Rhodes who presented the design formulae for the stepped impedance distributed low pass prototype filters with Chebyshev and maximally flat response [103]. Further modification to the method was proposed by Shih who applied the method to design the E-plane waveguide bandpass filters of the Chebyshev type [104]. Shih's contribution was an equivalent circuit of the prototype filter in the form of distributed network where the filter discontinuities are described in the form of scattering matrices. The method was used to design E-plane waveguide filters and was found to give accurate results for bandwidths up to 30 % and the ripple level of order 0.01 dB to 0.2 dB.

In this thesis the design method which use distributed step impedance prototype is applied for the synthesis of NRD-guide filters [105]. The formulae for both, Chebyshev and maximally flat (Butterworth), types of filter response are provided. In the method, the half-wave stepped impedance prototype filter is taken as a starting point to the synthesis. Each

gap in a filter, which corresponds to an impedance step in a prototype filter, can be treated as a discontinuity with certain scattering properties. Then, using the explicit formulae, one can determine the values of reflection coefficients S_{11_i} required at each discontinuity to meet the design specification. Finally, the values of resonators lengths d_i and the size of the air gaps l_i are calculated [106].

The characterization of an air gap reflection coefficients as a function of a gap length can be done using an arbitrary technique. In this work the *Quick-Wave* 3D-simulator based on FDTD method [74] is used, but any other method can be applied instead.

This method has one main advantage when compared to other filter synthesis methods applied to design the NRD-guide filters. In the procedure the requirements for the discontinuities are given in terms of scattering parameters. This fact is of significant importance because the description does not depend on the impedance definition. In an NRD-guide non-TEM hybrid modes can propagate and the first higher order mode, the LSM_{11} mode, is usually used. As noted in section 2.3 the impedance can be defined in different ways. The choice of the proper impedance definition is not obvious and usually has to be considered separately for each particular case. The use of scattering parameters to the description discontinuity properties eliminates this uncertainty.

The other advantage of the presented method is the characterization of a discontinuity using FDTD software. Although a filter is designed at given center frequency, the results of FDTD method are valid in certain frequency band. Hence, one run of the software produces data which allow one to design filters within certain frequency band.

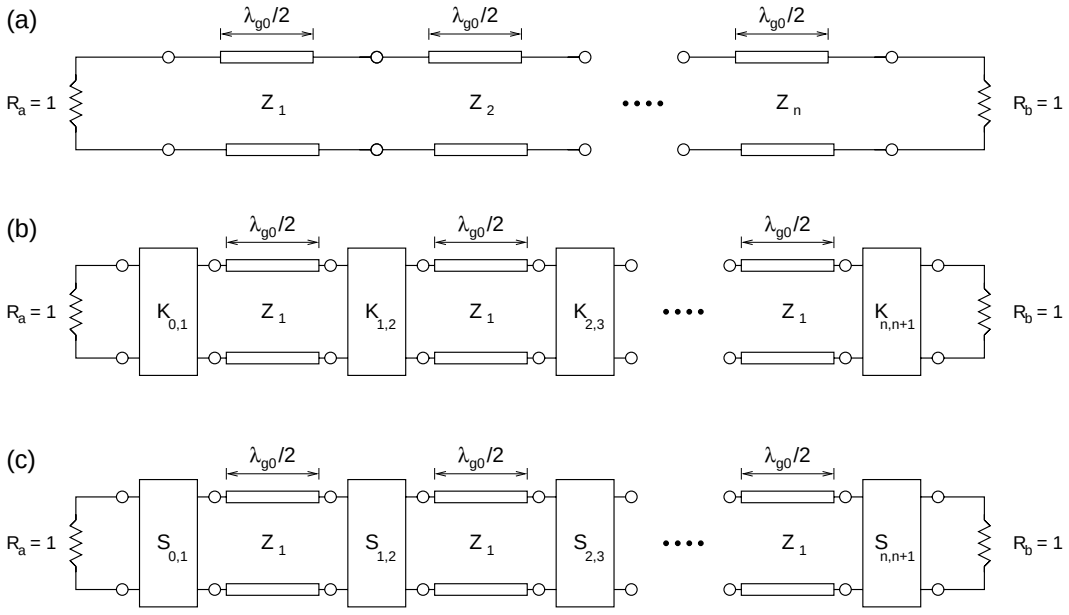

Figure 4.10: *Bandpass filter prototypes: (a) half-wave stepped impedance network, (b) half-wave filter with impedance inverters network, (c) half-wave filter with scattering matrices network.*

The design procedure differs slightly for equiripple and maximally flat response, therefore both cases are presented. First, the design of the filters with nearly optimal equiripple

response (Chebyshev), and next the maximally flat (Butterworth) design are discussed.

4.2.3.1 Filters with Chebyshev response

For design of a filter one has to specify desired filter parameters such as filter response, bandwidth, center frequency and filter attenuation in pass and stop bands. On given specifications the procedure can be divided into the following steps.

Step 1. The procedure starts from the computation of guide wavelengths $\lambda_{g1}, \lambda_{g2}$ which correspond to the defined band-edge frequencies f_1 and f_2.

Step 2. Next, the center guide wavelength λ_{g0}, which correspond to the center frequency f_0, and parameter α are determined from the following equation

$$\alpha = \frac{\lambda_{g1}}{\lambda_{g0}} \sin \frac{\pi \lambda_{g0}}{\lambda_{g1}} = -\frac{\lambda_{g2}}{\lambda_{g0}} \sin \frac{\pi \lambda_{g0}}{\lambda_{g2}}. \tag{4.8}$$

Step 3. The ripple level in the pass band is usually specified as a function of the maximum insertion loss L_{A_r} [dB]. In such case the parameter h is computed as follows

$$h = \sqrt{10^{L_{A_r}}/10 - 1}. \tag{4.9}$$

If the ripple level in the pass band is given as a function of a standing wave ratio $VSWR$ then

$$h = \frac{VSWR - 1}{2\sqrt{VSWR}}. \tag{4.10}$$

Step 4. When the parameters h, α and guide wavelengths are known, the number of a filter sections n is found using a standard technique from the condition of the attenuation level L_{A_s} in the stop band. For a reactance coupled filter the theoretical transmission characteristics are accurately described by the formula presented in [104]

$$\mid S_{12} \mid^2 = \frac{1}{1 + h^2 T_n^2 \left(\frac{\pi \sin\theta}{\theta \alpha}\right)} \tag{4.11}$$

where

$$\theta = \frac{\pi \lambda_{g0}}{\lambda_g} \tag{4.12}$$

λ_g is a guide wavelength, λ_{g0} is a guide wavelength computed using relation (4.8) and T_n is a Chebyshev polynomial of the first kind

$$T_n(x) = \cosh(n \cosh^{-1}). \tag{4.13}$$

Equation (4.11) is Levy's version of the formula presented by Young in [75]. It takes into account the frequency dependence of the discontinuities appearing in the filter structure. Levy shows [102] that it has significant influence on the filter characteristics and should not be neglected. In the case of the NRD-guide bandpass filters this formula is not valid for the

filters with relatively large bandwidths (10% and more). Therefore, for such bandwidths the frequency mapping in λ domain is used. Detail discussion on this subject is presented in appendix D.

Step 5. Once n is known, the synthesis procedure uses the first equivalent network, shown in Fig. 4.10(a), which is a half-wave step-impedance prototype. The filter is composed of a series of half-wave transmission line sections with different impedance each. One section corresponds to a resonator in a standard filter design technique. The required impedances for each section are computed using the following relations

$$Z_r = \frac{2\sin\left[\frac{(2r-1)n}{2n}\right]}{y\alpha} - \frac{\alpha}{4y}\left[\frac{y^2+\sin^2(\frac{r\pi}{n})}{\sin\left[\frac{(2r+1)\pi}{2n}\right]} + \frac{y^2+\sin^2\left[\frac{(r-1)\pi}{n}\right]}{\sin\left[\frac{(2r-3)\pi}{2n}\right]}\right] \tag{4.14}$$

for $r = 1, 2, \ldots, n$ and

$$Z_r = 1 \qquad\qquad r = 0, n+1 \tag{4.15}$$

where

$$y = \sinh\left[\frac{\sinh^{-1}\frac{1}{n}}{n}\right]. \tag{4.16}$$

The equation (4.14) published in [104] has contained printing error and has been corrected based on the paper by Rhodes [103].

Step 6. The filter realization from the cascade of transmission lines with different impedances each is highly impractical in most cases. When one intends to use an uniform guide to build a filter the discontinuities introduced by the impedance steps have to be inserted in a different way. An equivalent network shown in Fig. 4.10(b) is used to this purpose. Now the discontinuities are described by impedance inverters and all line sections have the same unit impedance. Using equations (4.14) $\div$ (4.16) the inversion coefficients K_i are calculated as follows

$$K_{r,r+1} = \sqrt{\frac{1+\left(\frac{\sin\left[\frac{r\pi}{n}\right]}{y}\right)^2}{Z_r Z_{r+1}}} \qquad r = 0, 1, \ldots, n. \tag{4.17}$$

Step 7. Finally, the parameters of the basic equivalent circuit are determined (Fig. 4.10(c)). In this network each discontinuity is represented by the reflection coefficients given by

$$(S_{11})_{r,r+1} = \frac{K_{r,r+1}^2 - 1}{K_{r,r+1}^2 + 1}. \tag{4.18}$$

The discontinuity is assumed to be lossless and reciprocal. Hence its scattering matrix S is unitary and all parameters of S matrix can be computed from $S_{11_{i,i+1}}$ parameter.

The method determines the required values of the reflection coefficients at each discontinuity of the half wave filter. The practical realization of the discontinuities depends on the technology applied to filter construction.

4.2.3.2 Filters with maximally-flat response

For the maximally flat response, the computation of reflection coefficients is similar to the Chebyshev case. The steps 1 to 3 and step 7 are the same. The steps 4 to 6 are modified as follows.

Step 4. Similarly to the Chebyshev case, the number of sections n is determined using standard technique which requires the knowledge of the attenuation level in the stop band. The theoretical response for band pass direct coupled cavity filters with maximally flat response can be approximated by the following equation [103]

$$\mid S_{12} \mid^2 = \frac{1}{1 + \left(\frac{\pi \sin\theta}{\theta\alpha}\right)^{2n}} \tag{4.19}$$

where θ is given by (4.12).

Step 5. Parameters for the equivalent network from Fig. 4.10 (a) are given by the formulae

$$Z_r = \frac{2\sin\left[\frac{(2r-1)\pi}{2n}\right]}{\alpha}\left[1 - \frac{\alpha^2\cos(\frac{-\pi}{n})}{4\sin\left(\frac{(2r-3)\pi}{2n}\right)\sin\left(\frac{(2r+1)\pi}{2n}\right)}\right] \tag{4.20}$$

for $r = 1, 2, \ldots, n$ and

$$Z_r = 1 \qquad\qquad r = 0, n+1. \tag{4.21}$$

Step 6. The parameters of impedance inverter network (Fig. 4.10 (b)) are determined as follows

$$K_{r,r+1} = \frac{1}{\sqrt{Z_r Z_{r+1}}} \qquad r = 0, 1, \ldots, n. \tag{4.22}$$

Finally, the required values of reflection coefficients for the network from Fig. 4.10 (c) are calculated using equation (4.18) (Step 7). As in the case of Chebyshev filters the form of the discontinuities depends on the guide chosen to build the filter.

4.2.4 Synthesis of an NRD-guide filter using half-wave step-impedance prototype

The first part of the design is independent on the technology used to build the filter. The way of determining the required values of the reflection coefficients at the discontinuities of the basic network equivalent circuit (Fig. 4.10 (c)) was presented in two previous sections for Chebyshev and maximally flat cases, respectively. The practical realization of a discontinuity in the form of an air gap between two NRD-guides (Fig. 4.11 (a)) is discussed in this section. The corresponding network representation of an air gap, in the form of a scattering matrix is presented in Fig. 4.11 (b). Gaps of different lengths result in different values of S_{11}. The relations between S_{11} and the gap length can be found using an arbitrary technique. Here

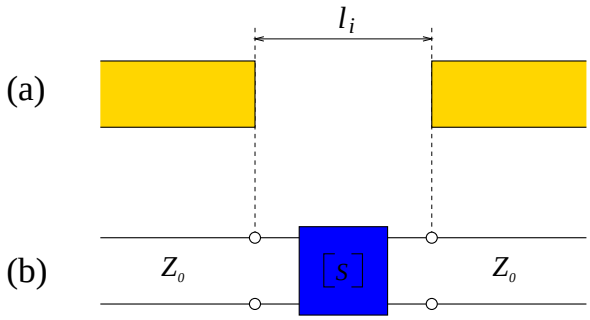

Figure 4.11: *(a) An air gap discontinuity in an NRD-guide and (b) its equivalent circuit representation when the network with scattering matrices is used.*

the FDTD software is used. For the sake of demonstration the results for the NRD-guide working in X-band are presented in Fig. 4.12. The NRD-guide parameters are as follows: $w = 10.16$ mm, $b = 15$ mm, $\epsilon_r = 2.53$ (Rexolite 1422); the calculations has been performed at $f_0 = 9.5$ GHz for the LSM_{11} mode. The dispersion characteristics for this guide are presented in Fig. 2.3.

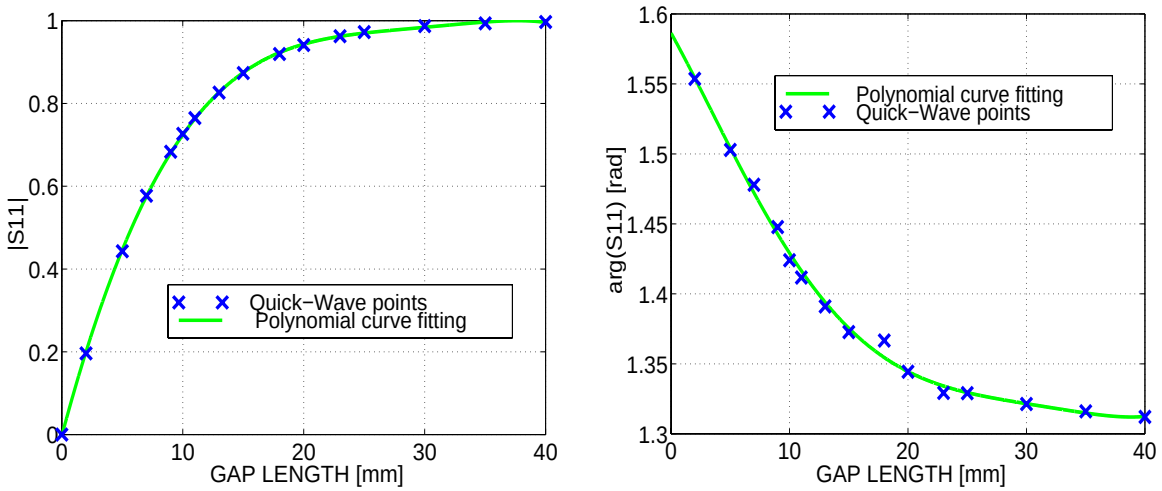

Figure 4.12: *Computed reflection coefficient for an NRD-guide gap as a function of gap length at frequency $f_0 = 9.5$ GHz: (a) amplitude of S_{11}, (b) phase of S_{11}. The NRD-guide parameters are given in text.*

Having calculated the required values of the reflection coefficients (equation (4.18)), one determines the gap lengths l_i using the results plotted in Fig. 4.12 (a). Next the lengths of the resonators are found. For a given filter prototype all S_{11}'s have to be real, so the phase angle should be 0 or π. To fulfil this condition, the reference planes (R-R in Fig. 4.13) for

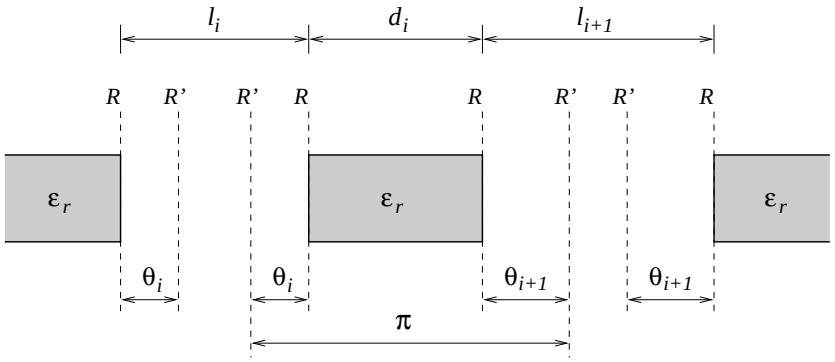

Figure 4.13: *A shift of $S_{11_{i,i+1}}$ reference planes for two adjacent gaps in NRD-guide filter.*

which these parameters were computed, should be moved towards the center of a gap to a new position (lines *R'-R'* in Fig. 4.13) by an angle θ_i computed from

$$\theta_i = \frac{\pi - \phi_i}{2} \tag{4.23}$$

where ϕ_i is a phase of a $S_{11_{i,i+1}}$ corresponding to l_i (Fig. 4.12 (b)). The electrical distance between the new reference planes of the two adjacent gaps is π for the half-wave filter. Hence, one can calculate the i-th dielectric resonator length d_i from the following relation

$$d_i = \frac{1}{2\beta_0}(\theta_i + \theta_{i+1}) \tag{4.24}$$

where β_0 is the propagation constant for center frequency f_0 of the LSM_{11} mode.

4.3 Design examples

The synthesis methods presented in the previous sections are used to design the air gap filters. The classical method which uses low pass prototype serves as a reference method, when the results obtained by half-wave step-impedance method are discussed. The computation of the parameters of the air gap discontinuities are done with the FDTD software.

Two groups of the air gap filters, working in two frequency bands, have been designed. For obvious reasons, the experimental verification of each synthesized filter is impossible. Therefore, the FDTD software is used as a basic tool to determine response of the filters.

- **Filters designed for U-band.** In the U band the filter with 2% bandwidth and center frequency $f_0 = 49.5$ GHz is investigated. The filter is designed using three synthesis methods. Then the obtained results are compared with the theoretical response. Because a practical realization and an experimental verification of the filter is impossible, the measurement data of the filter are taken from the plots published in [73].

- **Filters designed for X-band.** Several filters having different bandwidths and center frequency $f_0 = 9.5$ GHz are investigated. Both methods presented in this work are

applied to design each filters. The accuracy of the methods is tested; the results are compared with theoretical predictions. The selected filters designed using the half-wave step-impedance method are manufactured and measured in order to verify the accuracy of the method.

4.3.1 Examples of NRD-guide filters designed at $f_0 = 49.5$ GHz

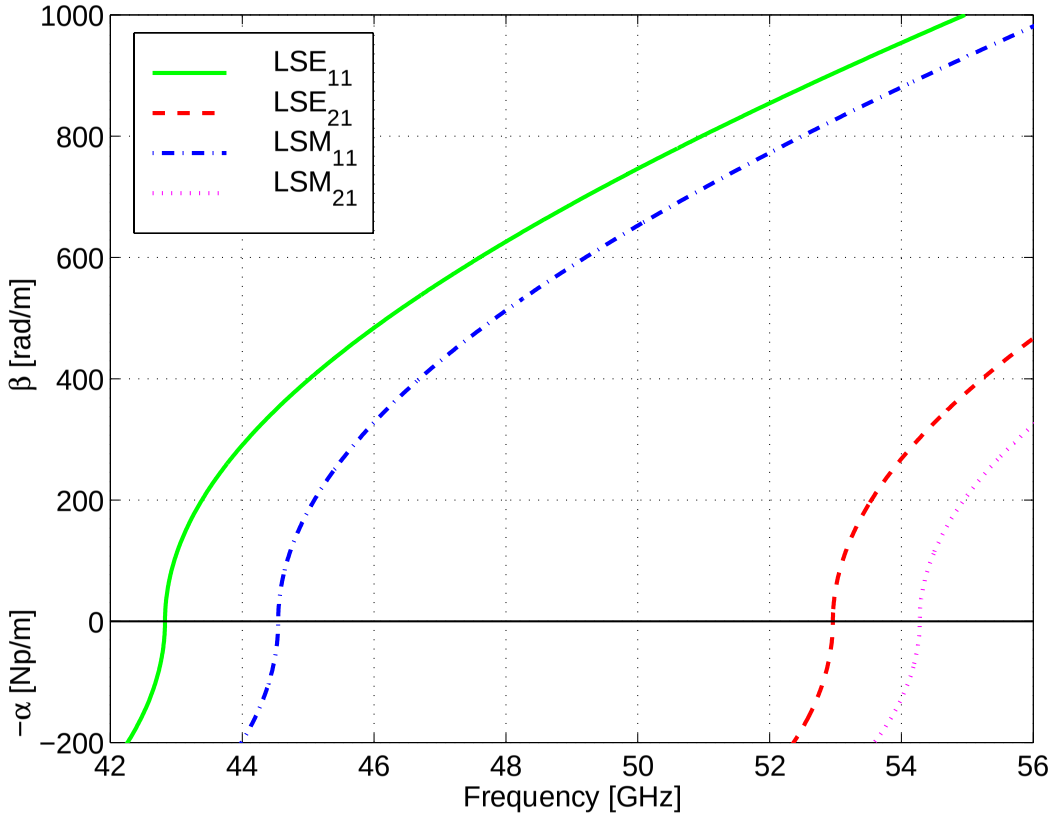

Figure 4.14: *Dispersion characteristics of the NRD-guide working at U-band. The NRD-guide parameters: width w=3.5 mm, height b=2.7 mm, $\epsilon_r = 2.04$ (Teflon).*

The NRD-guide designed to work at U-band has the following parameters: width $w = 3.5$ mm, height $b = 2.7$ mm, $\epsilon_r = 2.04$ (Teflon). The dispersion characteristics for this guide are presented in Fig. 4.14. The single mode bandwidth is limited from the bottom by the cut-off frequency of LSM_{11} mode $f_{c_{LSM11}} = 44.4$ GHz and from the top by the cutoff frequency of the first higher order mode LSM_{21} $f_{c_{LSM11}} = 54.2$ GHz. The lower order mode LSE_{11} also exists in the frequency band of interest, but its appearance can be neglected because, as an orthogonal mode to the LSM_{11}, should not be excited. This guide is used to build filters designed at frequency $f_0 = 49.5$ GHz. The frequency, where the guide becomes radiative, is determined by the plate separation $b = 2.7$ mm and equals $f_p = 55.6$ GHz, hence, in the investigated frequencies the guide possess its nonradiative character. Three methods used to design the filter are compared in order to test their accuracy. The three section filter

of Chebyshev response with 0.1 dB ripple level in the pass band has following parameters: center frequency $f_0 = 49.5$ GHz, 2 % bandwidth defined at band edge frequencies at which the attenuation level $L_{A_e} = 3$ dB.

4.3.1.1 Filter design using the low-pass prototype and the variational method

The first method, which was presented by Yoneyama in [73], uses a low pass prototype equivalent circuit to design the filter. The method is very similar to the method described in section 4.2.1. The main difference between them lies in the way the impedance inverters were determined. Yoneyama used variational method, while in the method described in section 4.2.1 FDTD software has been applied. The dimensions of the designed filter and values of the impedance inverters K and ϕ produced by the method are taken from the article and are presented in Fig. 4.15 (a) for completeness. The simulated filter response is presented in Fig. 4.15 (b) and (c) together with the theoretical prediction and the measurement. The experimental data are read from a small and hand made plot presented in the article, so they present only rough estimation of the measured values.

Gap length [mm]		Resonator length [mm]		Inverter parameters			
				K	Value	Φ	Value [rad]
l_1, l_4	1.6	d_1, d_3	2.72	K_{01}, K_{34}	0.34	Φ_1, Φ_4	-1.466
l_2, l_3	3.5	d_2	2.72	K_{12}, K_{23}	0.11	Φ_2, Φ_3	-1.422

(a)

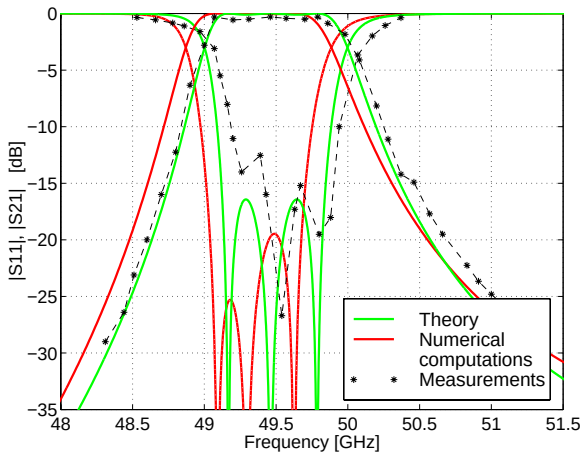

(b)

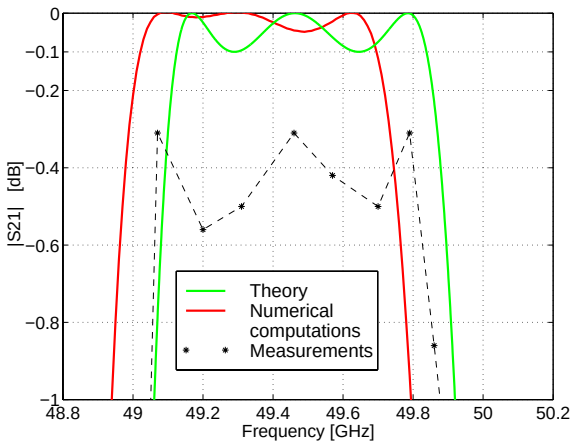

(c)

Figure 4.15: *(a) Filter dimensions and impedance inverters parameters of the filter with $f_0 = 49.5$ GHz and 2% bandwidth together with filter response : (b) general view, (c) detailed view in the pass band. The procedure with low pass prototype and variational method is used to design the filter. Filter dimensions and measurement data are taken from the article [73].*

4.3.1.2 Filter design using the low-pass prototype and the FDTD method

The second method used to design the filter is described in section 4.2.1. At the beginning, the short and open normalized susceptances b_s and b_o are calculated versus the gap length, for the guide used to build the filter, using the FDTD software (Fig. 4.16). Then the impedance inverter parameters are found from the equations (4.5) and (4.6); the results are plotted in Fig. 4.17. Normalized susceptances and inverter parameters are computed at $f_0 = 49.5$ GHz for the LSM_{11} mode. Finally, the filter dimensions are computed.

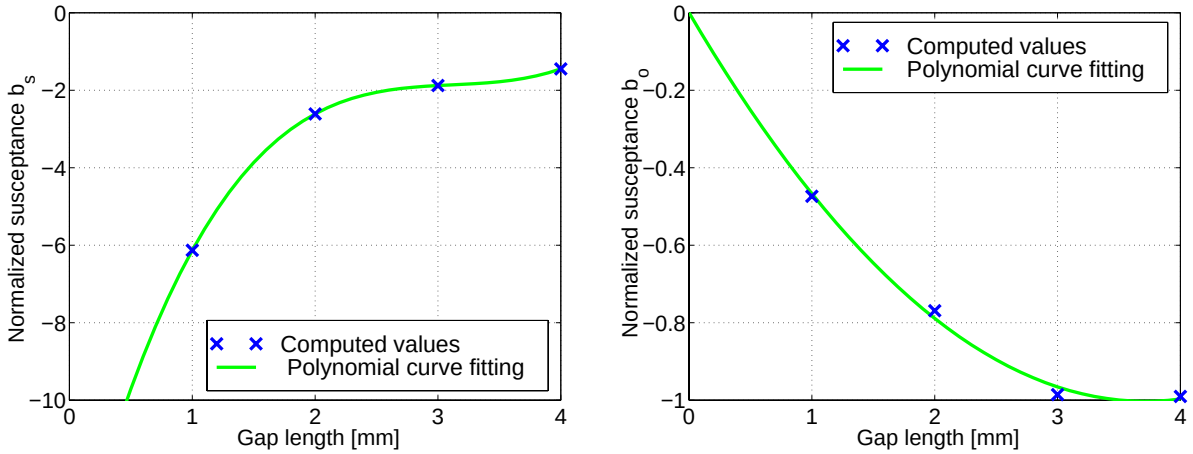

(a) (b)

Figure 4.16: *Results of normalized susceptances b_0 and b_s computation versus gap length: (a) electric wall boundary in the symmetry plane, (b) magnetic wall boundary in the symmetry plane. Computation were performed with the QuickWave-3D package.*

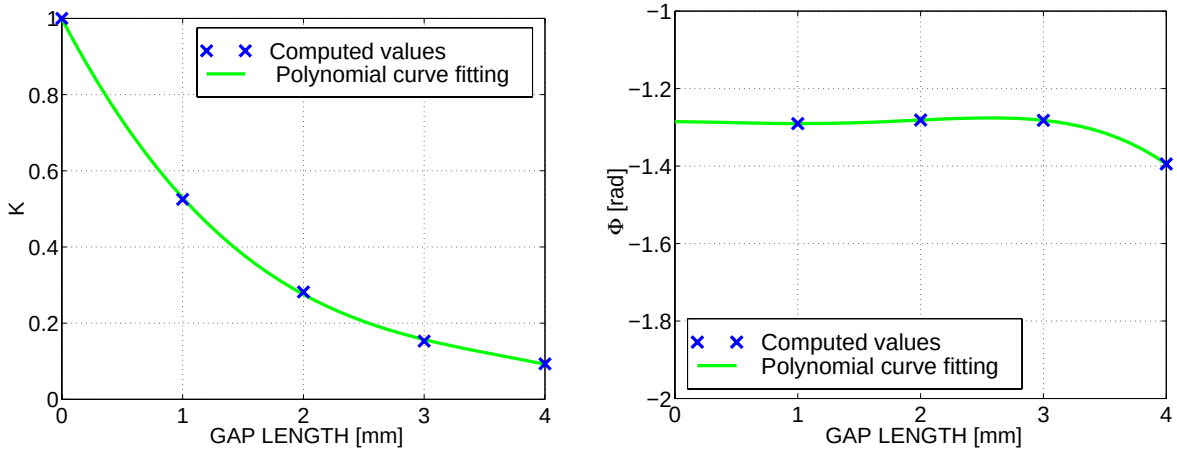

(a) (b)

Figure 4.17: *Computed parameters of impedance inverter versus gap length l: (a) inversion coefficient K and (b) phase angle ϕ.*

The parameters of the impedance inverters obtained with the method and the filter dimensions are shown in Fig. 4.18 (a). The simulated filter response and the corresponding theoretical characteristics are plotted in Fig. 4.18 (b) and (c).

Gap length [mm]		Resonator length [mm]		Inverter parameters			
				K	Value	Φ	Value [rad]
l_1, l_4	1.66	d_1, d_3	2.95	K_{01}, K_{34}	0.3402	Φ_1, Φ_4	-1.286
l_2, l_3	3.72	d_2	2.90	K_{12}, K_{23}	0.1097	Φ_2, Φ_3	-1.343

(a)

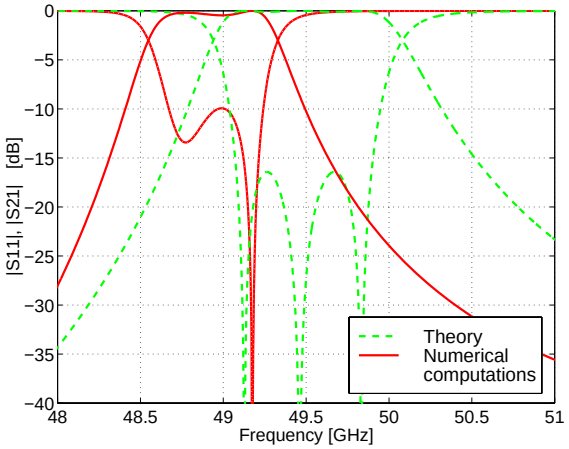

(b)

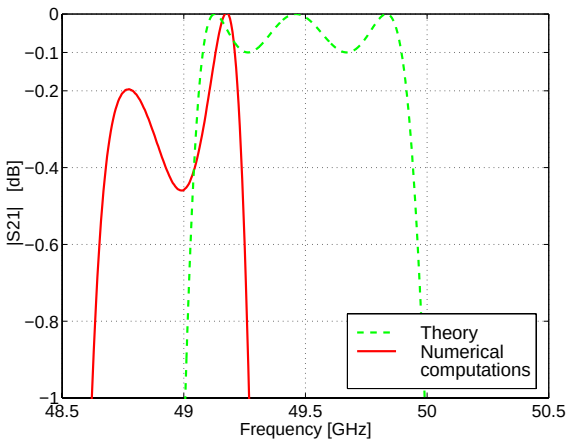

(c)

Figure 4.18: *Filter dimensions and impedance inverters parameters of the filter with* $f_0 = 49.5GHz$ *and 2% bandwidth together with filter response : (b) general view, (c) detailed view in the pass band. The procedure with low pass prototype and FDTD software were used to design the filter.*

4.3.1.3 Filter design using the half-wave step-impedance prototype

The third way of the filter design is to apply the method, described in section 4.2.3, with half-wave step-impedance prototype. The reflection coefficient S_{11} of the air gap discontinuity versus gap length is computed using FDTD software; results of the computations at $f_0 =$ 49.5 GHz for the LSM_{11} mode are plotted in Fig. 4.19.

During the design, the procedure determines the values of the elements of the equivalent circuits. These values are listed in Fig. 4.20 (a) together with the calculated filter dimensions. Values of Z_i are normalized to $Z_1 = Z_5 = 1$. The results of numerical simulation of the filter are presented in Fig. 4.20 (b) and (c) together with a theoretical response.

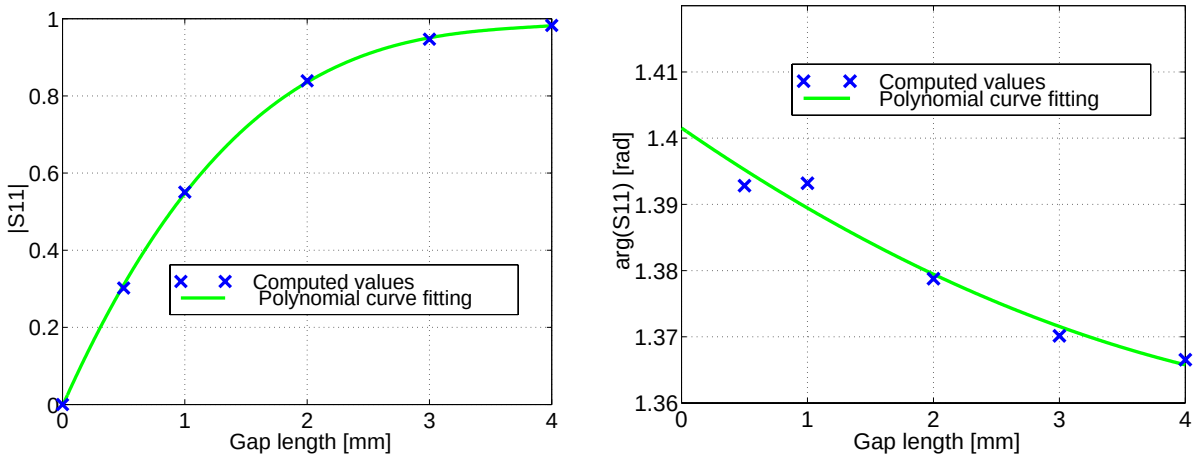

(a) (b)

Figure 4.19: *Reflection coefficient of an NRD-guide air gap as a function of gap length at frequency $f_0 = 49.5$ GHz: (a) amplitude of S_{11}, (b) phase of S_{11}. Guide parameters are given in the text.*

Gap length [mm]		Resonator length [mm]		Circuit parameters					
				Z	Value	K	Value	S_{11}	Value
l_1, l_4	1.69	d_1, d_3	2.64	Z_2, Z_4	8.5557	K_{01}, K_{34}	0.3419	S_{11_1}, S_{11_4}	0.7907
l_2, l_3	3.39	d_2	2.64	Z_3	16.8893	K_{12}, K_{23}	0.1116	S_{11_1}, S_{11_4}	0.9754

(a)

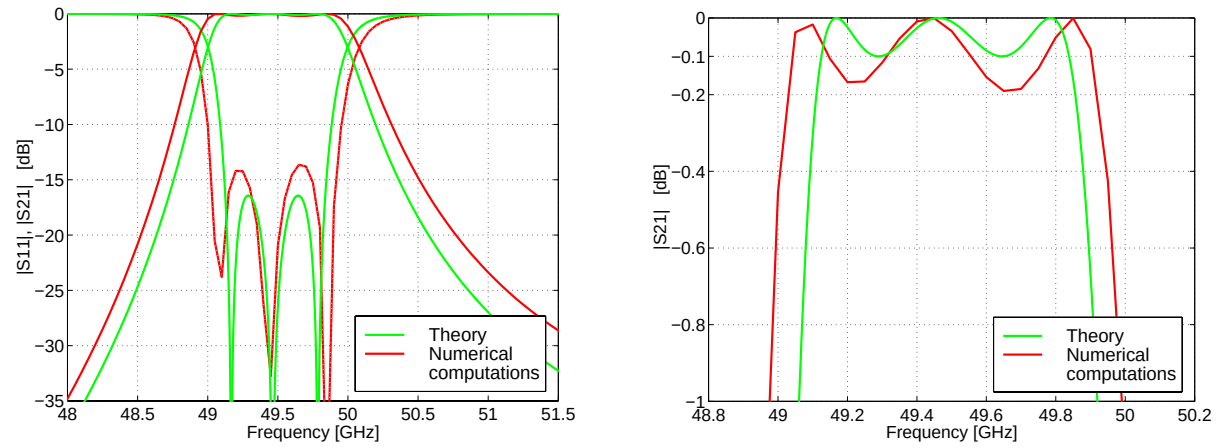

(b) (c)

Figure 4.20: *Filter dimensions and parameters of the equivalent circuits of the filter with $f_0 = 49.5GHz$ and $w_f = 2\%$ together with filter response : (b) general view, (c) detailed view in the pass band. The procedure with half-wave step-impedance prototype and FDTD software were used to design the filter.*

4.3.1.4 Comparison of the designs

The accuracy of the design is defined as a difference between the simulated and theoretically predicted results. To compare the filter parameters the following error definitions are introduced. The fractional bandwidth error Δw_f is computed as follows

$$\Delta w_f = \mid w_f^d - w_f^s \mid \quad [\%] \tag{4.25}$$

where fractional bandwidth w_f is specified as

$$w_f = \frac{\mid f_2 - f_1 \mid}{f_0} \cdot 100 \quad [\%] \tag{4.26}$$

and the center frequency error Δf_0 is defined as

$$\Delta f_0 = \frac{\mid f_0^d - f_0^s \mid}{f_0^d} \cdot 100 \quad [\%]. \tag{4.27}$$

In (4.25) and (4.27) the indices s and d denote the value obtained from simulation and the one given in the design specification, respectively. The selected parameters of the designed filters are summarized in Table 4.1.

Parameter	Low pass prototype + variational method	Low pass prototype + FDTD software	Half-wave step-impedance prototype + FDTD software
f_0 [GHz]	49.375	48.94	49.495
Δf_0 [%]	0.25	1.13	0.01
w_f [GHz]	1.01	0.78	1.17
w_f [%]	2.04	1.58	2.36
Δw_f [%]	0.04	0.42	0.36

Table 4.1: *Results of the three methods used to design the 3-pole 0.1dB Chebyshev filter with $f_0 = 49.5$ GHz and bandwidth $w_f = 2\%$.*

Results for a low pass prototype. The filter designed using low pass prototype (LPP) and variational method has bandwidth nearly equal to the predicted one. The bandwidth error equals only 0.04 %. All the same, the center frequency is significantly shifted towards lower frequencies by the value of 0.125 GHz ($\Delta f_0 = 0.25$ %).

The low pass prototype used together with FDTD software yields large shift of the center frequency ($\Delta f_0 = 1.13$ %) towards lower frequencies. Moreover, the bandwidth is reduced from 2% to 1.58%. In addition the maximal ripple level grows up to value of -0.46 dB at $f = 49$ GHz (Fig. 4.18). The comparison between two LPP methods shows that

the poor results in the second case are caused mainly by inaccurate FDTD computation of impedance inverter parameters. It has been observed that the magnitudes of reflection and transmission coefficients are computed accurately. However, the phase of a transmission coefficient is determined with greater accuracy than the phase of reflection coefficient. The latter one is used in calculation of filter dimensions in the low pass method therefore the inaccuracy in it is transferred directly to the filter response.

Results for a half-wave step-impedance prototype. The filter designed using a half-wave step-impedance prototype (HWSIP) together with FDTD software has the center frequency equal to the specified one ($\Delta f_0 = 0.01\%$). The filter bandwidth is wider than the desired one by 170 MHz ($\Delta w_f = 0.36\%$) and the ripple level in the pass band falls down to maximally -0.19 dB for certain frequency points (Fig. 4.20). Although the bandwidth is slightly wider than the specified one, further investigation of this problem showed that this drawback could be eliminated. Nearly the exact value of center frequency suggests, that the proper bandwidth width can be obtained by appropriate bandwidth scaling. Similar scaling was introduced by Cohn at the design of waveguide filters with shunt inductive post or iris [99]. This assumption was confirmed by the numerical tests. The bandwidth with the value almost the same as the designed one was obtained when the bandwidth was defined at 2 dB level instead of 3 dB one. In this case the designed filter has the parameters nearly equal to the designed ones. The straightforward incorporation such a scaling factor into the design procedure is not a trivial task because the factor depends on various coefficients such as bandwidth, center frequency and guide parameters. Nevertheless, the simple way to determine the scaling factor is to carry out the synthesis followed by the FDTD simulation. The scaling factor is then found by the ratio of a nominal bandwidth to the simulated one.

Concluding remarks. Comparing results for low pass prototype and half-wave step-impedance prototype some general remarks can be given. For the LPP, a significant shift of center frequency towards lower frequencies is observed in both LPP cases. The HWSIP yields the center frequency located exactly at the desired position. The bandwidth error and the ripple level are slightly larger in the HWSIP than for the more accurate LPP. In some systems, such as multiplexers and demultiplexers, the accurate design which preserves the center frequency position is of great importance. From this point of view the HWSIP yields better results than the LPP. Finally, the bandwidth error in HWSIP can be reduced by introducing an empirical scaling factor into the design procedure.

4.3.2 Examples of NRD-guide filters designed at $f_0 = 9.5$ GHz

The second group of filters was designed for the X-band. The following parameters were assumed about the NRD-guide: $w = 10.16$ mm, $b = 15$ mm, $\epsilon_r = 2.53$ (Rexolite 1422). The dispersion characteristics of this guide are shown in Fig. 2.3.

The series of filters, have been designed to test the validity of the synthesis methods. The three section Chebyshev filters have been designed using both low pass prototype and half-wave step-impedance prototype. The fractional bandwidth has been assumed to values of 1%, 1.9%, 5% and 10%. The ripple level L_{A_r} and the attenuation at band edge frequencies L_{A_e} have been chosen to have the same value of 0.5 dB. All filters have been designed at center frequency $f_0 = 9.5$ GHz.

4.3.2.1 Filter design using low-pass prototype

The calculated normalized susceptances b_s and b_o for the NRD-guide are shown in Fig. 4.7. The corresponding values of impedance inverter parameters K and ϕ are presented in Fig. 4.8. For each investigated filter the equivalent circuit parameters, filter dimensions and filter response are collected in Fig. 4.21 to Fig. 4.23.

Gap length [mm]		Resonator length [mm]		Inverter parameters			
				K	Value	Φ	Value [rad]
l_1, l_4	12.68	d_1, d_3	12.3	K_{01}, K_{34}	0.3118	Φ_1, Φ_4	-1.624
l_2, l_3	25.56	d_2	12.04	K_{12}, K_{23}	0.1173	Φ_2, Φ_3	-1.685

(a)

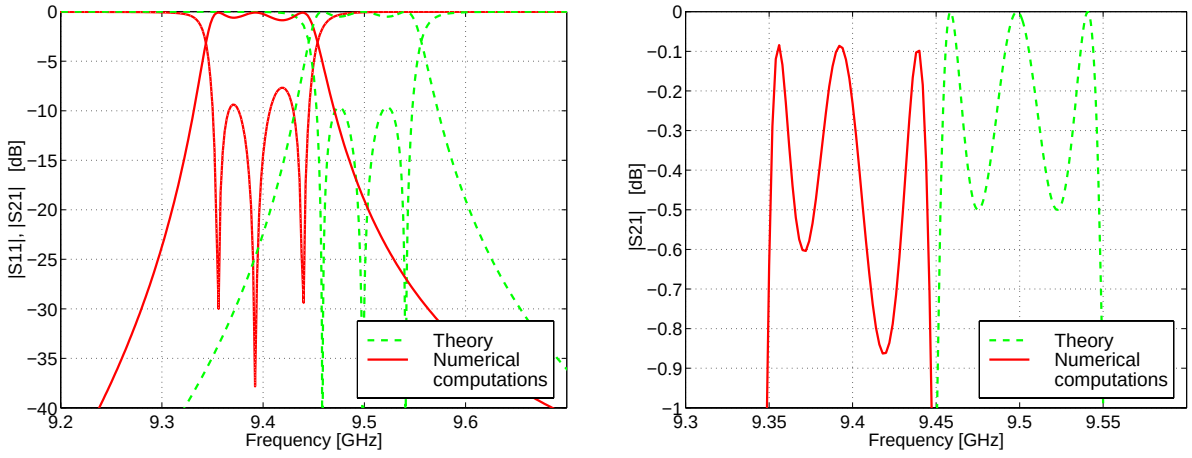

(b) (c)

Figure 4.21: *(a) Filter dimensions and impedance inverters parameters of the filter with $f_0 = 9.5GHz$ and fractional bandwidth $w_f = 1\%$ together with filter response: (b) general view, (c) detailed view in the pass band.*

Gap length [mm]		Resonator length [mm]		Inverter parameters			
				K	Value	Φ	Value [rad]
l_1, l_4	12.68	d_1, d_3	12.3	K_{01}, K_{34}	0.3118	Φ_1, Φ_4	-1.624
l_2, l_3	25.56	d_2	12.04	K_{12}, K_{23}	0.1173	Φ_2, Φ_3	-1.685

(a)

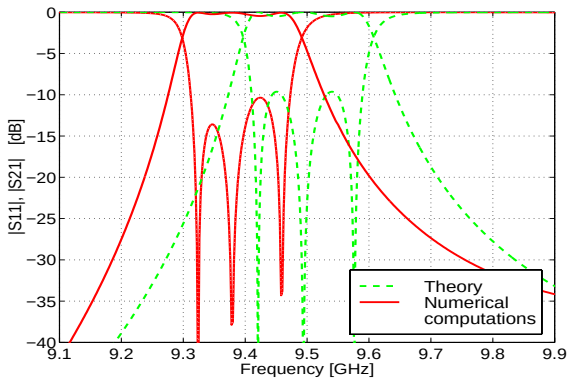

(b)

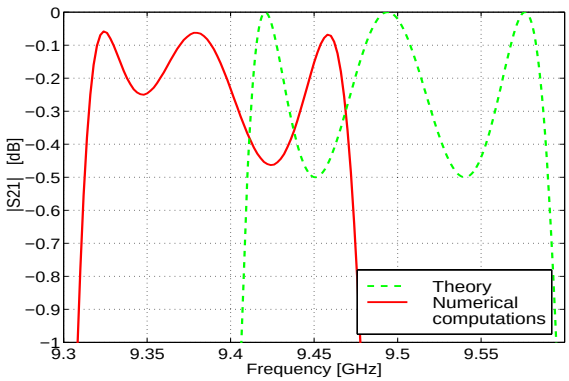

(c)

Gap length [mm]		Resonator length [mm]		Inverter parameters			
				K	Value	Φ	Value [rad]
l_1, l_4	12.68	d_1, d_3	12.3	K_{01}, K_{34}	0.3118	Φ_1, Φ_4	-1.624
l_2, l_3	25.56	d_2	12.04	K_{12}, K_{23}	0.1173	Φ_2, Φ_3	-1.685

(d)

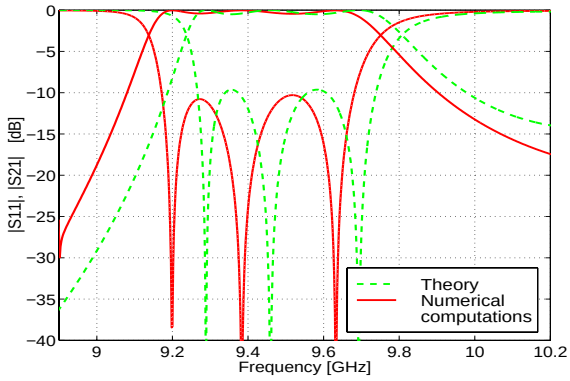

(e)

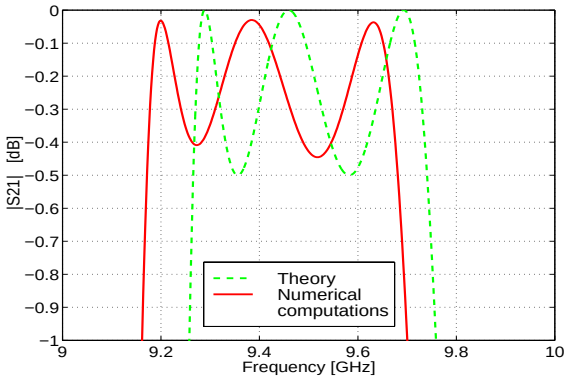

(f)

Figure 4.22: *(a) Filter dimensions and impedance inverters parameters of the filter with* $f_0 = 9.5GHz$ *and fractional bandwidth* $w_f = 1.9\%$ *together with filter response: (b) general view, (c) detailed view in the pass band. (d) Filter dimensions and impedance inverters parameters of the filter with* $f_0 = 9.5GHz$ *and fractional bandwidth* $w_f = 5\%$ *together with filter response: (e) general view, (f) detailed view in the pass band.*

Gap length [mm]		Resonator length [mm]		Inverter parameters			
				K	Value	Φ	Value [rad]
l_1, l_4	3.56	d_1, d_3	13.42	K_{01}, K_{34}	0.7163	Φ_1, Φ_4	-1.506
l_2, l_3	5.12	d_2	13.31	K_{12}, K_{23}	0.619	Φ_2, Φ_3	-1.532

(a)

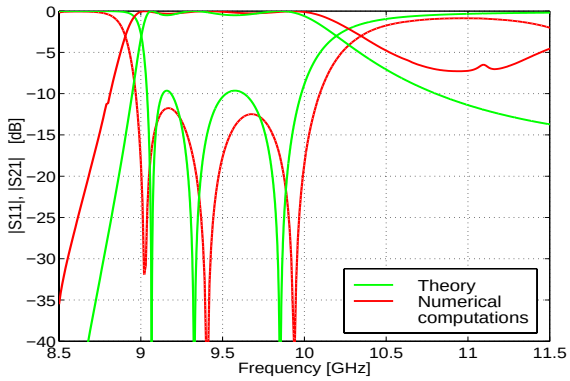

(b)

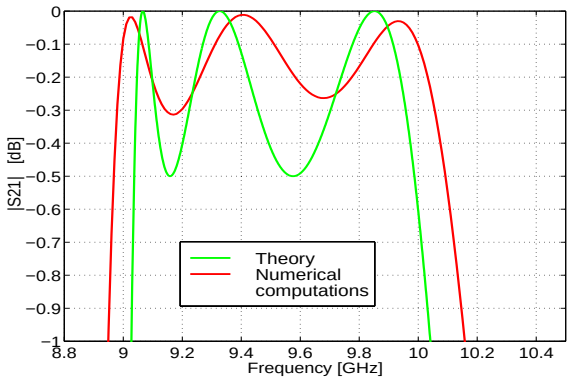

(c)

Figure 4.23: *(a) Filter dimensions and impedance inverters parameters of the filter with* $f_0 = 9.5GHz$ *and fractional bandwidth* $w_f = 10\%$ *together with filter response: (b) general view, (c) detailed view in the pass band.*

4.3.2.2 Filter design using half-wave step-impedance prototype

The results of filter design using the half-wave step-impedance prototype are presented in this section. The procedure requires computations of the air gap reflection coefficients versus the gap length. The results are shown in Fig. 4.12. Figures in this section show filter responses and the parameters of the equivalent circuits used in the design for 1%, 1.9%, 5% and 10% bandwidths. The design of the filter with 1.9 % bandwidth has been verified experimentally. The results obtained from measurement and corresponding discussion are presented in section 4.5.

Gap length [mm]		Resonator length [mm]		Circuits parameters					
				Z	Value	K	Value	S_{11}	Value
l_1, l_4	16.53	d_1, d_3	10.99	Z_2, Z_4	19.5201	K_{01}, K_{34}	0.2263	S_{11_1}, S_{11_4}	0.9025
l_2, l_3	33.11	d_2	10.80	Z_3	38.8145	K_{12}, K_{23}	0.0.619	S_{11_1}, S_{11_4}	0.9924

(a)

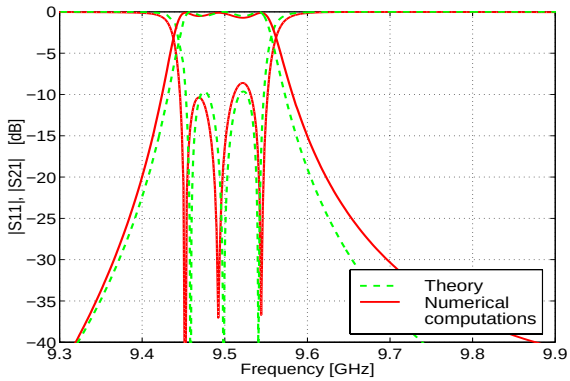

(b)

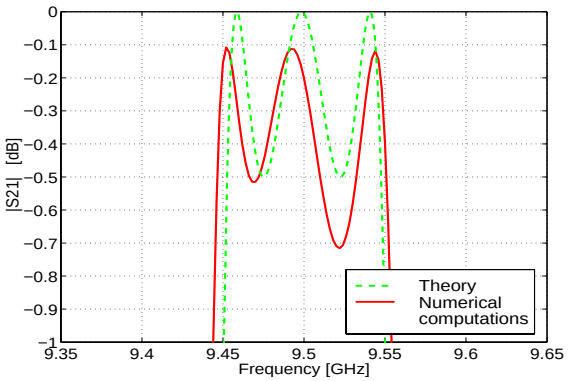

(c)

Figure 4.24: *(a) Filter dimensions and parameters of the equivalent circuits used in the HWSIP method for the filter with $f_0 = 9.5GHz$ and fractional bandwidth $w_f = 1\%$. Filter response: (b) general view, (c) detailed view in the pass band.*

Gap length [mm]		Resonator length [mm]		Circuits parameters					
				Z	Value	K	Value	S_{11}	Value
l_1, l_4	12.86	d_1, d_3	11.17	Z_2, Z_4	10.2929	K_{01}, K_{34}	0.3117	S_{11_1}, S_{11_4}	0.8229
l_2, l_3	25.78	d_2	10.89	Z_3	20.3478	K_{12}, K_{23}	0.1179	S_{11_2}, S_{11_3}	0.9725

(a)

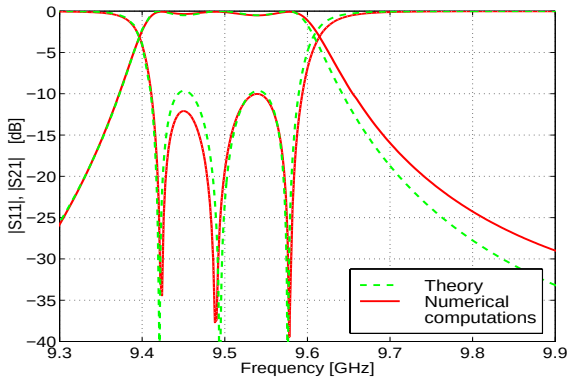

(b)

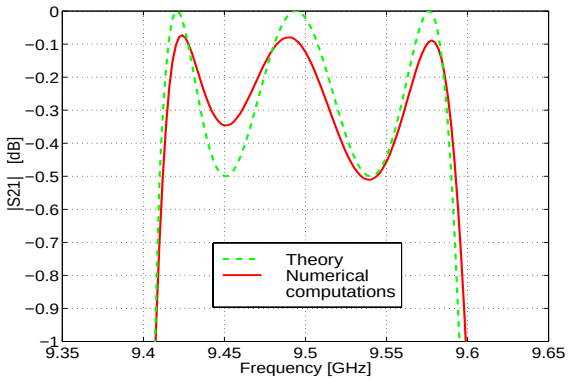

(c)

Figure 4.25: *(a) Filter dimensions and parameters of the equivalent circuits used in the HWSIP method for the filter with $f_0 = 9.5GHz$ and fractional bandwidth $w_f = 1.9\%$. Filter response: (b) general view, (c) detailed view in the pass band.*

Gap length [mm]		Resonator length [mm]		Circuits parameters					
				Z	Value	K	Value	S_{11}	Value
l_1, l_4	7.33	d_1, d_3	11.75	Z_2, Z_4	3.9309	K_{01}, K_{34}	0.5044	S_{11_1}, S_{11_4}	0.5984
l_2, l_3	12.57	d_2	11.47	Z_3	7.2461	K_{12}, K_{23}	0.3197	S_{11_1}, S_{11_4}	0.8145

(a)

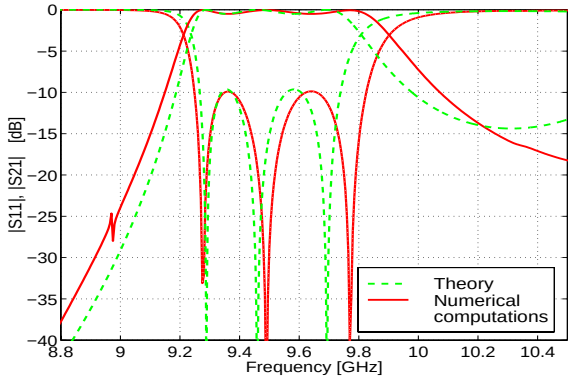

(b)

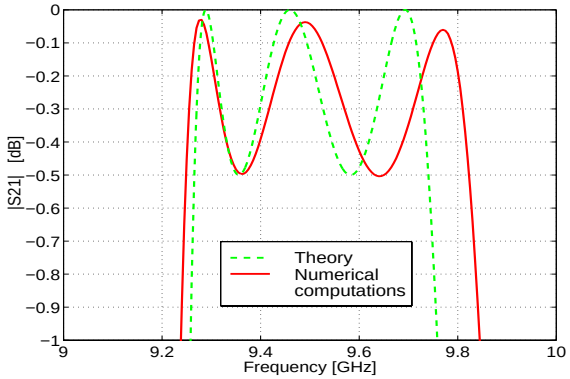

(c)

Figure 4.26: *(a) Filter dimensions and parameters of the equivalent circuits used in the HWSIP method for the filter with $f_0 = 9.5GHz$ and fractional bandwidth $w_f = 5\%$. Filter response: (b) general view, (c) detailed view in the pass band.*

Gap length [mm]		Resonator length [mm]		Circuits parameters					
				Z	Value	K	Value	S_{11}	Value
l_1, l_4	4.15	d_1, d_3	12.39	Z_2, Z_4	2.2438	K_{01}, K_{34}	0.6676	S_{11_1}, S_{11_4}	0.3834
l_2, l_3	5.08	d_2	12.33	Z_3	3.4387	K_{12}, K_{23}	0.6142	S_{11_1}, S_{11_4}	0.4521

(a)

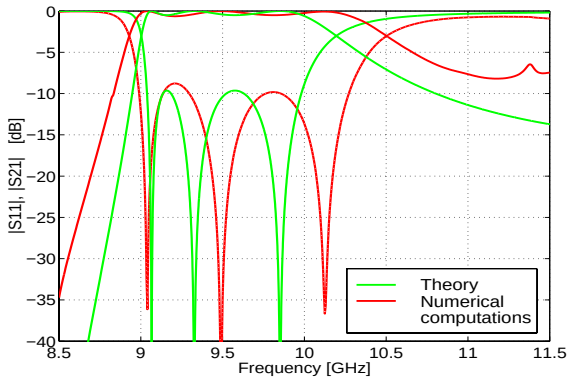

(b)

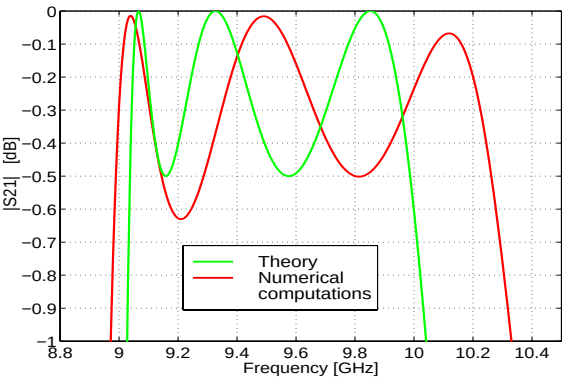

(c)

Figure 4.27: *(a) Filter dimensions and parameters of the equivalent circuits used in the HWSIP method for the filter with $f_0 = 9.5GHz$ and fractional bandwidth $w_f = 10\%$. Filter response: (b) general view, (c) detailed view in the pass band.*

4.3.2.3 Comparison of the designs

The results of the numerical verification of the Chebyshev type filters designed using low-pass and half-wave step-impedance prototypes are summarized in Tables 4.2 to 4.5. The definitions of center frequency and relative bandwidth errors are given by the equations (4.27) and (4.25). These errors, for the investigated filters, are plotted in Fig. 4.28.

Method	f_0 [GHz]	Δf_0 [GHz]	Δf_0 [%]	w_f [GHz]	w_f [%]	Δw_f [%]
Low pass prototype	9.398	0.102	1.077	0.094	1.0	< 0.01
Half-wave step-impedance prototype	9.499	0.001	**0.002**	0.104	1.098	$<$ **0.01**

Table 4.2: *Results of the two method used to design the filter with* $f_0 = 9.5GHz$ *and bandwidth* $w_f = 1\%$ *(0.095 GHz).*

Method	f_0 [GHz]	Δf_0 [GHz]	Δf_0 [%]	w_f [GHz]	w_f [%]	Δw_f [%]
Low pass prototype	9.392	0.108	1.136	0.16	1.7	0.2
Half-wave step-impedance prototype (HWSIP)	9.499	0.001	**0.015**	0.181	1.902	$<$ **0.01**

Table 4.3: *Results of the two method used to design the filter with* $f_0 = 9.5GHz$ *and bandwidth* $w_f = 1.9\%$ *(0.1805 GHz).*

Method	f_0 [GHz]	Δf_0 [GHz]	Δf_0 [%]	w_f [GHz]	w_f [%]	Δw_f [%]
Low pass prototype	9.42	0.08	0.81	0.509	5.41	0.41
Half-wave step-impedance prototype	9.532	0.032	**0.33**	0.574	6.02	1.02

Table 4.4: *Results of the two method used to design the filter with* $f_0 = 9.5GHz$ *and bandwidth* $w_f = 5\%$ *(0.475 GHz).*

Method	f_0 [GHz]	Δf_0 [GHz]	Δf_0 [%]	w_f [GHz]	w_f [%]	Δw_f [%]
Low pass prototype	9.51	0.01	0.14	1.124	11.82	1.82
Half-wave step-impedance prototype	9.60	0.1	1.1	1.27	13.26	3.26

Table 4.5: *Results of the two method used to design the filter with* $f_0 = 9.5GHz$ *and bandwidth* $w_f = 10\%$ *(0.95 GHz).*

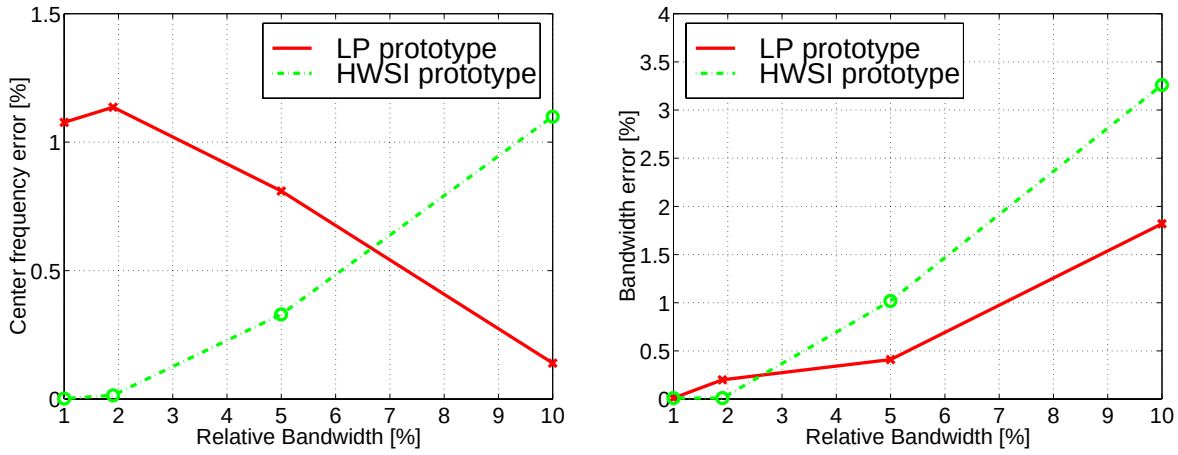

(a) (b)

Figure 4.28: *Results of the 3 section filters with* $f_0 = 9.5$ *GHz: (a) center frequency error, (b) fractional bandwidth error.*

Results for narrow bandwidths. For narrow bandwidths the center frequency error is very small (up to 0.3 % at 5% bandwidth) when the half-wave step-impedance prototype is used. In the case of the low pass prototype a significant shift of center frequency towards lower frequencies and greater center frequency error of 1% level are observed. Also, the bandwidth of the narrow band is better approximated for the HWSIP design ($\Delta w_f < 0.01$ % for 1.9% bandwidth) than for the LPP design (corresponding $\Delta w_f = 0.2$). Nevertheless, the bandwidth error is at relatively low level in both method. The ripple level does not fall below the specified -0.5 dB level for nearly all filters. Only do the filters with 1% bandwidth slightly exceed -0.5 dB ripple level for some frequency points. The LPP filter has a maximal ripple level equal -0.87 dB at $f = 9.42$ GHz (Fig. 4.21) and for the HWSIP filter it is -0.72 dB at $f = 9.55$ GHz (Fig. 4.24). Looking at the plots one can notice that the simulated results never reach the 0 dB level in the pass band. For narrow band filters the Q factor of the resonators is high, therefore the simulation time of the FDTD method should be much more longer in order to calculate filter response with sufficient accuracy.

Results for wide bandwidths. The results for 10% and possibly wider bandwidth should be discussed separately. The center frequency error decreases for LPP method and rapidly increases for HWSIP method. The bandwidth errors increase for both methods. A closer investigation of the filter dimensions shows that the gap lengths for both filters are significantly smaller than for the filters with narrower bandwidths. For smaller gaps the guides couple via higher order modes. Fields of these modes, although attenuated in the gap, can reach the second end of the gap. Both design methods neglect higher order modes. As a result one gets much worse filter responses.

Concluding remarks. In general, the results show, that the predicted and obtained values of center frequency are in very good agreement for the HWSIP method. Compared with the LPP method the advantage of the HWSIP method in this area is visible. The bandwidth error is on the same low level for both methods. As expected, the errors increase for wider bandwidths for both methods.

The limits of application of the HWSIP method depend on various factors such as the NRD-guide parameters, frequency band, center frequency, required accuracy. For the guide and center frequency selected in tests (both are considered to be typical), the application of the method with half-wave step-impedance prototype to design the filters is limited by the maximum 10 % bandwidth, assuming that the maximal center frequency error is allowed to be at 1% level. For such bandwidths, the HWSIP method allows one to build the filters with acceptable parameters. It should be highlighted here that preserving the accuracy of center frequency, the bandwidth error of the HWSIP method can be significantly reduced by incorporating scaling factor into procedure.

In general, the results obtained for filters with relatively wide bandwidths should be treated with special attention because, in some cases, the results could be highly inaccurate.

4.4 Numerical verification of method with half-wave step-impedance prototype

The previous section showed that the HWSIP method gives, in general better results than the LPP method. To investigate the method a little further many filtering structures with Chebyshev and maximally flat response have been designed. The number of filter sections n was treated as a parameter varied from $n = 2$ to $n = 5$. The fractional bandwidths were 1%, 1.9%, 5% and 10%. Two types of the filter response have been investigated:

- **Chebyshev (equiripple) response.** For this response the tested filters had the pass band ripple level L_{A_r} equal 0.1 dB and 0.5 dB and the attenuation level L_{A_e} of 0.1 dB, 0.5 dB at the band edge frequency.

- **Maximally flat (Butterworth) response.** The filters with maximally flat response were tested for $L_{A_e} = 3dB$ at band edge frequency.

The center frequency f_0 was assumed at 9.5 GHz for all filters. The numerical verification of the filter designs was carried out using the FDTD software, the parameters of each

design were compared with the corresponding theoretical predictions. To determine the range of applicability of the synthesis method, the relative bandwidth error and the relative center frequency error have been computed. The definitions of these errors are given by the equations (4.25) and (4.27). The errors are plotted versus the relative bandwidth. The NRD-guide used in the design is the same as for the filters discussed in section 4.3.2.

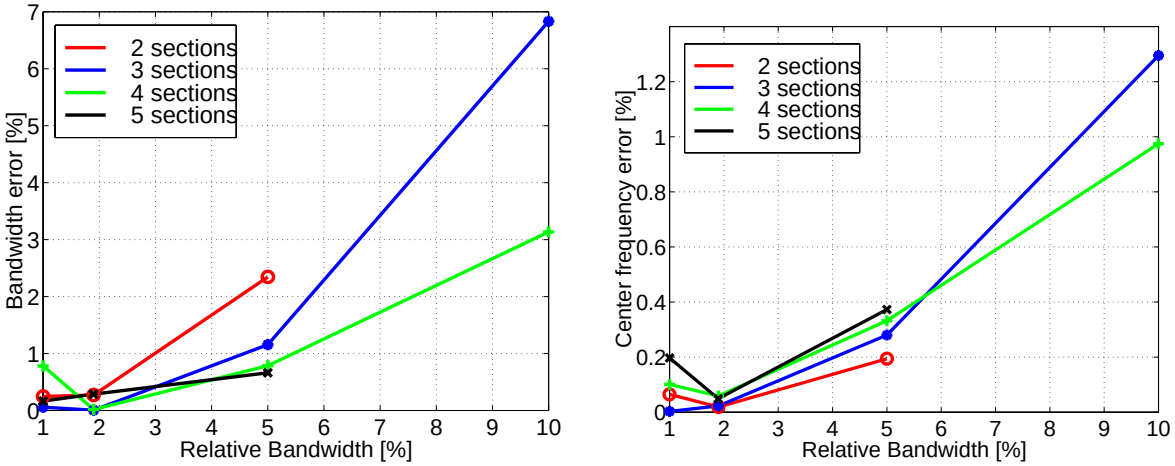

(a) (b)

Figure 4.29: *Numerical results for NRD-guide bandpass filters: (a) relative bandwidth error and (b) relative center frequency error. Filter parameters: Chebyshev response, 2–5 sections, $f_0 = 9.5$ GHz, ripple level $x = 0.1$ dB.*

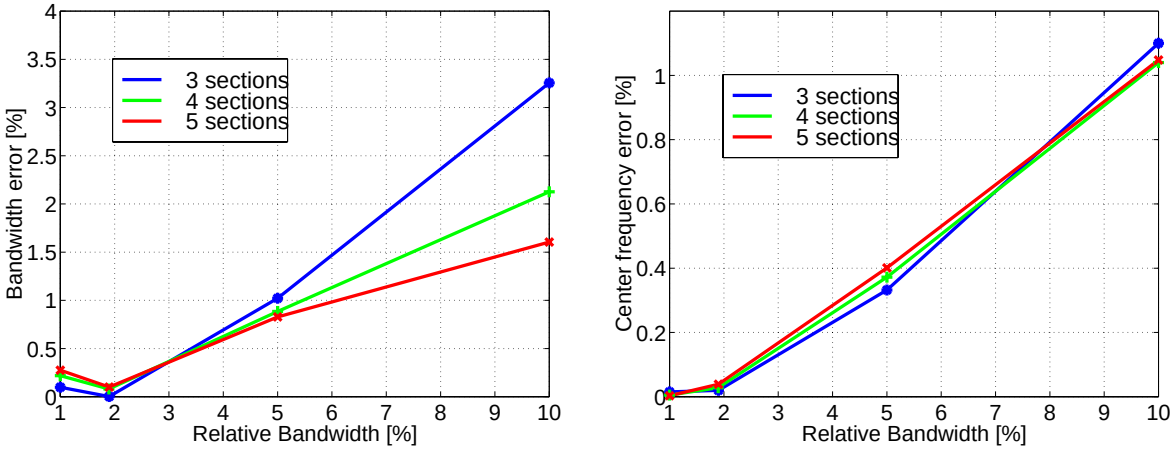

(a) (b)

Figure 4.30: *Numerical results for NRD-guide bandpass filters: (a) relative bandwidth error and (b) relative center frequency error. Filter parameters: Chebyshev response, 3–5 sections, $f_0 = 9.5$ GHz, ripple level $x = 0.5$ dB.*

Results for Chebyshev response. For the bandwidths up to 5% the Δw_f is on the level of 0.5 % for Chebyshev designs having 0.1dB and 0.5dB ripple level (Fig. 4.29 (a) and Fig. 4.30 (a)). The error reaches its lower limit of about 0.1 % or even less for 1.9% bandwidth for all discussed designs. For the increased values of bandwidth, the error becomes higher. The higher number of section n the filter has, the lower bandwidth error is observed, especially for wider bandwidths. Almost for every design the method assures the bandwidth error less than or equal to 1% for the designs with bandwidth up to 5%. The error rises to 2.4% at 5% bandwidth (Fig. 4.29 (b)) only for the 2 section 0.1dB design.

For both Chebyshev cases, the center frequency error Δf_0 slightly exceeds the 1% level only for a few designs with $w_f = 10\%$. The accuracy of the method is very high for the narrow-band designs. The Δf_0 is below 0.4 % level for almost all Chebyshev designs with relative bandwidth up to 5%. A special attention should be paid for the bandwidth around 2%. In this region the error falls below 0.1 %. In contrast to the bandwidth error, the Δf_0 does not depend on the number of filter sections. This effect is clearly seen in Fig. 4.30 (b).

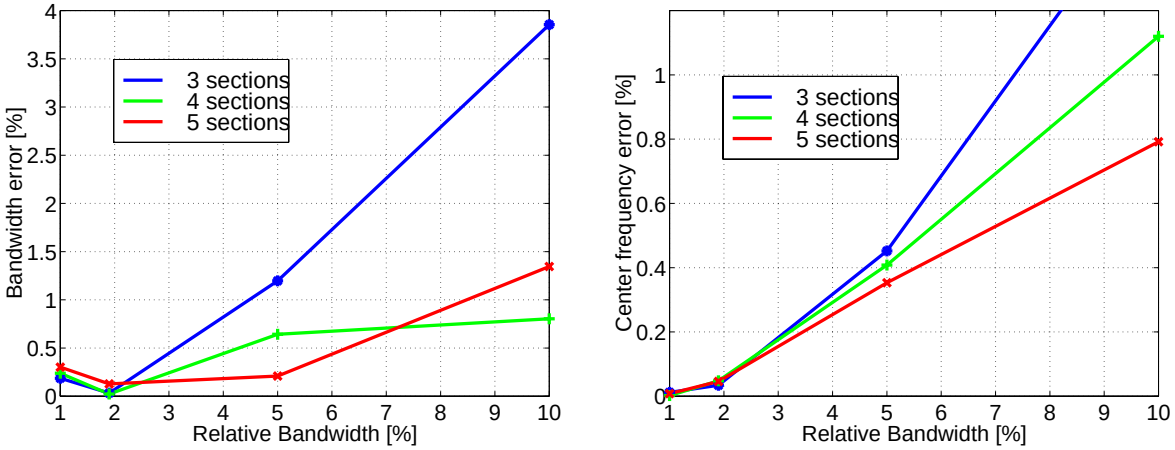

Figure 4.31: *Numerical results for NRD-guide bandpass filters: (a) relative bandwidth error and (b) relative center frequency error. Filter parameters: maximally flat response, 3–5 sections, $f_0 = 9.5$ GHz, band edge attenuation level $x = 3$ dB.*

Results for maximally flat response. Slightly different results are observed for the designs with maximally flat characteristics. The relative bandwidth error does not go beyond 1% level for the majority of the designs which have bandwidth in the range 1% to 5% (Fig. 4.31 (a)). Similarly to the Chebyshev case, Δw_f falls down to 0.2 % level or even less, for bandwidth of around 2%.

The center frequency error increases when the bandwidth becomes greater. Nevertheless, for almost all designs it does not rise above the 1% level. For narrow bandwidths Δf_0 has values lower than 0.5 % and reaches the maximum value at 0.4 % level for 5% relative bandwidth. The results obtained for the designs with bandwidth lower or equal 2% appear to be very good. For these designs the Δf_0 error is lower than 0.05 %. In contrast to the

Chebyshev designs, the accuracy of the method depends on the number of sections of filter. The filters with higher n have not only lower level of Δf_0 but also lower level of bandwidth error (Fig. 4.31 (b)).

Conclusions. The results of the discussion presented above can be summarized as follows.

- The high accuracy of the center frequency design is one of the important advantages of the method with HWSIP.
  - The Δf_0 does not exceed 1% for the majority of the designs, for both Chebyshev and maximally flat responses.
  - Extremely low level of center frequency error ($\Delta f_0 \leq 0.1\%$) is observed for almost all designs with narrow bandwidth (up to 2%)
  - The center frequency error is practically independent of the number of filter sections for the Chebyshev designs, while for the filters with maximally flat response the influence of n can be noticed only for wider bandwidths.
- The accuracy of the bandwidth in the HWSIP method is good for narrow bandwidth and decreases for larger bandwidths for all cases.
  - For both the Chebyshev and maximally flat cases, the bandwidth error does not exceed 1% level for almost all designs.
  - The improvement in bandwidth error is observed when the number of filter sections n is increased. This effect appears for the Chebyshev and maximally flat designs.

4.5 Experimental verification of the method with the half-wave step-impedance prototype

The comparison of filter design methods was based purely on numerical analysis. In order to investigate the level of confidence in these results, two filters working in X-band have been designed, manufactured and measured. The method with half-wave step-impedance prototype has been used to design the filters with Chebyshev and maximally flat characteristics. The NRD-guide used to construct the filters is the same as for the filters discussed in previous sections. Detailed parameters of the NRD-guide used can be found in section 2.4.4.

The vector network analyzer *Wiltron 37269A* has been used to perform the measurement. For each filter the cascade composed of two NRD-guide to rectangular waveguide transitions and the filter has been measured. The parameters of the transitions have been determined by applying the TRL calibration procedure. Then the filter parameters have been de-embedded from the measured data. The detailed description of measurement techniques used in the experimental verifications is outlined in appendix B.

Figure 4.32: *The NRD-guide filter designed using the HWSIP method. Filter parameters: Chebyshev characteristic type, 3 sections, $f_0 = 9.5$ GHz, ripple level $x = 0.5$ dB, bandwidth $w_f = 1.9\%$.*

The results obtained from measurements include the transmission losses inserted by the filter. To account for this, the level of the losses was calculated as follows. The transmission losses of the filter structure are caused by lossy dielectric and lossy conducting plates. In the investigated frequency band the total loss of an NRD-guide are caused mainly by the lossy dielectric, while the conductor losses are more than order of magnitude smaller (Fig. 2.18 in section 2.4.4). Therefore, only the losses introduced by dielectric resonators are taken into account and the conductor losses introduced by the parallel plate sections are neglected (see section 2.4 for detailed discussion about losses).

In order to compare the experimental results with theoretical predictions the losses introduced by the dielectric into the measured filter are subtracted from the measured characteristics. Then, for the obtained results, the bandwidth error and center frequency error of the filter are determined.

4.5.1 Results for filter with Chebyshev response

The results obtained from the HWSIP design for the Chebyshev filter with 3 sections, 1.9% bandwidth, 0.5 dB ripple level and $f_0 = 9.5$ GHz are listed in Table 4.6. The filter responses obtained from measurements are presented in Fig. 4.33 together with theoretical and simulated results.

The numerical results satisfy design specification very well, $\Delta f_0 < 0.02$ % and $\Delta w_f < 0.01$ %. Also very good agreement between theory and experimental results is observed (Table 4.6). The center frequency error equals only 0.05 % and the bandwidth error is at 0.03 % level.

The measurement plots include transmission losses of the filter structure, therefore the

theoretical approximation of the filter losses is also plotted. The agreement between theoretical loss prediction and the measured values is very good. In both cases the losses inserted by the filter are on the 0.25 dB level.

Verification method	f_0 [GHz]	Δf_0 [GHz]	Δf_0 [%]	w_f [GHz]	w_f [%]	Δw_f [%]
Numerical results (FDTD software)	9.499	0.001	**0.015**	0.181	1.902	$<$ **0.01**
Measurement results (+loss correction)	9.504	0.004	**0.05**	0.183	1.93	**0.03**

Table 4.6: *Results of the numerical and experimental verification for the filter design using HWSIP method with Chebyshev response. Filter has the center frequency* $f_0 = 9.5GHz$ *and bandwidth* $w_f = 1.9\%$ *(0.1805 GHz).*

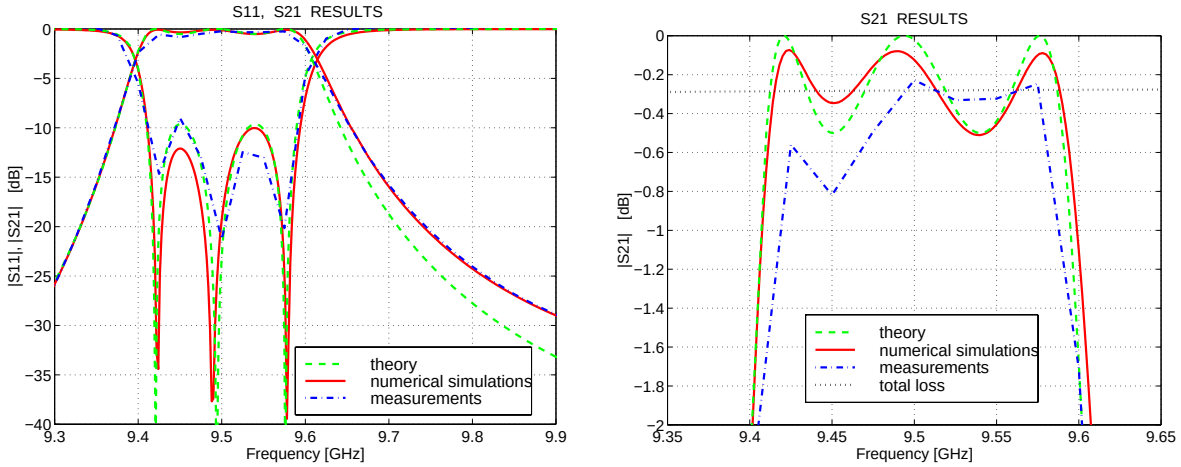

(a) (b)

Figure 4.33: *Numerical simulation and experimental results of the 3 section filter with* $f_0 = 9.5$ *GHz fractional bandwidth* $w_f = 1.9\%$*: (a) general view, (b) detailed view. The HWSIP method and FDTD software were used to design the filter.*

4.5.2 Results for filter with maximally flat response

For the maximally flat filter with 3 sections and 1.9% bandwidth the HWSIP design procedure gives the circuits parameters and filter dimensions presented in Table. 4.7. The filter responses: determined theoretically, computed numerically and the measured one are plotted in Fig. 4.34.

Gap length [mm]		Resonator length [mm]		Circuits parameters					
				Z	Value	K	Value	S_{11}	Value
l_1, l_4	10.23	d_1, d_3	11.29	Z_2, Z_4	6.5066	K_{01}, K_{34}	0.3902	S_{11_1}, S_{11_4}	0.7336
l_2, l_3	27.02	d_2	10.87	Z_3	12.745	K_{12}, K_{23}	0.1098	S_{11_3}, S_{11_2}	0.9762

Table 4.7: *Filter dimensions and parameters of the equivalent circuits of the 3 section maximally flat filter with $f_0 = 9.5GHz$ and $w_f = 1.9\%$. The HWSIP method and FDTD software were used to design the filter.*

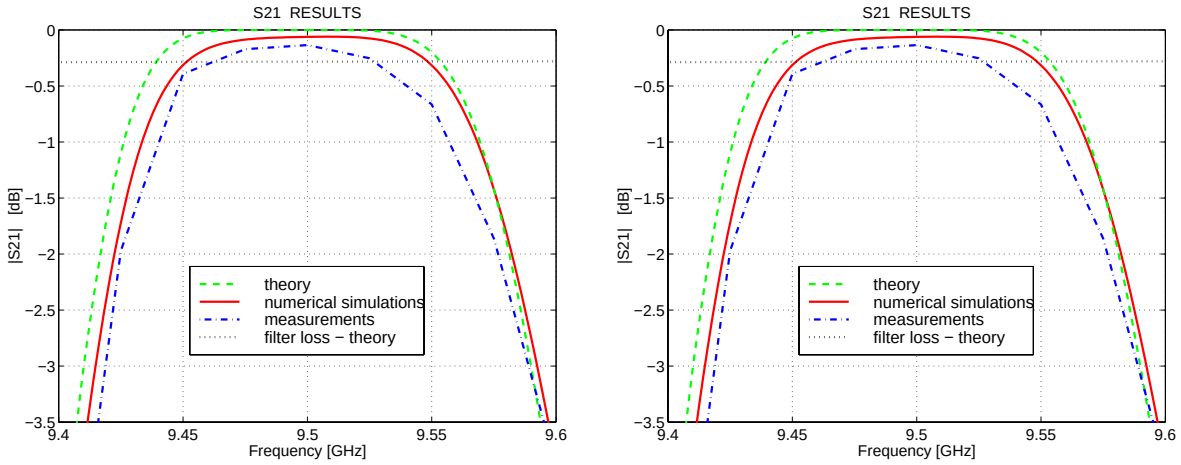

(a) (b)

Figure 4.34: *Numerical simulation and experimental results of the 3 section maximally flat filter with $f_0 = 9.5$ GHz and $w_f = 1.9\%$. The procedure with step-impedance half-wave prototype and FDTD software were used to design the filter.*

Verification method	f_0 [GHz]	Δf_0 [GHz]	Δf_0 [%]	w_f [GHz]	w_f [%]	Δw_f [%]
Numerical results (FDTD software)	9.503	0.003	**0.03**	0.177	1.86	**0.04**
Measurement results(+ loss correction)	9.504	0.004	**0.042**	0.177	1.86	**0.035**

Table 4.8: *Results of numerical and experimental verification of filter with maximally flat response, center frequency $f_0 = 9.5GHz$ and bandwidth $w_f = 1.9\%$ (0.1805 GHz).*

The agreement between the theory and measurement is very good. The shift of center frequency is less than 0.05 % and the bandwidth error is equal 0.035 % (Table 4.8). Also the numerically computed results fit well theoretical characteristics. The center frequency error Δf_0 is equal 0.03 % and the relative bandwidth error $\Delta w_f = 0.04$ %. The theoretical curves for transmission are in good agreement with the numerically computed ones. The reflection curve of measured filter has its maximal value -26.5 dB at 9.475 GHz and illustrates higher reflection of the filter in the passband than the predicted one, especially in the higher part of passband of the measured filter. This discrepancy is caused mainly by imperfect mechanical realization of the filter, nevertheless the reflections are kept on the acceptable level in the pass band.

The theoretically predicted losses are at the 0.28 dB level, while the measurement losses of the de-embedded filter are even smaller and equal 0.14 dB (Fig. 4.34 (b)). This disagreement is caused by inaccurate determination of the transitions parameters. The measurement results are de-embedded from the cascade transition - filter - transition using TRL calibration method. However, for this experiment the calibration data obtained at earlier measurements were used to determine the transition characteristics. For each measurement the transitions had to be re-mounted therefore their parameters may slightly vary due to inaccuracies in the mechanical fixing.

Chapter 5

Conclusions

The rapid development of the systems located at millimeter waves generates need for new technologies which enable construction of complete integrated circuits designed to work in commercial systems. One of the promising technologies is the NRD-guide technology, therefore in this thesis the methods of designs and analysis of selected passive elements built in this technology are investigated.

At the beginning of this thesis the parameters of an NRD-guide are described and simple NRD-guide discontinuity, used in bandpass filter design, is analyzed. Then, in the main part of the work, the method of design of selected passive elements such as transition from an NRD-guide to a rectangular waveguide, NRD-guide bandpass filters and NRD-guide couplers are proposed. The results of the research are summarized in the followed paragraphs.

NRD-guide. An NRD-guide is an semi-open structure, therefore, the preferable CAD software, suitable to analysis NRD-guide components, should have the absorbing boundary conditions implemented in order to obtain accurate results. However, very often in the CAD software, only closed structures can be analyzed and the NRD-guide structure has to be limited by inserting lateral PEC or PMC. In such case the knowledge of the distance d between a dielectric slab and the closing walls which assures accurate results is essential. In this work the influence of the closing walls position on the computation accuracy of the NRD-guide parameters such as phase constant and impedance has been investigated. Because no practical and universal remarks, devoted to this problem, can be found in the literature, the author proposed determination of d in terms of the guide wavelength of the LSM_{11} mode, the operating mode used in the NRD-guide. Such selection has additional advantage because it assures accurate results also for lower order LSE modes. Although these modes are usually treated as the parasitic ones, they are taken into consideration in analysis of some passive elements. The results of the author research showed, that the distance $d = \lambda_g/2$ assures the computation of the phase constant and both considered impedance types (i.e. wave and characteristic power-voltage impedances) with the relative error below 0.1 % level. This results are valid for the LSM_{11}, LSE_{11} and LSE_{10} ("distorted" TE_{10}) modes guided in a typical NRD-guide as well as for both types of the lateral screens.

When a simple air gap discontinuity, used in construction of NRD-guide filters, is considered, d have to be increased due to the scattering of the mode fields. It has been shown

that $d = 3\lambda_g/4$, where λ_g refers to the LSM_{11} mode, is sufficient to obtain accuracy better than 0.1 % when the magnitude and phase of scattering parameters are computed using the CAD software.

Although the formulae for transmission losses for selected modes have been published in earlier works, in this thesis the general formulae for calculation of dielectric and conducting losses of the LSM and LSE modes are provided. Then the losses of the typical NRD-guides working in the X and U-bands have been investigated. It has been shown that in the X-band the conducting losses can be neglected while in the higher frequency regions, such as U-band, both loss components have to be considered. Such observation simplifies the analysis and interpretation of the results obtained from measurements of the trial circuits which are usually built in lower frequencies (e.g. X-band) due to lower cost, easier manufacturing and higher availability of measurement systems.

Transition between a rectangular waveguide and an NRD-guide. The transition between a rectangular waveguide and NRD-guide has been designed in order to allow one the measurements of manufactured trial passive elements. In earlier works the classical TEM procedure using the wave impedance definition has been applied to design such transition. In this work the application of the characteristic power-voltage impedance has been proposed by the author. As a result, the transition with significantly better parameters has been achieved. The improvement for the typical NRD-guide designed for X-band of about 5-7 dB has been achieved when the results are compared with the designs where the wave impedance definition has been used. Nevertheless, the more thorough investigation of the method shows that its area of application is limited. This is because the NRD-guide supports only non-TEM modes. Although the additional phase correction procedure has been applied to the design in order to account the dispersive nature of the modes guided in the NRD-guide, it is practically impossible to achieve the results which assure matching better than 25-30 dB in the selected frequency band. This results has to be regarded as quite satisfactory since it is at the same level as for other types of transitions between non-TEM lines reported in literature [88].

On the other hand, the importance of application of a design procedure is presented. The results of the multimode analysis carried out in this thesis show, that the non-optimized transition with linear profiles possesses higher input reflection coefficient (by about 10-15 dB) and it does not assure the required conversion from the TE_{10} mode to the LSM_{11} mode. It has been observed, that in such example transition the parasitic LSE_{11} mode is excited and up to 35 % of the energy can be transferred to this mode.

In the practical measurement systems the parameters of the manufactured transitions have to be determined in order to obtain accurate results of a measured device. Therefore, the application of the TRL calibrating procedure to the NRD-guide technology has been proposed in this work. By the best author knowledge the TRL procedure is the first time applied to the NRD-guide technology. The procedure assures high accuracy and has several advantages such as an easy numerical implementation and simple construction of standard calibration circuits. For a typical NRD-guide working in the X-band a calibration kit has been developed and the related software has been created. Accordingly, the determination of

the manufactured transitions has been possible. Moreover, with the transitions parameters in hand, the application of the classical de-embedding procedure allows one to obtain the parameters of the measured device.

NRD-guide bandpass filters. To design of NRD-guide bandpass filters the method with Low Pass Prototype (LPP) has been used by other authors. In this work another synthesis method is proposed. The NRD-guide band pass filter configuration is similar to the E-plane waveguide bandpass filters. Such filters has been designed with high accuracy using the method with Half-Wave Step-Impedance Prototype (HWSIP). This was a rationale for selecting this method to design NRD-guide filters. To the best author knowledge this method has not been applied yet to the NRD-guide technology. When compared to the LPP method the HWSIP method gives better results in the center frequency design. It has been shown that for several narrow band designs the relative center frequency error falls down below 0.01 % error level, which is significantly better than in the LPP method. Also, for wider pass bands, accuracy in center frequency design is very high and more accurate than in the LPP method. It has to be noted that the relative bandwidth error is slightly greater than in the LPP method, but this drawback can be eliminated by applying a simple correction factor. The factor can be easily determined because the HWSIP method is very accurate in center frequency design. On the contrary for the LPP method the computation of such correction factor is rather difficult and depends on various coefficients.

Both methods use synthesis procedures and assume that the parameters of the discontinuities, appearing in the filter structure, are known. In this work the FDTD software is used to determine them. This selection of the software enables the generation of large data set in one software run. It allows one the design the filters having different center frequencies using the same data set.

The accuracy of the HWSIP method has been investigated thoroughly in order to determine the limits of application of this method to NRD-guide filter design. Therefore, numerical test have been performed for a large number of filter designs with different filter response, various relative bandwidth and number of sections. It is shown that for narrow band designs ($\leq 5\%$) the HWSIP method yields very good results. The accuracy of the method decreases when filters with wider bandwidths are considered [1].

The numerical results obtained using the HWSIP method were verified experimentally and very good agreement between theory and measurements was obtained.

NRD-guide couplers. Several aspects concerning NRD-guide couplers have been presented by the author in other publications. In this work the complete design procedure and several practical remarks are presented. The main advantage of the described procedure is simplicity of it application and low numerical costs. Moreover, the procedure allows one to design the couplers with different topologies.

Concluding remarks. This thesis shows that the selected passive elements built in NRD-guide technology can be designed using simple procedures. The procedures are characterized by very low numerical costs and require the usage of numerical methods only to

[1] The same is true for the LPP approach. Both methods fail because higher order modes interaction is neglected and large bandwidths imply small distance between discontinuities.

characterization of standard elements. The presented approaches gives good results when applied to design NRD-guide couplers and transitions between an NRD-guide and a rectangular waveguide. Very good results have been achieved in the design of bandpass filters. Selected design of filters, transitions and couplers have been verified experimentally validating the accuracy of the proposed techniques.

Appendix A

Proximity NRD-guide couplers

A.1 Introduction

Often encountered in the communication systems working in the millimeter-wave frequencies are the circuits which use directional proximity couplers. Such couplers built in the NRD-guide technology have been studied extensively by the author and the details on this subject can be found in other publications written by the author (i.e. report [107], master thesis [108] and the articles [24] [109]). In this appendix only the most important facts concerning NRD-guide couplers are collected together and the complete design procedure of them is briefly described. The theoretical results are verified experimentally in the K-band.

The NRD-guide couplers have several characteristics features:

- The relative bandwidth of $2 \div 10$ %. (It is possible to achieve the bandwidth of order 30 % by some simple modification of a basic structure.)
- Scalable coupling factor. Theoretically, the coupling factor is allowed to have any value. In real structures the most common value is -3 dB, rarely -6 dB or -20 dB.
- No radiation losses at the discontinuities and bends and small transmission losses.
- Large geometrical dimensions compared to the guided wavelength or the size of the active elements. This simplifies the fabrication.
- Simple, stable and compact mechanical construction.
- Easy technology of manufacturing with not restrictive tolerance requirements (cross-sectional dimensions of a coupler are of the order of several millimeters). It allows fast, massive and cheap production of couplers.

The above features made NRD couplers attractive in the constructing of low cost mixers [110], integrated transmitters and receivers [8] and antenna systems [23]. In the sections below the results of the numerical and experimental investigation of selected NRD coupler structures are presented.

A.2 Design of dielectric waveguide proximity couplers

The design procedure can be divided into the following steps.

Step 1. In order to design a proximity coupler one has to specify the coupler's parameters. First, the required coupling factor at center frequency f_0 is chosen. Then, the coupler structure and the guide type together with guide dimensions suitable for the selected frequency are selected. Finally, the parameters which can vary in the design are determined. They can be changed if the design procedure is repeated. These parameters are the minimal distance d_0 between guides and the parameters describing the coupler structure. For an example asymmetrical coupler investigated in the section follows, the coupler structure is determined by the radius R of the coupler branch (see Fig.A.2 (a)). Usually, the coupler structure and geometry is determined at the beginning and subsequently the distance d_0 which assure desired coupling factor is searched at a given frequency.

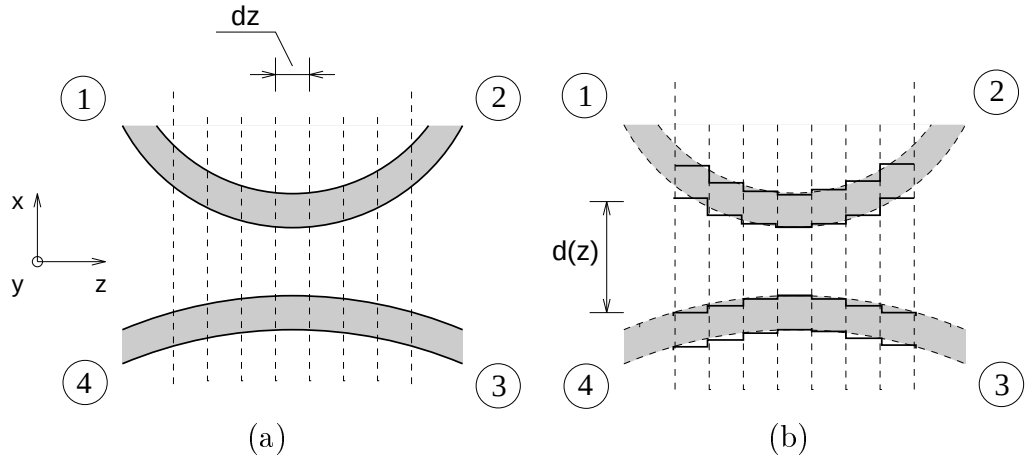

Figure A.1: *The method of analysis : (a) studied structure divided into segments, (b) analyzed equivalent structure.*

Step 2. To determine coupler characteristics one has to find its scattering matrix $\underline{\underline{S}}$. To this end, the coupler structure is divided into segments with uniform length dz (Fig.A.1 (a)). We assume that the distance between guides d in each segment is constant and known (Fig.A.1 (b)). The ideal matrix $\underline{\underline{S}}^i$ for each segment can be written as follows

$$\underline{\underline{S}}^i = \begin{pmatrix} 0 & S^i_{21} & S^i_{31} & 0 \\ S^i_{21} & 0 & 0 & S^i_{31} \\ S^i_{21} & 0 & 0 & S^i_{31} \\ 0 & S^i_{21} & S^i_{31} & 0 \end{pmatrix} \tag{A.1}$$

where

$$S_{21} = e^{-j(\frac{k^i_{ze}+k^i_{zo}}{2})dz} \cos(C^i dz) \tag{A.2}$$

$$S_{31} = -je^{-j(\frac{k^i_{ze}+k^i_{zo}}{2})dz} \sin(C^i dz). \tag{A.3}$$

To determine S^i_{21} and S^i_{31} we must know the coupling coefficient C^i between two parallel guides in each segment. Using the coupled mode method [111] one can express the coupling coefficient C^i as

$$C^i = \frac{k^i_{z_e} - k^i_{z_o}}{2} \tag{A.4}$$

where $k^i_{z_e}$ and $k^i_{z_o}$ are the longitudinal wavenumbers in the analyzed segment for the even and odd mode respectively. There are fundamental modes of the coupled guides and an interaction between them creates the coupling effect in coupled guides. The method of the computation of the wavenumbers k_{z_e} and k_{z_o} depends on the investigated guide type. For the NRD-guides the transverse resonance method can be applied. The scattering matrix $\underline{\underline{S}}$ of a whole structure is determined by cascading matrices for component sections. To calculate this matrix we use the transmission matrix formalism. It allows one to calculate the total characteristics of a chain consists of elements with length dz each. The total transmission matrix T is expressed by

$$\underline{\underline{T}} = \underline{\underline{T}}^1 \times \underline{\underline{T}}^2 \times \cdots \times \underline{\underline{T}}^{n-1} \times \underline{\underline{T}}^n. \tag{A.5}$$

The parameters of global matrix $\underline{\underline{S}}$ of a coupler are then given by

$$S_{21} = T_{33} \tag{A.6}$$

$$S_{31} = T_{34}. \tag{A.7}$$

Step 3. Having determined the matrix S of the coupler one can determine its transmission characteristics. The step 2 can be repeated for selected values of d_0 yielding the dependency of the coupling factor versus d_0 at given frequency which allows one to find the desired value of d_0. Another possible design procedure is to keep the d_0 constant changing the geometry of the coupler structure (in the cited example the radius R shall be changed).

The application of the presented procedure to the NRD-guide couplers is presented in the next section.

A.3 Design of NRD-guide couplers

A typical structure of an asymmetrical NRD-guide coupler is shown in Fig. A.2 (a). The structure consists of straight and curved NRD-guides. The coupled NRD-guide is a simple development of a single non-radiative guide structure [26]. It consists of two rectangular section dielectric rods (permittivity ϵ_r) separated by distance d and sandwiched between conducting plates (Fig. A.2 (b)). Similar to a single NRD-guide the modes of a coupled guide can be divided into two groups of hybrid modes denoted as $LSM^x_{e/o}$ and $LSE^x_{e/o}$ modes [65]. Indices e and o mean that the field variation in central air region is described by an even or odd function of x.

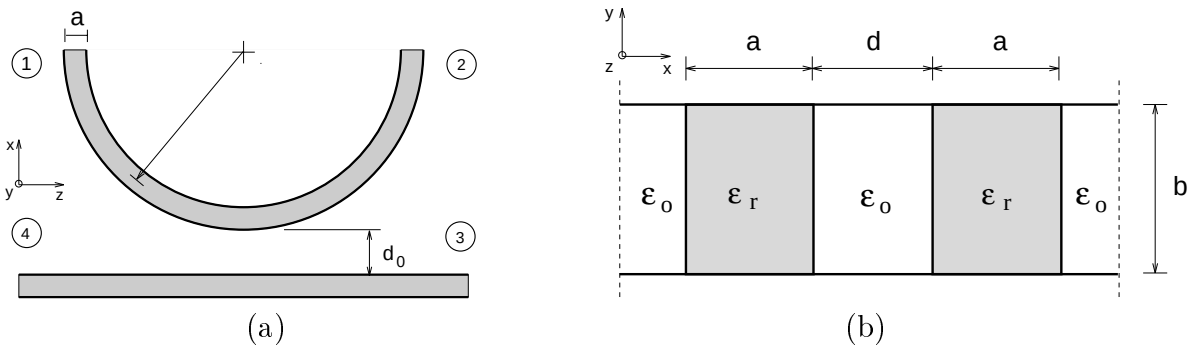

Figure A.2: *(a) The structure of the NRD-guide asymmetrical coupler. (b) Cross-section of coupled NRD-guide.*

As described in step 2 of the design procedure presented in previous section, in order to determine the scattering matrix $\underline{\underline{S}}$ of single section of coupler we have to calculate coefficient C, given by (A.4). This requires the knowledge of the longitudinal wavenumbers k_{z_e} and k_{z_o} of the fundamental modes in each coupler section. The propagation characteristics of the NRD-guide we can calculated using the transverse resonance method (TRM) [56] which is a method particularly suitable for the analysis of layered waveguides.

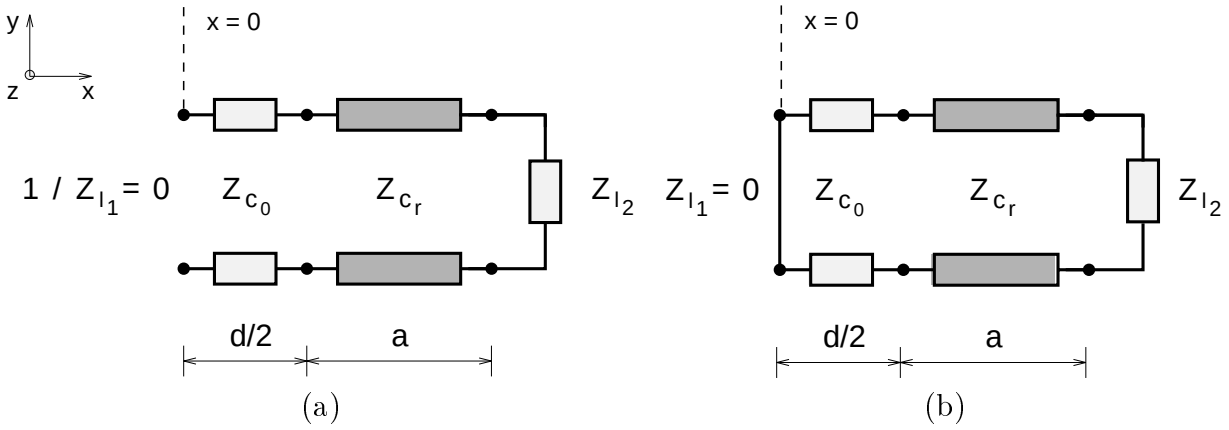

Figure A.3: *The equivalent circuits for coupled NRD-guide: (a) magnetic wall for $x = 0$, (b) electric wall for $x = 0$. Z_{c_0},Z_{c_r},Z_{l_1},Z_{l_2} – wave impedances.*

In general the application of the TRM to the coupled NRD-guide structure can be presented as follows. The cross-section of the multi-layer structure is represented by a transmission line equivalent circuit. Each section of the line in the equivalent circuit corresponds to one layer of the analyzed structure. Investigating the equivalent circuit for the even LSM modes (Fig.A.3) we get the following condition for the resonance

$$\tan k_{x_r} a = \frac{\frac{\epsilon_r \alpha_{x_0}}{k_{x_r}} \left[1 + \coth \frac{\alpha_{x_0} d}{2}\right]}{1 - \left(\frac{\epsilon_r \alpha_{x_0}}{k_{x_r}}\right)^2 \coth \frac{\alpha_{x_0} d}{2}} \tag{A.8}$$

and similarly for the odd LSM modes

$$\tan k_{x_r} a = \frac{\frac{\epsilon_r \alpha_{x_0}}{k_{x_r}} \left[1 + \tanh \frac{\alpha_{x_0} d}{2}\right]}{1 - \left(\frac{\epsilon_r \alpha_{x_0}}{k_{x_r}}\right)^2 \tanh \frac{\alpha_{x_0} d}{2}} \tag{A.9}$$

where α_{x_0} is the attenuation constant and k_{x_r} is the wavenumber, both in the x direction. The relation between k_{x_r} and α_{x_0} can be found using the separability condition for regions with dielectric constant ϵ_r and ϵ_0

$$\omega^2(\epsilon_r - 1)\epsilon_0\mu_0 = \alpha_{x_0}^2 + k_{x_r}^2. \tag{A.10}$$

Finally, the longitudinal wavenumber k_z can be found from the separability condition

$$k_z = \sqrt{\epsilon_r k_0^2 - k_{x_r}^2 - k_{y_r}^2}. \tag{A.11}$$

where

$$k_0 = \omega\sqrt{\epsilon_0\mu_0} \tag{A.12}$$

and the k_{y_r} is the wavenumber in the y direction

$$k_{y_r} = k_{y_0} = \frac{n\pi}{b} \qquad n = 0, 1, 2, ... \tag{A.13}$$

Solving (A.8) and (A.9) for different frequencies and using (A.11) to (A.13) for each section of the coupler we get the dispersion characteristics for k_{ze} or k_{zo} required for the coupling coefficient.

Having determined the coupling coefficient for the coupled NRD-guide guides the characteristics discussed in the step 3 of the procedure can be computed and the dimensions of the desired coupler determined.

A.4 Design example and experimental results

To verify the design method described in the preceding sections, we have designed an asymmetrical coupler (Fig.A.2 (a)) with the following specifications:

center frequency : $f_0 = 30$ GHz
relative 1dB bandwidth : $\Delta f/f_0 \geq 2.5\%$
coupling factor : -3 dB

It was assumed that the dimensions of the NRD-guide designed to work in K-band are: $w = 3.56$ mm, $b = 4.45$ mm, $\epsilon_r = 2.53$; the radius R=40 mm. The numerical analysis showed that the desired specification can be achieved for $d_0 = 1$ mm. The computed frequency behavior are shown in Fig. A.4 (solid lines). The results of experiments are displayed in Fig.A.4 (measured points). Good agreement between theory and experiment was observed. It was numerically simulated and experimentally verified that S parameters of the NRD-guide coupler structures are very sensitive to the d_0 parameter. Therefore, the

slight shift of the characteristics versus the frequency axis can be explained by difficulty in exact adjustment of d_0 in the measured structure (adjustment error ± 0.25 mm).

It can be noted from Fig.A.2 that the numerical analysis predicts two -3dB coupling points. One -3dB coupling point at 30 GHz and a second -3dB point which occurs at 37.5 GHz. The first -3dB coupling point gives a narrower band operation 0.75 GHz or 2.5 %. Much broader bandwidth can be obtained at 37.5 has the bandwidth with maximum 1dB imbalance is 2.8 GHz or 7.5 %.

The experiment confirms the theoretical findings. The measured bandwidth at 30.25 GHz is 2.5 % and at 36.2 GHz it is 7.5 %. These results show that it is possible to design a narrow-band or broadband -3dB coupler by selecting an appropriate -3dB frequency point. The desired value of center frequency can be designed by selecting dimensions and dielectric permittivity of dielectric rod or by changing parameters of a coupler structure d_0 and R. The isolation in the $28 \div 40$ GHz band is of order -35 dB. Some transmission losses were observed caused by dielectric losses of the NRD-guides and imperfect transitions used in measurement. This results in shifting of the measured characteristics, versus the S-parameter axis, towards the lower values.

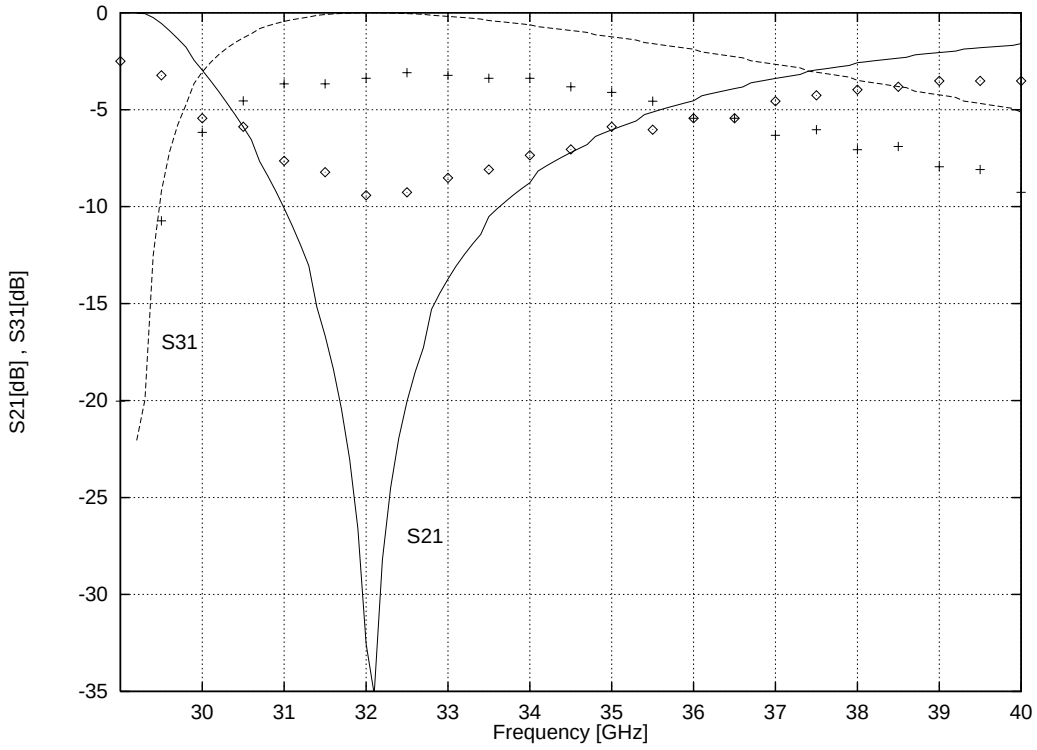

Figure A.4: *Asymmetrical NRD-guide coupler with $d_0 = 1.0$ mm. Solid lines: numerical analysis, magnitudes S_{21} and S_{31}. Points: measured data, $\diamond$ – magnitude S_{21}, $+$ – magnitude S_{31}.*

For the given coupler structure the dependency of transmission parameters versus d_0 has been investigated at the frequency $f_0 = 30$ GHz (Fig. A.5). The numerical analysis shows that, theoretically, couplers with coupling coefficient varied from nearly -50 to 0 dB can be realized. For weak couplings with S_{31} below -20 dB, the coupling is very sensitive to the

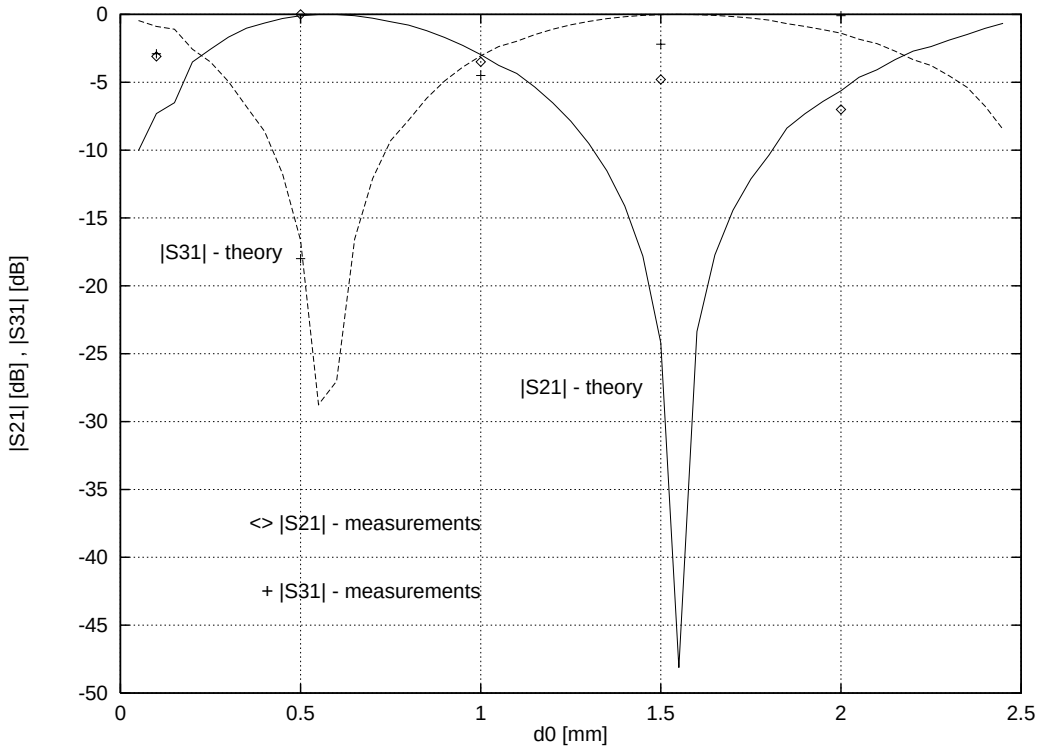

Figure A.5: *Transmission parameters of the asymmetrical NRD-guide coupler versus minimal distance d_0. Solid lines: numerical analysis, magnitudes S_{21} and S_{31}. Points: measured data, $\diamond$ – magnitude S_{21}, $+$ – magnitude S_{31}.*

inaccuracies in setting distance d_0. When usual -3 dB coupling is considered lower influence of the improper d_0 selection is observed. Numerical simulations are verified by experiments. Good agreement between theory and measurements is obtained.

A.5 Conclusions

The discussion concerned to NRD-guide couplers can be summarized as follows

- Couplers with different coupling coefficient can be designed.
- The coupling coefficient is very sensitive for the inaccuracy in d_0 fixing, especially for couplings below -20 dB.
- For some structures two points, each for different frequency, have the required coupling level.
- Experimental verification shows that dielectric losses can be on relatively high level and should be considered during the design.

Appendix B

TRL calibration

B.1 TRL calibration technique

The scattering parameters of a microwave device are usually measured using a vector network analyzer (VNA). In many practical situations, the VNA can not be connected directly to the DUT (Device Under Test) due to different waveguide types mounted at the VNA and DUT ports. Therefore, the transitions from one waveguide standard to another one have to be used, which means that instead DUT the cascade composed of two transitions and DUT is measured. In general, the transitions can be treated as the two port error boxes connected to the VNA ports, which introduce systematic errors into the measurements (Fig. B.1). To determine the parameters of these error boxes, various calibration techniques are used [112]. The accuracy of the measurements depends on the quality of calibration standards and accuracy of calibration method. For the systems where waveguides are used, the common choice is the TRL method (Thru-Reflect-Line) [113]. This method is selected due to its advantages over other standard calibration methods, such as OSL (Open-Short-Load) or SL (Sliding Load), which are suitable rather for calibrating coaxial line systems [114]. Therefore, in this work the TRL method is selected to determine the scattering parameters of the transitions between a rectangular waveguide and an NRD-guide. There are no commercially available calibration standards concerning NRD-guide circuits, therefore, the NRD-guide calibration kit, suitable for the TRL method, has been designed and manufactured. The TRL method and its application to NRD-guide filter measurements is described below.

TRL method. In the TRL method, three calibration circuits are defined. The "thru" circuit is composed of two error boxes connected in a cascade (Fig. B.2 (a)). The "reflect" circuit is created by termination the output ports of the error boxes by the devices with high input reflection coefficient, usually open or short devices are used (Fig. B.2 (c)). In the "line" circuit a piece of transmission line is inserted between the error boxes (Fig. B.2 (b)).

In the TRL procedure, firstly three calibration circuits are measured, then the parameters of the error boxes are determined. The procedure presented in this work is based on paper by Pantoja et al. [115].

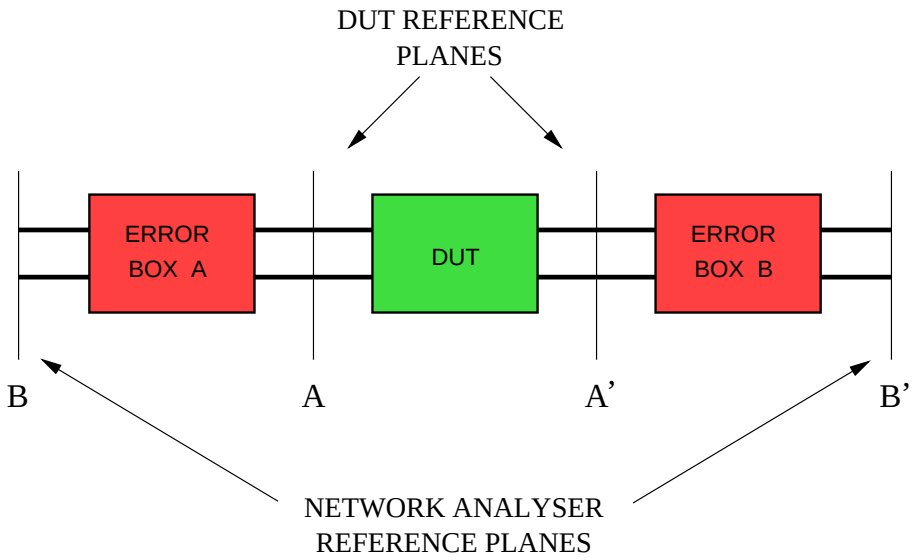

Figure B.1: *Typical measurement configuration: DUT with two error boxes. The reference planes of the VNA are located at planes B-B' while the required parameters of an DUT should be determined at DUT reference planes A-A'.*

At the beginning of the procedure the wave cascading matrix R is defined as

$$\begin{pmatrix} b_1 \\ a_1 \end{pmatrix} = \underline{\underline{R}} \begin{pmatrix} a_2 \\ b_2 \end{pmatrix}. \tag{B.1}$$

Matrix $\underline{\underline{R}}$ is related to the scattering matrix S

$$\underline{\underline{R}} = \frac{1}{S_{21}} \begin{pmatrix} -\Delta & S_{11} \\ -S_{22} & 1 \end{pmatrix} \tag{B.2}$$

where

$$\Delta = S_{11}S_{22} - S_{12}S_{21}. \tag{B.3}$$

The "thru" cascade (Fig. B.2 (a)) is described by the wave matrix $\underline{\underline{R_t}}$

$$\underline{\underline{R_t}} = \underline{\underline{R_a}}\,\underline{\underline{R_b}} \tag{B.4}$$

where $\underline{\underline{R_a}}$ and $\underline{\underline{R_b}}$ are the wave matrices of error boxes A and B. Similarly, the "line" cascade is described by $\underline{\underline{R_l}}$ matrix as follows

$$\underline{\underline{R_l}} = \underline{\underline{R_a}}\,\underline{\underline{R_{tl}}}\,\underline{\underline{R_b}} \tag{B.5}$$

where $\underline{\underline{R_{tl}}}$ is the wave matrix of the inserted transmission line. In the next step, $\underline{\underline{R_b}}$ is derived from (B.4) as

$$\underline{\underline{R_b}} = \underline{\underline{R_a^{-1}}}\,\underline{\underline{R_t}}. \tag{B.6}$$

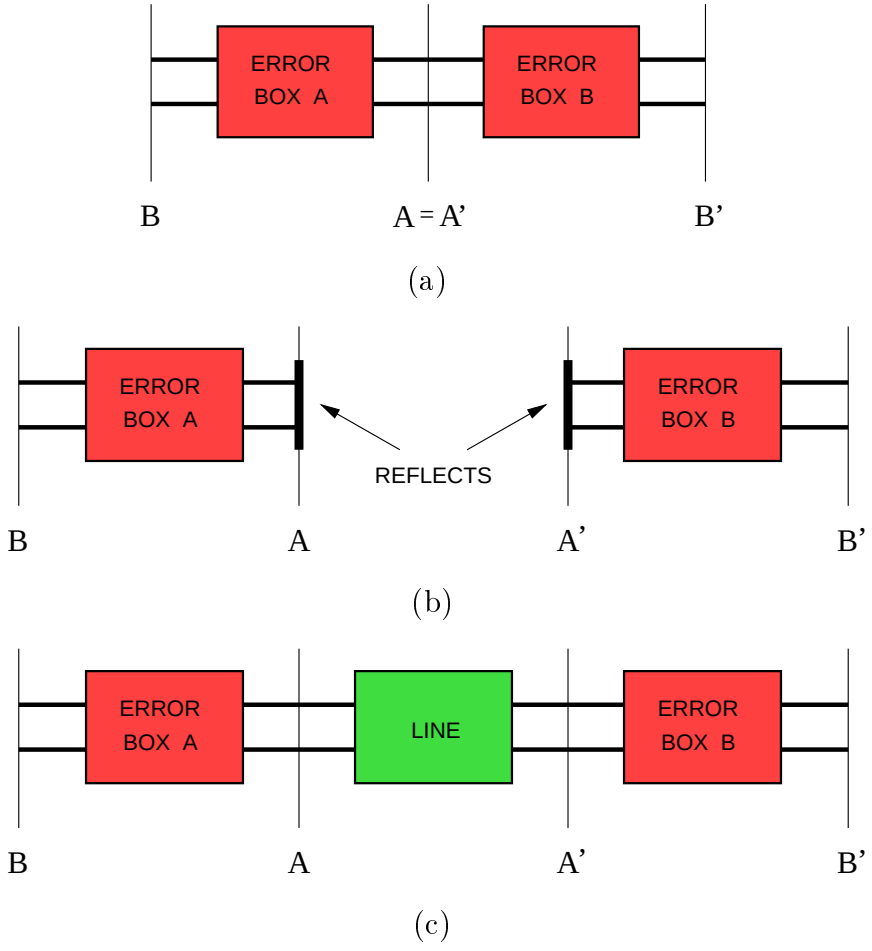

Figure B.2: *Three calibration circuits used in the TRL method: (a) thru, (b) reflect, (c) line.*

Using (B.6) $\underline{\underline{R_b}}$ is eliminated from (B.5) giving

$$\underline{\underline{T}}\,\underline{\underline{R_a}} = \underline{\underline{R_a}}\,\underline{\underline{R_{tl}}} \tag{B.7}$$

where

$$\underline{\underline{T}} = \underline{\underline{R_l}}\,\underline{\underline{R_t^{-1}}}\,. \tag{B.8}$$

For a line section of length l and the propagation constant γ, the matrix $\underline{\underline{R_{tl}}}$ has the form

$$\underline{\underline{R_{tl}}} = \begin{pmatrix} e^{-\gamma l} & 0 \\ 0 & e^{\gamma l} \end{pmatrix}. \tag{B.9}$$

Therefore, (B.7) can be written as

$$\begin{aligned} t_{11}r^a_{11} + t_{12}r^a_{21} &= r^a_{11}e^{-\gamma l} \\ t_{21}r^a_{11} + t_{22}r^a_{21} &= r^a_{21}e^{-\gamma l} \\ t_{11}r^a_{12} + t_{12}r^a_{22} &= r^a_{12}e^{\gamma l} \\ t_{21}r^a_{12} + t_{22}r^a_{22} &= r^a_{22}e^{\gamma l}. \end{aligned} \tag{B.10}$$

By combining equations of (B.10) two quadratic equations can be obtained

$$t_{21}\left(\frac{r^a_{11}}{r^a_{21}}\right)^2 + (t_{22}-t_{11})\frac{r^a_{11}}{r^a_{21}} - t_{12} = 0 \tag{B.11}$$

$$t_{21}\left(\frac{r^a_{12}}{r^a_{22}}\right)^2 + (t_{22}-t_{11})\frac{r^a_{12}}{r^a_{22}} - t_{12} = 0. \tag{B.12}$$

The roots of these equations $\left(\frac{r^a_{12}}{r^a_{22}}\right)$ and $\left(\frac{r^a_{11}}{r^a_{21}}\right)$ are related to the scattering parameters of the error box A as follows

$$\frac{r^a_{11}}{r^a_{21}} = \frac{\Delta_a}{S^a_{22}} = S^a_{11} - \frac{S^a_{12}S^a_{21}}{S^a_{22}} \tag{B.13}$$

$$\frac{r^a_{12}}{r^a_{22}} = S^a_{11}. \tag{B.14}$$

To determine the corresponding scattering parameters of the error box B, a similar procedure is applied. Matrix $\underline{\underline{R_a}}$ is obtained from (B.5)

$$\underline{\underline{R_a}} = \underline{\underline{R_l}}\,\underline{\underline{R_b^{-1}}}\,\underline{\underline{R_{tl}}}\,. \tag{B.15}$$

Then, by inserting $\underline{\underline{R_a}}$ to (B.4), we arrive at

$$\underline{\underline{R_b}}\,\underline{\underline{T}} = \underline{\underline{R_{tl}}}\,\underline{\underline{R_b}}\,. \tag{B.16}$$

The line section is characterized by (B.9), hence, the above equation can be presented in the following form

$$\begin{array}{rcl} t_{11}r^b_{11} + t_{12}r^b_{21} &=& r^b_{11}e^{\gamma l} \\ t_{21}r^b_{11} + t_{22}r^b_{21} &=& r^b_{21}e^{-\gamma l} \\ t_{11}r^b_{12} + t_{12}r^b_{22} &=& r^b_{12}e^{\gamma l} \\ t_{21}r^b_{12} + t_{22}r^b_{22} &=& r^b_{22}e^{-\gamma l}. \end{array} \tag{B.17}$$

Combining equations of (B.17) two quadratic equations are found

$$t_{12}\left(\frac{r^b_{11}}{r^b_{12}}\right)^2 + (t_{22}-t_{11})\frac{r^b_{11}}{r^b_{12}} - t_{21} = 0 \tag{B.18}$$

$$t_{12}\left(\frac{r^b_{21}}{r^b_{22}}\right)^2 + (t_{22}-t_{11})\frac{r^b_{21}}{r^b_{22}} - t_{21} = 0 \tag{B.19}$$

where roots of (B.18) and (B.19) (i.e. $\frac{r^b_{21}}{r^b_{22}}$ and $\frac{r^b_{11}}{r^b_{12}}$) are related to the scattering parameters of the error box B in the following manner

$$\frac{r^b_{11}}{r^b_{12}} = \frac{-\Delta}{S^b_{11}} = -S^b_{22} + \frac{S^b_{12}S^b_{21}}{S^b_{11}} \tag{B.20}$$

$$\frac{r_{21}^b}{r_{22}^b} = -S_{22}^b. \tag{B.21}$$

To obtain other parameters of the error boxes the information obtained from the "reflect" circuit is used. The reflection coefficients Γ_1 and Γ_2 at input ports of the error boxes A and B are given by

$$\Gamma_1 = S_{11}^a + \frac{S_{12}^a S_{21}^a}{1/\Gamma_R - S_{22}^a} \tag{B.22}$$

$$\Gamma_2 = S_{22}^b + \frac{S_{12}^b S_{21}^b}{(1/\Gamma_R) - S_{22}^b} \tag{B.23}$$

where Γ_R is the reflection coefficient of the device connected to the output ports of the error boxes A and B. Equations (B.22) and (B.23) can be written as

$$S_{22}^a \left(1 + \frac{X}{A}\right) = S_{11}^b \left(1 + \frac{Y}{B}\right) \tag{B.24}$$

where

$$X = \frac{S_{12}^a S_{21}^a}{S_{22}^a} \tag{B.25}$$

$$Y = \frac{S_{12}^b S_{21}^b}{S_{11}^b} \tag{B.26}$$

$$A = \Gamma_1 - S_{11}^a \tag{B.27}$$

$$B = \Gamma_2 - S_{22}^b. \tag{B.28}$$

For clarity, new coefficient C is now introduced using the results obtained from the "thru" configuration

$$S_{11}^t - S_{11}^a = \frac{S_{12}^a S_{21}^a S_{11}^b}{1 - S_{22}^a S_{11}^b} = C \tag{B.29}$$

where S_{11}^t is the input reflection coefficient of the "thru" configuration. Now, the following relation can be written

$$S_{22}^a S_{11}^b = \left(1 + \frac{X}{C}\right)^{-1}. \tag{B.30}$$

Taking (B.24) and (B.30) the S_{11}^b and S_{22}^a are found as

$$S_{11}^b = \pm \left[\left(1 + \frac{X}{A}\right) \left(1 + \frac{Y}{B}\right)^{-1} \left(1 + \frac{X}{C}\right)^{-1} \right]^{1/2} \tag{B.31}$$

$$S_{22}^a = S_{11}^b \left(1 + \frac{Y}{B}\right) \left(1 + \frac{X}{A}\right)^{-1}. \tag{B.32}$$

Till now all reflection coefficients of the error boxes A and B have been determined. The remaining transmission parameters are found by combining (B.25) and (B.26) which leads to the following relations

$$S_{12}^a S_{21}^a = X S_{22}^a \tag{B.33}$$

$$S_{12}^b S_{21}^b = Y S_{11}^b. \tag{B.34}$$

As a result, all scattering parameters of the error boxes A and B are determined.

In the method, only one choice of the root of (B.31) is correct. This root is selected in the following manner. Using (B.22) we have

$$\Gamma_R{}^{-1} = S_{22}^a + \frac{S_{12}^a S_{21}^a}{\Gamma_1 - S_{11}^a} = K e^{-j\alpha} \tag{B.35}$$

where α is the argument of middle part of (B.35) and K is its magnitude, Γ_R can be presented as

$$\Gamma_R = |\Gamma_R| e^{j\beta_R}. \tag{B.36}$$

Comparing (B.35) and (B.36) one can notice that the magnitude of Γ_R corresponds to K and its phase β_R corresponds to α. To make a correct choice in (B.31) the rough estimation of the phase β_R of the reflected device should be known. Wrong sign in (B.31) results in phase offset of α equal $\pi/2$, therefore, by comparing α with estimation of β_R obtained from (B.35) the proper selection can be done. It is worth to notice, that β_R can be estimated very roughly. Even if the estimation error equals nearly $\pi/4$ the accurate results are obtained.

The optimal selection of the line length in the "line" circuit is $\lambda/4$. For the line length equal $\lambda/2$ the system of equations (B.4) and (B.5) is ill-conditioned and the procedure yields unacceptable errors. This effect, which limits application of the method to a certain bandwidth, will be showed in one of the following sections. Various modification of the TRL method, such as the one presented in [116] which propose multiline TRL method eliminate this drawback, but the discussion of this problem is beyond the scope of this work and is not presented here.

The main advantages of the TRL method, applied to waveguide systems, can be summarized as follows

- The measurements of three, easy to construct, calibration circuits are required.
- For the non-ideal reflection with high reflection coefficient Γ_R only rough approximation of Γ_R phase is sufficient to obtain accurate results.
- Although the length of the measured line, in the "line" circuit, limits the method to certain bandwidth, easy modification of the TRL method can give accurate results in wider bandwidth.

B.2 NRD-guide TRL calibration kit

To perform measurements of NRD-guide components in the X-band NRD-guide calibration kit has been designed. The NRD-guide dimensions are the same as the ones specified for the NRD-guide filters (see chapter 4). The transitions between NRD-guide and rectangular waveguide, described in detail in chapter 3, are treated as the unknown error boxes A and B.

The "thru" calibration circuit is composed of two transitions connected back to back (Fig. B.4). In the "line" circuit the NRD-guide of the length $l = 13$ mm is inserted between transitions (Fig. B.5). Note, that for the selected NRD-guide and $f_0 = 9.5$ GHz $l \approx \lambda_g/4$, where λ_g is the guide wavelength of the LSM_{11} mode. The high reflective terminations are realized as the short circuits (Fig. B.3). For this choice the estimation of the phase β_R can be done with greater accuracy than required in the TRL method.

Figure B.3: *The "reflect" calibration circuit of the X-band NRD-guide calibration kit. The closing metal plates are taken away to demonstrate the entire circuit.*

B.3 De-embedding of the NRD-guide filter

In this section a practical application of the TRL method is presented. For the sake of an example, the results of the measurements of the 3 pole 0.5 dB Chebyshev NRD-guide filter with 2% bandwidth and center frequency $f_0 = 9.5$ GHz are presented. The filter is described

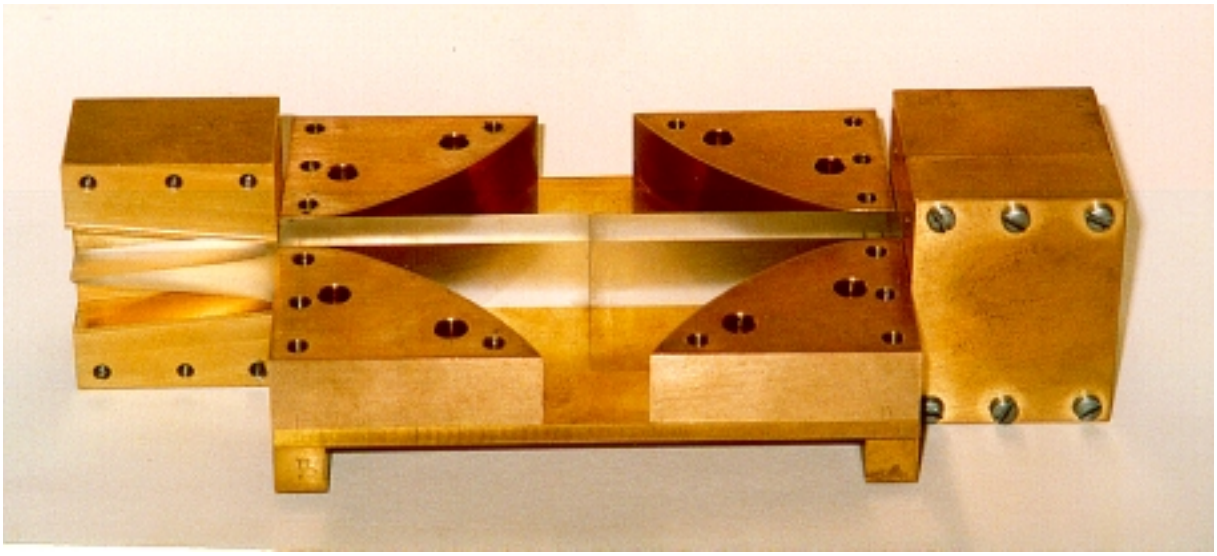

Figure B.4: *The "thru" calibration circuit of the X-band NRD-guide calibration kit. The upper metal plates are removed to demonstrate the circuit structure.*

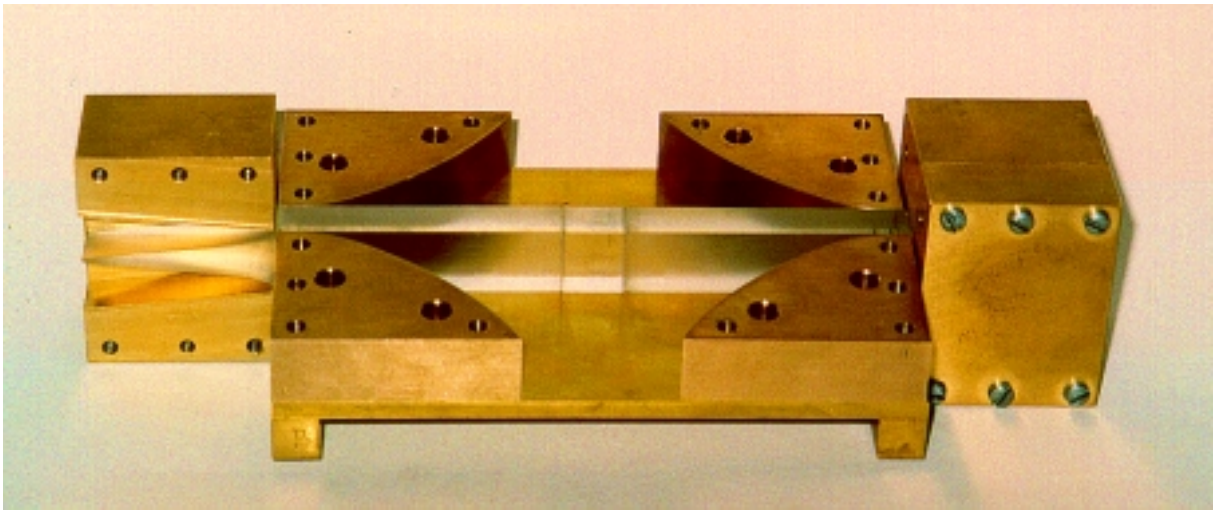

Figure B.5: *The "line" calibration circuit of the X-band NRD-guide calibration kit. The upper metal plates are removed in order to present the inside of the circuit.*

in section 4.3.2. The measurements have been performed using the vector network analyzer WILTRON 37269A.

In the first step, the VNA ports have been calibrated using standard TRL procedure implemented in the VNA. Then, the parameters of two transitions between an NRD-guide and a rectangular waveguide have been characterized using the TRL method together with the X-band NRD-guide calibration kit, both are described in the preceding sections. The transitions have been designed using the method described in chapter 3. Although the parameters of the transitions obtained from the calibration are described and discussed in

chapter 3, their characteristics are presented here in wider frequency band (Fig. B.7) to illustrate the importance of the proper line length selection. If the line length l in "line" calibration circuit is about $\lambda_g/4$ the accurate results are obtained. When the frequency increases also l is longer in terms of guide wavelength and reaches $\lambda_g/2$ near 11 GHz for the LSM_{11} mode. For this guide wavelengths the TRL method yields highly inaccurate results. This effect is clearly seen in (Fig. B.7) for both transmission and reflection coefficients at frequencies above 11 GHz.

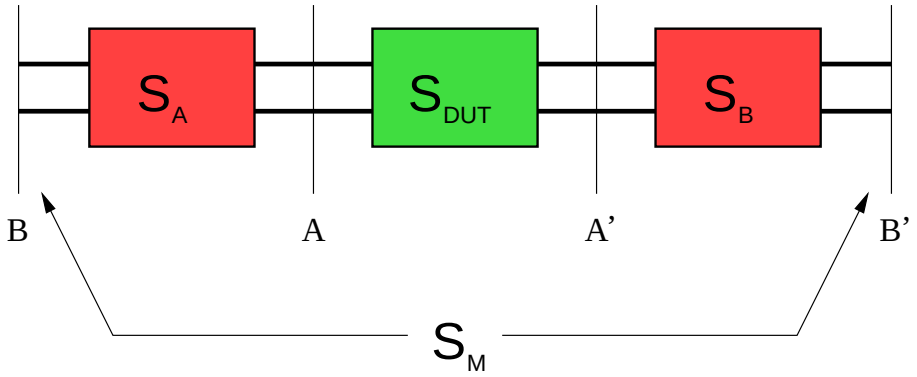

Figure B.6: *De-embedding of the NRD-guide filter: S_A and S_B are the scattering matrices of the error boxes A and B, S_{DUT} is the scattering matrix of DUT and the scattering matrix S_M corresponds to the cascade composed of two error boxes and DUT.*

Having determined the parameters of the transitions standard de-embedding procedure is applied to extract the filter parameters. The scattering parameters S_M of the cascade composed of error boxes and the filter have been measured at reference planes $B - B'$ (Fig. B.6); S_A and S_b denote scattering matrices of error box A and B, respectively[1]. To extract scattering parameters of the filter the scattering matrices are converted into the corresponding transmission matrices T for which the equation holds

$$\underline{\underline{T_M}} = \underline{\underline{T_A}}\,\underline{\underline{T_{DUT}}}\,\underline{\underline{T_B}}\,. \tag{B.37}$$

The matrix $\underline{\underline{T_{DUT}}}$ is found from

$$\underline{\underline{T_{DUT}}} = \underline{\underline{T_A^{-1}}}\,\underline{\underline{T_M}}\,\underline{\underline{T_B^{-1}}}\,. \tag{B.38}$$

Finally, the matrix $\underline{\underline{T_{DUT}}}$ is converted into the corresponding scattering matrix and the parameters of the filter measured at reference planes $A - A'$ are obtained (Fig. B.6. The parameters of the measured cascade and the de-embedded filter are shown in Fig. B.8.

[1]For consistency with the preceding sections, the transitions are described as the error boxes A and B and the filter is denoted as DUT.

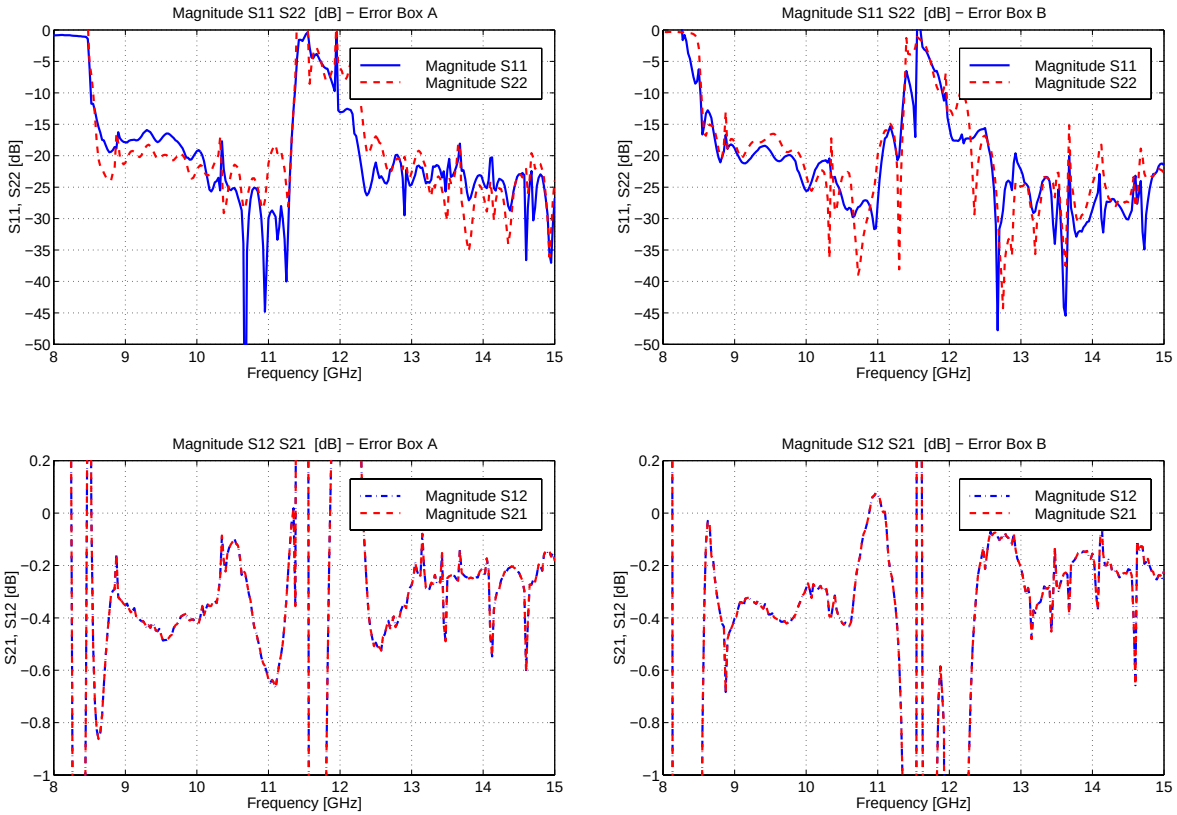

(a) (b)

Figure B.7: *De-embedded parameters of error boxes: (a) magnitudes of reflection and transmission coefficients of error box A, (b) magnitudes of reflection and transmission coefficients of error box B.*

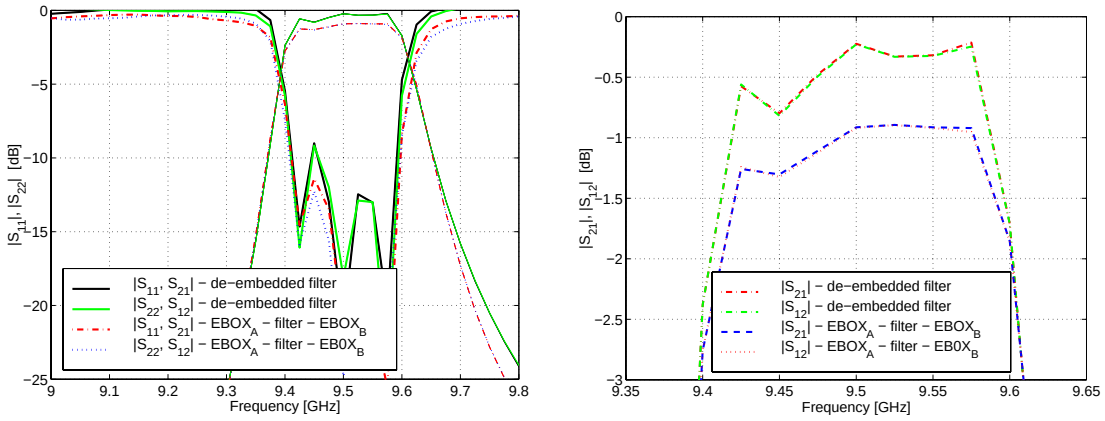

(a) (b)

Figure B.8: *De-embedding of the 3-pole 0.5 dB Chebyshev filter: (a) general view, (b) detailed view. The bandwidth is equal 2% and the center frequency* $f_0 = 9.5GHz$.

Appendix C

Fields in NRD-guide

In this appendix the field solutions for the structures with closing magnetic walls and with exponential field decay in the outer regions are shown. All symbols and indices are explained in section 2.2, where the NRD-guide structure with closing electric walls is analyzed. Therefore, here only the key expressions are presented. The coefficient $e^{-\gamma z}$ is omitted in all field equations for simplicity.

C.1 Field solution for the NRD-guide structure with exponential field decay

The guide structure with exponential field decay in outer regions A and C is shown in Fig. 2.2 (d). If the distance $d \to \infty$, the structure is treated as a semi open one. Below the solution for the LSE and LSM modes are presented.

C.1.1 Solution for LSE modes

The E_x component does not exist for the LSE modes, hence, the electric Hertz potential equals zero

$$\Psi_e = 0. \tag{C.1}$$

The magnetic Hertz potential has to fulfil the continuity conditions given by (2.9) and (2.10) at air dielectric interfaces. Therefore, the magnetic Hertz potential in each region is defined as follows

$$\Psi_{h_A} = Ae^{k_{x0}x}\cos(k_y y)e^{-\gamma z} \tag{C.2}$$

$$\Psi_{h_B} = [B\cos(k_{xd}x) + C\cos(k_{xd}x)]\cos(k_y y)e^{-\gamma z} \tag{C.3}$$

$$\Psi_{h_C} = De^{-k_{x0}(x_2-a)}\cos(k_y y)e^{-\gamma z}. \tag{C.4}$$

Substitution of the scalar potentials given by (C.2) ÷ (C.4) into the equations (2.23) ÷ (2.28) yields the field expressions

Region A

$$\begin{aligned} E_x &= 0 \\ E_y &= jA\omega\gamma e^{k_{x0}x}\cos(k_y y) \\ E_z &= -jA\omega k_y e^{k_{x0}x}\sin(k_y y) \\ H_x &= \tfrac{A}{\mu_0\mu(x)}(k_y^2-\gamma^2)e^{k_{x0}x}\cos(k_y y) \\ H_y &= -\tfrac{A}{\mu_0\mu(x)}k_{x0}k_y e^{k_{x0}x}\sin(k_y y) \\ H_z &= -\tfrac{A}{\mu_0\mu(x)}\gamma k_{x0}e^{k_{x0}x}\cos(k_y y) \end{aligned} \tag{C.5}$$

Region B

$$\begin{aligned} E_x &= 0 \\ E_y &= j\omega\gamma\left[B\cos(k_{xd}x)+C\sin(k_{xd}x)\right]\cos(k_y y) \\ E_z &= -j\omega k_y\left[B\cos(k_{xd}x)+C\sin(k_{xd}x)\right]\sin(k_y y) \\ H_x &= \tfrac{1}{\mu_0\mu(x)}(k_y^2-\gamma^2)\left[B\cos(k_{xd}x)+C\sin(k_{xd}x)\right]\cos(k_y y) \\ H_y &= -\tfrac{1}{\mu_0\mu(x)}k_{xd}k_y\left[-B\sin(k_{xd}x)+C\cos(k_{xd}x)\right]\sin(k_y y) \\ H_z &= -\tfrac{1}{\mu_0\mu(x)}\gamma k_{xd}\left[-B\sin(k_{xd}x)+C\cos(k_{xd}x)\right]\cos(k_y y) \end{aligned} \tag{C.6}$$

Region C

$$\begin{aligned} E_x &= 0 \\ E_y &= jD\omega\gamma e^{-k_{x0}(x_2-a)}\cos(k_y y) \\ E_z &= -jD\omega k_y e^{-k_{x0}(x_2-a)}\sin(k_y y) \\ H_x &= \tfrac{D}{\mu_0\mu(x)}(k_y^2-\gamma^2)e^{-k_{x0}(x_2-a)}\cos(k_y y) \\ H_y &= \tfrac{D}{\mu_0\mu(x)}k_{x0}k_y e^{-k_{x0}(x_2-a)}\sin(k_y y) \\ H_z &= -\tfrac{D}{\mu_0\mu(x)}\gamma k_{x0}e^{-k_{x0}(x_2-a)}\cos(k_y y). \end{aligned} \tag{C.7}$$

C.1.2 Solution for LSM modes

The structure is the same as in the case of LSE modes. For LSM modes the magnetic Hertz potential equals zero

$$\Psi_h = 0. \tag{C.8}$$

Hence, only the electric Hertz potential exist in the structure which can be written in each region as

$$\Psi_{h_A} = Ae^{k_{x0}x}\sin(k_y y)e^{-\gamma z} \tag{C.9}$$

$$\Psi_{h_B} = \left[B\cos(k_{xd}x)+C\cos(k_{xd}x)\right]\sin(k_y y)e^{-\gamma z} \tag{C.10}$$

$$\Psi_{h_C} = De^{-k_{x0}(x_2-a)}\sin(k_y y)e^{-\gamma z}. \tag{C.11}$$

The fields expressions are obtained by inserting the presented scalar potentials into the field equations (2.43) ÷ (2.48)

Region A

$$\begin{aligned} E_x &= \tfrac{A}{\epsilon_0\epsilon(x)}(k_y^2-\gamma^2)e^{k_{x0}x}\sin(k_y y) \\ E_y &= \tfrac{A}{\epsilon_0\epsilon(x)}k_{x0}k_y e^{k_{x0}x}\cos(k_y y) \\ E_z &= -\tfrac{A}{\epsilon_0\epsilon(x)}\gamma k_{x0}e^{k_{x0}x}\cos(k_y y) \\ H_x &= 0 \\ H_y &= -jA\omega\gamma e^{k_{x0}x}\sin(k_y y) \\ H_z &= -jA\omega k_y e^{k_{x0}x}\cos(k_y y) \end{aligned} \tag{C.12}$$

Region B

$$\begin{aligned} E_x &= \tfrac{1}{\epsilon_0\epsilon(x)}(k_y^2-\gamma^2)\left[B\cos(k_{\times d}\times)+C\sin(k_{\times d}\times)\right]\sin(k_y y) \\ E_y &= \tfrac{1}{\epsilon_0\epsilon(x)}k_{\times d}k_y\left[-B\sin(k_{xd}x)+C\cos(k_{xd}x)\right]\cos(k_y y) \\ E_z &= -\tfrac{1}{\epsilon_0\epsilon(x)}\gamma k_{xd}\left[-B\sin(k_{xd}x)+C\cos(k_{xd}x)\right]\sin(k_y y) \\ H_x &= 0 \\ H_y &= -j\omega\gamma\left[B\cos(k_{xd}x)+C\sin(k_{xd}x)\right]\sin(k_y y) \\ H_z &= -j\omega k_y\left[B\cos(k_{xd}x)+C\sin(k_{xd}x)\right]\cos(k_y y) \end{aligned} \tag{C.13}$$

Region C

$$\begin{aligned} E_x &= \tfrac{D}{\epsilon_0\epsilon(x)}(k_y^2-\gamma^2)e^{-k_{x0}(x_2-a)}\sin(k_y y) \\ E_y &= -\tfrac{D}{\epsilon_0\epsilon(x)}k_{x0}k_y e^{-k_{x0}(x_2-a)}\cos(k_y y) \\ E_z &= \tfrac{D}{\epsilon_0\epsilon(x)}\gamma k_{x0}e^{-k_{x0}(x_2-a)}\sin(k_y y) \\ H_x &= 0 \\ H_y &= -jD\omega\gamma e^{k_{x0}(x_2-a)}\sin(k_y y) \\ H_z &= -jD\omega k_y e^{k_{x0}(x_2-a)}\cos(k_y y). \end{aligned} \tag{C.14}$$

C.2 Field solution for the NRD-guide structure closed by magnetic walls

The NRD-guide structure with the side walls in the form of magnetic walls is shown in Fig. 2.2 (c). The expression for the LSE and LSM modes defined in this structure are written in the sections that follow.

C.2.1 Solution for LSE modes

For LSE modes only magnetic Hertz potential exists which can be written as

$$\Psi_{h_A} = A\cos(k_{x0}x)\cos(k_y y)e^{-\gamma z} \tag{C.15}$$

$$\Psi_{h_B} = \left[B\cos(k_{xd}x)+C\sin(k_{xd}x)\right]\cos(k_y y)e^{-\gamma z} \tag{C.16}$$

$$\Psi_{h_C} = D\cos(k_{x0}(a-x))\cos(k_y y)e^{-\gamma z}. \tag{C.17}$$

Inserting the magnetic Hertz potentials given by (C.15) ÷ (C.17) into the field equations (2.23) to (2.28), the fields description is obtained in the following form

Region A

$$\begin{aligned} E_x &= 0 \\ E_y &= jA\omega\gamma\cos(k_{x0}x)\cos(k_y y) \\ E_z &= -jA\omega k_y\sin(k_{x0}x)\sin(k_y y) \\ H_x &= \tfrac{A}{\mu_0\mu(x)}(k_y^2-\gamma^2)\cos(k_{x0}x)\cos(k_y y) \\ H_y &= \tfrac{A}{\mu_0\mu(x)}k_{x0}k_y\sin(k_{x0}x)\sin(k_y y) \\ H_z &= \tfrac{A}{\mu_0\mu(x)}\gamma k_{x0}\sin(k_{x0}x)\cos(k_y y) \end{aligned} \tag{C.18}$$

Region C

$$\begin{aligned} E_x &= 0 \\ E_y &= jD\omega\gamma\cos(k_{x0}(a-x))\cos(k_y y) \\ E_z &= -jD\omega k_y\cos(k_{x0}(a-x))\sin(k_y y) \\ H_x &= \tfrac{D}{\mu_0\mu(x)}(k_y^2-\gamma^2)\cos(k_{x0}(a-x))\cos(k_y y) \\ H_y &= -\tfrac{D}{\mu_0\mu(x)}k_{x0}k_y\sin(k_{x0}(a-x))\sin(k_y y) \\ H_z &= \tfrac{D}{\mu_0\mu(x)}\gamma k_{x0}\sin(k_{x0}(a-x))\cos(k_y y). \end{aligned} \tag{C.19}$$

The fields in region B are the same as for the structure with exponential field decay and LSE modes (equation C.6).

C.2.2 Solution for LSM modes

The fields of the LSM modes are derived from the electric Hertz potential. Its form is given below

$$\Psi_{e_A} = A\sin(k_{x0}x)\sin(k_y y)e^{-\gamma z} \tag{C.20}$$

$$\Psi_{e_B} = [B\cos(k_{xd}x) + C\sin(k_{xd}x)]\sin(k_y y)e^{-\gamma z} \tag{C.21}$$

$$\Psi_{e_C} = D\sin(k_{x0}(a-x))\sin(k_y y)e^{-\gamma z}. \tag{C.22}$$

The fields expressions are obtained by putting the presented Hertz potentials into the field equations (2.43) ÷ (2.48)

Region A

$$\begin{aligned} E_x &= \tfrac{A}{\epsilon_0\epsilon(x)}(k_y^2-\gamma^2)\sin(k_{x0}x)\sin(k_y y) \\ E_y &= \tfrac{A}{\epsilon_0\epsilon(x)}k_{x0}k_y\cos(k_{x0}x)\cos(k_y y) \\ E_z &= -\tfrac{A}{\epsilon_0\epsilon(x)}\gamma k_{x0}\cos(k_{x0}x)\sin(k_y y) \\ H_x &= 0 \\ H_y &= -jA\omega\gamma\sin(k_{x0}x)\sin(k_y y) \\ H_z &= -jA\omega k_y\sin(k_{x0}x)\cos(k_y y) \end{aligned} \tag{C.23}$$

Region C

$$\begin{aligned} E_x &= \tfrac{D}{\epsilon_0\epsilon(x)}(k_y^2-\gamma^2)\sin(k_{x0}(a-x))\sin(k_y y) \\ E_y &= \tfrac{D}{\epsilon_0\epsilon(x)}k_{x0}k_y\cos(k_{x0}(a-x))\cos(k_y y) \\ E_z &= -\tfrac{D}{\epsilon_0\epsilon(x)}\gamma k_{x0}\cos(k_{x0}(a-x))\sin(k_y y) \\ H_x &= 0 \\ H_y &= -jD\omega\gamma\sin(k_{x0}(a-x))\sin(k_y y) \\ H_z &= -jD\omega k_y\cos(k_{x0}(a-x))\sin(k_y y). \end{aligned} \tag{C.24}$$

The field expression for region B are presented in section C.1.2 (equation C.13).

Appendix D

Theoretical characteristics of NRD-guide bandpass filter

The ideal theoretical characteristic of a band pass filter can be approximated in various ways. The classical approximation is obtained by the low pass to band pass frequency mapping of the formulae derived for low pass filter. The frequency transformation usually used has the form

$$\frac{f'}{f_1'} = \frac{1}{w_f}\left(\frac{f}{f_0} - \frac{f_0}{f}\right) \tag{D.1}$$

where w_f and f_0 are fractional bandwidth and center frequency of a bandpass filter; f' and f_1' refer to low pass domain and w_f, f, f_0 refer to band pass domain. Similar frequency transformations, suitable for various filter configurations and bandwidth ranges, can be found in the work of Cohn [99]. All these frequency mappings are valid for filters built of TEM lines. In waveguides, non-TEM hybrid modes exist, therefore the transformation in wavelength domain is applied due to dispersive character of the waveguides. This transformation is expressed as follows (chapter 8 in [64])

$$\frac{f'}{f_1'} = \frac{2}{w_\lambda}\left(\frac{\lambda_{g0} - \lambda_g}{\lambda_{g0}}\right) \tag{D.2}$$

where λ_{g0} is the wavelength corresponding to the center frequency, and w_λ is the fractional bandwidth in guide wavelength domain. The parameters λ_g, λ_{g0} and w_λ refer to bandpass domain; f' and f_1' belong to low pass domain.

The transformations given by (D.1) and (D.2) yield good theoretical approximation of a filter response in many cases. However, for certain filter types, such as direct coupled cavity filter, they gives inaccurate results because the additional effects which change filter response are not taken into consideration.

The more accurate approximations of the response of direct coupled cavity filters are given by equations (4.11) and (4.19) for Chebyshev and maximally flat response, respectively. These relations take into account the reactive coupling which appear between sections, and allow one to determine the response of different waveguide filter configurations with high accuracy. Hence, these relations are used to describe response of majority of NRD-guide

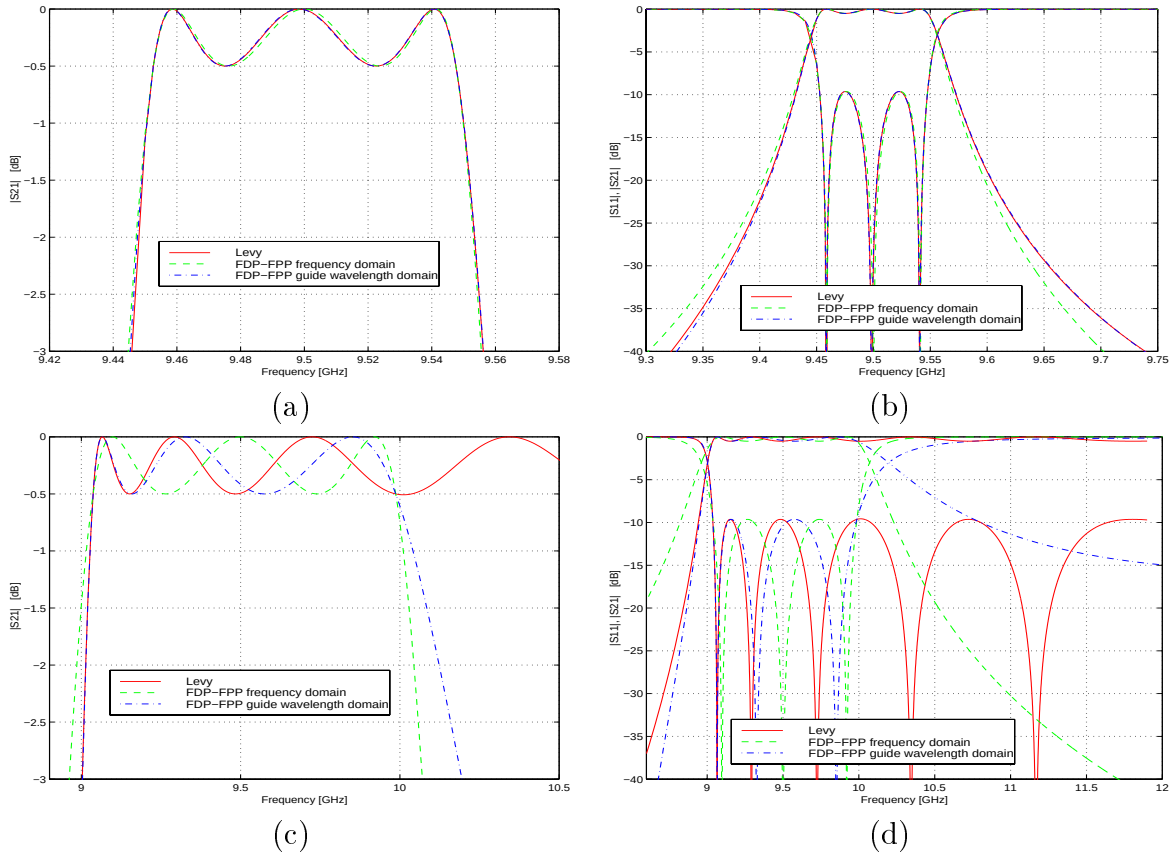

Figure D.1: *Ideal theoretical characteristics for three section 0.5dB Chebyshev filter designed for X-band: (a) 1% bandwidth - general view, (b) 1% bandwidth - detail view, (c) 10% bandwidth - general view, (d) 10% bandwidth - detail view. Filter and NRD-guide parameters are given in text.*

filters investigated in this work. Nevertheless, a closer investigation of accurate responses shows, that in the case of NRD-guide filters their estimation error grows rapidly when the bandwidth is increased. To present this effect three filter transformations are compared. The frequency transformation, the waveguide transformation and the accurate prediction given by (4.11) are applied to determine the response of three section 0.5dB Chebyshev NRD-guide filters with 1% and 10 % bandwidths. The filters are designed to work at X frequency band, their detailed parameters are described in chapter 4.

The results of filter with 1% bandwidth show, that in the pass band all three ways yield the same response (Fig. D.1 (a)). In the stop band the λ transformation and the accurate prediction are almost identical, only the frequency transformation offers slightly lower roll on at lower frequencies and higher roll off at higher frequencies (Fig. D.1 (b)). This similarity does not hold when the filter bandwidth is set to 10 %. Although in the pass band the three ways have the same accurate ripple level (Fig. D.1 (c)), the filter responses in the stop band are completely different (Fig. D.1 (d)). In the lower part of the stop band the λ transformation has the highest roll-on of the characteristic, the accurate prediction is very close to λ transformation, while the frequency transformation offers the

lowest level of attenuation. The difference between the investigated responses is very high at the upper part of the stop band. The frequency transformation gives the biggest attenuation, the λ transformation has the attenuation more than two times lower, while the accurate prediction has the lowest attenuation. The latter one does not fall below -0.5 dB level which suggests that the formula become completely inaccurate in this case. Therefore the λ transformation is used to determine theoretical response of the filters with 10 % bandwidth presented in chapter 4. This response is also in a good agreement with the results of the numerical simulation of the filters. The validation of this choice is confirmed by fairly well agreement of such theoretically predicted response with the results obtained from the numerical simulations.

Acknowledgments

First of all I would like to express my appreciation to Professor Michał Mrozowski who encouraged me to take up various challenging ideas and concepts and always has offered his support in finding solutions. His contribution to my development, not only professional, is hard to overestimate.

I am very grateful to my friends: Michał Patryk Dębicki, Jacek Mielewski, Piotr Przybyszewski and Michał Rewieński with whom I discussed not only electromagnetic problems and who have contributed to my work in various ways.

I would like to thank to people from the Department of Microwaves and Optical Telecommunication with whom I had pleasure to work. My special thanks go to Professor Jerzy Mazur for his aid in understanding electromagnetic problems and Professor Jerzy Chramiec for his help in measurements. I also thank Mr. Lucjan Wróbel and Mr. Janusz Harasimowicz for manufacturing trial circuits.

I am very grateful to Arkadiusz Rafflewski (Yellow Factory) for his help in design of cover page and aid in color printing and to Szczepan Wysocki for his graphical ideas.

I wish to thank to my family for their strong support during these years and confidence in my work.

I express my sincere gratitude to Paweł whose influence on this work and my life I still discover.

I also acknowledge the support of the Academic Computer Center (TASK) where the majority of numerical simulations were performed, the help of the Polish State Committee for Scientific Research which supported my studies under the contracts 8 T11D 028 10 and 8 T11D 028 15 and the aid of the Department of Microwaves and Optical Telecommunication at the Faculty of Electronics, Telecommunications and Informatics of the Technical University of Gdańsk where I has worked during my research.

Copyright note

Bibliography

[1] Holger H. Meinel. Commercial applications of millimeter-waves, history, present status and future trends. *IEEE Trans. Microwave Theory and Tech.*, MTT-43(7):1638–1653, July 1995.

[2] P. Russer. Si and SiGe millimeter-wave integrated circuits. *IEEE Trans. Microwave Theory and Tech.*, MTT-46(5):590–601, May 1998.

[3] Y. Qian and T. Itoh. Progress in active integrated antennas and their applications. *IEEE Trans. Microwave Theory and Tech.*, MTT-46(11):1891–1900, November 1998.

[4] Holger H. Meinel. Introduction to special issue on emerging commercial and consumer circuits, systems, and their applications. *IEEE Trans. Microwave Theory and Tech.*, MTT-43(7):1633–1637, July 1995.

[5] Z. Popovic and A. Mortazawi. Quasi-optical transmit/receive front ends. *IEEE Trans. Microwave Theory and Tech.*, MTT-46(11):1964–1975, November 1998.

[6] T. Yoneyama. Millimeter-wave research activities in Japan. *IEEE Trans. Microwave Theory and Tech.*, MTT-46(6):727–733, June 1998.

[7] M.E. Russell, A. Crain, A. Curran, R.A. Chamber, and C.A. Durbin amd W.F. Miccioli. Millimeter-wave radar sensor for automotive Intelligent Cruise Control (ICC). *IEEE Trans. Microwave Theory and Tech.*, MTT-45(12):2444–2453, May 1997.

[8] S. K. Koul. *Millimeter wave and optical dielectric integrated guides and circuits.* John Wiley & Sons, New York, 1997.

[9] K. Wu and L. Han. Hybrid integration technology of planar circuits and NRD-guide for cost-effective microwave and millimeter-wave applications. *IEEE Trans. Microwave Theory and Tech.*, MTT-45(6):946–954, December 1997.

[10] J. Luy, K. Strohm, H. Sasse, A. Schuppen, J. Buechler, M. Willitzer, A. Gruhle, F. Schaffler, U. Guettich, and A. Klaaben. Si SiGe MMIC's. *IEEE Trans. Microwave Theory and Tech.*, MTT-43(7):705–713, April 1995.

[11] C. Warns, W. Menzel, and H Schumacher. Transmission lines and passive elements for multilayer coplanar circuits on silicon. *IEEE Trans. Microwave Theory and Tech.*, MTT-46(5):616–621, May 1998.

[12] D.H. Schrader. *Microstrip circuit analysis.* Prentice Hall, Upper Saddle River, New Jersey, 1995.

[13] T. Rozzi and M. Mongiardo. *Open electromagnetic waveguides.* The Institution of Electrical Engineers, Herts, United Kingdom, 1997.

[14] R.M.Knox and P.P.Toulios. Integrated circuits for millimeter through optical frequency range. In Inst. of Brooklyn Politech, editor, *Proc.Symposium on Submillimeter Waves*, pages 497–516, New York, 1970.

[15] R. M. Knox. Dielectic waveguide microwave integrated circuits-an overview. *IEEE Trans. Microwave Theory and Tech.*, MTT-24(11), December 1976.

[16] T. Itoh. Inverted strip dielectric waveguide for millimeter wave integrated circuits. *IEEE Trans. Microwave Theory and Tech.*, MTT-24(11):821–827, November 1976.

[17] J.E. Goell. Rib waveguide for integrated optical circuits. *Appl. Opt.*, 12(12):2797–2798, December 1973.

[18] L.L. Xiao, L. Zhu, and W. X. Zhang. Analysis of the mono-groove NRD waveguide and antenna. *International Journal of Infrared and Millimeter Waves*, 10(3):361–70, March 1989.

[19] T. Yoneyama and S. Nishida. Nonradiative dielectric waveguide for millimeter-wave integrated circuits. *IEEE Trans. Microwave Theory and Tech.*, MTT-29:1188– 1192, November 1981.

[20] J.W.E Griemsmann and L. Birenbaum. A low-loss H-guide for millimeter wavelengths. In *Proc. Symposium on Millimeter Waves*, pages 543–562, Polytechnic Institute of Brooklyn, NY, USA, March 1959.

[21] S.J. Xu, X.Y. Zeng, T. Yoneyama, K. Wu, and K. M. Luk. A new asymmetrically grooved NRD guide leaky-wave antenna for millimeter-wave applications. *IEEE MTT-S Digest*, 1999.

[22] B. Bhat and S.K. Koul. *Analysis design and applications of fin lines.* Artech House, New York, 1987.

[23] K. Maamria, T. Wagatsuma, and T. Yoneyama. Leaky NRD-guide as a feeder for microwave planar antennas. *IEEE Trans. Microwave Theory and Tech.*, MTT-41(12):1680–1686, December 1993.

[24] Piotr Jędrzejewski, Gabrielle Landrac, and Michał Mrozowski. Design of NRD-guide couplers. In *XI International Microwave Conference MIKON'96*, pages 8–12, Warszawa, May 27-30 1996. volume 1.

[25] Dow-Chih Niu, T. Yoneyama, and T. Itoh. Measurement of NRD-guide leaky wave coupler in Ka band. *IEEE MTT-S Digest*, II-4:1207–1210, 1993.

[26] T. Yoneyama, N. Tozawa, and S. Nishida. Coupling characteristics of nonradiative dielectric waveguides. *IEEE Trans. Microwave Theory and Tech.*, MTT-31:648–654, August 1983.

[27] H. Yoshinaga and T. Yoneyama. Design and fabrication of a nonradiative dielectric waveguide circulator. *IEEE Trans. Microwave Theory and Tech.*, MTT-36(11):1526–1529, November 1988.

[28] Q. Lanfen and L. Yong Xiang. Rigorous fields theoretical design and optimization of novel window-coupled NRD-guide bandpass filters. In *Proc. Asia-Pacific Microwave Conf.*, pages 19–22, Tokyo, Japan, 1990. vol. 1.

[29] J.A.G. Malherbe and J.C. Olivier. The design of a slot array in nonradiating dielectric waveguide, Part I: Theory. *IEEE Trans. Microwave Theory and Tech.*, MTT-32(12):1335–1340, December 1984.

[30] J.A.G. Malherbe and J.C. Olivier. The design of a slot array in nonradiating dielectric waveguide, Part II: Experiment. *IEEE Trans. Microwave Theory and Tech.*, MTT-32(12):1341–1344, December 1984.

[31] T. Yoneyama. Recent development in NRD-guide technology. *Ann. Télécommun.*, 47(11-12):508–514, 1992.

[32] Y. Wang and L. Qi. NRD leaky-wave antenna for narrow beams in 94 GHz. *International Journal of Infrared and Millimeter Waves*, 16(11):2019–2024, November 1995.

[33] T. Yoneyama. *Nonradiative dielectric waveguide*, volume 11 of *Infrared and millimeter waves. Millimeter components and techniques*, chapter 2, pages 62–98. Academic Press, Orlando, FL, 1984.

[34] S. Qi, Ke Wu, and Z. Ou. Hybrid integrated HEMT oscillator with a multiple-ring nonradiative dielectric (NRD) resonator feedback circuit. *IEEE Trans. Microwave Theory and Tech.*, MTT-46(10):1552–1558, October 1998.

[35] A. Sayyah and Ke Wu. Efficient analysis of microstrip-coupled nonradiative dielectric (NRD) resonators for hybrid integrated circuits. *IEEE Trans. Microwave Theory and Tech.*, MTT-47(2):216–223, February 1999.

[36] S. Alei, C.D. Nallo, M. Fascetti, F. Ferezza, A. Galli, and G. Gerosa. Theoretical and experimental analysis of ferrite circular resonators in nonradiative dielectric structures. *IEEE MTT-S Digest*, pages 1655–1658, 1996.

[37] F. Ferezza, A. Galli, G. Gerosa, and P. Lampariello. Resonant frequencies and quality factors in lossy NRD cylindrical resonators. *International Journal of Infrared and Millimeter Waves*, 16(3):675–688, March 1995.

[38] T. Yoneyama and S. Nishida. Nonradiative dielectric waveguide T-junction for millimeter-wave applications. *IEEE Trans. Microwave Theory and Tech.*, MTT-33(11):1239–1241, November 1985.

[39] F. Kuroki and T. Yoneyama. Millimeter-wave junction circuits using nonradiative dielectric waveguide. *Electronics and Communications in Japan*, 75(7):11–18, July 1992.

[40] L. Han, Ke Wu, and R.G. Bosisio. An integrated transition of microstrip to nonradiative dielectric waveguide for microwave and millimeter-wave circuits. *IEEE Trans. Microwave Theory and Tech.*, MTT-44(7):1091–6, July 1996.

[41] A. Bacha and K. Wu. Toward an optimum design of NRD-guide and microstripline transition for hybrid-integration technology. *IEEE Trans. Microwave Theory and Tech.*, MTT-46(11):1796–1800, November 1998.

[42] Liang Han and Ke Wu. An integrated transition of CPW to NRD-guide for use in millimeter-wave circuits. *Asia-Pacific Microwave Conference Proceedings.*, 4:1277–80, December 1996.

[43] D. Dawn and M. Sachidanada. Analysis and design of strip line to nonradiative dielectric waveguide transition. In *Asia-Pacific Microwave Conference Proceedings.*, pages 15–18, Tokyo, Japan, December 1990.

[44] J.A.G. Malherbe, J.H. Cloete, and I.E. Losch. A transition from rectangular to nonradiating dielectric waveguide. *IEEE Trans. Microwave Theory and Tech.*, MTT-33, June 1985.

[45] K. Wu and L. Han. Integrated planar NRD oscillator suitable for low-cost millimeter-wave applications. *IEEE Microwave and Guided Wave Letters*, pages 126–128, 1996.

[46] Y. Suzuki, F. Kuroki, and T. Yoneyama. Frequency stabilization of NRD-waveguide Gunn oscillator at 60 GHz. *Electronics and Communications in Japan*, 78(5):40–47, May 1995.

[47] F. Kuroki and T. Yoneyama. Non-radiative dielectric waveguide circuit components using beam-lead diodes. *Electronics and Communications in Japan*, 73(2):71–76, February 1990.

[48] W. A. Artuzi and T. Yoneyama. A HEMT amplifier for non-radiative dielectric waveguide integrated circuits. *Electronics and Communications in Japan*, 74(5):1185–1190, May 1991.

[49] T. Yoneyama. Millimeter-wave transmitter and receiver using the nonradiative dielectric guide. *IEEE MTT-S Digest*, pages 1083–1086, 1989.

[50] I. Uchida, F. Kuroki, and T. Yoneyama. Miniaturization of 35-GHz NRD-guide transmitter and receiver. *Electronics and Communications in Japan*, 77(2):12–19, February 1994.

[51] F. Kuroki, M. Sugioka, S. Matsukawa, K. Ikeda, and T. Yoneyama. High-speed ASK transreceiver based on the NRD-guide technology at 60 GHz band. *IEEE Trans. Microwave Theory and Tech.*, MTT-46(10):806–809, October 1998.

[52] K. C. Gupta. Emerging trends in millimeter-wave CAD. *IEEE Trans. Microwave Theory and Tech.*, MTT-46(6):747–755, June 1998.

[53] C.D. Nallo, F. Ferezza, A. Galli, and P. Lampariello. Comparative modal analysis of NRD parallelepiped dielectric resonators. *International Journal of Infrared and Millimeter Waves*, 17(8):1403–1418, March 1996.

[54] M. Davidowitz. A model for slot-coupled nonradiative dielectric waveguide and microstrip line. *Int J Microwave Millimeter-Wave CAE*, pages 388–396, July 1997.

[55] J. Huang, K. Wu, F. Kuroki, and T. Yoneyama. Filter-like design and optimization of NRD-guide mode suppressors. *IEEE MTT-S Digest*, pages 995–998, 1995.

[56] T. Itoh. *Numerical techniques for microwave and millimeter-wave passive structures.* John Wiley & Sons, New York, 1989.

[57] Dębicki P., Jędrzejewski P., Mielewski J., Mrozowski M. Nyka K., Przybyszewski P., Rewieński M., Rutkowski T., and Kręczkowski A. Coping with numerical complexity in computational electromagnetics. In *XI International Microwave Conference MIKON'98*, pages 176–198, Kraków, May 20-22 1998.

[58] N. Jain and P. Onno. Methods of using commercial electromagnetic simulators for microwave and millimeter-wave circuit design and optimization. *IEEE Trans. Microwave Theory and Tech.*, MTT-45(5):724–746, May 1997.

[59] Y. Endo and T. Yoneyama. Finite element analysis of discontinuities in nonradiative dielectric waveguide. *Electronics and Communications in Japan*, 72(11):102–112, January 1989.

[60] M.P. Dębicki, P. Jędrzejewski, J. Mielewski, P. Przybyszewski, and M. Mrozowski. Application of the Arnoldi method to the solution of electromagnetic eigenproblems on the multiprocessor Power Challenge architecture. Technical Report 19/1995, Wydział Elektroniki, Politechnika Gdańska, Gdańsk, 1995.

[61] M.P. Dębicki, P. Jędrzejewski, J. Mielewski, P. Przybyszewski, and M. Mrozowski. Solution of electromagnetic eigenproblems on multiprocessor superscalar computers. In *Progress in Applied Computational Electromagnetics (ACES 96) Symposium*, Monterey, CA, March 18-22 1996.

[62] M.P. Dębicki, P. Jędrzejewski, J. Mielewski, P. Przybyszewski, and M. Mrozowski. Zastosowanie systemów wieloprocesorowych o architekturze superskalarnej do rozwiązywania macierzowych zagadnień własnych (Solution of matrix eigenproblems on multiprocessor superscalar computers). In *Zaawansowane technologie informatyczne w nauce polskiej*, pages 225–234, Kraków, 21-23 Października 1995.

[63] M.P. Dębicki, P. Jędrzejewski, J. Mielewski, P. Przybyszewski, and M. Mrozowski. Zastosowanie metody Arnoldiego do rozwiązywania elektromagnetycznych zagadnień własnych z wykorzystaniem systemów wieloprocesorowych o architekturze superskalarnej (Application of the Arnoldi method to solution of electromagnetic eigenproblems on multiprocessor superscalar computers). In *VIII Krajowe Sympozjum Nauk Radiowych*, Wrocław, 15-16 Lutego 1996.

[64] G.L. Matthaei, L. Young, and E.M.T. Jones. *Microwave filters, impedance-matching networks and couplings structures.* McGraw-Hill, New York, 1964.

[65] R.E. Colin. *Field theory of Guided Waves.* McGraw-Hill, New York, 1960.

[66] C.A. Balanis. *Advanced Engineering Electromagnetics*. John Wiley & Sons, Arizona State University, 1989.

[67] M. Mrozowski. *Properties and analysis of guided electromagnetic waves*. Research Studies Press, London, 1997.

[68] C. Nallo, F. Ferezza, A. Galli, and P. Lampariello. Analysis of the effects of metal discontinuities in nonradiative dielectric waveguide. *IEEE MTT-S Digest*, pages 233–236, 1995.

[69] J.S. Izadin and S.M. Izadin. *Microwave transition design*. Artech House, Norwood, MA 02062, 1997.

[70] J.R Brews. Characteristic impedance of microstrip line. *IEEE Trans. Microwave Theory and Tech.*, MTT-35(1):30–34, December 1987.

[71] L. Qi, M. Zhu, and H. Ma. Characteristic impedance of nonradiative dielectric waveguide and its application. *International Journal of Infrared and Millimeter Waves*, 12(2):125–129, January 1991.

[72] A. D. Berk. Variational principles for electromagnetic resonators and waveguides. *IRE Transactions on Antennas and Propagation*, pages 104–111, April 1956.

[73] T. Yoneyama, F. Kuroki, and S. Nishida. Design of nonradiative dielectric waveguide filters. *IEEE Trans. Microwave Theory and Tech.*, MTT-32(12):1659–1662, December 1984.

[74] W. Gwarek, M. Celuch-Marcysiak, M. Sypniewski, and A. Więckowski. *QuickWave - 3D manual*. `http://www.ire.pw.edu.pl/qw3d`, 1997.

[75] L Young. Direct-coupled cavity filters for wide and narrow bandwidths. *Proc. IRE*, IRE-xx:162–178, 1963.

[76] D.M. Pozar. *Microwave engineering*. John Wiley & Sons, New York, 2nd edition, 1998.

[77] Alex. H. Hall. Impedance matching by tapered or stepped transmission lines. *Microwave Journal*, pages 109–114, March 1966.

[78] R. E. Colin. The optimum tapered transmission line matching section. *Proc. IRE*, pages 539–548, 1956.

[79] R. W. Klopfstein. A transmission line taper of improved design. *Proc. IRE*, 44(1):31–35, January 1956.

[80] R. P. Hecken. A near-optimum matching section without discontinuities. *IEEE Trans. Microwave Theory and Tech.*, MTT-20(11):734–739, November 1972.

[81] C. O. Lund. A broadband transition from co-axial to helix. *RCA Rev.*, pages 133–142, March 1950.

[82] F. Bolinder. Fourier transform in the theory on inhomogeneous transmission lines. *Trans. Roy. Inst. Technol. Stockholm*, pages 1–83, 1951.

[83] T. Yoneyama and S. Nishida. Nonradiative dielectric waveguide circuit components. *International Journal of Infrared and Millimeter Waves*, 4(3):439–449, 1983.

[84] Y. Ishikawa, T. Tanizaki, and A. Saitoh. Complex permittivity measurement of dielectric materials using Nonradiative Dielectric Guide at millimeter wavelength. *Electronics and Communications in Japan*, 79(2):55–69, 1996.

[85] F. E. Gardiol. Higher-order modes in dielectrically loaded rectangular waveguides. *IEEE Trans. Microwave Theory and Tech.*, MTT-16(11):919–924, November 1968.

[86] R. Litwin and M. Suski. *Technika Mikrofalowa*. Wydawnictwa Naukowo-Techniczne, Warszawa, 1972.

[87] P. Jędrzejewski. Tanie elementy pasywne dla układów mikrofalowych na pasmo fal milimetrowych zbudowane w oparciu o linię niepromieniującą do zastosowań w masowych systemach telekomunikacyjnych, grant KBN nr 1143/T11/96/10 (Low cost passive elements built in NRD-guide for application in modern telecommunication systems). Technical Report 21/97, Wydział Elektroniki, Politechnika Gdańska, Gdańsk, 1997.

[88] P. Parmanick and P. Bhartia. A generalized theory of tapered transmission line matching transformers and asymmetric couplers supporting non-TEM modes. *IEEE Trans. Microwave Theory and Tech.*, MTT-37(8):1184–1190, August 1989.

[89] C. Schieblich, J. K. Piotrowski, and J. H. Hinken. Synthesis of optimum fin line tapers using dispersion formulas for arbitrary located slot widths and locations. *IEEE Trans. Microwave Theory and Tech.*, MTT-32(12):1638–1645, December 1984.

[90] F. Ferezza, A. Galli, G. Gerosa, G. Guglielmi, and P. Lampariello. Analisi e realizzazione di filtri in guida NRD. In *IX Riunione Nazionale di Eletromagnetismo*, Assisi, Italy, October 5-8 1992.

[91] F. Ferezza, A. Galli, G. Gerosa, and P. Lampariello. Studies on NRD filtering structures. *Ann. Télécommun.*, 47(11-12):545–547, 1992.

[92] J.C. Olivier and J.A.G Malherbe. A bandpass filter using circular discontinuities in nonradiative dielectric waveguide. *IEEE MTT-S Digest*, pages 419–422, 1987.

[93] F. Boone and Ke Wu. A multiple strip nonradiative dielectric guide filter design. In *Antem - Symposium on antenna technology and applied electromagnetics*, pages 815–818, Montreal, Quebec, Canada, August 6-9 1996.

[94] J. Huang, K. Wu, T. Wang, and R.G. Bosisio. Rigorous fields theoretical design and optimization of novel window-coupled NRD-guide bandpass filters. In *Proc. Asia-Pacific Microwave Conf.*, pages 79–82, Tokyo, Japan, December 1994. vol. 1.

[95] C.D. Nallo, F. Ferezza, A. Galli, G. Gerosa, M. Guglielmi, and P. Lampariello. Experimental investigation of NRD-guide dual-mode filters. *IEEE MTT-S Digest*, pages 237–240, 1994.

[96] J. Huang and K. Wu. A two-path multimode bandpass filters using the nonradiative dielectric (NRD) waveguide technology. *IEEE MTT-S Digest*, pages 1547–1550, 1995.

[97] J.A.G. Malherbe and J.C. Olivier. A bandstop filter constructed in coupled nonradiative dielectric waveguide. *IEEE Trans. Microwave Theory and Tech.*, MTT-34(12):1408–1412, December 1986.

[98] J.A.G. Malherbe and J.C. Coetzee. Bandstop filter in nonradiative dielectric waveguide using rectangular resonators. *IEEE Trans. Microwave Theory and Tech.*, MTT-35(12):1161–1163, December 1987.

[99] S.B. Cohn. Direct-coupled-resonator filters. *Proc. IRE*, IRE-xx:186–196, 1957.

[100] Y. Konishi and K. Uenakada. The design of a bandpass filter with inductive strip-planar circuit mounted in waveguide. *IEEE Trans. Microwave Theory and Tech.*, MTT-22:869–873, 1974.

[101] D. F. Williams and E. Schwarz. Design and performance of coplanar waveguide bandpass filters. *IEEE Trans. Microwave Theory and Tech.*, MTT-31:558–566, July 1983.

[102] R Levy. Theory of direct-coupled-cavity filters. *IEEE Trans. Microwave Theory and Tech.*, MTT-15:340–348, 1967.

[103] D.J. Rhodes. Design formulas for stepped impedance distributed and digital wave maximally flat and Chebyshev low-pass prototype filters. *IEEE Trans. on Circuits and Systems*, CAS-22:866–874, 1975.

[104] Y. Shih. Design of waveguide E-plane filters with all-metal inserts. *IEEE Trans. Microwave Theory and Tech.*, MTT–32:695–704, 1984.

[105] Mrozowski M. Jędrzejewski P. Design of NRD-guide filters. In *XI International Microwave Conference MIKON'98*, pages 3–7, Kraków, May 20-22 1998.

[106] Piotr Jędrzejewski and Michał Mrozowski. Application of FDTD method to NRD-guide bandpass filter design using half-wave step-impedance prototype. In *1999 International Conference on Computational Electromagnetics and its Application (ICCEA'99)*, Beijing, China, Nov, 1-4 1999. (accepted).

[107] Piotr Jędrzejewski. Coupleurs en guides dielectriques. Technical report, Ecole Nationale Supérieure des Télécommunications de Bretagne (ENSTB), Brest, September 1994.

[108] Piotr Jędrzejewski. Dielektryczne sprzęgacze zbliżeniowe (Dielectric proximity couplers). Master's thesis, Politechnika Gdańska, Gdańsk, Luty 1995.

[109] Piotr Jędrzejewski, Gabrielle Landrac, and Michał Mrozowski. Dielektryczne sprzęgacze zbliżeniowe zbudowane w oparciu o linię niepromieniującą (Proximity NRD-guide couplers). In *Krajowe Sympozjum Telekomunikacji '95*, pages 226–283, Bydgoszcz, 6-8 Września 1995. tom D.

[110] T. Yoneyama. Millimeter wave integrated circuits using non-radiative dielectric waveguides, Yagi symposium on advanced technologies, bringing the gap between light and microwave. In *Proc. of the Second Sendai International Conference*, pages 57–66, Japan, September 1990.

[111] H.G. Unger. *Planar optical waveguides and fibers.* Oxford University Press, Oxford, 1977.

[112] H. Eul and B. Schiek. A generalized theory and new calibration procedures for network analyzer self-calibration. *IEEE Trans. Microwave Theory and Tech.*, MTT-39(4):724–731, April 1991.

[113] G.F. Engen and C.A. Hoer. "Thru-Reflect-Line": An improved technique for calibrating the dual six-port automatic network analyzer. *IEEE Trans. Microwave Theory and Tech.*, MTT-12(12):987–993, December 1979.

[114] C. Tsironis. Calibration of network analyzers for tuner characterization. *Microwave Journal*, pages 116–122, November 1994.

[115] R.R. Pantoja, M.J. Howes, J.R. Richardson, and R.D. Pollard. Improved calibration and measurement of the scattering parameters of microwave integrated circuits. *IEEE Trans. Microwave Theory and Tech.*, MTT-37(11):1675–1680, November 1989.

[116] R.B. Marks. A multiline method of network analyzer calibration. *IEEE Trans. Microwave Theory and Tech.*, MTT-39(7):1205–1215, July 1991.